



SAIMM

JOURNAL OF THE SOUTHERN AFRICAN INSTITUTE OF MINING AND METALLURGY

VOLUME 118 NO. 6 JUNE 2018



Infacon XV: International Ferro-Alloys Congress



Infacon XV: Edition

The best blast, on time, every time

The future of mining is electronic initiation

DetNet continues to strive towards excellence in electronic initiation. As a world leader in our field, we aim to deliver the latest technology, consistent quality, and improved loading and fragmentation, all to ensure mining becomes more sustainable today and into the future. You can rely on DetNet to provide the best blast, on time, every time.



OFFICE BEARERS AND COUNCIL FOR THE 2017/2018 SESSION

Honorary President

Mxolisi Mgojo
President, Minerals Council South Africa

Honorary Vice Presidents

Gwede Mantashe
Minister of Mineral Resources, South Africa

Rob Davies
Minister of Trade and Industry, South Africa

Mmamoloko Kubayi-Ngubane
Minister of Science and Technology, South Africa

President

S. Ndlovu

President Elect

A.S. Macfarlane

Senior Vice President

M.I. Mthenjane

Junior Vice President

Z. Botha

Immediate Past President

C. Musingwini

Honorary Treasurer

J.L. Porter

Ordinary Members on Council

V.G. Duke	G. Njowa
I.J. Geldenhuys	S.M. Rupprecht
M.F. Handley	A.G. Smith
W.C. Joughin	M.H. Solomon
E. Matinde	D. Tudor
M. Motuku	D.J. van Niekerk
D.D. Munro	A.T. van Zyl

Past Presidents Serving on Council

N.A. Barcza	R.G.B. Pickering
R.D. Beck	S.J. Ramokgopa
J.R. Dixon	M.H. Rogers
M. Dworzanowski	D.A.J. Ross-Watt
H.E. James	G.L. Smith
R.T. Jones	W.H. van Niekerk
G.V.R. Landman	R.P.H. Willis

G.R. Lane-TPC Mining Chairperson
Z. Botha-TPC Metallurgy Chairperson

A.S. Nhleko-YPC Chairperson
K.M. Letsoalo-YPC Vice Chairperson

Branch Chairpersons

Botswana	L.E. Dimbungu
DRC	S. Maleba
Johannesburg	J.A. Luckmann
Namibia	N.M. Namate
Northern Cape	W.J. Mans
Pretoria	R.J. Mostert
Western Cape	R.D. Beck
Zambia	D. Muma
Zimbabwe	S. Matutu
Zululand	C.W. Mienie

Corresponding Members of Council

Australia: I.J. Corrans, R.J. Dippenaar, A. Croll,
C. Workman-Davies

Austria: H. Wagner

Botswana: S.D. Williams

United Kingdom: J.J.L. Cilliers, N.A. Barcza

USA: J.-M.M. Rendu, P.C. Pistorius

PAST PRESIDENTS

*Deceased

* W. Bettel (1894–1895)	* H. Simon (1957–1958)
* A.F. Crosse (1895–1896)	* M. Barcza (1958–1959)
* W.R. Feldtmann (1896–1897)	* R.J. Adamson (1959–1960)
* C. Butters (1897–1898)	* W.S. Findlay (1960–1961)
* J. Loevy (1898–1899)	* D.G. Maxwell (1961–1962)
* J.R. Williams (1899–1903)	* J. de V. Lambrechts (1962–1963)
* S.H. Pearce (1903–1904)	* J.F. Reid (1963–1964)
* W.A. Caldecott (1904–1905)	* D.M. Jamieson (1964–1965)
* W. Cullen (1905–1906)	* H.E. Cross (1965–1966)
* E.H. Johnson (1906–1907)	* D. Gordon Jones (1966–1967)
* J. Yates (1907–1908)	* P. Lambooy (1967–1968)
* R.G. Bevington (1908–1909)	* R.C.J. Goode (1968–1969)
* A. McA. Johnston (1909–1910)	* J.K.E. Douglas (1969–1970)
* J. Moir (1910–1911)	* V.C. Robinson (1970–1971)
* C.B. Saner (1911–1912)	* D.D. Howat (1971–1972)
* W.R. Dowling (1912–1913)	* J.P. Hugo (1972–1973)
* A. Richardson (1913–1914)	* P.W.J. van Rensburg (1973–1974)
* G.H. Stanley (1914–1915)	* R.P. Plewman (1974–1975)
* J.E. Thomas (1915–1916)	* R.E. Robinson (1975–1976)
* J.A. Wilkinson (1916–1917)	* M.D.G. Salamon (1976–1977)
* G. Hildick-Smith (1917–1918)	* P.A. Von Wielligh (1977–1978)
* H.S. Meyer (1918–1919)	* M.G. Atmore (1978–1979)
* J. Gray (1919–1920)	* D.A. Viljoen (1979–1980)
* J. Chilton (1920–1921)	* P.R. Jochens (1980–1981)
* F. Wartenweiler (1921–1922)	* G.Y. Nisbet (1981–1982)
* G.A. Watermeyer (1922–1923)	* A.N. Brown (1982–1983)
* F.W. Watson (1923–1924)	* R.P. King (1983–1984)
* C.J. Gray (1924–1925)	* J.D. Austin (1984–1985)
* H.A. White (1925–1926)	* H.E. James (1985–1986)
* H.R. Adam (1926–1927)	* H. Wagner (1986–1987)
* Sir Robert Kotze (1927–1928)	* B.C. Alberts (1987–1988)
* J.A. Woodburn (1928–1929)	* C.E. Fivaz (1988–1989)
* H. Pirow (1929–1930)	* O.K.H. Steffen (1989–1990)
* J. Henderson (1930–1931)	* H.G. Mosenthal (1990–1991)
* A. King (1931–1932)	* R.D. Beck (1991–1992)
* V. Nimmo-Dewar (1932–1933)	* J.P. Hoffman (1992–1993)
* P.N. Lategan (1933–1934)	* H. Scott-Russell (1993–1994)
* E.C. Ranson (1934–1935)	* J.A. Cruise (1994–1995)
* R.A. Flugge-De-Smidt (1935–1936)	* D.A.J. Ross-Watt (1995–1996)
* T.K. Prentice (1936–1937)	* N.A. Barcza (1996–1997)
* R.S.G. Stokes (1937–1938)	* R.P. Mohring (1997–1998)
* P.E. Hall (1938–1939)	* J.R. Dixon (1998–1999)
* E.H.A. Joseph (1939–1940)	* M.H. Rogers (1999–2000)
* J.H. Dobson (1940–1941)	* L.A. Cramer (2000–2001)
* Theo Meyer (1941–1942)	* A.A.B. Douglas (2001–2002)
* John V. Muller (1942–1943)	* S.J. Ramokgopa (2002–2003)
* C. Biccard Jeppe (1943–1944)	* T.R. Stacey (2003–2004)
* P.J. Louis Bok (1944–1945)	* F.M.G. Egerton (2004–2005)
* J.T. McIntyre (1945–1946)	* W.H. van Niekerk (2005–2006)
* M. Falcon (1946–1947)	* R.P.H. Willis (2006–2007)
* A. Clemens (1947–1948)	* R.G.B. Pickering (2007–2008)
* F.G. Hill (1948–1949)	* A.M. Garbers-Craig (2008–2009)
* O.A.E. Jackson (1949–1950)	* J.C. Ngoma (2009–2010)
* W.E. Gooday (1950–1951)	* G.V.R. Landman (2010–2011)
* C.J. Irving (1951–1952)	* J.N. van der Merwe (2011–2012)
* D.D. Stitt (1952–1953)	* G.L. Smith (2012–2013)
* M.C.G. Meyer (1953–1954)	* M. Dworzanowski (2013–2014)
* L.A. Bushell (1954–1955)	* J.L. Porter (2014–2015)
* H. Britten (1955–1956)	* R.T. Jones (2015–2016)
* Wm. Bleloch (1956–1957)	* C. Musingwini (2016–2017)

Honorary Legal Advisers

Scop Incorporated

Auditors

Genesis Chartered Accountants

Secretaries

The Southern African Institute of Mining and Metallurgy
Fifth Floor, Minerals Council South Africa Building
5 Hollard Street, Johannesburg 2001 • P.O. Box 61127, Marshalltown 2107
Telephone (011) 834-1273/7 • Fax (011) 838-5923 or (011) 833-8156
E-mail: journal@saimm.co.za

Editorial Board

R.D. Beck
P. den Hoed
M. Dworzanowski
B. Genc
M.F. Handley
R.T. Jones
W.C. Joughin
H. Lodewijks
J.A. Luckmann
C. Musingwini
S. Ndlovu
J.H. Potgieter
N. Rampersad
T.R. Stacey
M. Tlala

Editorial Consultant

D. Tudor

Typeset and Published by

The Southern African Institute of Mining and Metallurgy
P.O. Box 61127
Marshalltown 2107
Telephone (011) 834-1273/7
Fax (011) 838-5923
E-mail: journal@saimm.co.za

Printed by

Camera Press, Johannesburg

Advertising Representative

Barbara Spence
Avenue Advertising
Telephone (011) 463-7940
E-mail: barbara@avenue.co.za
ISSN 2225-6253 (print)
ISSN 2411-9717 (online)



Directory of Open Access Journals



THE INSTITUTE, AS A BODY, IS NOT RESPONSIBLE FOR THE STATEMENTS AND OPINIONS ADVANCED IN ANY OF ITS PUBLICATIONS.

Copyright© 2018 by The Southern African Institute of Mining and Metallurgy. All rights reserved. Multiple copying of the contents of this publication or parts thereof without permission is in breach of copyright, but permission is hereby given for the copying of titles and abstracts of papers and names of authors. Permission to copy illustrations and short extracts from the text of individual contributions is usually given upon written application to the Institute, provided that the source (and where appropriate, the copyright) is acknowledged. Apart from any fair dealing for the purposes of review or criticism under **The Copyright Act no. 98, 1978, Section 12**, of the Republic of South Africa, a single copy of an article may be supplied by a library for the purposes of research or private study. No part of this publication may be reproduced, stored in a retrieval system, or transmitted in any form or by any means without the prior permission of the publishers. **Multiple copying of the contents of the publication without permission is always illegal.**

U.S. Copyright Law applicable to users in the U.S.A.

The appearance of the statement of copyright at the bottom of the first page of an article appearing in this journal indicates that the copyright holder consents to the making of copies of the article for personal or internal use. This consent is given on condition that the copier pays the stated fee for each copy of a paper beyond that permitted by Section 107 or 108 of the U.S. Copyright Law. The fee is to be paid through the Copyright Clearance Center, Inc., Operations Center, P.O. Box 765, Schenectady, New York 12301, U.S.A. This consent does not extend to other kinds of copying, such as copying for general distribution, for advertising or promotional purposes, for creating new collective works, or for resale.



SAIMM

JOURNAL OF THE SOUTHERN AFRICAN INSTITUTE OF MINING AND METALLURGY

VOLUME 118 NO. 6 JUNE 2018

Contents

Journal Comment: Infacon XV by R.T. Jones	iv
President's Corner: Upskilling the heroes of the mining industry by S. Ndlovu	v
Obituary—Dee Bradshaw by Campus Communications, University of Cape Town	vi

INFACON XV: INTERNATIONAL FERRO-ALLOYS CONGRESS 2018

Changing nickel and chromium stainless steel markets – a review by H.H. Pariser, N.R. Backeberg, O.C.M. Masson, and J.C.M. Bedder <i>This market review covers the changing fortunes of the nickel and chromium markets, which are intimately tied to stainless steel production, and discusses possible future trends.</i>	563
Tariff developments for electricity-intensive industry in South Africa by C.S. Mahony and J.M. Baartman <i>South Africa has experienced above-inflation electricity price increases over the past decade. Reduced consumption by large industrial consumers reduces the system load factor, exerting upward pressure on the unit cost of electricity. Eskom proposes to introduce a suite of more cost-reflective tariffs aimed at stabilizing, and even growing, consumption by electricity-intensive customers with high load factors.</i>	569
Reduction of Kemi chromite with methane by M. Leikola, P. Taskinen, and R.H. Eric <i>Kemi chromite ore from Finland was reduced in CH₄-H₂ gas mixtures at temperatures from 1100° to 1350°C. The results of this work showed that the reduction is highly efficient, and high extents of reduction can be reached faster at lower temperatures compared to carbothermic reduction.</i>	575
NaOH-assisted direct reduction of Ring of Fire chromite ores, and the associated implications for processing by S. Sokhanvaran, D. Paktunc, and A. Barnes <i>Studies of the chromite ores in the 'Ring of Fire' region of northern Ontario have focused on developing alternative approaches for producing ferrochrome at lower temperatures and with fewer greenhouse gas emissions. This paper summarizes the key findings of the latest work, including the role of NaOH in the reduction processes, and parameters influencing the degree of metallization and alloy particle growth. The implications of the results with respect to benefits, challenges, and opportunities for processing Ring of Fire chromite into saleable chrome units are discussed.</i>	581
Carbonylation of nickel and selectively reduced laterite ore by Y. Cui, G. Zhang, S. Jahanshahi, and O. Ostrovski <i>Carbonylation of nickel obtained by reduction of nickel oxide and selectively reduced Australian laterite ore was studied at temperatures of 80-100°C and CO gauge pressures of 0-56 atm. Sulphur-containing catalysts were found to accelerate the reaction for pure nickel, but were ineffective in the case of selectively reduced ore.</i>	589

International Advisory Board

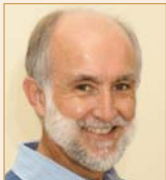
R. Dimitrakopoulos, *McGill University, Canada*
D. Dreisinger, *University of British Columbia, Canada*
E. Esterhuizen, *NIOSH Research Organization, USA*
H. Mitri, *McGill University, Canada*
M.J. Nicol, *Murdoch University, Australia*
E. Topal, *Curtin University, Australia*



Contents (continued)

Effect of electrode shape on the current distribution in submerged arc furnaces for silicon production – A modelling approach by Y.A. Tesfahunegn, T. Magnusson, M. Tangstad, and G. Saevarsdottir	595
<i>This work presents computations of electrical current distributions inside an industrial submerged arc furnace for silicon production. A qualitative analysis of the results showed that the 3D modelling approach that was developed gave reasonable results.</i>	
Thermodynamic evaluation of Sr-containing Si metals and silicate melts for Si-Sr alloy production by K. Tang, L.K. Jakobsson, and K. Hildal	601
<i>Reliable thermodynamic descriptions of the Si-based Sr-Al-Ca-Fe-Mg metal and SiO₂-SrO-CaO-MgO-Al₂O₃ oxide systems are essential for the understanding and optimizing of the production of Si-Sr alloys. Thermodynamic modelling of the relevant binary, ternary, and quaternary systems was conducted, and the newly developed thermochemical databases examined by comparing the calculated equilibrium distribution of Sr between metal and slag with recent experimental data.</i>	
3D models of proximity effects in large FeSi and FeMn furnaces by E.V. Herland, M. Sparta, and S.A. Halvorsen	607
<i>A numerical study of the proximity effects between the currents in the electrodes and alloy, and the induced currents in the lining and shell utilizing realistic 3D geometries of ferromanganese and ferrosilicon furnaces, is presented. The results show that there are strong skin and proximity effects in the conductive material layers within the furnace.</i>	
The use of satellite observations of fire radiative power to estimate the availabilities (activity patterns) of pyrometallurgical smelters by J.P. Beukes, P.G. Van Zyl, M. Sofiev, J. Soares, H. Liebenberg-Enslin, N. Shackleton, and A.-M. Sundström	619
<i>It is important to model the contribution, transport, and impact of pollutants emitted by pyrometallurgical smelters. In this paper the authors demonstrate how fire radiative power (FRP) observations by the Moderate Resolution Imaging Spectroradiometer (MODIS) instruments on board the Aqua and Terra satellites can be used to estimate the availabilities of pyrometallurgical smelters. Such temporal activity patterns will assist modellers to re-create air quality scenarios for regions more accurately.</i>	
Impact of air granulation on the ferrochrome value chain in metallurgical smelter complexes by F. Hannemann, M. Bradfield, M. Mahdi, L.L.C. So, and D. Metcalfe	625
<i>Air granulation is being tested to evaluate its effect on the ferrochrome value chain within a typical South African metallurgical complex. The results of this first-of-its-kind work are reported, and strategies for its successful integration explored.</i>	
Basic parameters in the operation and design of submerged arc furnaces, with particular reference to production of high-silicon alloys by T.E. Magnussen	631
<i>A review of the basic parameters in the operation of submerged arc furnaces is presented. A case study shows how the furnace dimensioning and design affects the furnace efficiency and hence the specific energy consumption.</i>	
Chrome ore mineralogy and the furnace mass and energy balance by N.J. Sweeten, S.M.C. Verryn, J. Oberholzer, and J.H. Zietsman	637
<i>The results of mineralogical analyses of South African, Zimbabwean, and Khazakstan chrome ores are presented, and the energy balance results based on standard chemical assays compared to those based on mineralogical information, using EMSIM as the calculation tool.</i>	
Working towards an increase in manganese ferroalloy production in South Africa – a research agenda by J.D. Steenkamp, W.G. Bam, E. Ringdalen, M. Mushwana, S.A.C. Hockaday, and N.A. Sithole	645
<i>A research agenda aimed at increasing manganese ferroalloy production in South Africa has been developed. Inputs were obtained from various role-players in the value chain to develop a technology roadmap that could then facilitate the implementation of such an agenda.</i>	
Influence of the power supply on the behaviour of DC plasma arcs – a modelling study by Q.G. Reynolds	655
<i>Computational plasma arc models were developed using open-source software tools to gain insight into the nature of interactions between the DC rectifier's transient behaviour, passive circuit elements, and the dynamics of the arc. The effect of parameters such as choke inductance and thyristor firing angle is examined and interpreted to enable the optimization of the design and operation of DC furnace power supplies in the future.</i>	
Fluxing of South African chromite ore with colemanite by M.W. Erwee, I.J. Geldenhuys, M.B. Sitefane, and M. Masipa	661
<i>Laboratory-scale smelting tests were conducted to evaluate a variety of boron-containing materials to replace conventional fluxes. The results of the tests and modelling work are presented in this paper.</i>	

Infacon XV



The Fifteenth International Ferro-Alloys Congress (Infacon XV) was held in Cape Town from 25 to 28 February 2018, and was attended by 450 delegates from 32 countries. After a cycle of four congresses in the northern hemisphere (New Delhi, India, 2007; Helsinki, Finland, 2010; Almaty, Kazakhstan, 2013; and Kyiv, Ukraine, 2015), it was appropriate that Infacon should return to South Africa at a time of great change in the region.

This series of congresses began in Johannesburg in 1974 under the guidance of Professor Robbie Robinson, then Director General of the National Institute for Metallurgy (NIM), the predecessor of Mintek; he also became President of SAIMM in 1975. (Robbie remained an active contributor to the Journal of the SAIMM until shortly before his passing away at the age of 86 in 2016.) In 1974, Robbie was the Chairman of the Organizing Committee of the First International Congress on Ferro-Alloys (Infacon) – a partnership between what is now Mintek, the SAIMM, and FAPA (Ferro-Alloy Producers' Association). He also established an international governance structure that is now known as the International Committee on Ferro-Alloys (ICFA), which is made up of representation from major countries that produce and consume ferro-alloys. ICFA was chaired for many years, until the most recent congress, by Dr Nic Barcza (President of the SAIMM in 1996–1997).

The Infacon series of conferences continues to thrive, and Infacon has become established as the premier technical conference serving the international ferro-alloys industry. It has been held in twelve different countries around the world, and continues to grow in size and stature.

Infacon XV covered the major ferro-alloys (especially FeCr and FeMn) extensively. The primary focus was on the technical aspects of production processes, furnaces, and power supplies, but safety, environmental, and legislative topics were also covered. The discussions reflected many of the needs and challenges faced by ferro-alloy producers today.

This congress reflected a changing industry in a changing world. There have been major structural changes in the ferro-alloys industry over the past few years, as companies seek to find the global economic optimum of where and how important metals are produced. For example, in 2012, China replaced South Africa as the leading producer of ferrochromium. More recently, we see further evidence of change in South Africa's new political leadership, and a mood of optimism is now coming to the fore. The current drought in Cape Town emphasized the importance of adapting to a changing climate, and prompted delegates to reflect on how, as responsible citizens of our planet, we can improve the environmental performance and energy efficiency of our industry. South Africa has played a leading role in the global ferro-alloys industry for a long time. Even if the nature of its contribution changes, the country will continue to be a major player in this arena.

Delegates were pleased to have Infacon return to Cape Town – a city of great scenic beauty and world heritage sites. A welcoming function was held the evening before the conference at 'On the Rocks' in Bloubergstrand, with a spectacular view of Table Mountain and the sunset over Robben Island. The conference dinner was held at Kirstenbosch National Botanical Gardens, accompanied by an extensive and wide-ranging cultural programme of dancing and singing.

The peer review process was taken very seriously, and the organizers have drawn on the expertise and insights of a group of 146 specialists from around the world who generously offered constructive criticism and suggestions. These contributions improved the quality of papers greatly. About 150 papers were selected from 199 abstracts submitted. Each paper was thoroughly reviewed by at least two independent specialists in that field. We are grateful to the expert reviewers who gave of their time freely in undertaking this monumental task, and appreciate their valuable technical and editing contributions. We also appreciate the time and effort that authors put into their papers and presentations.

Infacon is based on the principle that the sharing of technical information benefits the industry. The publication of scientific and engineering work is vital. The Infacon series of congresses is well known for the quality of its papers, due largely to the considerable work that is put into reviewing. ICFA has a policy of making papers from all Infacon conferences, current and past, freely available via open access. Past papers are now available online.

I am very grateful to the members of the Organizing Committee (and their employers – Mintek and the University of the Witwatersrand), the reviewers, authors, and presenters – all of whom have put so much into the congress. Special thanks are due to the SAIMM conferencing and publishing teams for hosting and ensuring the smooth running of this event. The Ferro-Alloy Producers' Association (FAPA) encouraged its members to open their operations to visitors, and a well-supported programme of post-conference technical tours was arranged. The experienced International Advisory Committee was always ready and available to offer support and guidance. The support of our sponsors and exhibitors is also greatly appreciated. In particular, we should like to acknowledge our platinum sponsor Hatch, gold sponsors Furncor and Ripasso Energy, and silver sponsors Metix, RHI Magnesita, Vatvedt Group, W.L. Gore & Associates, and Dneprohydromach.

At the conclusion of the conference an African drum, a tangible symbol of Infacon XV, was handed over by Professor Hurman Eric, on behalf of South Africa, to Benjamin Ravary from Norway, as that is where the next Infacon will be held in 2021.

R.T. Jones



Upskilling the heroes of the mining industry



I recently had the pleasure and opportunity to listen to one of the most well-known and admired person in South Africa; the former Public Protector, Advocate Thuli Madonsela. She gave keynote addresses at the International Women's Day celebration hosted by the Motsepe Foundation and at the pre-AGM dinner for the Chamber of Mines (now known as the Minerals Council South Africa, or MCSA). On both occasions, she gave a remarkably inspiring and thought-provoking speech on what it means to lead and fight for what you believe in. At the MCSA dinner, she not only spoke of the need for ethical leadership but also discussed the importance of being attuned to the needs and realities of a country. She talked of being persecuted for her stance on corruption, and I realized that South Africa admires her for her stance and the contribution she made to the betterment of the country. In her speech at the Women's Day celebration event, she spoke of some unsung and unseen heroes; those 'signposts' that make huge differences for others without much benefit to themselves.

During Advocate Madonsela's talk, my thoughts wandered to the unsung heroes in the mining and minerals sector. The unsung heroes that oftentimes work under challenging environments and conditions in order to build a legacy for future generations. Not the managers and executive officers but the low-skilled and semi-skilled employees like miners, drivers and operators that work at the 'coalface' of all the operations. These are an incredible underrated group of people that are the invisible driving force behind countless measures that contribute to the bottom line. They play an unrecognized, and very often, unacknowledged, but very significant role in the mining sector and hence, in unlocking economic growth and development in countries that are dependent on mining.

It is worthy of note that because the individuals in this workforce are semi-skilled, they are usually the first to lose their jobs when mining companies face challenging downturns and have to downsize. And since they usually do not have other critical skills or knowledge other than mining, they are not insulated against job loss and find themselves faced with a depressing future. In addition, the changing mining landscape, depth of mining, and technological advances suggest that mining operations will need to move from labour-intensive to knowledge-based operations as mechanization and automation become inevitable. Such an approach needs a workforce that possesses more than basic skills. However, there is currently a major disconnect between the low-skilled and semi-skilled nature of the workforce and the skills that the industry needs to ensure its future success. As a result, skills development is very crucial. Stakeholders such as industry, educators, and government need to work together to ensure an upskilled and future-ready workforce. By offering meaningful as well as stimulating work and opportunities for development through training and upskilling, the industry will be able to attract and retain the best talent, thus eliminating uncertainty in the market. A further significant benefit is that skills development can assist in enabling workers to find alternative forms of employment when the industry moves through cyclic downturns and moreover, when it moves into a more mechanized space in the future. In addition, the entire economy can benefit because of the potential transportability of skills to other sectors.

The skills development approach requires flexibility on the part of the mining companies and educational sector. Most mainstream educational institutions have fixed curricula and requirements that are not very accommodative to training and upskilling low-skilled and semi-skilled groups of workers. The Technical Vocational Educational and Training Colleges, although designed to fill such a gap, are not very well funded and struggle to successfully run these training programmes. Government intervention in this respect is needed. Mining companies tend to cite the loss in production time associated with skills development and training, and are thus sometimes reluctant to release workers for training opportunities. An alternative approach is for more company on-site training and investment in training academies to address the skills problem in the mining industry. As Advocate Thuli Madonsela emphasized, it takes a leadership that is attuned to the needs and realities of a country for a new dawn to emerge. If mining companies and countries want to remain more competitive and stay ahead of the race, then training at all levels remains an imperative. And in all this, our hero who has steadfastly held the anchor at the forefront of the operations should not be forgotten.

S. Ndlovu
President, SAIMM

Obituary—Dee Bradshaw

22 September 1958–7 June 2018

Emeritus Professor Dee Bradshaw passed away on 7 June 2018 after a courageous battle with cancer, just a few months short of her 60th birthday. Throughout her illness, Dee remained a leading light and inspiration to students, colleagues, and professionals across the globe. A major highlight for her in 2018 was the launch of her book 'Green Mining: Beyond the Myth' at the Two Oceans Aquarium ahead of the annual Mining Indaba - attended by senior representatives of the Minister of the Presidency, AngloGold Ashanti, and the University of Cape Town (UCT) as well as colleagues, students, friends, and family. The book culminates a career of thought leadership, a passion for people and minerals in collectively addressing complex, intractable problems in society.

Dee was born in Masvingo in Zimbabwe, the eldest of four children. She arrived at UCT in the late 1970s as a young undergraduate student entering a traditionally male-dominated discipline and graduated with a BSc in Chemical Engineering in 1981. With a young family to support, Dee started work as a part-time research assistant in the Flotation Group at UCT in 1983. Over the course of 25 years in this group, Dee emerged as an independent researcher with an international profile for her expertise in flotation chemistry, both in industry and academia. She also initiated several new research activities, including the Depressant Research Facility and Process Mineralogy - both of which are still going strong in the Centre for Minerals Research. Following an industry-based sabbatical in 2007, Dee moved to Australia to take up a Professorship at the Julius Kruttschnitt Mineral Research Centre at the University of Queensland in Brisbane. Dee returned to UCT in 2015 to take up a National Research Foundation South African Research Chair in Mineral Beneficiation and step in as Director of the interdisciplinary Minerals to Metals research grouping hosted by the Department of Chemical Engineering - posts which were both aimed at building a platform for sustainable development in Africa through metals and minerals, and which she held until her retirement in February 2018.

Dee Bradshaw was ever passionate about inspiring, nurturing, challenging, creating opportunities, guiding and mentoring countless young lives across the world in the minerals industry and beyond. In 2013 she received an award from the University of Queensland for excellence in postgraduate supervision, which recognized her as a leader who nurtures and develops her graduate students, a concept she called 'Living Gold'. Just a few weeks prior to her passing, she established the 'Dee Bradshaw and Friends International Travel Scholarship' for postgraduate students in the minerals discipline as her legacy to UCT. Donations to this initiative can be made at

http://www.ebe.uct.ac.za/sites/default/files/image_tool/images/50/News/2018/Dee%20Bradshaw%20%26%20Friends%20donation%20letter.pdf

The SAIMM, and the Western Cape Branch in particular, is deeply indebted to Dee for her dedicated and passionate contributions over almost four decades. She will long be remembered by all those with whom she came into contact - and as the 'Living Gold' continues to live on.



Photograph courtesy of
Julian Goldswain

Campus Communications
University of Cape Town



Changing nickel and chromium stainless steel markets – a review

by H.H. Pariser, N.R. Backeberg, O.C.M. Masson, and J.C.M. Bedder

Synopsis

This review covers the changing fortunes of the nickel and chromium markets, which are intimately tied to stainless steel production. Over the last few decades, growth in the stainless steel market has outpaced that of the carbon steel, aluminium, copper, and zinc markets, and as a result, demand for nickel and chromium has benefited. The emergence of China as the world's largest stainless steel producer – estimated at 54% of world supply in 2017 – means the country needs increasing quantities of chrome ore: Chinese imports increased by 29% year-on-year in 2017. The dynamics of the chrome trade are heavily skewed towards South Africa and China, but how long will this continue? The sheer size of China's stainless steel industry means that it is also the largest consumer of primary nickel, thanks to the industry's reliance on primary units, mostly in nickel pig iron. We estimate that stainless steel production accounted for 68% of global primary nickel demand in 2017, but this ratio is set to decline in the years ahead as the increased electrification of automotive transport leads to higher requirements for nickel in batteries.

Keywords

stainless steel, nickel, chromium, ferrochrome, scrap.

Introduction

Stainless steel remains the principal end-use for chromium and nickel units. Stainless steel is a generic term for corrosion-resistant alloy steels containing 10.5% or more chromium. In the AISI (American Iron and Steel Institute) classification of steels, stainless steel must contain 10% or more chromium; in the BSI (British Standards Institution) classification, it must contain 11.5% chromium or more. The addition of 10% chromium to a steel gives corrosion resistance in mild environments; additions of over 18% chromium give protection in more aggressive environments in the chemical, petrochemical, process, and power industries. Nickel is mostly added to improve the formability and ductility of stainless steel. In 1960, nickel demand in stainless steel was 219 kt, accounting for no more than 34% of the global nickel demand. This grew to a 68% market share in 2017, accounting for approximately 1470 kt of primary nickel. Alloying with these elements brings out different crystal structures in stainless steel to impart different properties in machining, forming, and welding.

Roskill Pariser presents a market review for the nickel and chromium stainless steel

markets, with historical data as of 19 January 2018. The data presented in this paper is sourced from Roskill Pariser Steel Alloys and Roskill Information Services, unless stated otherwise. It includes certain statements that may be deemed 'forward-looking'.

Although we have made every reasonable effort to ensure the veracity of the information presented, we cannot expressly guarantee the accuracy and reliability of the estimates, forecasts, and conclusions contained herein. Accordingly, the statements in the presentation should be used for general guidance only.

Stainless steel

Stainless steel has been one of the fastest-growing metal products over the past decades, outperforming carbon steels and aluminium as well as other base metals, owing to rapid growth in demand from sectors such as construction, transportation, and consumer products (Figure 1).

Stainless steel demand in the 1950s to 1970s was defined by the post-war reconstruction period. Before the 1960s, the US stainless steel market was leading global development, until a few stainless steel producers in Japan and in Europe steadily increased their market shares to overtake the USA in the late 1960s. Prior to 1980 China had been sporadically melting stainless steel, but only became a noteworthy supply source from the year 2000 onwards.

In recent years, China has developed into the global market leader, thanks to the rapidly growing Asian stainless demand and China's capability of meeting this demand with 'unconventional' raw material usage – in particular nickel pig iron (NPI), but also due to

* Roskill Pariser Steel Alloys, UK.

© The Southern African Institute of Mining and Metallurgy, 2018. ISSN 2225-6253. This paper was first presented at the INFACON XV: International Ferro-Alloys Congress, 25–28 February 2018, Century City Conference Centre and Hotel, Cape Town, South Africa

Changing nickel and chromium stainless steel markets – a review

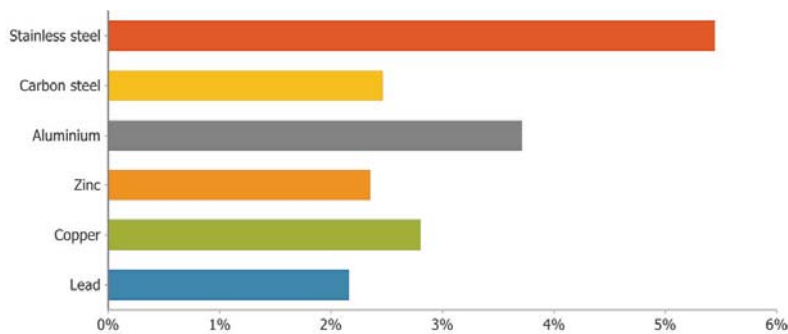


Figure 1—Comparison of growth rates of stainless steel to other metals, 1980 to 2015 (source: ISSF)

state-supported capital expenditure on modern stainless steelmaking equipment.

Japan has become a technology leader in a range of stainless steel applications for the automotive industry and various other consumer goods, while European stainless steel producers have focused on a wide range of applications in equipment used in demanding environments such as chemical plants, power stations, and other industrial applications, as well as household appliances, consumer goods, and automotive parts.

In the USA, market performance has been relatively steady over the last five years. In contrast, the performance in Japan has been more volatile, while China's stainless output resumed its upwards path in 2016 and 2018, following a modest decline in 2015. In 2017, we estimate that China accounted for 54% of world crude stainless steel production.

End-use structure of stainless steel

It is a hopeless task quantifying the thousands of different applications for stainless steels. The top five end-use segments, which we outline here, account for some 77% of the recent markets.

The dominant end-use applications for stainless steels are still in machinery and equipment, followed by basic metals as well as fabricated metal products. These three product groups account for some 58% of the aggregated market volume in industrialized countries, while in developing and emerging countries their share is as high as 69% (Figure 2). Motor vehicles play an important role in industrialized countries, accounting for some 12.4% while their ratio in developing and emerging countries is not more than 5.3%.

One market segment with a strong regional application is architecture, building, and construction (ABC). Globally, ABC accounts for some 13% of stainless steel consumption, but we observe wide variations on a regional basis. Japan, for instance, has traditionally had a strong preference for stainless steel roofing and bath tubs, but these applications are rarely found in European countries.

We follow quarterly stainless supply and demand volumes, which show an almost steady performance reflecting the stabilizing impact from the steady growth performance of China. In earlier decades, the market went through significant fluctuations due to stocking and de-stocking activity. The two diagrams in Figure 3 illustrate the developments in stainless steel demand over the last seven

years. Demand growth in developing and emerging countries amounts to some 6.3% annually, which is more than twice as fast as in industrialized countries.

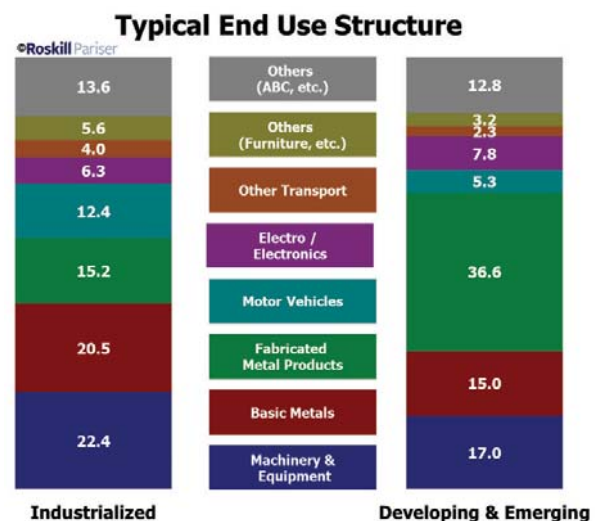


Figure 2—Typical end-use structure in industrialized and developing and emerging countries

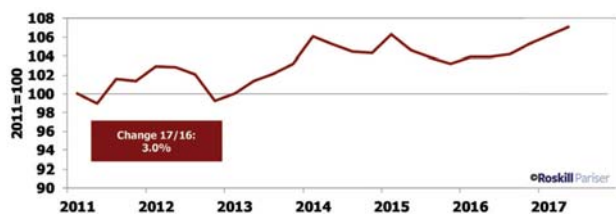


Figure 3a—Weighted stainless steel demand index in industrialized countries

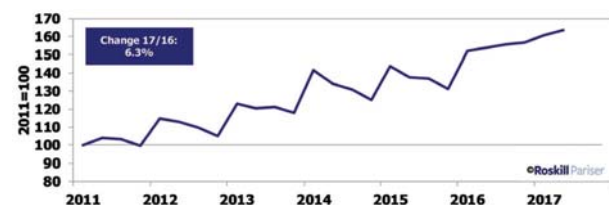


Figure 3b—Weighted stainless steel demand index in developing and emerging countries

Changing nickel and chromium stainless steel markets – a review

Stainless steel price and market balance

One of the key reasons for the steady demand growth in stainless steel is relative price stability. Stainless steel prices are published by various sources, but we found that our own evaluation of service centre sales prices provides a more realistic picture of the market over the past 6–8 years.

In our opinion, the lack of reliable price information is a major handicap for the global stainless steel market. Modern price hedging under the prevailing circumstances is hardly possible.

We have followed stainless steel prices regularly since 1967, the first year that a generally accepted definition for stainless steel was introduced. Since then, nominal stainless steel prices have remained within a narrow range, close to the 1967 base year (Figure 4). Major price increases occurred during periods of high nickel prices, as was the case in 1989–1990 and again two decades later in 2008–2010. However, stainless steel prices have usually weakened again after the short high-price periods. In contrast, since 2005 stainless steel prices have stabilized above the base year value in a range of some 120–130 index points.

A price comparison with other commodities shows that iron and steel prices have outgrown stainless steel prices significantly, while prices for non-ferrous alloys, which include mostly copper alloys and aluminium, have also outperformed stainless steel.

Nickel

'I have called it "Nickel"': Axel Fredrik Cronstedt, 1722–1765

China has developed into the largest market for primary nickel. The country is forecast to account for almost 57% of global nickel consumption in 2018. The second largest regional market is the European Union accounting for 13.5%, whereas markets combined under 'Other Asia' rank third with a global share of almost 10%. All other regions remain well below the 5% market position.

Primary nickel markets have been divided into Class I and Class II materials, and chemical products used in the battery industry. We forecast the use of primary nickel in batteries to rise by an average of over 20% per year between 2017 and 2027. The scale of growth reflects not only the expected size of the market a decade from now, but also its current small size. The main driver behind the forecast increase in this market's

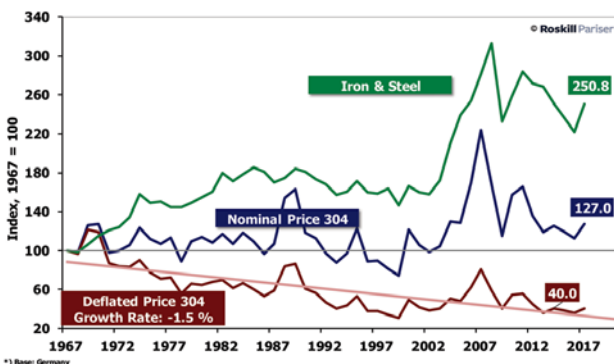


Figure 4—Stainless steel price competitiveness indexed to 1967

size is the electrification of the automotive industry. Nickel demand will benefit not only from the substitution of internal combustion engines in cars by lithium-ion batteries, but also from changes in battery chemistries towards increasing concentrations of nickel, which will give the market an additional boost, primarily from nickel sulphates. The details of this research have been recently published in Roskill's broader battery materials analytics and bespoke research.

The changing product mix is marginally influencing the Class I nickel segment, including carbonyl nickel pellets, electrolytic nickel cathodes, and briquettes, expanding by only 1.2% per annum over the same period, and reaching a level of some 1 Mt by 2027.

Class II materials are primarily applied for stainless steel melting and include the classical ferronickel qualities, but also utility nickel, nickel oxide sinter, and NPI. This product group is expected to expand by 4.9% per annum between 2017 and 2027 to 1.7Mt.

Overall, nickel supply might need to reach some 3.1 Mt by 2027, 1 Mt more than in 2017, to keep up with rising demand, particularly from the batteries sector. For 2018 we assume a market volume of nickel at approximately 2.1 Mt. Electrolytic nickel cathodes should remain the main product group, followed closely by NPI, both accounting for around 600 kt. Ferronickel is the third largest product at 450 kt, with nickel briquettes accounting for just over 200 kt. The balance includes nickel oxide sinter, carbonyl nickel pellets, and sulphates (Figure 5).

Nickel pig iron in China

The development of the NPI market enabled China to feed its rising stainless steel production. NPI output grew strongly between 2005 and 2014 but slowed from 2015 onwards, primarily due to lack of sufficient feed material. Production has moved back to over 100 kt per quarter recently as the ore availability has started to improve.

Over the years, Chinese producers of NPI have changed their product mix. Almost 80% of the current output consists of high-grade materials containing more than 10% Ni, while low-grade materials with no more than 2% Ni have diminished to approximately 20%. Medium-grade NPI, containing 4–6% Ni, was popular at the beginning of the decade, when it accounted for some 30% of the total NPI output, but this market has virtually ceased to exist, falling below 1% in 2016.

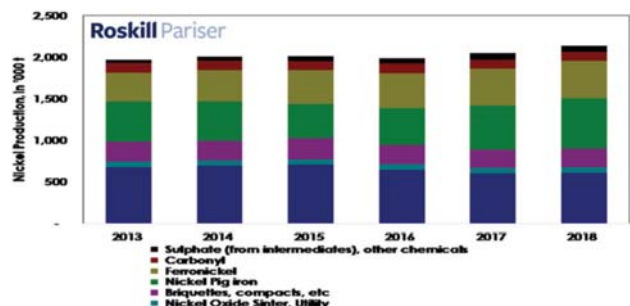


Figure 5—Nickel supply by type, 2013–2018

Changing nickel and chromium stainless steel markets – a review

Nickel price developments since January 2016

Nickel prices went into 2016 at particularly low levels, of around US\$8 000 per ton. However, as the market began to tighten after several years of chronic oversupply, prices began to improve. In the second half of 2016, prices were comfortably over the US\$10 000 per ton level, and traded within a range of around US\$9 000–11 000 per ton until the third quarter of 2017 (Figure 6). Since then, however, the growing realization that the strong prospects for nickel demand in batteries should sustain strong demand growth, coupled with a continued market deficit, has supported a further price appreciation. By early 2018, the LME nickel cash price had approached the US\$13 000 per ton level. One factor that could hold back prices is the stock that was accumulated during the recent period of sustained market surpluses.

Chromium

Without chromium there is no stainless steel!

From a stainless steels producer's point of view, two types of chromium ferroalloys are to be distinguished: charge chrome and the high-carbon (HC) ferrochrome (FeCr). In a stainless steel mill, most of the required ferrochrome is added directly into the electric arc furnace (EAF), with the stainless producer having the choice of adding either charge chrome or HC ferrochrome. When the steel has been decarburized and tapped from the EAF, the stainless producer will then usually add a small amount of medium-low carbon (MLC) ferrochrome to 'trim up' the chrome specification of the steel.

There are usually significant differences between the levels of certain impurities present in charge chrome *vis-à-vis* HC ferrochrome, especially silicon. The scrap ratio used in stainless steel mills has a significant effect on the type of ferrochrome consumed, as there are almost always far more impurities in all grades of ferrochrome than in stainless steel scrap. The use of scrap also has significant impacts the quantity of primary ferrochrome consumed.

Charge chrome contains some 50% chromium and 6–8% carbon, and is primarily applied for stainless steel melting. In Asian countries – particularly in China and India – HC ferrochrome grades are predominantly produced, typically containing 60–70% chrome and varying carbon contents.

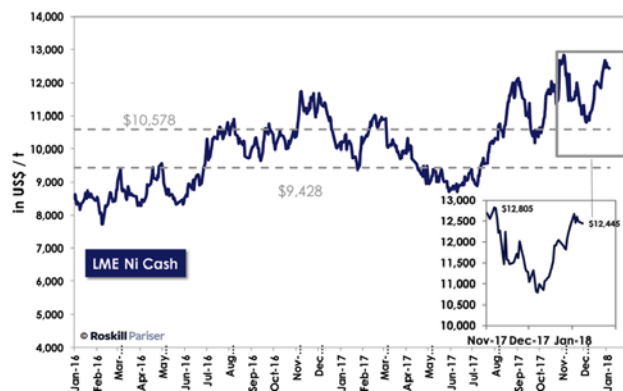


Figure 6 – Nickel price developments since January 2016

Historically, charge chrome production has significantly outweighed HC ferrochrome production in terms of tonnage, following a growth of 7.3% per annum since 2000, whereas HC ferrochrome grew slightly slower at 5.4% per annum (Figure 7).

Power supply restrictions have favoured the use of HC ferrochrome, which is expected to grow at 3.3% per annum in the long term to 2030, compared to a 2.2% per annum growth in production of charge chrome.

Chrome ore

World mine production of chromite closely follows trends in ferrochrome production, which accounts for nearly 90% of consumption. Chrome ores are mined globally, but output is highly concentrated in terms of both geographical area and producing countries. Since 2007, the supply volumes have expanded by 3.6% annually, and are expected to reach almost 37 Mt in 2018.

Five countries produce more than 1 Mt/a of chromite. The expectations in 2018 are for South Africa to account for 60% of world output, including production from the UG2 Reef. Kazakhstan (13%), India (9%), Turkey (4%), and Finland (3%) are the other major producers. In total, these five countries accounted for 89% of chromite production. In South Africa, the contribution of UG2 chromite is estimated to account for over 10% of the annual supply.

Exports of chrome ore from South Africa reached almost 12 Mt in 2017, of which 11 Mt were directly and indirectly supplied to China. Shipments from South Africa ramped up in 2005–2008 as China's stainless steel boom set in, to an average 425 kt/month until 2012. Exports grew to 700 kt/month in 2013, but settled back to 590 kt/month in 2014, with less than 66% shipped to China in that year. Since 2015, monthly exports have increased sharply to an average of 970 kt by 2017.

The natural counterpart in the trade of chrome ore is China's rapidly expanding stainless steel industry, which obtains the bulk of its chrome ore from South Africa (approximately 72% in 2017). Minor chromite deposits are available in China, but the country's large stainless steel industry is dependent on imports. Other important suppliers of chromite to China include Turkey, Albania, and Pakistan (Figure 8). According to preliminary 2017 data, China's chrome ore imports expanded last year by 29%.

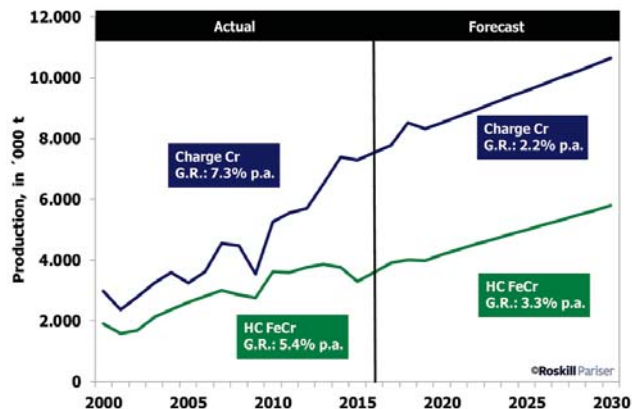


Figure 7 – Charge chrome and HC ferrochrome production comparison

Changing nickel and chromium stainless steel markets – a review

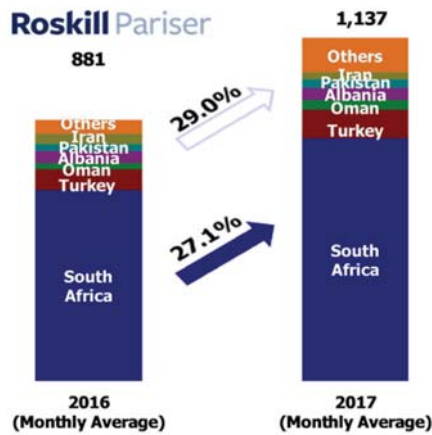


Figure 8—Average monthly Chinese imports of chrome ore for 2016 and 2017

Ferrochrome production

We estimate last year's global ferrochrome production at approximately 11.7 Mt. Three countries produced more than 1 Mt of HC ferrochrome/charge chrome in 2017. China and South Africa together accounted for 68% of the total output, with Kazakhstan contributing a further 12%. India fell just below the 1 Mt mark (Figure 9). Ferrochrome prices have largely followed ore prices, although the changes both up and down have been more subdued.

In 2016, demand for ferrochrome increased to 11.1 Mt, followed by another expansion to 12.5 Mt in 2017. For the immediate future, in 2018 destocking is anticipated while demand is expected to decline by some 191 kt. Cutbacks are expected in the EU and various other countries, but China is likely to increase its consumption again.

Real ferrochrome demand is expected to increase by 3.6% to just over 12 Mt in 2018, while apparent consumption could rise by 4.4% to 12.3 Mt. A ferrochrome production of 12.5 Mt corresponds to a capacity utilization ratio of 74%, and leads to a minor supply surplus of 216 kt. However, if the supply is compared with 'real' demand, the surplus would be as high as 489 kt.

Production costs

For more than three decades our analysts have reviewed the global production costs on an ex-works basis. It appears that the most favourable conversion costs are identified for Kazakhstan, which has for years been the most competitive supplier. Kazakhstan is followed by South Africa's Glencore-Merafe joint venture, while Finland's Outokumpu Group ranks third. These three ferrochrome producers accounted for approximately half of the global production last year.

China's ferrochrome smelters are often not competitive and are relatively small by international standards. Typically, they rank 13th and 20th in this comparison. We presently estimate 2017 average 'C3 cost' (in US cents) at 66.7 US cents per pound Cr content and we expect a marginal increase to 66.8 US cents per pound Cr for 2018.

A direct 2017 cost comparison between South Africa and China reveals the following conclusions:

- South Africa has a cost advantage of 17.7 US cents per pound Cr when it comes to chrome ore input
- There is a disadvantage of 4.1 US cents per pound Cr for South Africa in reductants and other cost components
- Energy costs in South Africa are 7.4 US cents per pound higher than in China
- Semi-fixed costs of 5.94 US cents per pound compare with those of China at 2.89 US cents per pound
- Aggregated total direct cash cost in South Africa last year amount to 54.11 US cents per pound, while China's total cost amount to 75.76 US cents per pound.

Chrome ore prices

Ferrochrome prices follow broadly similar trends to chromite prices and are broadly cyclical, reflecting trends in the stainless steel industry, although with a time lag. The past two years have seen numerous price swings in the chrome ore and ferrochrome markets. Prices for chrome ore roughly quadrupled over the course of 2016, remaining extremely high in early 2017 before falling substantially in Q2 and bottoming out in Q3 (Figure 10). Prices have recovered slightly as of early 2018, with UG2 ore (42% CIF China) at US\$206 per ton in January 2018, compared to the US\$395 per ton high experienced in January 2017. Ferrochrome prices have largely moved in tandem with ore prices over this period, though the changes both up and down have been more subdued.

Stainless steel scrap

The neglected commodity

Stainless steel scrap is often ignored by those who monitor raw material markets. Stainless scrap is more complex than other raw materials and often follows its own trend. Last year, the global external scrap availability amounted to some 10.5 Mt, corresponding to approximately 85 kt of contained nickel units and some 180 kt of chromium units. In the case of China, stainless steel scrap played a role in the early 2000s, but this was before a domestic scrap market could be developed. China jumped onto NPI, which took over a similar role as scrap in Western countries. Frequent discussions with Chinese market participants provided a repeated answer: 'We do not understand the scrap market'. But for how long?

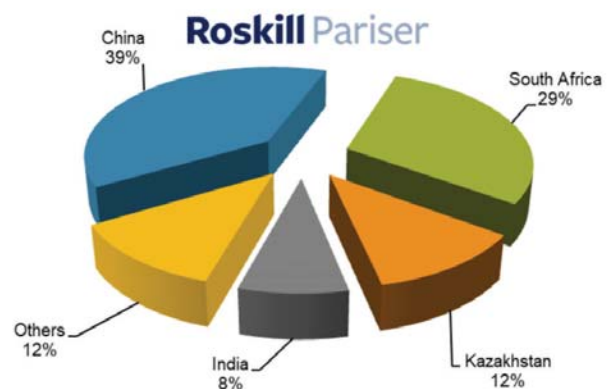


Figure 9—Ferrochrome production by region, 2017

Changing nickel and chromium stainless steel markets – a review



Figure 10—Chinese prices for Turkish ore grading 41% Cr and South African UG2 ore grading 42% Cr (source: Metal Bulletin)

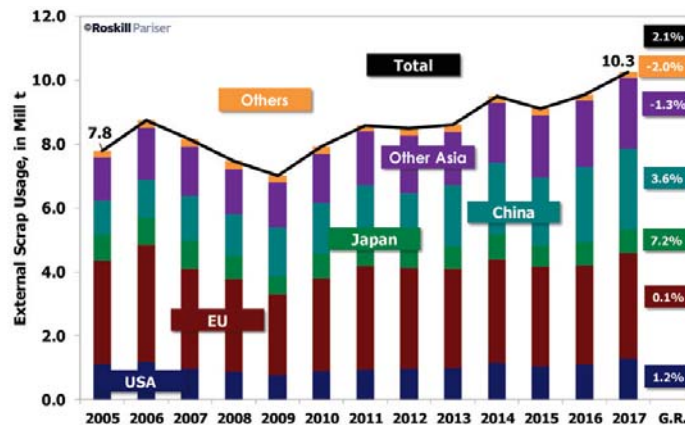


Figure 11—External stainless steel scrap consumption, 2005–2017

Countries within the EU form the largest stainless scrap market. The scrap market is highly organized and well developed, although Asia – in particular South Korea and Taiwan – followed the European expertise, whereas Japan went its own way, developing sophisticated sampling and sorting techniques. The USA has been the nucleus of the modern scrap industry and is still a major source of scrap supplies. As already stated, China lags behind this trend in scrap supplies. In part, this lag reflects the long life-cycle of stainless steel products. Chinese consumption of consumer goods only started to accelerate during the last 20 years. As such, in the future more scrap will be available in China. This should lead to a convergence in regional consumption of stainless steel scrap, with China's scrap utilization ratio creeping up towards the levels seen in Europe.

In traditional industrialized countries, prices for stainless steel scrap follow primary nickel prices. The so-called intrinsic value of important elements such as nickel and chrome is evaluated and these are typically traded at changing discounts below the primary price. Unfortunately, the number of competent scrap traders is diminishing, and for this reason it is more and more difficult to obtain consistent price information.

The same reasons apply for the evaluation of chrome units contained in stainless steel scrap. However, the available information is more consistent and transparent. The evaluation of chrome in stainless steel scrap is relatively stable at about 20% of the charge chrome price.

Conclusions

The market overview can be summarized as follows.

1. Ni-containing batteries might challenge the growing nickel requirements for stainless steel. Recycling of spent batteries becomes an issue.
2. Chrome markets are dominated by South Africa, but more chrome units are converted in China – how long will this remain so?
3. China's ferrochrome production has lost its competitive advantage in terms of production costs. Should China reduce production or even possibly exit from chrome conversion?
4. How long until China's scrap market begins to mimic those of the rest of the world? When scrap ratios increase because of the increased maturity of the market, ferrochrome consumption from primary sources will undergo a drastic change.

References

- ROSKILL PARISER STAINLESS STEEL. 2018. Stainless Steel & Alloys Weekly. <https://roskill.com/market-report/stainless-steel-alloys-weekly/>
- ROSKILL. 2018. Nickel: Global Industry, Markets & Outlook, 14th Edition. <https://roskill.com/market-report/nickel/>
- ROSKILL. 2018. Nickel Sulphate: Global Industry, Markets & Outlook, 1st Edition. <https://roskill.com/market-report/nickel-sulphate/>
- ROSKILL. 2018. Chromium: Global Industry, Markets & Outlook, 14th Edition. <https://roskill.com/market-report/chromium/> ◆



Tariff developments for electricity-intensive industry in South Africa

by C.S. Mahony and J.M. Baartman

Synopsis

It is common cause that South Africa's mining and industrial sectors are struggling to compete in global markets. Electricity pricing is frequently cited as one of the primary causes; typically current price levels, uncertainty around future prices, or both.

From a low base by international standards, South Africa has experienced above-inflation electricity price increases over the past decade. Eskom's sales data confirms a declining trend in electricity sales to its large industrial consumers, particularly since 2011; attributable to efficiency gains, an increase in cogeneration, as well as cutbacks and closures across a range of market segments. High and/or rising electricity prices inevitably pose the greatest threat to the most electricity-intensive users, including the ferroalloy producers. Logically, other competitiveness factors, such as manpower and logistics costs, rise in relative importance as electricity intensity decreases.

Reduced consumption by large industrial consumers reduces the system load factor, exerting upward pressure on the unit cost of electricity at the generation level. Furthermore, as large users contribute significantly to the subsidization of other users' prices, falling consumption risks ever-increasing cross-subsidy contributions by the remaining contributors, further increasing prices.

In response, Eskom proposes to introduce a suite of more cost-reflective tariffs aimed at stabilizing, and even growing, consumption by electricity-intensive customers with high load factors, who stand to gain the most from more cost-reflective electricity pricing, while contributing meaningfully to keeping the unit cost of electricity down.

Keywords

ferroalloys, electricity-intensive industry, electricity price, electricity cost.

Introduction

Given South Africa's rich mineral endowment, it is inevitable that a substantial portion of its electricity is consumed in the mining and further processing of a wide range of ores. Metallurgical processes are characteristically very electricity-intensive; ferroalloy manufacture alone accounted for an estimated 7.5% of South Africa's total electricity consumption in 2017, despite the severe cutbacks in the country's output of both manganese and silicon alloys in recent years.

The decline in consumption of grid-supplied electricity by South Africa's key industrial consumer (KIC) segment (≥ 100 GWh/a) in recent years has been widespread,

with 12 of the 21 sub-segments tracked by Eskom registering declines over the past 11 years. Since the end (31 March) of Eskom's 2011 financial year (FY), the downward trend has been more consistent. In fact, if data for the aluminium smelter sub-segment is excluded for this period (on the basis that pricing to these consumers was not based on standard tariffs; *i.e.* contractual pricing applies), there is fairly convincing evidence that price elasticity has become a significant factor in determining purchases of grid-supplied electricity by Eskom's KICs, as demonstrated in Figure 1. It should be noted that while the vast majority of South Africa's KICs are supplied by Eskom, some are supplied by municipal electricity undertakings.

Based on feedback from its KICs, Eskom attributes the observed trend primarily to a combination of improved energy efficiency (in line with the global trend), an increase in self-generation, switching to alternative energy sources, limited investment in new capacity, as well as total or partial plant closures. The latter two factors strongly suggest that South Africa's KICs, most of whom compete in global commodity markets, are struggling to remain globally competitive. Feedback from KICs confirms this view, but it must be noted that other cost elements contribute to the lack of competitiveness, in particular for the less electricity-intensive KICs. It is clear that more competitive electricity costs would help to stabilize consumption and potentially reverse the trend to some degree.

* Eskom, South Africa.

© The Southern African Institute of Mining and Metallurgy, 2018. ISSN 2225-6253. This paper was first presented at the INFACON XV: International Ferro-Alloys Congress, 25-28 February 2018, Century City Conference Centre and Hotel, Cape Town, South Africa

Tariff developments for electricity-intensive industry in South Africa

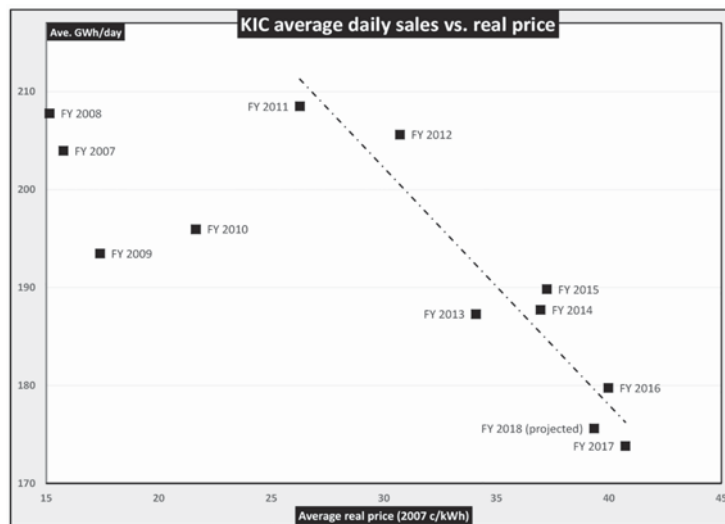


Figure 1—Sales to Eskom KICs (excluding AI) vs real price

Electricity cost considerations

Offtake of grid-supplied electricity

Although there has been some growth in electricity consumption in past years in the residential and services segments, as well as in selected KIC sub-segments, this growth has been offset by reductions in other KIC sub-segments and among smaller secondary industries. More recently, a growing trend towards rooftop solar photovoltaic generation for own use has emerged, particularly in the services and higher-LSM residential segments, posing another threat to growth in grid-supplied electricity. When the cost of storage options becomes competitive, this trend is likely to increase. At present, only the lower-LSM residential sub-segment is showing consistent growth in consumption, driven by ongoing electrification. If present trends persist, total grid-supplied consumption might decrease over time, particularly in the absence of substantial economic growth.

High unit fixed cost of electricity

With South Africa's electricity generation fleet primarily consisting of large 'base-load' coal and nuclear plant, it is inevitable that the cost of energy generation will primarily be fixed; with transmission and distribution networks as well as committed centralized renewable energy purchases, adding further fixed cost elements. To compound matters further, South Africa has recently invested in two new, large, coal-fired generation plants and several renewable plants, on top of investing a considerable amount to return mothballed stations to service in order to deal with the capacity crisis (2008-2014). A combination of stagnant offtake and rising fixed costs inevitably implies that the unit fixed cost of electricity in South Africa must increase in real terms, exerting upward pressure on prices. Unit fixed costs would rise even more strongly were total grid-supplied electricity to decrease.

Deteriorating system load factor

For the most part, South Africa's KICs operate at load factors above the system load factor, which implies more efficient

utilization of South Africa's predominantly base-load fleet (*i.e.* generation plant designed to operate most efficiently when running continuously). At the other extreme, consumption by lower-LSM residential consumers tends to be concentrated during peak periods, particularly in the evening, with the opposite effect. The combination of falling KIC offtake, while lower-LSM offtake continues to rise, implies a deterioration in the system load factor over time. In turn, this implies that the ratio between installed capacity and energy dispatched will increase and that the generation ramp-ups to both the morning and evening peaks can be managed only by keeping more generators in 'spinning reserve'. Both of these outcomes will further increase the unit cost of electricity in real terms. It should be noted that an increase in photovoltaic generation, whether grid-contracted or privately used, leads to a dip in demand from the rest of the fleet during the day, which intensifies the impact of a deteriorating load factor. Increased use of energy storage can help to dampen the impact, but is still too expensive to justify the investment required.

Rationale for a new industry tariff

On the basis of the considerations outlined below, Eskom took a decision to develop a new suite of tariffs that would be specifically targeted at qualifying KICs, whether supplied by Eskom or by municipal licensees. The interim name is 'EIIC tariff suite', the acronym meaning 'electricity-intensive industry consumer'.

Economic imperative

South Africa's KICs are largely capital-intensive mining and industrial consumers. In the long run, the South African government favours transforming the economy from the historical mix of primary and heavy secondary industry to a much less capital-intensive, more labour-absorbing mix of secondary and tertiary elements. However, the lack of headway to date indicates that this transformation will take many years to achieve. In the interim, it appears vital to preserve a substantial portion of the capital-intensive

Tariff developments for electricity-intensive industry in South Africa

economic base as, along with the tertiary services sector, it provides the bulk of current economic activity, employment, and tax revenue.

Optimizing unit fixed cost

It may be deduced from the previous section (Electricity cost considerations) that the fixed cost component of the unit electricity cost could potentially be stabilized, and even reduced, by increasing the offtake of grid-sourced electricity. In general, this can only be achieved with a sustained higher level of economic growth, particularly as, globally, electricity intensity is on a downward trend. On the other hand, many of our KICs' markets are influenced more by global economic activity and trends than by local ones, implying that targeted tariff development can potentially be applied to sustain and potentially grow offtake from this segment, notwithstanding low economic growth within South Africa. A successful electricity price intervention in the KIC segment would have a favourable effect on fixed unit costs via both the volume and load factor effects. In turn, this would beneficially affect electricity prices for other consumers.

Tariff cross-subsidies

Megaflex is the tariff that applies to most of the KICs supplied by Eskom, while the relevant municipal licensees apply their own tariffs. Eskom's *Megaflex* tariff for non-municipal customers incorporates three transparent cross-subsidies, namely:

- ▶ The *Affordability Subsidy* (AS) – funded by Eskom's direct industrial and business customers
- ▶ The *Electrification and Rural Subsidy* (ERS) – funded by Eskom's direct industrial and business customers and municipalities
- ▶ The *Urban Low Voltage Subsidy* (ULV) – funded by all Eskom's customers on urban tariffs that take supply at 66 kV or a higher voltage.

Importance of cross-subsidies

A study carried out for NER (Adams, 2004), found that the average impact of cross-subsidies (then only ERS, ULV, and municipal subsidies) on the contributors' effective price levels across all South African tariffs averaged about 7%. As this figure included the cross-subsidies in municipal tariffs, the percentage in Eskom's tariffs was definitely lower at the time. The study concluded that this extent of cross-subsidy was quite acceptable, particularly in light of the highly competitive prices paid by South African industry at the time. In the intervening years, particularly since 2009, dramatically increasing costs have inevitably resulted in Eskom's tariffs increasing at rates well above South African inflation (both CPI and PPI). In an effort to address affordability for low-usage residential customers, the National Electricity Regulator (NERSA) responded by introducing the AS. Collectively, the above cross-subsidies currently make up some 10–16% of the all-in average prices (in cents per kWh) paid by Eskom's industrial customers on *Megaflex*; those at the lower end of the range not being required to pay the ULV.

The fact that the cross-subsidy share of Eskom's industrial prices has increased at a faster rate than the corresponding cost of supply stands in stark contrast to the views expressed in both the Electricity Pricing Policy (EPP)

(DME, 2008) and the Guidelines on Cross-subsidies (NER, 2005). The following extracts from the latter document are particularly pertinent.

- ▶ *Cross-subsidies should be eliminated gradually in a phased in manner over a period of 10 years*
- ▶ *(stated as a cross-subsidy principle) Social 'obligation', so that the economy and society as a whole benefits. Application should not jeopardise the efficiency and the competitiveness of the benefactor customer class.*

It is clear that tariff cross-subsidies have actually increased in percentage terms (of far higher prices, in real terms). Furthermore, many KICs argue that current electricity price levels present a major threat to the survival of several industry sub-segments. As the KICs are seeking more cost-reflective prices, by implication the cross-subsidies they pay have become unaffordable, effectively a violation of the principle quoted above.

Cross-subsidies arising from costing methodology

By their very nature, all costing methodologies that are applied to apportion costs between consumers that share resources will result in cross-subsidies. In the case of electricity, consumers share resources throughout the value chain, from generation to billing, which implies multiple cross-subsidies that arise from the complexity of the cost allocation methodology applied, as well as the level of detail available in respect of usage patterns. In general, these cross-subsidies are too small to cause significant price distortion, particularly between high-level consumer groupings (*e.g.* residential *vs.* industrial). Other than the load factor cross-subsidy discussed below, Eskom has not identified any other individual cross-subsidies that distort prices sufficiently to warrant consideration in the context of the EIIC.

Load factor cross-subsidy

Megaflex tariff energy rates are differentiated seasonally, per time-of-use (TOU) period, by transmission zone, and by voltage group. However, they do not accurately reflect the relative costs of supply for consumers that have vastly different load factors, owing to the fact that all retail energy rates are derived from a single set of (internal) wholesale rates, which have already been differentiated seasonally and per time-of-use period. By implication, the energy costing methodology adopted by Eskom up to now results in a non-transparent cross-subsidy; users with load factors higher than the system load factor being the contributors, to the ultimate benefit of other consumers' prices. While contributing consumers are almost exclusively supplied on either *Megaflex* or *Nightsave Large*, recipients are spread across all consumer classes and tariffs, including *Megaflex*.

EIIC tariff eligibility

The eligibility criteria will be finalized in due course, but current thinking is along the lines outlined in the sub-sections below. The ultimate objective is that consumers that merit qualification should do so, while those that ought not to qualify are excluded. In this context, the authors appreciate that some modifications, or even additions, to the eligibility criteria outlined above are almost inevitable over time and may well be introduced before the criteria are finalized.

Tariff developments for electricity-intensive industry in South Africa

Power system factors

As one of the key drivers for the introduction of the new tariff is to optimize the power system, it was essential that EIIC eligibility should be structured accordingly. Three factors have been chosen, as follows.

- *Annual consumption*—Primarily to limit qualifying consumers to those with the greatest potential to optimize the system. Likely initial threshold – 80 GWh/a. for at least two of the past three calendar years.
- *Average monthly load factor*—To ensure that qualifying consumers will maintain or increase the system load factor. Likely threshold – 0.75 (75%) monthly average for at least two of the past three calendar years. Consumer response to time-of-use and seasonal price signals will be taken into account in determining eligibility.
- *Average monthly power factor*—To minimize grid expenditure required to optimize power factor. Likely threshold – 0.96 (96%) monthly average for at least two of the past three calendar years.

It is anticipated that all the above criteria would be mandatory and subject to annual review. Conditional leniency could be allowed for start-ups.

Economic policy alignment factors

Economic benefit is arguably the most important driver for the introduction of the new tariff. Accordingly, alignment to the South African government's industrial policy and strategy is paramount, so consumers will have to meet at least one of the following criteria.

- *Strategic industry*—Endorsement by either the Department of Trade and Industry (DTI) or the Department of Mineral Resources (DMR), in consultation with National Treasury (NT), that the consumer produces a sufficient quantity of at least one product deemed by the government to be of strategic importance to the country.
- *Strategic value chain*—Endorsement by the DTI, in consultation with NT, that at least one of the consumer's products is considered to be a key element of a value chain that the government considers to be of strategic importance to the country.

The above endorsements would need to be renewed annually, to ensure sustained alignment in the event of changes to government policy.

Economic efficiency factors

In the interest of economic efficiency, it is considered crucial that consumers should demonstrate a real need to access the most cost-reflective tariff available in the country. Accordingly, consumers will be required to meet both of the following criteria.

- *Electricity intensity*—Intended to ensure that the cost of electricity plays a primary role in determining qualifying consumers' ability to compete effectively in the markets in which they operate. The qualifying electricity intensity threshold has not yet been determined, but it will be defined in terms of the ratio between annual energy consumed (in kWh) and the

'rand value added' for that period, where rand value added equals gross margin plus manpower cost. In line with the other threshold-based criteria, this threshold will need to have been met for at least two of the past three years, though in this instance the consumer's financial year will be used.

- *Lack of pricing power*—Intended to ensure that qualifying consumers are not able to pass on cost increases in their product prices without significant risk of losing market share to producers outside South Africa. It is possible that a signed declaration from the consumer may be considered sufficient, but a more likely outcome is that the consumer's declaration will require endorsement by an external party considered to have the necessary expertise and to be independent of the consumer.

Eligibility in respect of electricity intensity will be subject to annual review, while the declaration in respect of pricing power will need to be renewed annually, to ensure sustained alignment in the event of sustained changes in the markets served.

Conceptual tariff design

As with the eligibility criteria, the tariff design will be finalized in due course. Current thinking is along the lines outlined in the sub-sections below. The first two deal specifically with reducing or eliminating the cross-subsidies discussed earlier, with the objective of enhancing cost-reflectivity; the third addresses the TOU issue, which has long been problematic for several customers.

More cost-reflective energy rates

As indicated earlier, the suggested EIIC tariff load factor threshold is 0.75, the intent being to differentiate the wholesale energy rates used for the EIIC tariff from those used to determine other Eskom tariffs. However, it goes without saying that a single load factor band spanning 0.75–1.00 would still imply a considerable degree of cross-subsidization in favour of relatively lower load factor consumers. The current proposal is to create three energy rate bands in the EIIC tariff, as follows.

- Band 1: EIIC-qualified consumers with load factors from 0.90 upward would gain access to the lowest energy rates
- Band 2: EIIC-qualified consumers with load factors from 0.825 upward (but below 0.90) would gain access to mid-range energy rates
- Band 3: EIIC-qualified consumers with load factors from 0.75 upward (but below 0.825) would gain access to the highest EIIC energy rates, though slightly lower than the Megaflex rates.

Seasonal and time-of-use considerations

In order to allow for qualifying consumers that opt to use less energy during the high-demand season (June–August), and/or to reduce usage during peak periods when energy rates are higher, two potential solutions are under consideration, namely:

- *Seasonal variation*—Permitting consumers to qualify in different bands for the two seasons, e.g. band 2 for the

Tariff developments for electricity-intensive industry in South Africa

low-demand season and band 3 for the high-demand season

- ▶ *Peak reduction*—Excluding peak periods from the load factor calculations.

There is also a possibility that an alternative rate structure will be offered to the higher bands (1 and 2) wherein the differentiation between seasonal (and potentially also time-of-use) rates is removed, which would benefit qualifying consumers that maintain consistent load profiles throughout the year, either by choice or because their processes cannot tolerate much variation. The availability of this option is likely to be contingent on participant consumers contracting to provide interruptible load as outlined below.

Reduced cross-subsidy contributions

The key purpose of the economic eligibility criteria outlined above is to enable eligible consumers to gain access to lesser contributions to the AS, ERS, and ULV cross-subsidies, in the interests both of enhanced cost-reflectivity and greater affordability. The intent is to link the level of benefit to electricity intensity so as to align affordability with consumers' sensitivity to electricity prices. The details of the mechanism will follow analysis of electricity intensity values obtained from a substantial sample of Eskom's KICs, but it is likely that 2–3 bands will be established, with subsidy contributions lowest for the highest intensity band. Whether or not cross-subsidy contributions can be completely eliminated for the highest band remains to be tested.

Other products

Eskom is currently in the process of reviewing its approach to contracting with its customers for *Interruptibility*, a product that permits willing and able consumers to provide demand-side support to the grid, both during peak periods and during system emergencies. The changes envisaged would enable the National System Operator to cut costs by utilizing a portfolio of contracted interruptibility as a virtual 'peaking' power station. The cost benefits would be shared with participating consumers.

Other opportunities are also being explored, including the possible introduction of a super-off-peak tariff and a so called 'take-or-pay' option, whereby volume risk in the power system is reduced; again applying the shared-benefit principle.

Implications for consumers

At this stage, the implications of introducing EIIC tariffs for Eskom's other tariffs are not clear; the final outcome depending on a number of variables, including:

- ▶ Final tariff design
- ▶ Projected impact on total and unit cost of supply
- ▶ Projected impact on KIC prices and consumption volumes
- ▶ Projected tariff and price implications for other consumers
- ▶ Projected overall revenue, bottom line, and cash flow implications
- ▶ Decisions around the motivation, quantum, and future funding of cross-subsidies.

International trends

KIC electricity prices

On average, across all customer segments, South African prices compare favourably to global peers. In fact, in US dollar terms, South Africa electricity prices have been relatively constant over the last few years, owing to depreciation of the rand. However, South Africa's KIC prices are increasingly becoming less competitive relative to other countries in which electricity-intensive industries operate. While it is always difficult to obtain information on 'special pricing arrangements' in other countries, what is available has indicated that KICs in certain other jurisdictions are experiencing falling prices. According to data from a German study, compiled jointly by Ecofys, Fraunhofer-ISI, and GWS (EFG), (Grave *et al.*, 2015), lower prices were available for very large (so called 'privileged') consumers in Canada (Quebec), France, and the USA (Texas) than for South African KICs in 2014. Information obtained confidentially from a global commodity producer confirms this, further indicating that KIC prices in these and other jurisdictions actually dropped in US dollar terms between 2014 and 2017, while US dollar-denominated (Eskom) KIC prices in South Africa rose about 9% over the same period. Although the volatile rand/dollar rate improves the competitiveness of South Africa's KIC prices from time to time, industry cannot plan on this basis.

Price variation with load factor

In many jurisdictions, KICs now purchase energy on wholesale markets, following the deregulation of traditional, regulated electricity arrangements. In these markets, KIC purchase prices are invariably influenced by load factor. Even prior to deregulation, it was fairly commonplace for industry tariffs to be differentiated on the basis of load factor (EDF, 1995).

Different pricing approaches for KICs

The prevailing situation in South Africa is that socio-economic cross-subsidies increase electricity prices to KICs, impacting global competitiveness. In countries covered by the German study (Grave *et al.*, 2015), privileges depend either on tax treatment or on a range of other factors such as purchase volume, load factor, supply voltage, industry sector, and electricity intensity. For example, in Germany the prevailing combination of the above benefits leads to prices for 'privileged' industrial consumers being less than half of what would apply without those privileges. In France, it was noted that a consortium of very large consumers was able to negotiate a long-term, fixed price agreement with EDF. According to information provided to Eskom on a confidential basis, a range of further benefits has been made available to what might be termed 'ultra-privileged' large consumers in France, reducing effective prices even further.

Stakeholder engagement

The EIIC tariff concept represents a fairly radical departure from South Africa's past electricity tariff practice. Therefore, decision-making will be influenced as much on the wide-ranging economic implications thereof as on the structural

Tariff developments for electricity-intensive industry in South Africa

details of the tariff itself. Consequently, it is anticipated that stakeholder engagement will be both extensive and intensive. Aside from consumer and municipal representative groupings, those to be consulted must necessarily include (at least) NERSA along with several government departments including the NT, DTI, DMR, the Department of Energy (DoE), and the Department of Economic Development.

Approvals

Although Eskom's Board has approved the EIIC tariff concept, final approval of the detailed tariff design will be required in due course. Furthermore, any tariff change, including the introduction of a new tariff, is subject to approval by NERSA. In this context, it is conceivable that the DoE may issue policy guidance to NERSA.

Conclusions

Eskom believes that it is critically important for South Africa that steps are taken to sustain and grow industry, not least by enhancing the competitive position of those industries that compete in the global marketplace, simultaneously providing both direct and indirect employment to many thousands of South Africans, contributing substantially to the fiscus, and enhancing the value of the currency.

That said, Eskom readily acknowledges that the proposed introduction of the EIIC tariff suite is but one part of a comprehensive set of initiatives South Africa needs to implement in order to achieve the desired outcome.

Finally, it is encouraging to note that measures taken elsewhere to protect KICs struggling to remain competitive do not differ fundamentally from Eskom's proposals.

Acknowledgements

The authors wish to thank Eskom for granting permission to publish this paper. Thanks are also due to the many colleagues who, along with a range of customers and government officials, have both supported the initiative and contributed positively to the development of the EIIC tariff concept. Details of the Eskom tariffs referred to herein may be obtained on the Tariffs and Charges page of Eskom's website.

References

- ADAMS, I. 2004. Allocation methodology for cross subsidies in electricity tariffs on the basis of a macro-economic impact study. Report for the National Electricity Regulator, now NERSA.
- DEPARTMENT OF MINERALS AND ENERGY. 2008. Electricity pricing policy (EPP) of the South African electricity supply industry. December.
- ELECTRICITÉ DE FRANCE (now EDF). 1995. Verbal communication. June.
- Grave, K., Hazrat, M., Boeve, S., von Blücher, F., Bourgault, C., Breitschopf, B., FRIEDRICHSEN, N., ARENS, M., AYDEMIR, A., PUDLIK, M., DUSCHA, V., ORDONEZ, J., LUTZ, C., GROSSMANN, A., and FLAUTE, M. 2015. Electricity Costs of Energy Intensive Industries; an International Comparison. Report for the German Ministry of Economic Affairs and Energy. July.
- NATIONAL ELECTRICITY REGULATOR (now NERSA). 2005. Regulatory guidelines on cross subsidies. ◆



THE SAMREC and SAMVAL CODES

Advanced Workshop: Can you face your peers?

14–15 August 2018

The Wits Club, University of the Witwatersrand, Johannesburg

The object of the interactive workshop is to address the more complex application of the codes through case studies. It will be assumed that the participants are fully conversant with the SAMREC and SAMVAL codes and are able to discuss their perspective on aspects of the case studies. The emphasis will be on being able to face one's peers and include both compliance and best practice aspects of the codes.

The workshop will take the form of group discussions of various case studies to facilitate discussion. Various topics have been selected and will be discussed in conjunction with discussions around Precious Metals, Coal, Diamonds and Valuation covering Exploration Results, Mineral Resources, Mineral Reserves and Valuations.

Participants will be supplied with material to review prior to the workshop. They will be placed in groups to discuss and dissect the material – 2 or 3 groups will be asked to present their findings at the end of each session. Each case study is designed for a 3 hour morning or afternoon session.

The workshop is intended to allow mining industry professionals to improve their knowledge and application of the advanced aspects of the SAMREC and SAMVAL Codes.

For further information contact:

Yolanda Ndimande, Conference Co-ordinator, Tel: +27 (0) 11 834-1273/7
E-mail: yolanda@saimm.co.za, Website: <http://www.saimm.co.za>



NB: Documents for the workshop will be provided electronically on receipt of registration/payment



Reduction of Kemi chromite with methane

by M. Leikola*, P. Taskinen*, and R.H. Eric* †

Synopsis

Kemi chromite ore from Finland was reduced in $\text{CH}_4\text{-H}_2$ gas mixtures at temperatures from 1100° to 1350°C. Experimental variables were time, temperature, and the CH_4 content of the gas mixture. The phases in reacted samples were determined by XRD and quantitative phase analysis was performed using the Rietveld method. Particle morphology and phase compositions were determined using SEM and EDS analysis. Reduction proceeded through a shrinking core model in two stages. In the first stage, hydrogen and carbon from the cracking of methane reduced the iron and some chromium to carbides. The chromium in the remaining spinel was reduced during the second stage. Iron was essentially reduced in full after 30 minutes when the temperature reached 1300°C, and at 1350°C it was completely reduced within 20 minutes. At this highest temperature, all of the chromium was eventually reduced, the residue consisting of aluminum and magnesium oxides with varying amounts of silica. At the surface of the particle iron and chromium, together with carbon, formed two alloys, an iron-dominated and a chromium-based one. The iron-based phase was partially molten at the higher temperatures. At 1300°C and 1350°C the metallization was complete. Reduction of Kemi chromite with a $\text{CH}_4\text{-H}_2$ mixture is judged as highly efficient, since high of reduction extents could be reached faster at lower temperatures compared to carbothermic reduction. This is attributed to the very high activity of carbon (way above 1.0) due to the cracking of methane into hydrogen and carbon at around 550°C in the presence of a solid phase.

Keywords

chromite, solid-state prereduction, methane, hydrogen.

Introduction

Stainless steel is, and will continue to be, a crucial material for modern civilization, as more materials are consumed by the growing population world. Chromite ore contains chromium and iron along with other elements (Lyakishev and Gasik, 1998). It is the raw material for producing ferrochrome, mainly a mixture of iron and chromium, which is used as an alloying material in the process of manufacturing stainless steel (Murthy, Tripathy, and Kumar, 2011). In chromite ores, the major metal cations are often in the forms Fe^{2+} , Fe^{3+} , and Cr^{3+} , and the general formula is FeCr_2O_4 , which has a spinel-type structure. Depending on the deposit, other cations such as Al^{3+} and Mg^{2+} can be found occupying some of the interstitial octahedral and tetrahedral sites of the spinel (Lyakishev and Gasik, 1998).

Reduction of the iron and chromium oxide components is needed to produce metallic ferrochrome. Currently, this is done in electric submerged arc furnaces (SAFs) using coke as the reductant. This requires high temperatures and therefore the furnace consumes a lot of electricity (Basson and Daavittila, 2013). It is possible to prereduce the chromite ore pellets in solid form before charging them into the SAF. This procedure lowers the electricity consumption in the SAF, due to the lesser extent of the Boudouard reaction.

The solid-state prereduction can be performed by utilizing carbon (Niayesh and Dippenaar, 1992; Kekkonen, Xiao, and Holappa, 1995), a methane-hydrogen mixture (Anacleto and Ostrovski, 2004; de Campos and Eric, 2006), or hydrogen (Arvanitidis, 1996). Reduction of chromite with a methane-hydrogen gas mixture is the most energy-efficient, since reduction takes place at a lower temperature (Anacleto and Ostrovski, 2004; de Campos and Eric, 2006). This is due to the high activity of the carbon (Anacleto and Ostrovski, 2004). At temperatures above 550°C, due to the cracking of methane, the activity of precipitating carbon starts to rise exponentially, well exceeding 1.0 (with respect to pure solid graphite, which would have unit activity). This is well known thermodynamically and is due to the fact the precipitated carbon is not yet in graphitic form (Taskinen, Fabritius, and Eric, 2014). The reaction mechanism is based on the adsorption of methane onto the active oxide surface. After adsorption, the methane cracks into hydrogen gas and solid carbon as described in Equations [1]–[6]:

* Department of Chemical and Metallurgical Engineering, Aalto University, Espoo, Finland.

† School of Chemical and Metallurgical Engineering, Johannesburg, South Africa

© The Southern African Institute of Mining and Metallurgy, 2018. ISSN 2225-6253. This paper was first presented at the INFACON XV: International Ferro-Alloys Congress, 25–28 February 2018, Century City Conference Centre and Hotel, Cape Town, South Africa.

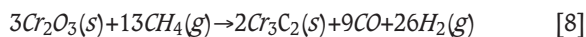
Reduction of Kemi chromite with methane



resulting in the overall reaction of methane adsorption on the oxide's active surface as in Equation [7]



The overall reaction for reduction of chromium by methane oxide can be represented as:



This reaction mechanism has been proposed for both pure chromium oxide (Anacleto and Ostrowski, 2004) and natural chromite (de Campos and Eric, 2006). In the present work, the aim was to investigate the characteristics of methane reduction for a specific chromite mined in Kemi, Finland.

Materials and methods

Chromite ore from Kemi has a relatively low Cr/Fe ratio, but due to the mine's proximity to a stainless steel plant, it is nevertheless a profitable deposit for mining (Huovinen, 2007). XRD analysis of the received concentrate indicated that Mg-Al-Cr-Fe spinel was the main mineral in the sample, with very little separate silica phase. A chemical analysis of the raw material is presented in Table 1.

The particle size distribution of the concentrate is shown in Figure 1. The analysis was done using a Mastersizer 2000 from Malvern Instruments. Five measurements were conducted using 4 bar dispersion pressure and Fraunhofer approximation for the calculations.

The reduction experiments were conducted on a loose bed of chromite concentrate powder in a closed, horizontal-tube electric furnace. One gram of Kemi chromite concentrate was

Table 1

Chemical analysis (wt%) of chromite ore concentrate used in this study

Mg	Al	Ca	Ti	Cr	Cr met	Fe	Fe met	SiO ₂	Total
6.5	6.6	0.41	0.28	29.9	0.02	17.6	0.21	3.4	64.71

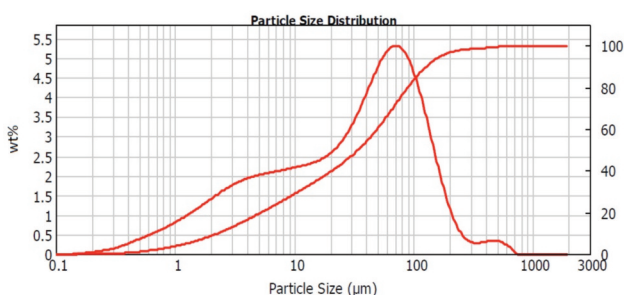


Figure 1—Particle size distribution of the chromite concentrate

reduced for various time intervals (10, 20, 30, 60, 90, and 120 minutes) in controlled atmospheres of varying CH₄/H₂ contents (10, 20, and 30 vol% CH₄). Gas flow through the furnace was kept constant at 1 l/min. The reduction temperatures were 1100, 1200, 1300, and 1350°C. Argon was used for a reference test and as an inert gas for purging the furnace. The gas components used were instrumental argon (Ar 99.999%), industrial hydrogen (H₂ 99.99%), and industrial methane (CH₄ 99.5%), all supplied by AGA, a member of the Linde Group. Alumina crucibles were used as sample holders for the chromite concentrate.

Phase characterization of the reduced samples was done by X-ray diffraction (XRD), using an X'pert PRO by PANalytical. Quantitative phase analysis was by the Rietveld method (Hem *et al.*, 2009) with PANalytical's X'Pert HighScore Plus program. SEM-EDS analysis was performed using a LEO model 1450 VP and Oxford Instruments INCA software. The amount of carbon in the samples was determined using an Eltra CS-2000 S/C analyser.

The isothermal sections and liquidus contour diagrams of the C-Cr-Fe system were calculated with MTDATA software (Davies *et al.*, 2002) using the iron-base alloy database TCFE (National Physical Laboratory, 2015). The calculation included 21 possible condensed phases. The gas phase was excluded because it is of only minor importance in the calculations and phase equilibria of the system.

Results and discussion

Reduction mechanism

SEM analysis clearly showed that an outer layer of metal carbides formed, with inner layers of partially reduced chromite. Beneath the partially reduced regions, there was an unreacted core with the same composition as the raw material. This is referred to as a shrinking core mechanism and it has been observed previously for chromite reduction with methane (de Campos and Eric, 2006). The shrinking core was observed throughout the experimental series and it appeared to form in two stages. In the first stage, the iron is completely reduced along with part of the chromium. In the second stage, the rest of the chromium is reduced completely.

An example of the first reduction stage can be seen in Figure 2, where the outer layer is almost white, the partially reduced area is a darker gray, and the unreacted core is a lighter gray. Reduction was carried out at 1100°C, with 10 vol% CH₄, for 20 minutes. EDS analyses were performed on the points indicated in the image. The compositional trends are shown in Figure 3. An EDS analysis of the raw material is also illustrated (dashed lines) in order to demonstrate that the core is, in fact, unreacted chromite ore. Small amounts of calcium and titanium are excluded from the data for clarity reasons.

Spectra 4 to 7 are taken from the unreacted core. Their compositions match relatively well with the dashed lines representing the raw material before reduction. Spectrum 3, which falls inside the darker grey area, has a significantly lower iron content, indicating that iron has been reduced to the metallic form and diffused to the surface, represented by spectrum 1. The amounts of chromium and magnesium are higher in spectrum 3, because most of the iron has been removed from this area. Spectrum 1 is on the white outer rim

Reduction of Kemi chromite with methane

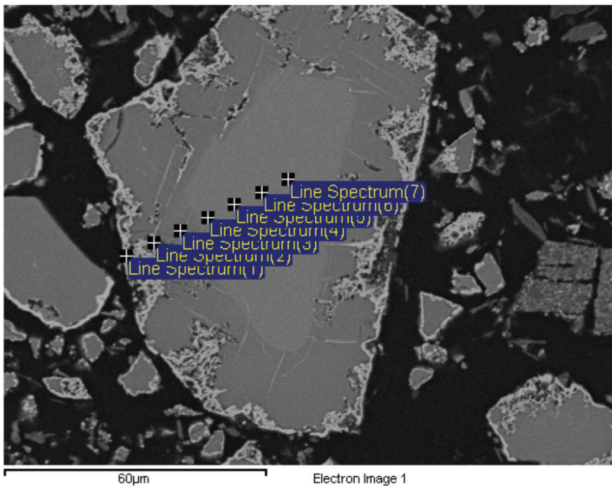


Figure 2—SEM micrograph of a sample reduced at 1100°C, using 10 vol% CH₄, for 20 minutes

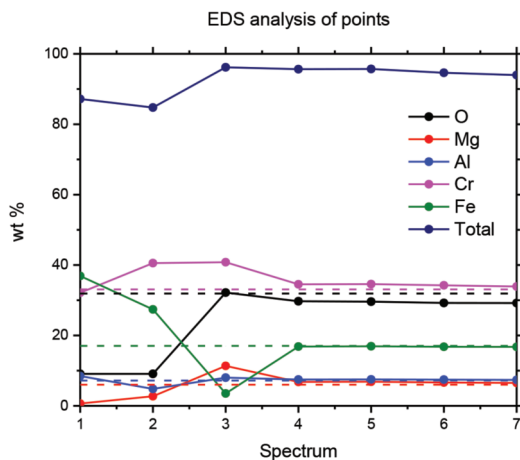


Figure 3—EDS analysis of the particle in Figure 2. Solid lines represent the analysis results, and dashed lines indicate the composition of the raw material

of the particle. It consists mostly of iron and chromium, with the oxygen content considerably lower than in other regions. This indicates that the outer layer is mostly metallic chromium and iron.

Figure 4 and Table II show the SEM micrograph and EDS analysis for a particle in the second stage of the shrinking core process, where iron has been almost completely reduced and chromium reduction is advancing. Table II shows the average EDS analysis results for the white areas, dark grey rims around the white beads, and central areas. Reduction was performed at 1300°C, with 30 vol% CH₄, for 120 minutes. The small amounts of calcium and titanium were again excluded from the data for clarity reasons.

The iron content is very low (< 1 wt%) outside the white areas. The chromium concentration here behaves more like the iron did in the sample depicted in Figure 2, first decreasing, but then increasing towards the centre. This indicates that almost all the iron has been reduced and has accumulated in the white areas as carbides, while chromium reduction is advancing towards the core of the particle.

It can be seen from Table II that the bright areas in Figures 2–4 consist mostly of iron and chromium. However, the samples for SEM analysis were coated with carbon and therefore the EDS analysis excludes all carbon. The total mass of material is lower in the lighter areas, and therefore it can be concluded that there is also carbon in the light areas on the edges of the particles. This indicates that iron and chromium might form carbides as they are reduced, which was observed by Soykan, Eric, and King (1991) with solid carbon as the reductant.

Figures 2 and 4 both show that the reduction also advances within the particle along cracks that form along the crystalline structure of the chromite spinel. This has also been observed in other studies (de Campos and Eric, 2006; Soykan, Eric, and King, 1991; Perry, Finn, and King, 1988).

In addition to the particles reducing through the shrinking core mechanism, collapsed particles were present in all the samples. The shrinking core mechanism was observed to be dominant in the earlier stages of the reduction. As reduction progresses, the particles start to collapse, resulting in reduction also inside the particle and not just on the outer surface, and in small cracks inside the particle. This is evident in Figure 5, which compares the particles reduced at 1300°C with varying methane concentrations for 10 min and

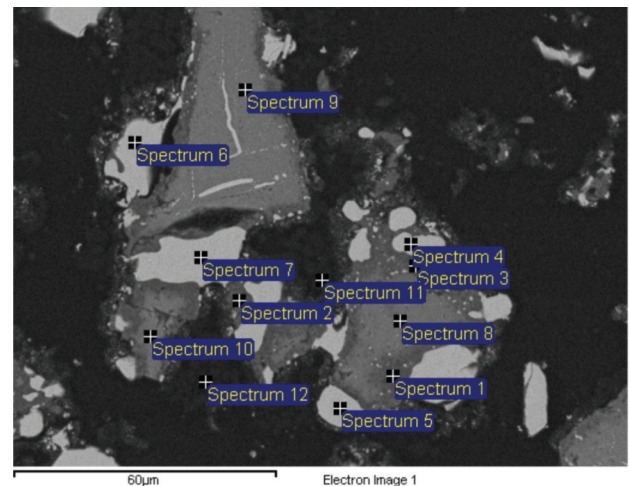


Figure 4—SEM micrograph of a sample reduced at 1300°C, using 30 vol% CH₄, for 120 minutes

Table II

EDS analyses of different phases in Figure 4 (wt%)

Element	White	Dark grey	Centre
O	0.43	35.55	30.50
Mg	0.00	19.94	12.50
Al	0.00	18.62	9.45
Si	0.00	5.92	0.06
Ca	0.00	0.65	0.00
Ti	0.00	0.22	0.86
Cr	44.62	6.11	36.34
Fe	38.48	0.86	0.76
Total	83.52	87.86	90.32

Reduction of Kemi chromite with methane

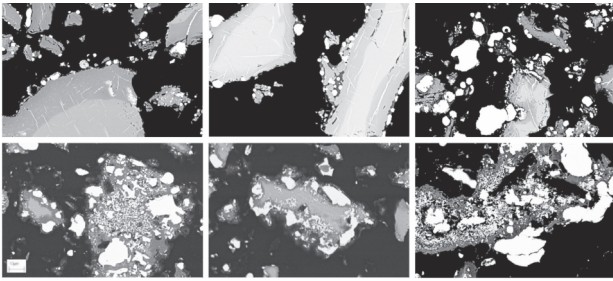


Figure 5—SEM micrographs of samples reduced for 10 minutes (upper row) and 90 minutes (lower row). The reduction was done at 1300°C with 10, 20, and 30 vol% CH₄ (left to right)

90 minutes' reduction time. The upper row of micrographs is with 10 minutes' reduction time and the lower is with 90 minutes. The methane contents of the gas mixture are 10, 20, and 30 vol%. This illustrates a change in the reduction mechanism with reduction time.

Iron metallization

The first stage of reduction advances significantly in the first 10 minutes at all temperatures and with all CH₄-H₂ mixtures. A micrograph and EDS analysis of the reduced areas in the sample reduced with 10 vol% CH₄ at 1100°C for 10 minutes are shown in Figure 6. The white reaction product layers on the edges of the particles are clearly visible.

At 1300°C practically all the iron was reduced and had diffused into the metallic phase (white areas). Figure 7 compares two micrographs of samples reduced at 1300°C with 10 vol% CH₄ for 20 and 30 minutes. Table III shows the EDS analyses of the grey areas in the centre of the particles.

After 20 minutes, the centre of the particle still contains unreduced material (in spectra 3 to 5), where the iron content is around 15 wt%, which is very close to the 17 wt% of the raw material. However after 30 minutes' reduction time, this phase is no longer detectable and the iron content throughout the particle's grey centre is around 1 wt%. The same phenomenon occurs at 1300°C regardless of the methane content used. When the temperature increases to 1350°C, the unreacted phase is barely detectable after 20 minutes' reduction time.

Chromium metallization

Generally, the iron-depleted, but still chromium-rich, intermediate phase disappeared at 1350°C with a reduction time of 60 minutes or more and a CH₄ content of 10 or 20

vol%. With 30 vol% CH₄, reduction for 30 minutes resulted in the disappearance of the phase, indicating that full reduction was achieved. A typical micrograph and EDS analysis of the samples reduced at 1350°C for 90 minutes are shown in Figure 8 and Table IV. Only two phases remain in the particle; the light grey areas of iron-chromium carbide and grey areas consisting of Mg-Al spinel with some Si, Ca, and traces of Fe and Cr.

Full chromite reduction at 1350°C was also supported by the XRD analyses and Rietveld calculations. The chromite concentrations in samples reduced at 1350°C are presented in Figure 9. Utilizing 20 vol% methane resulted in faster reduction than 30 vol% methane. This could be due to more solid carbon accumulating on the surface of the sample at 30 vol% methane, hindering diffusive gas flow to the chromite surface.

Iron- and chromium-based alloys

During the second stage of reduction, the fraction of chromium in the reduced phase increases as the process advances. More chromium accumulates in the reduced (white) metallic areas, until the phase becomes saturated with it. At this point a chromium-based phase starts to form within the reduced phase. The two phases are visible in several samples and were analysed where the surface areas were large enough for EDS analysis. Figure 10 shows a SEM micrograph in which the two phases are clearly distinguishable at the right-hand side of the image. At the left-hand side, the phases have begun to separate, but the

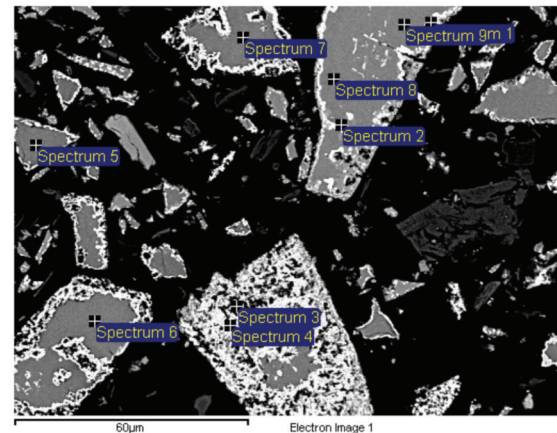


Figure 6—SEM micrograph of a sample reduced at 1100°C with 10 vol% CH₄ for 10 minutes

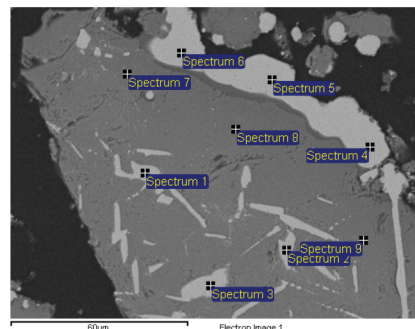
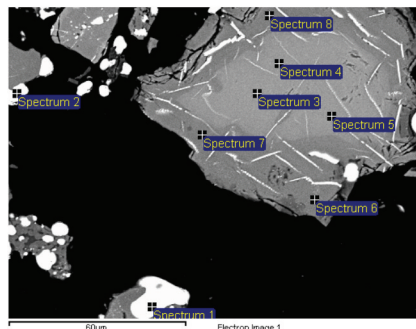


Figure 7—SEM micrographs of samples reduced at 1300°C using 10 vol% CH₄, for 20 minutes (left) and 30 minutes (right)

Reduction of Kemi chromite with methane

Table III
EDS analyses (wt%) of samples reduced at 1300°C with 10 vol% CH₄

Spectrum	O	Mg	Al	Ti	Cr	Fe	Total
20 min							
Spectrum 3	29.79	6.84	7.87	0.22	33.78	15.86	94.36
Spectrum 4	29.44	6.73	7.68	0.28	33.57	15.73	93.43
Spectrum 5	29.15	6.86	7.61	0.29	33.79	15.39	93.09
Spectrum 6	32.79	12.50	8.36	0.39	40.15	0.79	94.98
Spectrum 7	33.88	12.50	8.88	0.31	39.50	2.24	97.33
Spectrum 8	31.52	12.17	8.44	0.31	40.16	1.00	93.60
30 min							
Spectrum 7	30.68	10.14	11.93	0.45	36.11	1.34	90.65
Spectrum 8	31.37	9.96	11.93	0.50	35.68	0.91	90.35
Spectrum 9	30.62	9.45	12.15	0.35	35.38	1.06	89.02

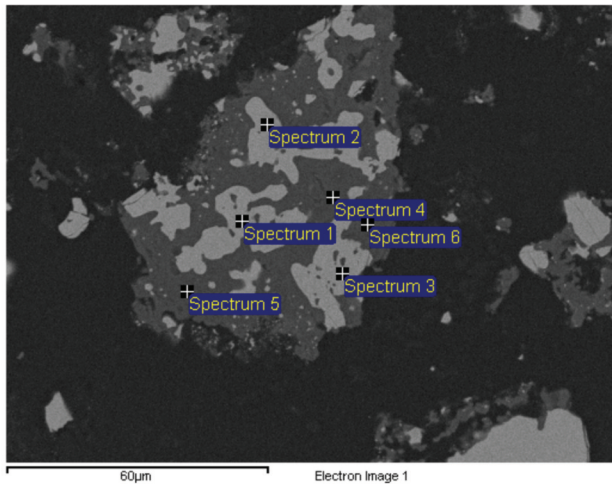


Figure 8—SEM micrograph of a sample reduced at 1350°C with 20 vol% CH₄ for 90 minutes

Table IV
EDS analyses (wt%) of a sample reduced at 1350°C with 20 vol% CH₄ for 90 minutes

Spectrum	O	Mg	Al	Si	Ca	Cr	Fe	Total
Spectrum 1						57.15	26.10	83.25
Spectrum 2						56.28	25.26	81.55
Spectrum 3						56.72	26.03	82.75
Spectrum 4	40.94	28.77	6.30	15.56	2.33	0.81		94.71
Spectrum 5	43.92	24.16	20.59	7.69	1.56	2.28	0.55	101.16
Spectrum 6	39.36	30.97	3.02	14.87	2.45	0.51		91.18

surface of the particle was not suitable for EDS analysis. This image shows how the separation of the two phases progresses through growth of smaller formations towards larger phase areas as diffusion progresses. The EDS analyses for the two phases in the right-hand side particle are listed in Table V.

The darker grey phase consists mostly of chromium and the brighter grey phase contains mostly iron. Therefore, the darker phase is the new, chromium-based alloy. In both examples, the brighter phase has a higher total analysis,

which indicates that the darker phase contains more carbon than the bright phase. A rough evaluation of the Cr-Fe-C ternary plot at 1300°C, presented in Figure 11, indicates that the iron-based phase is partly molten, but the chromium-based phase is completely solid. The sharp corners of the areas of chromium-based alloy in Figure 10 also confirm that the phase is formed as a solid. The composition of the iron-based phase is depicted with green lines in Figure 11, and that of the chromium-based phase with red lines.

The compositions of the phases in Figure 11 were calculated as an average from all the analyses of the two phases throughout the samples where they were present. Carbon was then assumed to balance the total to 100%, but it should be noted that some silica remains in the iron-based phase, and a very small amount of oxygen is present at some of the analysis points. Also, the ternary plot represents a system in equilibrium, but all the obtained results are from systems that most probably are not in equilibrium, but at a stage of transformation. The illustration is therefore just an approximation of a more complex system.

Summary and conclusions

Chromite concentrate from the Kemi deposit in Finland was reduced in CH₄-H₂ atmospheres. Altogether 72 experiments were conducted with three variables: temperature, time, and

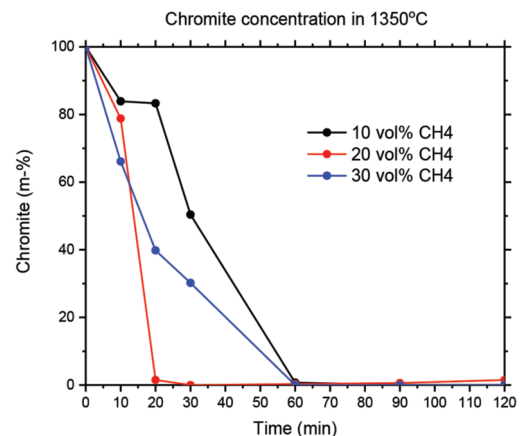


Figure 9—Chromite concentration after reduction at 1350°C, from XRD analyses and Rietveld calculations

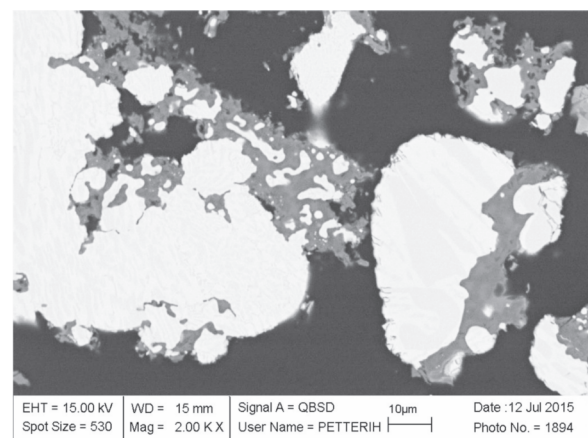


Figure 10—SEM micrograph of a sample reduced at 1350°C with 30 vol% CH₄ for 20 minutes

Reduction of Kemi chromite with methane

Table V

EDS analyses of the two reduced phases at the right-hand side in Figure 10 (wt%)

Phase	O	Si	Cr	Fe	Total
Bright phase 1		3.13	35.35	50.50	88.99
Bright phase 2		3.39	35.78	50.24	89.40
Dark phase 1	0.52		70.22	10.33	80.55
Dark phase 2			65.80	15.16	81.48
Average					
Bright phase		3.26	35.57	50.37	89.20
Dark phase	0.26		68.01	12.75	81.02

the content of methane in the feed gas mixture. The reduction temperatures were 1100°, 1200°, 1300°, and 1350°C and the reduction times 10, 20, 30, 60, 90, and 120 minutes. Three methane contents were used; 10, 20, and 30 vol%, with the balance H₂.

The reduction was observed to proceed mainly through a shrinking core mechanism in two stages. In the first stage, carbon from the cracking of methane reduces the iron and some chromium to carbides. After this, and partly overlapping with the first stage, a second stage of reduction begins, in which the chromium in the remaining spinel is reduced. The second reduction stage takes place at 1200°C and above.

Iron was essentially completely reduced after 30 minutes at 1300°C. As the temperature was increased to 1350°C, the iron was almost completely reduced from the chromite after 20 minutes. At the highest temperature, 1350°C, all of the chromium was eventually reduced after 30-60 minutes, resulting in residual aluminum and magnesium oxides with varying amounts of silica being left from the original Kemi chromite. As chromium reduction proceeded, two separate metallic phases were formed in the reduced areas, one iron-based and one chromium-based.

Metallization was observed to start immediately after the chromite was exposed to CH₄-H₂ mixtures, as chromite reduction to metal was observable after only 10 minutes of reduction time. At temperatures of 1300°C and 1350°C, metallization was completed within the duration of the experiments, as only very small amounts of iron and chromium remained in the unreacted zones. Therefore, reduction of Kemi chromite with a CH₄-H₂ mixture can be regarded as highly efficient compared to reduction with only solid carbon as the reductant. Similar levels of almost complete reduction of chromite spinels by ordinary carbothermic reduction require temperatures over 1500°C. This can be attributed to the high thermodynamic activity of carbon when it is provided by cracking of methane into carbon and hydrogen.

Acknowledgements

The authors are grateful to Tekes and Finland Academy for providing the part-time Finland Distinguished Professor position to R.H. Eric and funds for this research project. The CMEco project and the Technology Industries of Finland Centennial Foundation are acknowledged for their collaboration and support.

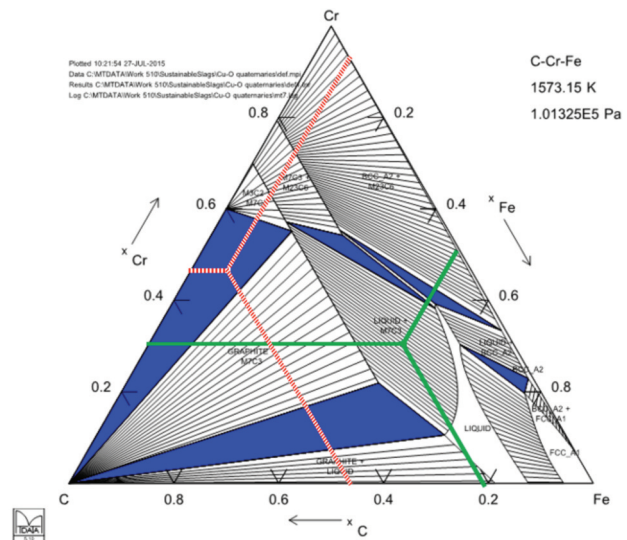


Figure 11—Fe-Cr-C ternary plot at 1300°C (mol fraction). Composition of the iron-based (bright) phase is illustrated in green, and that of the chromium-based (darker) phase in red

References

- ANACLETO, N. and OSTROVSKI, O. 2004. Solid-state reduction of chromium oxide by methane-containing gas. *Metallurgical and Materials Transactions B*, vol. 35, no. 4. pp. 609–615.
- ARVANITIDIS, I., ARTIN, C., CLAESON, P., JACOBSSON, H., JOHANSSON, P., RASSMUS, J., and SWARTLING, D. 1996. Study of the kinetics of reduction of iron chromate by hydrogen. *Scandinavian Journal of Metallurgy*, vol. 25, no. 4. pp. 141–147.
- BASSON, J. and DAAVITILA, J. 2013. High carbon ferrochrome technology. *Handbook of Ferroalloys*. Gasik, M.I. (ed.). Elsevier. Chapter 9. pp. 317–363.
- DE CAMPOS, M. and ERIC, R.H. 2006. Reduction behaviour of chromite in the presence of a hydrocarbon gas. *Proceedings of the Sohn International Symposium. Advanced Processing of Metals and Materials*. Vol. 1. Wiley.
- DAVIES, R.H., DINSDALE, A.T., GISBY, J.A., ROBINSON, J.A.J., and MARTIN, S.M. 2002. MTDATA - Thermodynamic and phase equilibrium software from the National Physical Laboratory. *Calphad*, vol. 26, no. 2. pp. 229–271.
- HEM, S.R., LOUW, J.D. DE V., GATESHKE, M., GÖSKE, J., RINDBÆK LARSEN, O., and STRANGWAYS, J. 2009. Sample preparation for quantitative Rietveld analysis, phase identification and XRF in one step: automated sample preparation by Centaurus. *Proceedings of the 7th International Heavy Minerals Conference*. Southern African Institute of Mining and Metallurgy, Johannesburg. pp. 49–56.
- HUOVINEN, I. 2007. Kemin kromiitin Cr/Fe-suhde kromiitin raekoon funktona Pohjois-Viian, Eljjarven ja Eljjarven E-malmioissa. Pro gradu, Department of Geosciences, University of Oulu. 104 pp.
- KEKKONEN, M., XIAO, Y., and HOLAPPA, L. 1995. Kinetic study on solid state reduction of chromite pellets. *Proceedings of the 7th International Ferroalloys Congress (INFACON 7)*, Trondheim, Norway. Tveit, H., Tuset, J.K., and Page, I.G. (eds). Norwegian Ferroalloy Producers Research Organization (FFF). pp. 351–360.
- LYAKISHEV, N.P. and GASIK, M.I. 1998. *Metallurgy of Chromium*. 1st edn. Allerton Press, New York.
- MURTHY, Y.R., TRIPATHY, S.K., and KUMAR, C.R. 2011. Chrome ore beneficiation challenges & opportunities – A review. *Minerals Engineering*, vol. 24, no. 5. pp. 375–380.
- NATIONAL PHYSICAL LABORATORY, 2015. MTDATA - Databases. <http://www.npl.co.uk/science-technology/mathematics-modelling-and-simulation/mtdata/databases/> [accessed 13 August 2015].
- NIAYESH, M.J. and DIPPENAAR, R.J. 1992. The solid-state reduction of chromite. *Proceedings of INFACON 6*, Cape Town. South African Institute of Mining and Metallurgy, Johannesburg. pp. 57–63.
- PERRY, K.P.D., FINN, C.W.P., and KING, R.P. 1988. An ionic diffusion mechanism of chromite reduction. *Metallurgical Transactions B*, vol. 19, no. 4. pp. 677–684.
- SOYKAN, O., ERIC, R.H., and KING, R.P. 1991. The reduction mechanism of a natural chromite at 1416°C. *Metallurgical Transactions B*, vol. 22B. pp. 53–63.
- TASKINEN, P., FABRITIUS, T., and ERIC, R.H. 2014. A new FIDIPro project: Sustainable production of ferroalloys. *Materia*, vol. 1, no. 5. pp. 46–50. ◆



NaOH-assisted direct reduction of Ring of Fire chromite ores, and the associated implications for processing

by S. Sokhanvaran*, D. Paktunc*, and A. Barnes†

Synopsis

As part of a broader programme to fully characterize the chromite ores discovered in the 'Ring of Fire' region of northern Ontario, NRCan and private research facilities in Canada have performed extensive test work over the past six years. The studies focused on developing alternative approaches for producing ferrochrome at lower temperatures and with fewer greenhouse gas emissions. The use of various fluxes or catalysts for accelerated direct reduction had yielded promising results, particularly with caustic soda (NaOH). The initial work had been protected by a patent known as the 'KWG process'. The most recent work by NRCan has confirmed that the addition of NaOH to chromite ores in carefully controlled amounts leads to high degrees of metallization at much lower temperatures than would be achieved by conventional smelting technologies, at greatly accelerated reactions rates.

This paper summarizes the key findings of the latest work, including the role of NaOH in the reduction process and parameters influencing the degree of metallization and alloy particle growth. The paper will also discuss the implications of the results with respect to benefits, challenges, and opportunities for processing Ring of Fire chromite ores into saleable chrome units.

Keywords

chromite, ferrochrome, prereduction, direct reduction, catalysts, Ring of Fire.

Introduction

Chromium is one of the essential commodities for today's life, with applications in stainless and high-alloy steels, providing enhanced corrosion resistance and improved mechanical properties. Chromium is usually added to the steel in the form of ferrochrome (FeCr) alloy. The 'Ring of Fire' chromite deposit in northern Ontario presents an opportunity for Canada to enter the globally strategic market. It contains the only commercial quantities of chromite in North America and is the fourth largest deposit in the world. The resources, including Measured, Indicated, and Inferred, are 300 Mt grading approximately 33% Cr₂O₃. However, the remote location of the deposits makes development challenging. The preference for processing the chromite ore to marketable ferrochromium alloy within Ontario constitutes an additional challenge due to high electricity costs.

Currently, 80% of the world's FeCr is produced in submerged arc furnaces. There are four technologies currently used for the production of ferrochrome alloys. These are

the conventional semi-closed furnace, the Outotec process, the DC arc furnace, and the Premus process. Disadvantages of the smelting processes include high energy consumption, between about 3.4 and 4.6 MWh per ton of ferrochrome produced (Ugwuegbu, 2012; Cramer, 2016), and generation of greenhouse gas emissions as high as 1 t of CO₂ per ton of ferrochrome produced. Under current market conditions with oversupply of FeCr (Kelly and Matos, 2014), production of ferrochrome at a competitive cost is a key factor if Canada is to enter this market. This requires either optimization of current processes or development of new processes that require less energy and can operate with a smaller environmental footprint.

The Premus (Naicker, 2006) technology has the lowest specific electrical energy consumption but it has a slightly larger carbon footprint. The raw materials, including chromite ore, reductants, and clay binder are milled, pelletized, indurated, and fed to a rotary kiln where they are partially prereduced. The hot, prereduced, and sintered pellets are then charged into closed submerged arc furnaces. Prereduction of the pellets in addition to charging them hot reduces the overall amount of electrical energy needed for ferrochrome production.

Processes that maximize the extent of solid-state prereduction hold the best potential to reduce overall specific electrical energy consumption. The use of additives to enhance reduction kinetics has been extensively studied. In cases where the reaction is controlled by diffusion of ions, fluxing agents can enhance the rate of reaction by forming a liquid layer around chromite grains to enable

* Canmet Mining, Canada.

† Metallurgical Process Consultants Ltd, Canada.

© The Southern African Institute of Mining and Metallurgy, 2018. ISSN 2225-6253. This paper was first presented at the INFACON XV: International Ferro-Alloys Congress, 25-28 February 2018, Century City Conference Centre and Hotel, Cape Town, South Africa

NaOH-assisted direct reduction of Ring of Fire chromite ores

faster diffusion or transport of the reducible ions. The presence of flux on the surface of chromite during all stages of reduction provides an enhanced access to Cr and Fe oxides remaining in the shrinking core of chromite and enables the reduction reactions to continue (Dawson and Edwards, 1986).

The influence of various fluxing agents on the direct reduction of chromite has been extensively investigated by numerous researchers. The list of additives includes halides (Dawson and Edwards, 1986; Katayama, Tokuda, and Ohtani 1985; Li *et al.* 2011), hydroxides (Winter, 2015), carbonates (van Deventer, 1988; Neizel *et al.*, 2013), oxides (Sudar Murti *et al.*, 1983; van Deventer, 1988; Neuschütz *et al.*, 1995; Ding, 1997; Ding and Warner, 1997; Lekatou and Walker, 1997; Weber and Eric, 2006; Wang, Wang, and Chou, 2015), and borates (Bisaka, Makwarela, and Erwee, 2016; Lu, 2012; Katayama, Tokuda, and Ohtani, 1985). Borate was reported to be the most effective additive among other available options (Katayama, Tokuda, and Ohtani, 1985; Li *et al.*, 2011).

Work performed in South Africa by Barnes, Finn, and Algie (1983) on the prereduction of UG2 chromites, and early TGA testing of the Ring of Fire ores indicated that a prereduction route was worth investigating for the Canadian ores. In 2013, based on the improvements seen with UG2 ores, prereduction test work involving the use of small amounts of alkali salts was conducted on the Ring of Fire chromites. Results from small-scale TGA tests in a Netsch TGA/DSC/MS were particularly encouraging, with dramatic improvements in both the reaction rates and extent of reduction at temperature compared to uncatalysed ores, as well as lower temperatures for the onset of reduction (Barnes, Muinonen, and Lavigne, 2015)

Natural Resources Canada (NRCAN) has been directed through Budget 2015 to provide significant support for the development of methods for direct reduction of chromite using various fluxes or catalysts. Part of this study is focused on the effective role of caustic soda (NaOH) in direct

reduction. The initial work has been protected by a patent application for the 'KWG process' (Barnes, Muinonen, and Lavigne, 2015; Winter, 2015). Further investigations by NRCAN confirmed that the addition of NaOH to chromite ores led to accelerated reaction rates and high degrees of metallization at lower temperatures than would be achieved by conventional smelting technologies. Carbothermic reactions referred to in this paper involved combinations of NaOH, chromite, and carbon under an argon atmosphere.

Experimental approach

The ore and concentrate samples were premixed with varying proportions of graphite and additive. The mixtures were subjected to two different types of experiments: thermal analysis measurements and furnace tests as described in a previous publication by the lead authors (Sokhanvaran and Paktunc, 2017). The chemical compositions of ores from three different Ring of Fire deposits used in the experiments are shown in Table I, in comparison to various South African chromite ores used for benchmarking.

A comparison of the chemical compositions of the ores based on their potential reducibility (*i.e.* refractory/nonrefractory ratio) (Slatter, 1980) reveals that South African ores are easier to reduce as they are less refractory. However, owing to the lower Cr/Fe ratio of these ores, the grade of ferrochromium produced is lower than that potentially obtainable from the Canadian ores. The reducibility index initially developed by Barnes and Eric (1995) also predicted a lower reducibility index.

Results and discussion

Reducibility of different ores

The reducibility of three different chromite ores, based on TGA analysis, is shown in Figure 1. It is worth noting that, from a mineralogical perspective, the Canadian ore contains hydrous silicate gangue minerals. This is reflected in larger mass losses by the Black Thor and Black Horse ores during

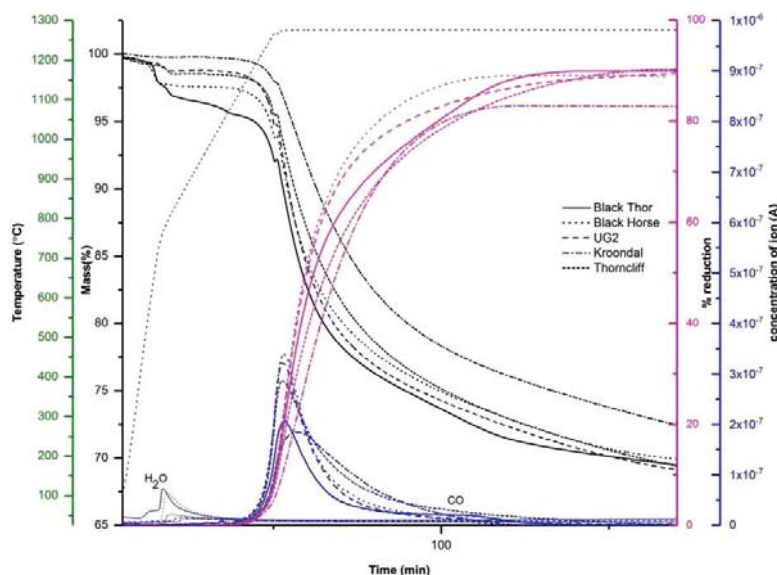


Figure 1—Thermogravimetric analysis (ore:graphite approx. 100:22)

NaOH-assisted direct reduction of Ring of Fire chromite ores

the first stage of heating, associated with the H₂O peak. To isolate the effect of dehydroxylation from the mass loss due to reduction, the purple curves illustrate the mass loss associated with reduction of each mixture containing 100 g of ore (the mass loss due to dehydroxylation was subtracted from the curve). This graph also illustrates that reduction starts in all of these cases at about the same temperature (above 1200°C). The extent of reduction for all these ores seems to be similar considering the small difference in the amount of removable O₂ from each ore (Table I). The UG2 achieved the highest degree of reduction, whereas the Black Thor ore has the lowest, as would be expected from the R: non-R ratio. This high ratio for Black Thor ore predicts a lower degree of reduction, and also a more sluggish reduction, as illustrated by the mass loss curve for this ore.

Effect of NaOH on reducibility of Canadian and South African ores

The effects of NaOH on the reduction of UG2 and Black Thor ores are similar, as shown in Figure 2. NaOH decreases the reduction temperature and increases the rate and degree of reduction. For both ores, the addition of NaOH results in three stages of mass loss and two major CO peaks. Although the total mass loss increased with the addition of NaOH, it is difficult to confirm that NaOH addition results in a higher degree of reduction, due to the possible decomposition of NaOH and the presence of Na and H₂ in the gas phase.

The first mass loss peak, which is associated with the water peak, is due to the evaporation of absorbed water from NaOH. The intensity of water evolution from the Black Thor ore is greater than that observed in the case of UG2, which can be ascribed to the difference in the mineralogy of the two ores and dehydroxylation of the Black Thor ore during heating. As was explained previously (Sokhanvaran and Paktunc, 2017), the second stage of mass loss associated with the first CO peak is due to reaction between NaOH and C, as well as the start of Fe reduction. This endotherm commences at 750°C in both cases, which shows the accelerating role of NaOH in Fe reduction. Assuming that the mass loss associated with the reaction of NaOH is the same in both samples (due to the identical masses of NaOH added), the larger mass loss observed for UG2 is probably due to the greater amount of Fe₂O₃ present in this ore.

The third stage of mass loss, also associated with a CO peak, can be explained as the mass loss due to the reduction of Cr and Fe. Commencement of this reaction causes another endotherm on the DSC curve at 910°C for the Black Thor ore

and 1000°C for UG2 ore. This reaction occurs at a faster rate above 1000 and 1075°C, respectively, for these ores. The greater mass loss at this stage in the case of Black Thor ore can be explained by the higher concentration of Cr₂O₃ compared to UG2. As mentioned earlier, mass loss is not a sufficient indicator of the degree of reduction; in this case, however, the higher mass loss in the last stage compared to the total mass loss in the absence of the additive in both cases indicates that the reduction progresses to a higher degree in the presence of NaOH.

The effect of NaOH on the direct reduction of chromite ore has been discussed elsewhere (Sokhanvaran and Paktunc 2018). This additive reacts with all reactants present in the mixture: ore, gangue, and carbon. The reaction of the octahedrally coordinated ions in chromite with NaOH forms NaAlO₂ and NaCrO₂, leaving behind the tetrahedrally coordinated cations as monoxide phases (*i.e.* MgO and FeO). Destruction of the chromite crystal structure enhances the reduction mechanism. NaOH also reacts with the silicate gangue minerals to form a sodium aluminosilicate phase as a slag surrounding the original chromite particles. This slag phase is molten and provides a medium for transporting Fe and Cr ions to the reduction sites. NaOH also interacts with carbon, which results in the acceleration of the Boudouard reaction and generation of CO and Na vapour.

Characterization of the reduction products

As the TGA test results showed that the addition of NaOH to the feed mixture improves the reduction reaction, larger scale furnace tests were conducted to confirm the effectiveness of this additive on Black Horse ore. The chemical compositions of the two feeds are listed in Table II. The first sample contains less than the stoichiometric amount of carbon for complete metallization, and the second one contains just enough to remove oxygen from the reducible cations in the ore.

Both of these mixtures were heated to 1250°C for 1 hour. The SEM micrographs of the samples after reduction are shown in Figure 3.

The metallic phases in these micrographs are the hexagonal carbide (Figure 3b) and the coarse lumpy alloy (Figure 3d). The chemical compositions of the metallic phases forming in each sample are plotted in Figure 4. As illustrated, the concentration of Cr in the metallic phase of sample A1 is lower than in sample A2. This confirms that Cr reduction was not complete in A1, due to the carbon deficiency. The higher concentration of Cr in the metallic phase of sample A2 as well

Table I

Composition of chromite ores

Ore (75-106 μm)	Cr/Fe (mole ratio)	Cr ₂ O ₃ (wt%)	Fe ₂ O ₃ (wt%)	MgO (wt%)	Al ₂ O ₃ (wt%)	SiO ₂ (wt%)	R:non-R (by mass)	Removable O ₂ (wt%)
Black Thor	1.97	43.11	21.40	13.60	13.50	5.67	2.50	20.0
Black Horse	2.1	46.92	23.02	12.00	13.20	4.24	2.64	21.7
Black Bird conc.	2.1	47.32	24.10	10.20	12.55	3.09	2.58	22.2
UG2	1.3	41.57	33.09	10.13	15.68	3.01	1.87	23.1
Kroondal	1.5	44.17	30.18	10.05	15.22	2.79	2.10	23.0
Thornclyff	1.5	43.07	29.47	10.23	14.87	3.28	2.10	22.5

R: refractory; non-R: nonrefractory

NaOH-assisted direct reduction of Ring of Fire chromite ores

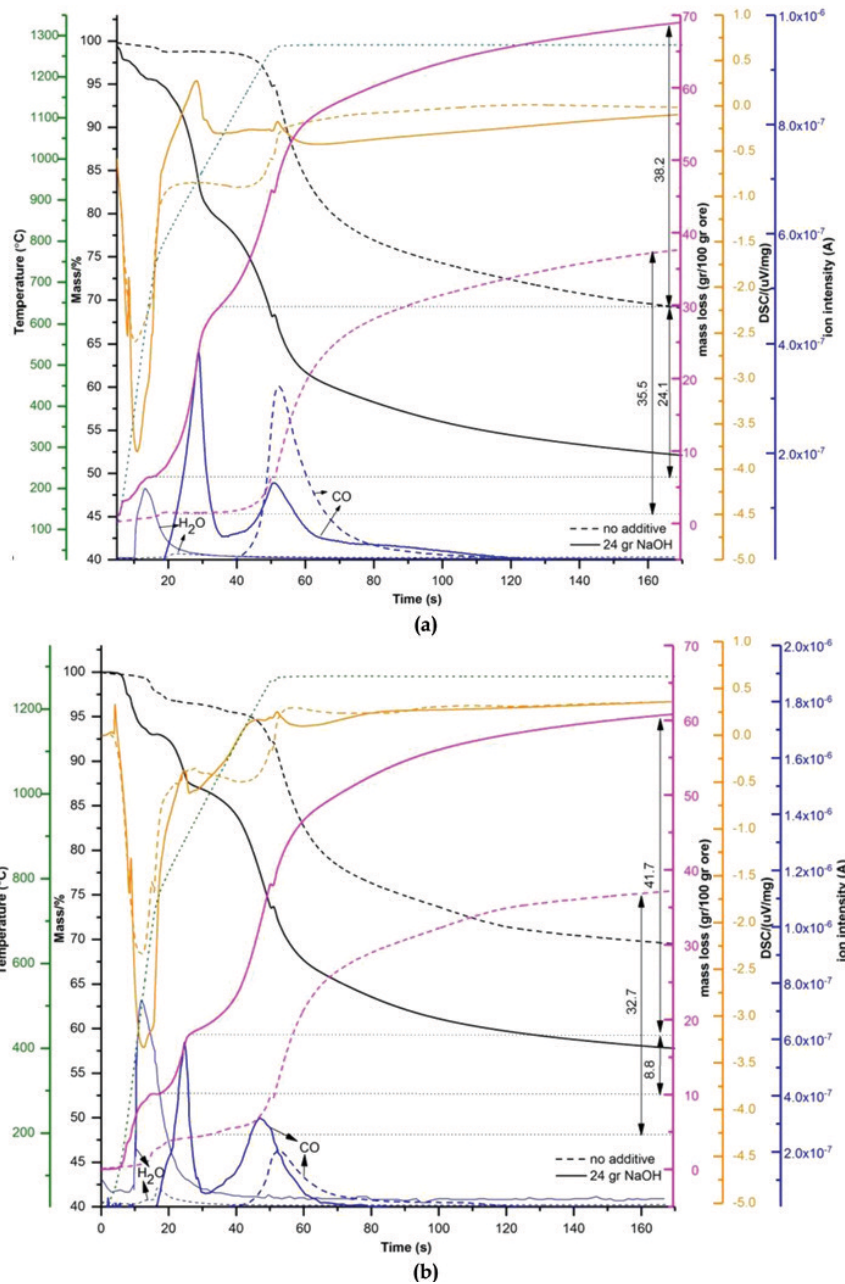


Figure 2—Effect of NaOH addition on reducibility (ore: graphite: NaOH approx. 100: 22: 24); (a) UG2, (b) Black Thor

Table II

Composition of the mixture used for the initial large-scale test by KWG

	Ore (g)	C (g)	NaOH (g)	Temp (°C)	Weight loss (%)
A-1	100	11.0	6.1	1250	9.7
A-2	100	17.6	6.5	1250	15

as large particle size of the alloy (Figures 3c and 3d) confirms that a higher degree of reduction was achieved in this sample, consistent with thermochemical theory.

The large particle size of the alloy provides an opportunity for subsequent physical separation of the

metallic phase from the residual phases in the sample. The result of gravity separation by simple superpanning is shown in Figure 5, which illustrates the potential of this technique for separation of a marketable metallic product. However, further work is needed to investigate the factors influencing the morphology and degree of reduction, as well as the relationship between product grade and recovery.

CanmetMINING conducted further investigations on ore and concentrate samples from the Ring of Fire deposits. For this study, 100 g of the Black Thor ore and Black Bird concentrate were each mixed with 22 g of graphite, both with and without NaOH (12 g). The mixtures were reduced at 1300°C for 1 hour. The mass loss was normalized for a mixture containing 100 g of ore in all cases for comparison. The mass losses from the reduction of the Black Thor

NaOH-assisted direct reduction of Ring of Fire chromite ores

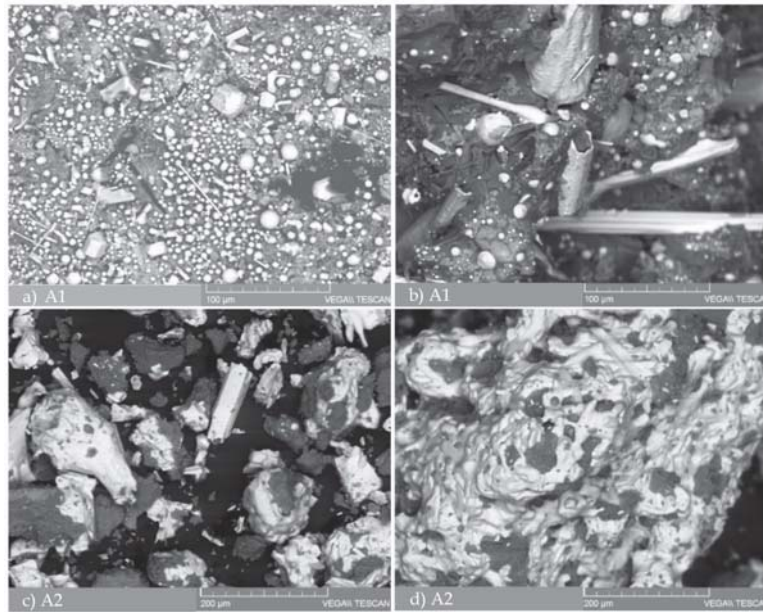


Figure 3—Micrographs of samples after reduction at 1250°C for 1 hour. (a, b) sample A1; (c, d) sample A2

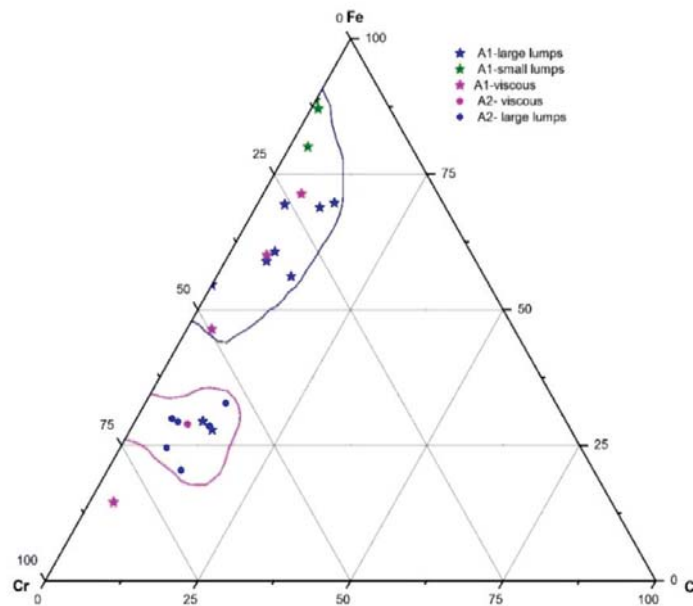


Figure 4—Chemical compositions of metallic phases formed in samples A1 and A2

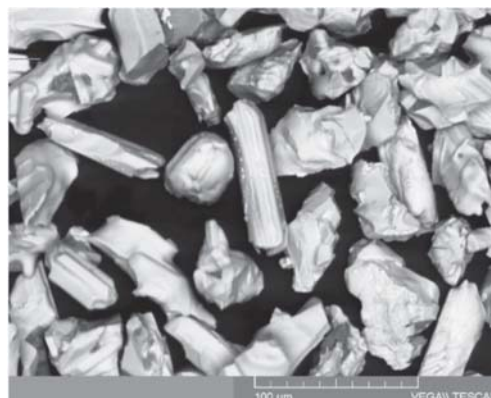


Figure 5—Metallic products concentrated by superpanning of combined A1 and A2 products from direct reduction of ore with NaOH

NaOH-assisted direct reduction of Ring of Fire chromite ores

samples were 24.8 g without NaOH and 38 g in the presence of NaOH. The mass losses for Black Bird samples, which were both subjected to 2 hours' reduction, were 29.4 and 43.2 g, respectively. The mass losses for both ore and concentrate increased with the addition of NaOH. The micrographs of the samples are shown in Figure 6. Higher degrees of reduction as a result of NaOH addition are obvious in both cases. The degree of Cr metallization measured by the XAFS method for sample (c) is 38.4%, and 85.5% for sample (d).

Changes in the morphology of both the metallic and residual chromite particles were observed with the NaOH addition. The metallic phases formed mainly inside the chromite particles without much metallization around the graphite and chromite particles as was the case in the absence of NaOH, implying the involvement of CO in the reduction. The chemical compositions of the alloy phase formed in each of these samples, as well as the chemical composition of the residual chromite, are shown in Figure 7.

The increase in Cr content of the alloy phase (Figure 7a) for the Black Thor samples clearly illustrates the enhancement of reduction as a result of NaOH addition. This improvement is illustrated in Figure 7b by the decrease in the Cr plus Fe contents and increase in the Mg plus Al contents of the residual chromite. This change in chemical composition is less obvious in samples containing Black Bird concentrate as the reduction in this sample was significant even without NaOH, due to the longer residence time. However, the total degree of metallization increased dramatically, as shown in Figures 6a and 6b.

The alloy particles formed with 6 g NaOH addition were larger than those with 12 g NaOH. This may indicate that although a higher NaOH concentration may be beneficial in terms of improving the degree of reduction (Sokhanvaran and Paktunc, 2017), it may have an adverse effect on crystal nucleation by accelerating the rate of CO generation (the first CO peak in Figure 2). The optimum condition that results in

both a high degree of reduction and large alloy particles lies somewhere between these two levels, and requires further investigation.

Implications for processing

Barnes, Muinonen, and Lavigne (2015) discussed the broader techno-economic implications of a process that could take advantage of the improved kinetics and lower operating temperature, but without a specific process configuration in mind. An early Metsim model, based loosely on the Premus kiln process, provided provisional mass and energy balance data used for a high-level look at the carbon footprint implications. The high gas volume generated using reformed natural gas in a vertical shaft reactor such as in the Midrex process was considered impractical and the focus on reactor type moved toward rotary or linear hearth furnaces. Early in 2017, the possibility of utilizing the Envirosteel concept was raised and Erasmus (private communication) performed some preliminary calculations based on UG2 chromite reduction which showed that the reverberatory nature of the ESS furnace configuration allowed much better energy utilization while still maintaining reducing conditions in the bed.

Subsequent modelling on Ring of Fire ore containing six units NaOH addition to 100 units of ore has confirmed the initial conclusions. In this model, combustion of the CO-rich off-gas in the freeboard region of the reactor provides sufficient energy to raise the internal temperature to 1400°C and sufficient surplus heat to sustain the endothermic reduction reactions at 1250°C (calculated in the modelling to be 2.03 MWh per ton FeCr alloy produced).

From a process efficiency perspective, the kinetics of the last 15% of metallization is extremely sluggish and this has been recognized by Glencore in their Premus operations. The operating conditions for a commercial process would therefore logically target 80-85% metallization, and apparently be 'undercoked' from a stoichiometric perspective.

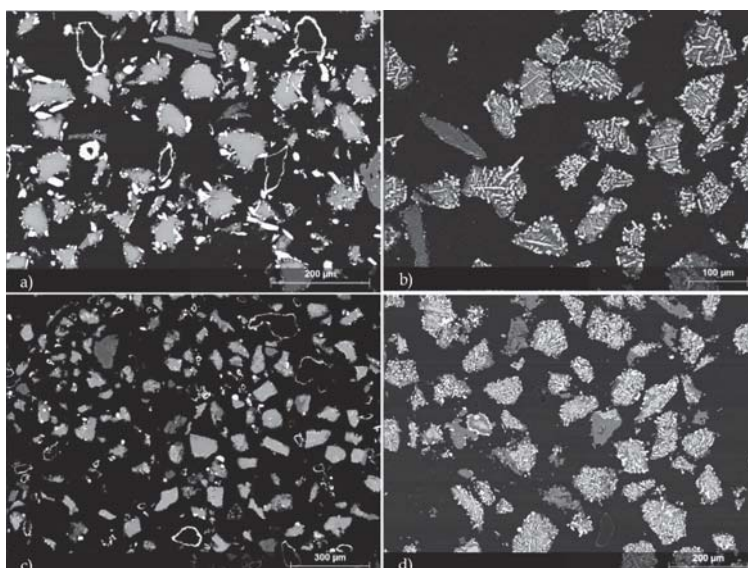


Figure 6—SEM micrographs of sample cross-sections after reduction at 1300°C. (a) Black Bird concentrate: graphite = 100:22, reduced for 2 h; (b) Black Bird concentrate: graphite: NaOH = 100:22:12, reduced for 2 h; (c) Black Thor ore: graphite = 100:22, reduced for 1 h; (d) Black Thor ore: graphite: NaOH = 100:22:12, reduced for 1 h

NaOH-assisted direct reduction of Ring of Fire chromite ores

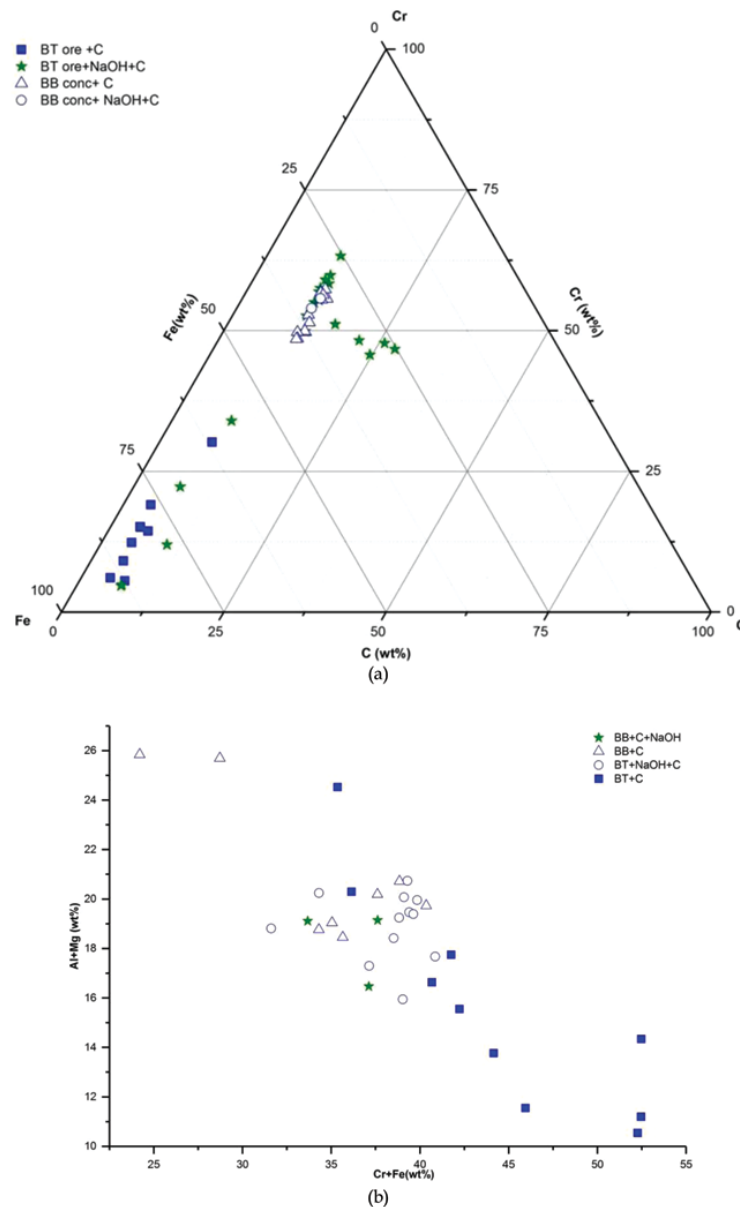


Figure 7—Chemical compositions of phases formed in Figure 6; (a) alloy phases, (b) residual chromite

Table III

Summary of process conditions for reverberatory (ESS) reduction

Preheating unit	Target 700°C for solids, 1100°C for gas
Natural gas	300 kg gas per ton ore
Air	3000 kg per ton ore
Reduction unit freeboard	Target 1400°C gas temperature
Hot gas	3300 kg per ton ore
Reduction zone	
In: Ore, 1 t	46.9% Cr ₂ O ₃ ; 23% FeO
Flux (NaOH)	60 kg per ton t ore
Reductant (anthracite)	210 kg per ton ore; 92% C , 5% SiO ₂ , 3%Al ₂ O ₂
Out: Alloy	440 kg per ton ore; grade: 53.9% Cr; 37.6% Fe; 8.3% C
Residual oxides	465 kg per ton ore 26.7% Cr ₂ O ₃ ; 101 % Na ₂ O; 29% Al ₂ O ₃ ; 20% MgO; 13.6% SiO ₂
Metal recovery to alloy	Cr 73.5%; Fe 99.6%

Since Rankin’s work (Rankin and Finn, 1978; Rankin, 1979) had shown conclusively that indirect reduction of chromium oxides in chromite is indeed possible at high partial pressure of CO, where CO is regenerated via the Boudouard reaction with solid carbon in the vicinity, and indirect reduction of iron oxides contributes to the overall reduction, slightly more metallization is obtained than would be calculated by assuming only direct reduction via carbon. The alkali salt catalyses the CO regeneration and improves the kinetics of the important gaseous reduction reaction.

As noted in the experimental results, a lower degree of Cr metallization would be acceptable as it is consistent with the economic argument by Kleynhans *et al.*, (2017) on the financial benefits to be gained by preoxidation of chromite prior to reduction, for maximizing unit throughput. Similarly, smaller reactors, with higher specific throughput and lower unit capital cost, maximize the benefits to be derived from the enhanced reaction kinetics using NaOH.

NaOH-assisted direct reduction of Ring of Fire chromite ores

Discussion and conclusion

Laboratory work has consistently confirmed the catalytic action of small amounts of caustic soda on the reduction kinetics of Canadian chromite. The ability of caustic soda to destruct the chromite spinel structure in the absence of a reductant, the 'buffering' influence of the sodium on the Boudouard reaction, and the presence of a small amount of slag above 720°C would contribute synergistically to the efficiency of the overall reduction reactions.

Capitalizing on these benefits does, however, require considerably more work at larger scale since the major challenges are related to reactor design. It is recognized that conversion of promising laboratory-scale test work to a viable commercial processes is a long and arduous process. Currently, the scarcity of sufficient Canadian ore for test work is one of the impediments to progressing this promising route.

It is worth pointing out that the greatest value in the prereduction option will likely be the ability to treat fines and concentrates generated during the mining and processing of the high-grade massive ores, since the Ring of Fire ores are competent, and the mining and transportation costs for these ores are significant. Until detailed mining plans are developed, speculation over the role that prereduction will play in the commercial exploitation of the Ring of Fire is premature.

Acknowledgements

This research is funded by Natural Resources Canada's Rare Earth and Chromite R&D programme. Contributions of the following are acknowledged: Judith Price for polished section preparation, KWG Resources for providing ore samples, and XPS for performing the furnace tests and TGA-DSC analyses. X-ray absorption spectroscopy experiments were performed at the PNC-CAT beamline, Advanced Photon Source, Argonne National Laboratory, which is supported by the US Department of Energy under Contracts W-31-109-Eng-38 (APS) and DE-FG03-97ER45628 (PNC-CAT) through a General User Proposal to one of the lead authors (DP) and a Partnership Proposal funded by the Natural Sciences and Engineering Research Council of Canada through a major facilities access grant to the Canadian Light Source.

References

BARNES, A.R. and ERIC, R.H. 1995. The relative reducibilities of chromite ores and relative reactivity of carbonaceous reductants. *Proceedings of INFACON VII*, Trondheim, Norway, 11-14 June 1995. Tveit, H., Tuset, J.K., and Page, I.G. (eds.). Norwegian Ferroalloy Producers Research Organization (FFF).

BARNES, A.R., FINN, C.W.P., and ALGIE, S.H. 1983. The prereduction and smelting of chromite concentrate of low chromium-to-iron ratio. *Journal of the South African Institute of Mining and Metallurgy*, vol. 83, no. 3. pp. 49-54.

BARNES, A.R., MUINONEN, M., and LAVIGNE, M. J. 2015. Reducing energy consumption by alternative processing routes to produce ferrochromium alloys from chromite ore. *Proceedings of COM 2015. The Metallurgical Society of CIM*. pp. 1-22.

BISAKA, K., MAKWARELA, M.O., and ERWEEI, M.W. 2016. Solid-state reduction of South African manganese and chromite ores. *Proceedings of the XXVIII International Mineral Processing Congress (IMPC 2016)*, Québec City, 11-15 September 2016. pp. 1-16.

CRAMER, M. 2016. Review and analysis of international experiences in chromite mining and ferrochrome production, and implications for the development of Canadian deposits. Unpublished Technical Report, CanmetMINING, Natural Resources Canada.

DAWSON, N.F. and EDWARDS, R.I. 1986. Factors affecting the reduction rate of chromite. *Proceedings of INFACON IV*, Rio de Janeiro, Brazil, 31 August - 3 September, 1986. Associação Brasileira dos Produtores de Ferro-Ligas-Abrafe. pp. 105-113.

DING, Y. L. 1997. Catalytic reduction of carbon-chromite composite pellets by lime. *Thermochimica Acta*, vol. 292. pp. 85-94.

DING, Y.L. and WARNER, N.A. 1997. Reduction of carbon-chromite composite pellets with silica fluxes. *Ironmaking and Steelmaking*, vol. 24, no. 4. p. 283.

KATAYAMA, H.G., TOKUDA, M., and OHTANI, M. 1985. Promotion of the carbothermic reduction of chromite ore by the addition of borates. *Tetsu-to-Hagané*, vol. 72, no. 10. pp. 1513-1520. https://doi.org/10.2355/tetsutohagane1955.72.10_1513

KELLY, T.D. and MATOS, G.R. 2014. Historical statistics for mineral and material commodities in the United States. <https://minerals.usgs.gov/minerals/pubs/historical>.

KLEYNHANS, E.L.J., BEUKES, J.P., VAN ZYL, P.G., and FICK, J.I.J. 2017. Techno-economic feasibility of a preoxidation process to enhance prereduction of chromite. *Journal of the Southern African Institute of Mining and Metallurgy*, vol. 117, no. 5. pp. 457-468. doi: 10.17159/2411-9717/2017/v117n5a8

LEKATOU, A. and WALKER, D. 1997. Effect of silica on the carbothermic reduction of chromite. *Ironmaking & Steelmaking*, vol. 24, no. 6. p. 133.

LI, J., BAI, G., and LI, G. 2011. Solid-state reduction properties of carbon-bearing chromite pellets. *Chinese Journal of Non Ferrous Metals*, vol. 21, no. 5. pp. 1159-1164.

LI, G., LI, J., RAO, M., BAI, G., and JIANG, T. 2011. Reduction of carbon-burdened chromite pellets. *Proceedings of the 2nd International Symposium on High Temperature Metallurgical Processes*. Wiley. pp. 245-253.

LU, W.K. 2012. Process of the production and refining of low-carbon DRI (direct reduced iron). US patent application WO/2012/149635A1. <http://google.com/patents/WO2012149635A1?cl=ko>

Naiker, O. 2006. The development and advantages of Xstrata's Premus Process. *Proceedings of INFACON IX*, Quebec City, Canada, 3-6 June 2001. pp. 112-119.

NEIZEL, B.W., BEUKES, J.P., VAN ZYL, P.G., and DAWSON, N.F. 2013. Why is CaCO₃ not used as an additive in the pelletised chromite pre-reduction process? *Minerals Engineering*, vol. 45. pp. 115-120. doi: 10.1016/j.mineng.2013.02.015

NEUSCHUTZ, D., JAN EN, P., FRIEDRICH, G., and WIECHOWSKI, A. 1995. Effect of flux addition on the kinetics of chromite ore reduction with carbon. *Proceedings of INFACON VII*, Trondheim, Norway, 11-14 June 1995., Tveit, H., Tuset, J.K., and Page, I.G. (eds.). Norwegian Ferroalloy Producers Research Organization (FFF). pp. 371-382.

RANKIN, W.J. 1979. The composition and structure of chromite during reduction with carbon. *Archiv für das Eisenhüttenwesen*, vol. 50, no. 9. pp. 373-378.

RANKIN, W.J. and FINN, C.W. 1978. Solid state reduction by graphite and carbon monoxide of chromite from the Bushveld Complex. Mintek, Randburg, South Africa.

SLATTER, D. 1980. The chromium resources of Zimbabwe. Institute of Mining Research. University of Zimbabwe.

SOKHANVARAN, S. and PAKTUNC, D. 2018. Effect of NaOH addition on the direct reduction of chromite ore: I: the mechanism. [in preparation].

SOKHANVARAN, S. and PAKTUNC, D. 2017. The effect of fluxing agent on direct reduction of chromite ore. *Proceedings of COM 2017*. Canadian Institute of Mining, Metallurgy and Petroleum, Vancouver.

SUNDAR MURTI, N.S., SHAH, K., GADGEEL, V.L., and SESHADRI, V. 1983. Effect of lime addition on rate of reduction of chromite by graphite. *Transactions of the Institution of Mining and Metallurgy*, vol. 92. pp. C172-C174.

UGWUEGBU, C. 2012. Technology innovations in the smelting of chromite ore. *Innovative Systems Design and Engineering*, vol. 3, no. 12. pp. 48-55.

VAN DEVENTER, J.S.J. 1988. The effect of additives on the reduction of chromite by graphite. *Thermochimica Acta*, 127, pp. 25-35.

WANG, Y., WANG, L., and CHOU, K.C. 2015. Effects of CaO, MgO, Al₂O₃ and SiO₂ on the carbothermic reduction of synthetic FeCr₂O₄. *Journal of Mining and Metallurgy Section B: Metallurgy*, vol. 51, no. 1. pp. 17-24. doi: 10.2298/JMMB140625024W

WEBER, P. and ERIC, R.H. 2006. The reduction of chromite in the presence of silica flux. *Minerals Engineering*, vol. 19. pp. 318-324. doi: 10.1016/j.mineng.2005.07.010

WINTER, F. 2015. Production of chromium iron alloys directly from chromite ores. US patent US2016/0244864 A1. ◆



Carbonylation of nickel and selectively reduced laterite ore

by Y. Cui, G. Zhang, S. Jahanshahi, and O. Ostrovski

Synopsis

Carbonylation of nickel obtained by reduction of nickel oxide and selectively reduced Australian laterite ore was studied at temperatures of 80–100°C and CO gauge pressures of 0–56 atm. The effects of sulphur-containing catalysts on the nickel carbonylation were also examined. The results show that the extent of nickel carbonylation increased with increasing temperature from 80 to 100°C at constant CO pressure. The carbonylation of nickel at 100°C and CO gauge pressure 27 atm. was close to completion after 5.5 hours of reaction. At all temperatures, the effect of CO pressure was very strong when the gauge pressure was increased from zero to 14 atm. Sulphur-containing catalysts accelerated the carbonylation reaction. The time for complete carbonylation of nickel was reduced from 5.5 hours in the non-catalytic reaction to 2 hours in the catalytic carbonylation at 100°C and CO gauge pressure 14 atm. The extent of carbonylation of nickel from the selectively reduced laterite ore with particle size 53–200 µm at 100°C and CO gauge pressure 41 atm. was below 50%. The use of catalysts in the carbonylation of selectively reduced ore was ineffective. The rate of reaction increased with decreasing particle size and increasing gas flow rate.

Keywords

nickel, laterite ore, carbonylation, selective reduction.

Introduction

The major source of nickel is sulphide ores, which have a relatively high nickel content and can be easily upgraded by beneficiation. However, depletion of sulphide deposits and increasing demand for nickel has led to the increasing utilization of laterite ores. Laterite ores cannot be efficiently upgraded by physical means, which leads to significant challenges in the extraction of nickel.

Nickel carbonylation is broadly used for refining of nickel produced by the pyrometallurgical processing of laterite ore (Vale, 2017). Nickel and iron form carbonyls, which are separated by distillation. Terekhov and Emmanuel (2013) studied the reduction of limonite and saprolite ores at 650°C followed by carbonylation of nickel and iron by CO at 180°C and 60 atm. pressure. The extraction of Ni from limonite ore (48 hours' reaction time) was above 92%. Extraction of Ni from saprolite ore was faster; reaching 95.6% in 18 hours (Terekhov and Emmanuel, 2013)

This paper presents the results of a study of carbonylation of nickel produced by reduction of NiO and nickel from selectively reduced laterite ore. The aim is to examine the

feasibility of the alternative technology for the extraction of nickel from laterite ore by selective reduction followed by carbonylation.

Experimental

Carbonylation of pure nickel and nickel in selectively reduced laterite ore was studied at temperatures of 80–100°C and CO gauge pressures of 0–56 atm. Nickel was produced by reduction of NiO by hydrogen at 500°C. Laterite ore was selectively reduced using a CO-CO₂ gas mixture containing 60 vol.% CO at 750°C. Reduction experiments were conducted in a horizontal furnace (Ceramic Engineering, Sydney, Australia).

Carbonylation experiments were conducted in a flexible U-shaped reactor (max. pressure 68 atm.) immersed in an oil bath. The schematic set-up for the carbonylation experiments is shown in Figure 1.

The reaction temperature was controlled by the oil bath. The outlet gas flow rate was adjusted by a needle valve and monitored by a gas flow meter. Pressure was regulated by the valve regulator. Carbonyls were absorbed using three Dreschel bottles filled with *aqua regia*. A fourth absorption bottle, filled with 20 wt% sodium hydroxide solution, was used to treat the corrosive chlorine gas from the Dreschel bottles.

Samples were placed in the reactor, which was immersed in the oil bath and connected to the gas system. To reduce oxides that could be formed on the surface of the reduced samples, the samples were heated to 150°C in hydrogen for 2 hours. When the oil bath reached the

* School of Materials Science and Engineering, University of New South Wales, Sydney, Australia.
© The Southern African Institute of Mining and Metallurgy, 2018. ISSN 2225-6253. This paper was first presented at the INFACON XV: International Ferro-Alloys Congress, 25–28 February 2018, Century City Conference Centre and Hotel, Cape Town, South Africa



Carbonylation of nickel and selectively reduced laterite ore

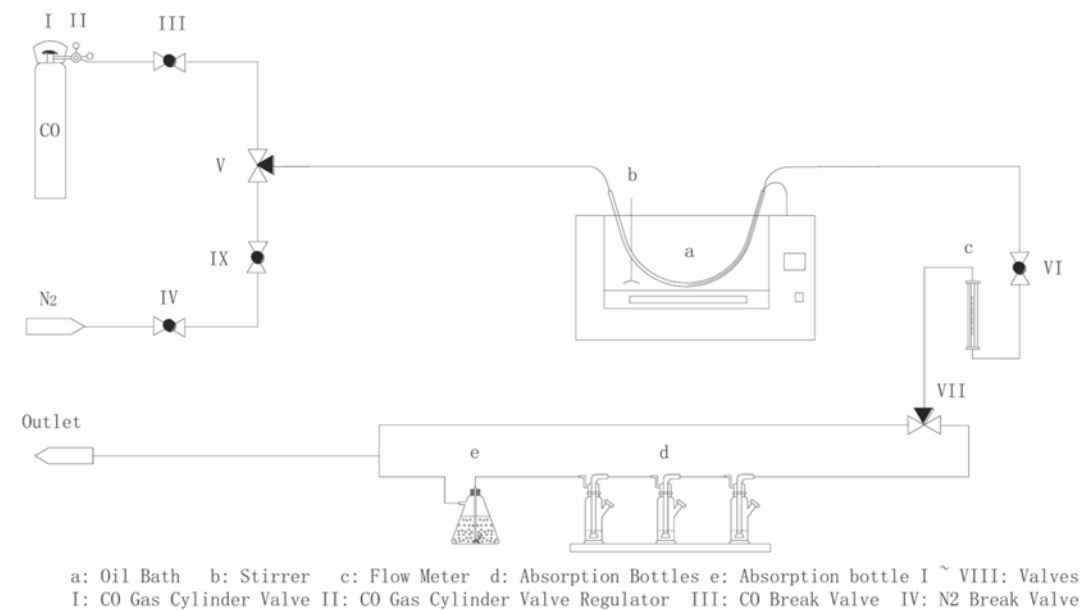


Figure 1—Schematic set-up for the carbonylation experiments

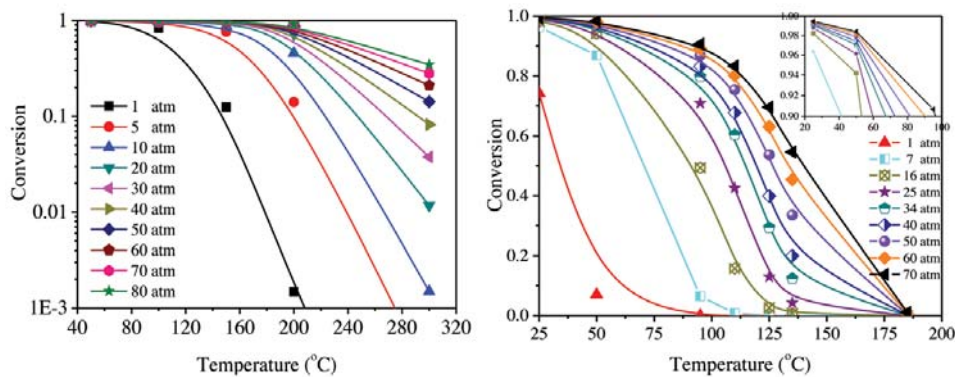


Figure 2—Calculated effect of temperature on conversion of Ni to Ni(CO)₄ (left) and conversion of Fe to Fe(CO)₅

experimental temperature, carbon monoxide was introduced into the reactor and the CO pressure was raised to the experimental value at a specific flow rate. During the experiment, samples were taken from the solutions in the Dreschel bottles at specified intervals and diluted to 10 ml for analysis by ICP-OES. When the experiment was finished, the CO gas was switched off, and the system was purged with hydrogen for 20 minutes at a flow rate of 1 L min⁻¹ at atmospheric pressure to remove residue CO and carbonyls. The *aqua regia* in the Dreschel bottles was diluted with deionized water to 1000±2 mL and analysed by ICP-OES.

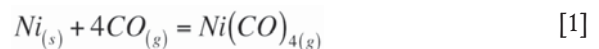
The extent of nickel and iron carbonylation (y) was calculated from the concentration of the metals in the absorbent:

$$y = \frac{\text{mass of converted metal}}{\text{initial mass of metal}} * 100$$

Thermodynamic analysis

Carbonylation of nickel and iron can be represented by

Equations [1] and [2]:



Equilibrium constants for the reactions are (Ross, Haynie, and Hochman, 1964):

$$\log K(Ni) = 8546/T - 21.64 \quad [3]$$

$$\log K(Fe) = 8940/T - 30.0 \quad [4]$$

where T is the temperature in kelvin.

The calculated effect of temperature on carbonylation of nickel and iron at CO pressures 1–80 atm. is shown in Figure 2.

At equilibrium, the conversion of both Ni and Fe to carbonyls increases with decreasing temperature and increasing CO pressure. Conversion of Ni to Ni(CO)₄ at

Carbonylation of nickel and selectively reduced laterite ore

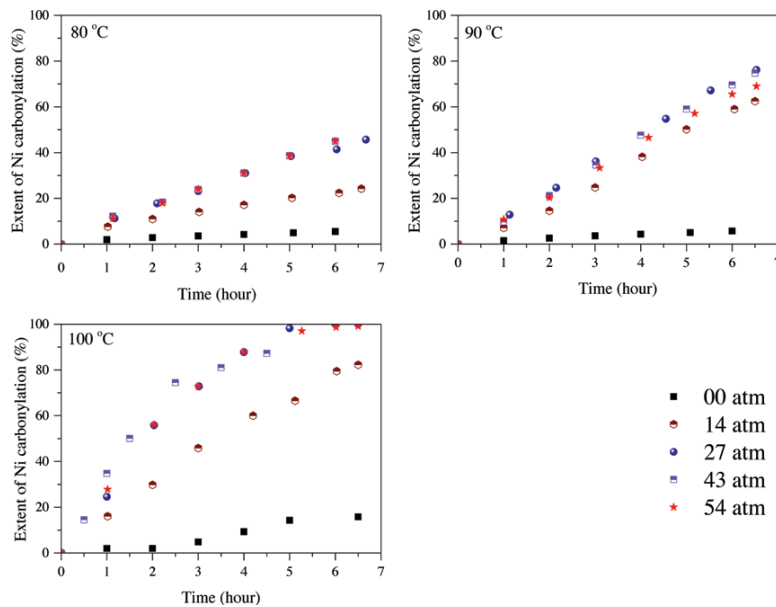


Figure 3—Measured carbonylation of nickel at 80, 90, and 100 °C and CO gauge pressure 0–54 atm

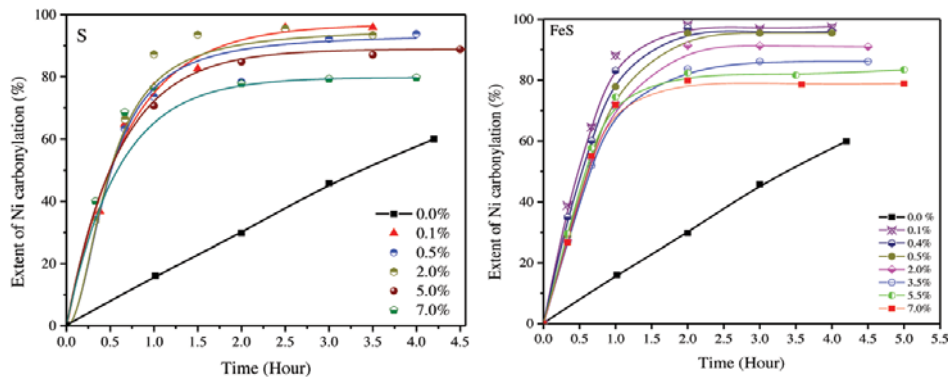


Figure 4—Catalytic carbonylation of nickel at 100 °C and CO pressure 14 atm. with addition of S and FeS

temperatures below 100 °C under CO pressure below 20 atm. is above 95%. Conversion of iron under the same conditions is much lower, less than 50% at 100 °C under CO pressure of 20 atm. Thermodynamic analysis shows that a high extent of nickel carbonylation can be achieved at temperatures below 100 °C and CO pressure above 20 atm. Carbonylation of iron at 100 °C requires higher pressure, above 30 atm.

Experimental results

Non-catalytic carbonylation of pure nickel

Nickel was obtained by reduction of NiO (99%, the main impurity was SiO₂) by hydrogen at 500 °C. The particle size of the NiO was less than 45 μm. Non-catalytic carbonylation of pure nickel was studied at 80–100 °C and CO pressures of 1–55 atm. The gas flow rate in the carbonylation experiments was 0.5 L min⁻¹. Figure 3 presents the extent of Ni carbonylation as a function of the reaction time at 80, 90,

and 100 °C and CO gauge pressures 0, 14, 27, 43, and 54 atm.

The carbonylation rate increased with increasing temperature; the degree of carbonylation after 5 hours' reaction reached over 99% at CO gauge pressure 27 atm. when the temperature increased to 100 °C. The carbonylation rate also increased with increasing CO gauge pressure from 0 to 27 atm; a further increase in CO pressure had only a minor effect on the rate of reaction.

The rate of Ni carbonylation decreased with increasing particle size (in the range 0.3–2.7 μm); the effect of the particle size was strong when the mean particle size was above 1.1 μm.

The effect of gas flow rate on Ni carbonylation was examined in the range 0.14–0.5 L min⁻¹ at 100 °C and CO gauge pressure 27 atm. An increased gas flow rate increased the rate of Ni carbonylation.

Carbonylation of nickel and selectively reduced laterite ore

Catalytic carbonylation of nickel

Catalytic carbonylation of Ni was studied using sulphur and iron sulphide. In these experiments, nickel (about 1.3 g) was mixed with a catalyst (0.1–0.7 wt%) before carbonylation. Carbonylation curves obtained in experiments with different contents of sulphur are shown in Figure 4. Sulphur-containing catalysts greatly accelerated the carbonylation reaction. The addition of 0.1 wt% S shortened the reaction time for 60% carbonylation from 4.2 hours in the non-catalytic carbonylation to less than 40 minutes in the catalytic reaction. The catalytic effects of sulphur and iron sulphide were very similar. However, increasing the catalyst content from 0.1 to 7.0 wt% S resulted in a decrease in the extent of nickel carbonylation, from above 90% to 80%.

In the study of the effects of other parameters on the catalytic carbonylation of nickel, 0.1 wt% sulphur in the form of FeS was added to the nickel.

The effect of temperature on the catalytic carbonylation of nickel was examined in the range of 80–100°C at a CO pressure of 14 atm. with a gas flow rate of 0.5 L min⁻¹. The sample (1.3 g) contained 0.1 wt% sulphur in the form of FeS. Carbonylation curves obtained in experiments at 80, 90 and 100°C are shown in Figure 5. The carbonylation rate increased with increasing temperature from 80 to 90°C, but a further increase in temperature from 90 to 100°C had only a minor effect on the reaction rate.

The effect of CO pressure on the catalytic carbonylation of nickel was studied at 100°C and CO pressures of 14 and

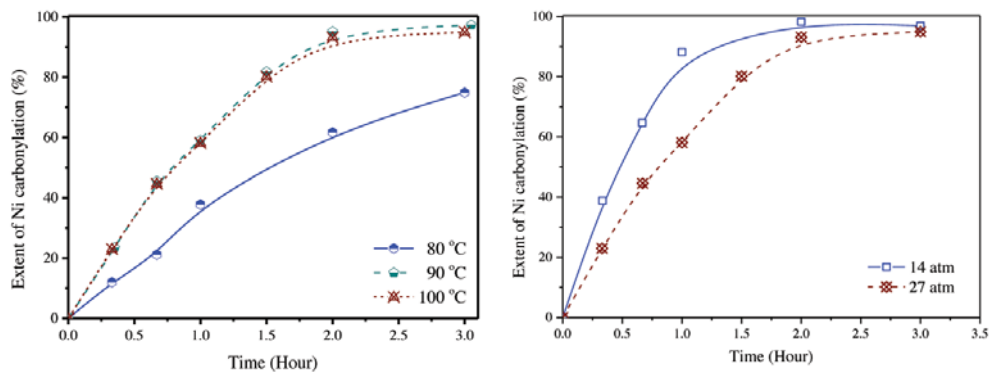


Figure 5—Effects of temperature (at CO gauge pressure 14 atm.) and CO gauge pressure (at 100°C) on the catalytic carbonylation of nickel

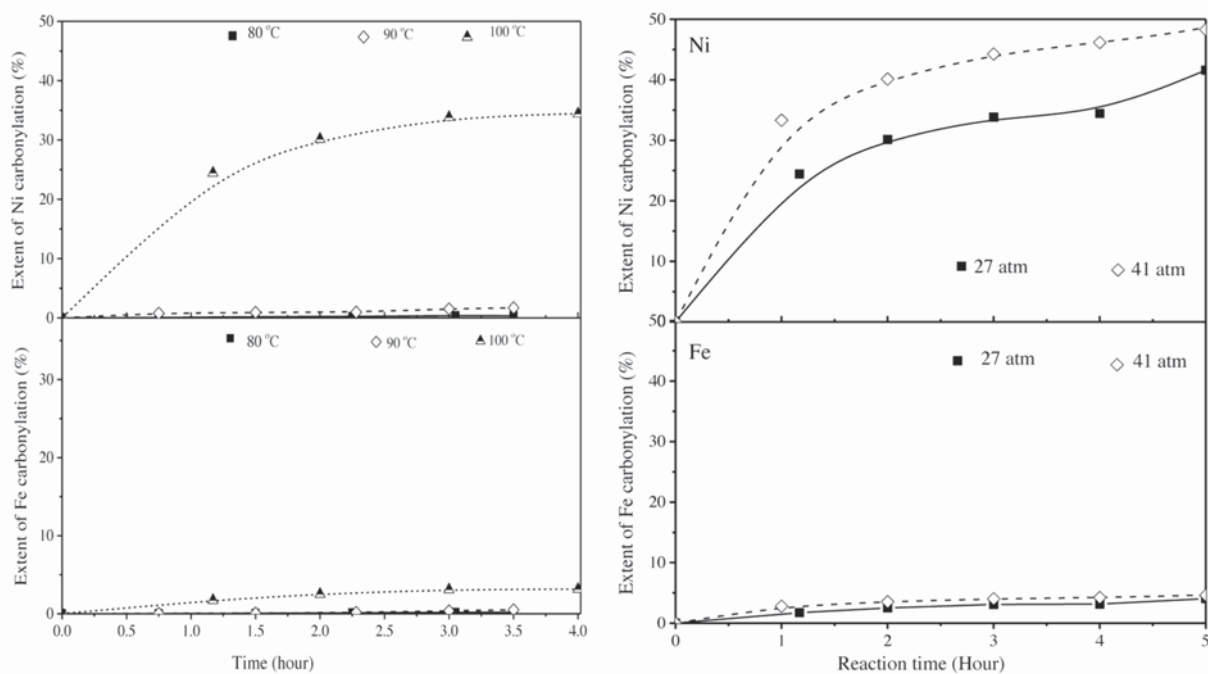


Figure 6—Effect of temperature on the non-catalytic carbonylation of nickel and iron from selectively reduced laterite ore at CO gauge pressure 27 atm., and effect of CO pressure at 100°C

Carbonylation of nickel and selectively reduced laterite ore

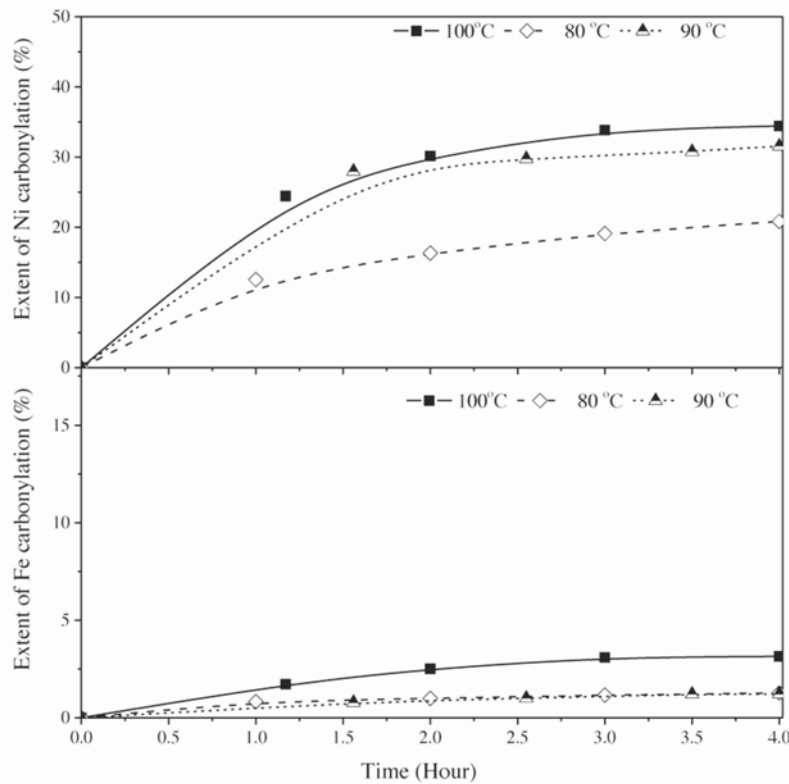


Figure 7—Catalytic carbonylation of nickel and iron from the selectively reduced laterite ore at 80, 90 and 100°C; CO gauge pressure 27 atm

27 atm. (Figure 5). The rate of carbonylation at 27 atm. CO pressure was lower than at 14 atm. in the first two hours of reaction. The extents of nickel carbonylation after 3 hours' reaction at both CO pressures were very close; 97% at a CO gauge pressure of 14 atm. and 95% at 27 atm.

Carbonylation of selectively reduced laterite ores

Garnierite laterite nickel ore containing 1.66% Ni, 11.7 Fe, and 0.045 Co (by mass) with a particle size <53 μm was reduced in a CO–CO₂ gas mixture containing 60 vol.% CO at 750°C. The extents of reduction of nickel, cobalt, and iron oxides from the ore reached 91, 85, and 19% respectively. Ni, Co, and Fe oxides were reduced to the ferroalloy in the form of fine (sub-micrometre) particles which were homogeneously distributed in a silicate matrix.

Non-catalytic carbonylation

The effect of temperature on the non-catalytic carbonylation of selectively reduced laterite ore was studied using a sample mass of 1.5 g at 80, 90 and 100°C under CO gauge pressure 27 atm. The results are shown in Figure 6. Carbonylation of both nickel and iron at 80 and 90°C was very slow, but the reaction rate increased significantly when the temperature was increased to 100°C. The extent of nickel carbonylation at 100°C after 3.5 hours' reaction reached 34%, while the extent of iron carbonylation was only 3.1%.

Increasing the CO gauge pressure from 27 to 41 atm. increased the rate of carbonylation of nickel in the first hour of reaction but had no discernible effect on the carbonylation

of iron. The extent of Ni carbonylation at 100°C and CO gauge pressure 41 atm. after 5 hours' reaction was close to 50%.

Catalytic carbonylation of selectively reduced laterite ore

Catalytic carbonylation of selectively reduced laterite ore was studied using hydrogen sulphide (H₂S), which was introduced to the system with carbon monoxide at a concentration of 1.0 vol.%.

Carbonylation curves for nickel and iron at 80, 90, and 100°C are plotted in Figure 7. Increasing the temperature from 80 to 90°C increased the rate of carbonylation of nickel but had no effect on the carbonylation of iron. A further increase in temperature to 100°C led to a marginal increase in the extent of carbonylation of nickel (less than 2% after 4.5 hours' reaction), and increased the rate of iron carbonylation, although the extent of iron carbonylation at 100°C after 4 hours' reaction remained low, less than 3%.

Discussion

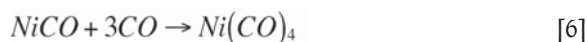
The carbonylation process proceeds by external and internal mass transfer of gaseous CO and Ni(CO)₄, adsorption of CO on the Ni particles, and the formation and desorption of Ni(CO)₄.

Thermodynamic analysis shows that the carbonylation reaction is favoured by lower temperatures (Figure 2). The strong positive effect of increased temperature on the Ni carbonylation indicates that the kinetic factor dominates the thermodynamic factor; it also indicates that the chemical

Carbonylation of nickel and selectively reduced laterite ore

reaction contributed to the rate-controlling steps in the carbonylation reaction.

Nickel carbonylation by reaction [1] proceeds through the formation of intermediate species (Redmon, 1980):



The formation of intermediate NiCO requires a large activation energy and can be the slowest step in the chemical reaction (Redmon, 1980).

The rate of the non-catalytic carbonylation of Ni can be presented as (for the first-order irreversible reaction):

$$R = SkP_{\text{CO}} \quad [7]$$

where S is the interfacial gas-solid area, k is the reaction rate constant, and P_{CO} is the CO pressure at the gas-solid interface.

The rate constant as a function of temperature is described by the Arrhenius equation:

$$k = Ae^{-\frac{E_a}{RT}} \quad [8]$$

where A is a frequency factor or pre-exponential factor, E_a is the activation energy (J mol^{-1}), R is the gas constant ($\text{J}\cdot\text{mol}^{-1}\cdot\text{K}^{-1}$), and T is temperature (K).

The activation energy determined from the experimental data at temperatures between from 80 and 100°C and CO gauge pressure 54 atm. was found to be 114 $\text{kJ}\cdot\text{mol}^{-1}$; this is in a reasonable agreement with the activation energy of 127 kJ mol^{-1} theoretically estimated by Redmon (1980). It follows from Equations [7] and [8] that the rate of the chemical reaction increases with increasing temperature and CO pressure, which was observed experimentally.

Mass transfer of CO and $\text{Ni}(\text{CO})_4$ in the gas phase also contributed to the rate-limiting factors as the rate of Ni carbonylation increased with increasing CO flow rate. It should be noted that increasing the CO pressure at a constant gas flow rate decreases the gas velocity in the reactor. Therefore, in the non-catalytic carbonylation of Ni and laterite ore, the positive effect of CO pressure on the rate of chemical reaction dominated over the negative effect on the mass transfer in the gas phase.

The use of sulphur catalysts changes the reaction mechanism; carbonylation proceeds through the formation of nickel sulphide (Ni_3S_2) which is converted to $\text{Ni}(\text{CO})_4$. The rate of chemical reaction in the catalytic carbonylation of nickel is much higher than in non-catalytic carbonylation. An increase in temperature from 90 to 100°C had a minor effect on the rate of catalytic carbonylation. This indicates that the chemical reaction did not contribute to the rate control of catalytic carbonylation at 90–100°C; mass transfer in the gas phase became the rate controlling stage. In this case, the increase in the CO pressure decreased the rate of carbonylation as it decreased the gas velocity in the reactor.

The nickel oxide used for the production of Ni contained a small amount of impurities; the reduction of NiO to Ni was

95–97%. Impurities and NiO were not carbonylated under the experimental conditions used. Internal mass transfer through the residue of Ni carbonylation also contributed to the rate control, which was particularly significant in the carbonylation of selectively reduced laterite ore.

Conclusions

- ▶ The rates of non-catalytic carbonylation of both nickel and laterite ore increased with temperature and CO pressure, although in the case of laterite ore, an increase in temperature from 80 to 90°C had only a minor effect, while a further increase to 100°C significantly accelerated the rate of carbonylation.
- ▶ The non-catalytic carbonylation of Ni at 100°C and CO gauge pressure 43–54 atm. was close to completion after about 5 hours' reaction; it was far from completion at 80 and 90°C.
- ▶ Catalytic carbonylation of nickel and selectively reduced laterite ore exhibited a different behaviour to non-catalytic carbonylation. The rate of carbonylation of both Ni and laterite ore increased with increasing temperature from 80 to 90°C, and was only slightly affected by a further increase in temperature to 100°C. Increasing the CO gauge pressure decreased the rate of catalytic carbonylation of both Ni and laterite ore.
- ▶ The use of catalysts accelerated Ni carbonylation and had a marginal effect on the carbonylation of laterite ore.
- ▶ Carbonylation of iron from the selectively reduced laterite ore was slow; the extent of reaction was about 3% in both non-catalytic and catalytic carbonylation.
- ▶ The rate of non-catalytic carbonylation of Ni and laterite ore was controlled by the chemical reaction and external and internal mass transfer of gaseous CO and $\text{Ni}(\text{CO})_4$. Chemical reaction did not contribute to the rate of catalytic carbonylation at 90–100°C.

Acknowledgements

This paper is based on the PhD thesis by Cui (2015). Financial support for this research was provided by the Australian Research Council (ARC Discovery Project DP1094880).

References

- CUI, Y. 2015. Carbonylation of nickel and iron from reduced oxides and laterite ore. PhD thesis, University of New South Wales, Sydney.
- ROSS, L.W., HAYNIE, F.H., and HOCHMAN, R.F. 1964. Thermodynamic functions of nickel carbonyl and iron pentacarbonyl. *Journal of Chemical and Engineering Data*, vol. 9, no. 3, pp. 339–340.
- REDMON, L.T. 1980. Final report on kinetics of $\text{Ni}(\text{CO})_4$ formation to U.S. Air Force Office of Scientific Research. <http://www.dtic.mil/dtic/tr/fulltext/u2/a207136.pdf>
- TEREKHOV, D.S. and EMMANUEL, N.V. 2013. Direct extraction of nickel and iron from laterite ore using the carbonyl process. *Minerals Engineering*, vol 54, pp. 124–130.
- VALE. 2017. Second quarter 2017 production report. <http://www.vale.com/indonesia/EN/aboutvale/news/id/Pages/second-quarter-2017-production-report.aspx> ◆



Effect of electrode shape on the current distribution in submerged arc furnaces for silicon production – A modelling approach

by Y.A. Tesfahunegn*, T. Magnusson†, M. Tangstad‡, and G. Saevarsdottir*

Synopsis

This work presents computations of electrical current distribution inside an industrial submerged arc furnace for silicon production. A 3D model has been developed in ANSYS Fluent using an electrical potential solver. The electrode, arc, crater, crater wall, and side arcs that connect the electrode and crater wall are considered for each phase. The shape of the electrodes is considered as a truncated right cone. We assume that several concentrated side-arcs are distributed around the circumference of the electrode near the electrode tip. The number of side arcs varies, depending on the slope of the slant height. Four simulation conditions are considered by changing the conductivity of the charge and by adding or removing main arcs on seven different configurations of side arcs. The phase voltages in the electrode and current distributions in crater wall are presented. The total current in the crater wall is reduced by 20 to 35% when the charge conductivity is changed by two orders of magnitude, and the phase voltage is very high when the main arc is not taken into consideration. Qualitative analysis shows that our modelling approach gives reasonable results.

Keywords

silicon smelting, submerged arc furnace, electrode shape, current distribution, current paths.

Introduction

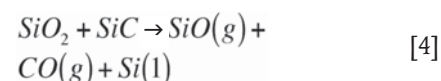
Current distribution is critical for proper operation of submerged arc furnaces for silicon production. Control systems do not offer this information as it is not directly measurable, but metallurgists operate furnaces based on their experience and interpretation of available data. A number of recent dig-outs of industrial furnaces have expanded the available information on location-dependent charge properties, thus enabling numerical models with reasonably realistic domain configurations to be constructed. This has the potential to enhance understanding of critical process parameters, allowing more accurate furnace control.

In the silicon production process, quartz and carbon materials are fed into a submerged arc furnace. The raw material mix constitutes the furnace charge. Three electrodes penetrate the charge from above. Electrical energy is provided by the current passed to the charge through the electrodes, each of which carries one of the three phases of 50 Hz AC current, cancelling out at a star point in the charge.

The overall reaction for producing silicon is:



This reaction, however, takes place through a series of sub-reactions, changing the properties of the charge along the way as intermediary reaction products are formed. The current passes from the electrodes through the raw material charge and an electric arc burning at the tip of the electrode. The arc, which consists of thermal plasma in the range of 10 000–30 000 K (Saevarsdottir *et al.*, 2001), provides heat for the energy-consuming silicon-producing reaction (Equation [4]), while the SiC-forming reaction and SiO(g) condensation reactions (Equations [2] and [3]) take place at a lower temperature higher up in the furnace (see Schei, Tuset, and Tveit, 1998).



It is extremely important for the silicon recovery in this process that there is a balance between the high-temperature reaction [4] and the low-temperature reactions [2] and [3]. Therefore, it is necessary that sufficient heat is released in the arc to drive reaction [4], while a certain part should be released in the raw material charge to drive reactions [2] and [3]. The stoichiometry of reaction [4] is affected by the temperature, and the ratio is decreased at

* School of Science and Engineering, Reykjavik University, Iceland.

† United Silicon, Iceland.

‡ Department of Material Science and Engineering, NTNU, Norway.

© The Southern African Institute of Mining and Metallurgy, 2018. ISSN 2225-6253. This paper was first presented at the INFACON XV: International Ferro-Alloys Congress, 25–28 February 2018, Century City Conference Centre and Hotel, Cape Town, South Africa

Effect of electrode shape on the current distribution in submerged arc furnaces

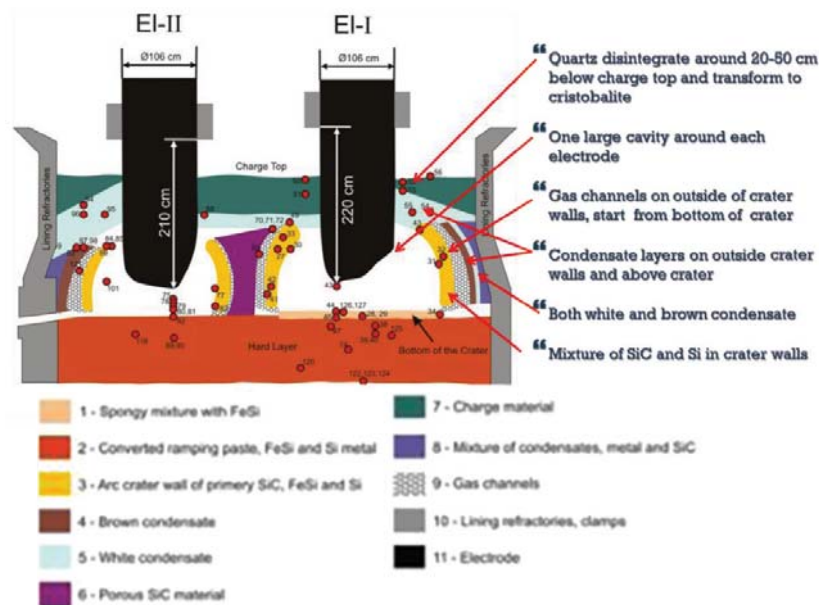


Figure 1—Reaction zones in a 17.5 MW industrial FeSi furnace (Tranell *et al.*, 2010)

higher temperature, thus enabling a better silicon recovery. Therefore, sufficient arcing is important for good silicon recovery.

The current distribution is not well known for silicon furnaces, and cannot be directly measured. Saevarsdottir *et al.* (2011) calculated that the arc could be a maximum of 10-15 cm in length, based on the electrical parameters. Although there have been publications on this subject, (for example Saevarsdottir and Bakken, 2010), results from an accurate model where the current distribution can be calculated have not been published to date.

The geometry of the zones in a silicon furnace depends on the operational history, and hence a number of different geometries, sizes, and compositions are possible in the various parts of the furnace. A report on recent excavations of industrial furnaces published by Tranell *et al.* (2010) describes the various zones in a FeSi furnace. The results are summarized in Figure 1. Myrhaug (2003) reported similar features from an excavation of a pilot-scale furnace operating at around 150 kW. Tangstad, Ksiazek, and Andersen (2014) published results from excavations of industrial furnaces, where the interior of the furnace is divided into zones according to the materials present and their degree of conversion. Mapping the material distribution forms a basis for quantifying the location-dependent physical properties of the charge materials, such as the electrical conductivity.

A master's thesis by Krokstad (2014) describes measurements of the electrical conductivity of silicon carbide, and Vangskåsen (2012) looked in detail at the metal producing mechanisms. Molnas (2010) and Nell (2013) have also published data on digout samples and material analysis. These are some of the basic requirements necessary to set up a reasonably realistic modelling domain with the correct physical properties. Therefore there is now a unique opportunity to create a model that enables understanding of the current distribution in the furnace. These results can be used in the development of furnace control strategies in order to improve silicon recovery and current efficiency.

Some researchers have published results on the current distribution in submerged arc furnaces using computational fluid dynamics (CFD) and the finite element method (FEM). Diahnaut (2004) presented computations of the electrical field in a SAF using CFD. The author showed the effect of contact resistance by studying the contact between two coke particles, before dealing with a full-scale furnace. The furnace was partitioned into layers to take account of different materials, and no assumptions were made regarding the current path. Bezuidenhout, Eksteen, and Bardshaw (2009) applied CFD to a three-phase electric smelting furnace to investigate the electrical aspects, thermal aspects, and flow behaviour. They demonstrated the relationships between the electrode positions, current distribution, and slag electrical resistivity. Darmana *et al.* (2012) used CFD to develop a modelling concept applicable for SAFs that considers various physical phenomena such as thermodynamics, electricity, hydrodynamics, heat radiation, and chemical reactions. Wang *et al.* (2014) investigated the thermal behaviour inside three different electric furnaces for MgO production.

This paper presents computations of electrical current distributions inside an industrial submerged arc furnace for silicon production. A 3D model has been developed in ANSYS Fluent (ANSYS Inc., 2017a) using an electrical potential solver. The electrode, central arc, crater, crater wall, and side arcs that connect the electrode and crater wall are considered for each phase. The geometry of the electrode, for the purposes of the 3D model, is considered as a truncated right conical shape. The upper surface of the electrode is the base of the cone with a radius equals to the radius of the electrode. The radius of the bottom surface of the electrodes changes as the slope of the slant height changes. We assume that several concentrated side-arcs are distributed around the circumference of the electrode near the bottom of the electrodes, and the circular distances between each side arc are held constant. In this paper, the term 'side arc' is used for the configuration with an arc/arcs connecting the electrode and the crater wall. Depending on the slope of the slant

Effect of electrode shape on the current distribution in submerged arc furnaces

height, the number of side arcs also varies. As this analysis pertains to a stationary case, speculation on the possible effect of variability of the phase voltage within the AC (alternating current) period is beyond the scope of this paper. The phase voltages in the electrodes and current distributions in crater walls for different slant height slope are presented.

Computational model

In this section, we describe the mathematical modelling, furnace geometry, material properties, mesh generation, and boundary conditions.

Mathematical modelling

In this paper, we will focus only on the electrical aspects of the SAF. The 3D electrical model is developed in ANSYS Fluent using an electrical potential solver. It will capture neither the time-dependent effects nor the induced magnetic field or the resulting magnetic forces in the system. Since the model considered in this paper is very complex, a quasi-static approach using the potential solver is deemed appropriate as first approach to predict current distributions. For a complete understanding, the time-dependent magnetic effects must be incorporated. A method that includes these effects has been developed and is currently being implemented in ANSYS Fluent. The electrical potential equation is therefore given by the Laplace equation (Darmana *et al.*, 2012):

$$\nabla \cdot (\sigma \nabla \varphi) = 0 \quad [5]$$

where φ and σ are the scalar potential and electrical conductivity, respectively. Equation [5] is solved using the finite volume method implemented in ANSYS Fluent, version 17.2, based on the User Defined Scalar (UDS) solver. Once it is solved, the electric field (E) and hence the electric current density (J) can be determined using Ohm's Law as shown in Equations [6] and [7], respectively.

$$E = -\nabla \varphi \quad [6]$$

$$J = \sigma E \quad [7]$$

Furnace geometry and material properties

The computational domain is based on the actual design of a 32 MW industrial furnace. A simplified schematic drawing of the furnace is shown in Figure 2. Due to the proprietary nature of the information, the dimensions of the furnace are not indicated. The furnace is partitioned into different zones based on the material properties. The modelling includes the furnace lining, three truncated right conical electrodes, the charge, molten material, three arcs below the electrodes, side arcs, and three craters with crater walls consisting of carbides. For brevity, a section of the furnace and one electrode is depicted in Figure 2. For each phase, two arcs are included: the main arc, burning below the electrode, with arc length of 10 cm and diameter of 5 cm (Saevarsdottir and Bakken, 2010), and a shorter arc connecting the crater wall to the side of the electrode. The curvature of the three crater walls is assumed to be a section of a circle with a diameter of 100 cm (Saevarsdottir, 2002). The crater wall thickness and the circular distance between adjacent side-arcs are set to 30 cm. In this study, seven different configurations of side

arcs are simulated, *i.e.*, 4, 5, 6, 7, 11, 12, and 14 arcs. The furnace geometry has been created using ANSYS ICEM-CFD (ANSYS Inc., 2017b) mesh generator software. The electrical conductivity for each of the zones is assumed to be constant. The conductivity of each zone is taken from various literature sources and is summarized in Table I. Two values of charge conductivity are considered, which differ by two orders of magnitudes. Due to the uncertainty in the physical properties of the material in the furnace and the variability between furnaces, it was decided to use two extreme values of charge conductivity to estimate the importance of the result. Alumina brick is an electrically insulating material with high resistivity.

Mesh generation and boundary conditions

Mesh generation is a crucial part of any computational method. It has a significant influence on the runtime and memory use for simulation, as well as the accuracy and stability of the solution. The material volumes described in the preceding subsection were meshed using ICEM-CFD version 17 (2017). The mesh is generated using an unstructured grid because of the complexity of the furnace geometry. After performing a preliminary grid convergence study, different maximum element sizes are set on different parts of the furnace. The maximum elements sizes on arcs, electrodes, crater wall are 2, 10, and 10 cm, respectively, and on the remaining parts 30 cm. To reduce the cell count, the fine unstructured mesh is converted to a polyhedral mesh in ANSYS Fluent, reducing the cell count to almost one-third, enabling faster convergence and saving computational expense.

Table I

Electrical conductivity of different zones

Zones	Electrical conductivity (S/m)
Electrode (Krokstad, 2014)	225 000
Arc (Saevarsdottir, 2002)	7000
Crater	1e-14
Carbide (Krokstad, 2014)	400
Charge (Diahnaut, 2004)	0.15, 15
Molten Si (Sasaki, 1995)	138 8900
Carbon block (Krokstad, 2014)	225 000
Alumina brick	1e-14

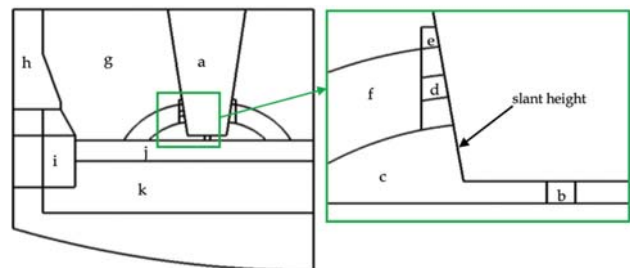


Figure 2—Schematic of the industrial silicon SAF with different zones: (a) electrode, (b) arc, (c) crater, (d) side arc, (e) gap, (f) carbide, (g) charge, (h) alumina brick, (i) carbon block and carbide, (j) molten material, and (k) carbon block

Effect of electrode shape on the current distribution in submerged arc furnaces

The model boundary conditions were specified to resemble the actual furnace as closely as possible. The outer furnace walls are set as a nonconductive wall. The top surfaces of the electrodes are defined as conductive walls by applying the respective phase currents as current density. A total current of 99 kA was applied at the top of electrode 1, and a corresponding current density of -49.500 kA on phases 2 and 3, giving a balanced system. The data is based on the design and operational criteria for the modelled furnace. The interface walls between different zones are implemented as coupled boundary conditions.

Numerical cases

In this section, we study the effect of electrode shape on current distribution through different parts of the furnace, as well as the phase voltages on the electrodes. In this study, three factors have been considered. The first factor is the number of side arcs, with seven levels; the second is the charge conductivity, with two levels (0.15 and 15 S/m); and the third is the consideration of main arcs, with two levels (with and without main arcs). Therefore, a total of 28 simulation cases have been performed. For discussion purposes, we group them into four categories. In each category, all the seven levels of side-arcs are considered. We vary only the other two factors, *i.e.*, charge conductivity and presence of main arcs. The four cases are summarized in Table II.

For all cases, the simulations were performed by a second-order upwind scheme based on an implicit formulation. Asymptotic convergence to a steady-state solution is obtained for each case. The solution convergence criterion for all models is the one that occurs first of the following: a reduction of the residuals by twelve orders of magnitude, or a maximum number of iterations of 3000. The simulation time per case is around three hours.

For each simulation, lumped current values for various parts of the furnace were calculated from the current density using ANSYS Fluent's surface integrator. By integrating the current density component along the furnace height direction multiplied by the normal vector for the area associated with it, we obtain the current passing through the area.

As direct experimental verification of these results is not possible, it is reasonable to verify our results based on qualitative analysis. Figure 3 shows current flow on a cross-section through two electrodes. As described in the computational model section, a positive current is applied to electrode 1, and a negative current to electrodes 2 and 3. Current always flows from positive to negative or from high to low potential. As expected, the current flows from electrode 1 to electrodes 2 and 3 (not shown here) through the charge, molten Si, and crater wall. Note that for visualization purposes, the arrows indicate vector direction only, and colour indicates magnitude. To check the amount of current passing through various parts of the furnace, a cross-section between the bottom surface of the electrodes and molten Si is shown in Figure 4. This figure shows the magnitude of current density distribution for the four cases with seven side arcs. In the first two cases (a and b) there is no central arc. The only difference between the two cases is the charge conductivity. It can be seen that the current density of the charge is increased by three orders of magnitude in (b). At the same time, it is decreased in the crater walls. The same trend can be observed between cases (c) and (d). Moreover, it can be seen that the maximum current density is in the main arcs.

Figure 5 shows the total current through the crater wall for the first electrode of the four cases. The same relationship is observed at the other electrodes. The vertical axis is the normalized current (the fraction of the phase current) and the horizontal axis is the number of side arcs. In all cases, the

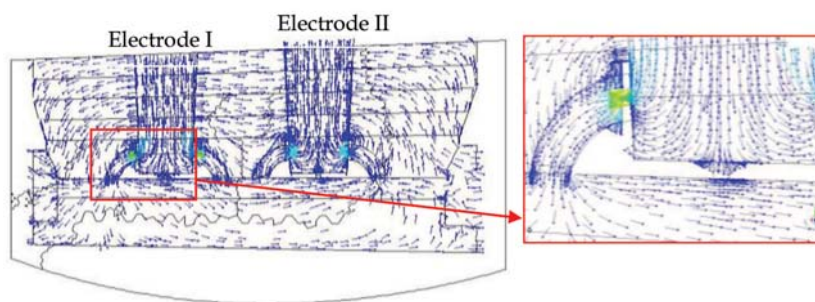


Figure 3—Current flow

Case	No. of side arcs (4, 5, 6, 7, 11, 12, and 14)	Charge conductivity		Main arcs	
		0.15 S/m	15 S/m	Not included	Included
a	✓	✓		✓	
b	✓		✓	✓	
c	✓	✓			✓
d	✓		✓		✓

Effect of electrode shape on the current distribution in submerged arc furnaces

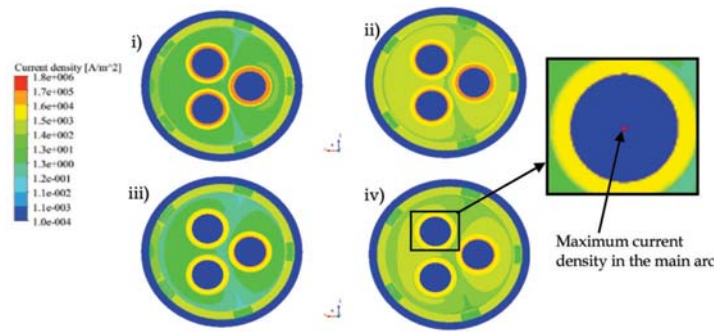


Figure 4—Current density for (i) case a, (ii) case b, (iii) case c, and (iv) case d

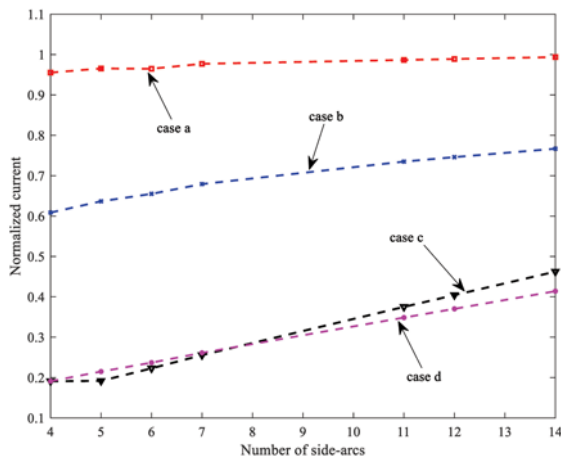


Figure 5—Current distributions on the crater wall based on the four cases

current on the crater wall is increased as the number of side arcs increase. The main difference between the cases is the degree to which the current increases. A nonlinear relationship is observed in all cases. The current is decreased by approximately 20 to 35% when the charge conductivity is changed by two orders of magnitude (from case a to b), whereas moving from case c to d, the reduction is approximately 0.06 to 6%.

The industrial furnace considered this study operated at a phase voltage between 100 and 140V. As can be seen in Table III, at least 14 and 12 side arcs are required to generate the correct phase voltage for cases a and b, respectively, whereas in the other instances 4 to 7 side arcs are needed. Using the experimentally obtained electrical properties of SiC (Krokstad, 2014), the resistance in the side-arc/carbide system is too high to obtain a reasonable furnace resistance (and thus voltage) without the presence of a central arc burning against molten Si. This fits poorly with industry observations of electrode movements by tenths of centimeters at a time, which is hard to reconcile with a central bottom arc no longer than 10-15 cm. Hence, to achieve an acceptable phase voltage the carbide layer in the crater wall must be saturated in metal or similar material. Such SiC-metal composite structures have been encountered in excavations (Tranell *et al.*, 2010) as illustrated in Figure 1. This would lead to a much higher conductivity than that observed for the dry carbide.

In general, the trend that can be observed in Table III is that as the number of side arcs increases (increasing slope of the slant height), the voltage decreases. Further study is required to confirm if this trend is present in the case of AC. Also, increasing the charge conductivity decreases the voltage. This means that the resistance of the furnace decreases due to the increasing electrical conductivity of the system.

Conclusions

This paper presents computations of electrical current distributions inside an industrial submerged arc furnace for silicon production. A 3D model has been developed in ANSYS Fluent using an electric potential solver. The electrodes, arcs, crater, crater wall, and side arcs that connect the electrode and crater wall are considered for each phase. The shape of the electrodes is considered as a truncated right cone. We assume that several concentrated side-arcs are distributed around the circumference of the electrode near the bottom of the electrodes. Depending on the slope of the slant height, the number of side arcs varies. The phase voltage in the electrodes and current distributions in crater walls for different slant height slopes (number of side arcs) are presented. Variation in the number of side arcs has been considered, and each case was simulated four times, changing the charge conductivity and adding or removing a central arc. It was observed that the total current in the crater wall is decreased by 20 to 35% when the charge conductivity is changed by two orders of magnitude without a main arc. However, the decrease is negligible when the central arc is included. The phase voltage is very high when the main arc is not taken into account – in this case, to obtain a reasonable

Table III

Phase 1 voltages of the four cases

Number of side arcs	a (V)	b (V)	c (V)	d (V)
4	631.78	346.22	148.33	124.44
5	488.01	295.94	137.95	116.75
6	395.77	259.02	129.39	110.35
7	329.19	226.11	120.40	103.26
11	197.66	153.19	98.15	85.20
12	177.78	143.27	92.34	81.25
14	147.13	120.15	82.87	73.71

Effect of electrode shape on the current distribution in submerged arc furnaces

furnace resistance, the carbide layer in the crater-wall must be saturated in metal or similar material that has a higher conductivity than the dry carbide.

Acknowledgements

The Icelandic Technology Development Fund is gratefully acknowledged for their funding of this work.

References

- ANSYS Inc. 2017a. FLUENT, ver. 17.0. Canonsburg, PA.
- ANSYS Inc. 2017b. ICEM-CFD, ver. 17.0. Canonsburg, PA.
- BEZUIDENHOUT, J., EKSTEEN, J., and BARDSHAW, S. 2009. Computational fluid dynamic modelling of an electric furnace used in the smelting of PGM containing concentrates. *Minerals Engineering*, vol. 22. pp. 995–1006. doi:https://doi.org/10.1016/j.mineng.2009.03.009
- DARMAHA, D., OLSEN, J., TANG, K., and RINGDALEN, E. 2012. Modelling concept for submerged arc furnaces. *Proceedings of the Ninth International Conference on CFD in the Minerals and Process Industries*. CSIRO, Melbourne.
- DHAINAUT, M. 2004. Simulation of the electric field in a submerged arc furnace. *INFACON X. Proceedings of the Tenth International Ferroalloys Congress*, Cape Town, South Africa. Southern African Institute of Mining and Metallurgy, Johannesburg.
- KROKSTAD, M. 2014. Electrical resistivity of industrial SiC crusts. MSc thesis, NTNU, Trondheim, Norway.
- MYRHAUG, E. 2003. Non-fossil reduction materials in the silicon process - properties and behavior. PhD thesis, NTNU, Trondheim, Norway.
- MØLNÅS, H. 2010. Investigation of SiO condensate formation in the silicon process. Project report in TMT 4500. NTNU, Trondheim, Norway.
- NELL, J. and JOUBERT, C. 2013. Phase chemistry of digout samples from a ferrosilicon furnace. *INFACON XIII. Proceedings of the Thirteenth International ferroalloys congress*, Almaty, Kazakhstan.
- SAEVARSDOTTIR, G. and BAKKEN, J. 2010. Current distribution in submerged arc furnaces for silicon metal/ ferrosilicon production. *INFACON XII. Proceedings of the 12th International Ferroalloys Congress*, Helsinki, Finland, 6–9 June 2010.
- SAEVARSDOTTIR, G., BAKKEN, J., SEVASTYANENKO, V., and LIPING, G. 2001. Arc simulation model for three-phase electro-metallurgical furnaces. *INFACON IX. Proceedings of the 9th International Ferroalloys Congress*, Quebec City, Canada.
- SAEVARSDOTTIR, G., BAKKEN, J., SEVASTYANENKO, V., and LIPING, G. 2011. High power ac arcs in metallurgical furnaces. *High Temperature Material Processes*, vol. 15, no. 3. doi: 10.1615/HighTempMatProc.v5.i1.20
- SASAKI, H., IKARI, A., TERASHIMA, K., and KIMURA, S. 1995. Temperature dependence of the electrical resistivity of molten silicon. *Japanese Journal of Applied Physics*. doi:https://doi.org/10.1143/JJAP.34.3426
- SCHAI, A., TUSET, J., and TVEIT, H. 1998. Production of High Silicon Alloys. Tapir Forlag, Trondheim, Norway.
- SÆVARSDOTTIR, G. 2002. High current ac arcs in silicon and ferrosilicon furnaces. PhD thesis, NTNU, Trondheim, Norway.
- TANGSTAD, M., KSIAZEK, M., and ANDERSEN, J. 2014. Zones and materials in the Si furnace. *Proceedings of Silicon for the Chemical and Solar Industry XII*, Trondheim, Norway.
- TRANELL, G., ANDERSSON, M., RINGDALEN, E., OSTROVSKI, O., and STEINMO, J.J. 2010. Reaction zones in a FeSi75 furnace - results from an industrial excavation. *INFACON XII. Proceedings of the 12th International Ferroalloys Congress*, Helsinki, Finland, 6–9 June 2010. pp. 709–715.
- VANGSKÅSEN, J. 2012. Metal-producing mechanisms in the carbothermic silicon process. MSc thesis, NTNU, Trondheim, Norway.
- WANG, Z., FU, Y., WANG, N., and FENG, L. 2014. 3D numerical simulation of electrical arc furnaces for the MgO production. *Journal of Materials Processing Technology*. pp. 2284–2291. doi:http://dx.doi.org/10.1016/j.jmatprotec.2014.04.033



ASM Conference 2018

'Fostering a regional approach to ASM transformation
in sub-Saharan Africa'

10–11 SEPTEMBER 2018

Nasrec, Johannesburg (Electra Mining)

WHO SHOULD ATTEND

- Government Officials and Regulators
- Academics, Trainers and Educators
- ASM operators
- ASM associations
- Mine Affected Communities
- Civil Society Organizations
- Community liaison officials at the mines
- ASM consultants
- Closure practitioners
- Community engagement practitioners
- Health and Safety Practitioners
- Development practitioners
- Futurists and forward thinkers



For further information contact:

Yolanda Ndimande • Conference Co-ordinator • SAIMM
Tel: +27 11 834-1273/7 Fax: +27 11 833-8156 or +27 11 838-5923
E-mail: yolanda@saimm.co.za • Website: http://www.saimm.co.za





Thermodynamic evaluation of Sr-containing Si metals and silicate melts for Si-Sr alloy production

by K. Tang*, L.K. Jakobsson†, and K. Hildal†

Synopsis

Reliable thermodynamic descriptions of the Si-based Sr-Al-Ca-Fe-Mg metal system and SiO_2 -SrO-CaO-MgO- Al_2O_3 oxide system are essential for the understanding and optimizing the production of Si-Sr alloys. Phase relations of all SrO containing binary and ternary subsystems were evaluated and thermodynamically modelled based on the existing literature data. Phase equilibria in the SiO_2 -SrO-CaO-MgO- Al_2O_3 higher-order oxide system were thus possible to calculate by the CALPHAD method. A thermodynamic description of the Si-Sr-Al-Ca-Fe-Mg metal system was developed based on assessment of all binary systems as well as all Si containing ternary subsystems. The newly developed thermochemical databases can be used to calculate the equilibrium distribution of Sr between metal and slag. The theoretical Sr distribution maps for both pure Si and 75FeSi alloys in different SrO-containing slags are reported.

Keywords

thermodynamic evaluation, Si-Sr-Al-Ca-Fe-Mg metal, SiO_2 -SrO-CaO-MgO- Al_2O_3 oxide, Sr equilibrium distribution.

Introduction

Strontium distribution equilibria between the Si-based metals and SrO-containing silicate melts are of great importance for the development of new ferrosilicon products. To describe the complex phase equilibria between the Sr-containing Si metals and silicate slags, thermodynamic descriptions of the Sr-containing metal and oxide phases are essential. This paper summarizes our recent work on thermodynamic modelling of the Si-rich Si-Sr-Al-Ca-Fe-Mg metal and SiO_2 -SrO-CaO-MgO- Al_2O_3 oxide systems.

Thermochemical descriptions of the above metal and oxide phases were input into databases for the FactSage™ software package. The model calculations for the phase equilibrium relations in the SiO_2 -SrO- Al_2O_3 ternary oxide system were verified by laboratory experiments. The metal/slag strontium distribution equilibria at elevated temperatures were then evaluated thermodynamically. The present equilibrium simulations can serve as a 'map' for the metallurgist to design and optimize Si-Sr ferroalloy production.

Thermodynamic assessments

The metal system

Thermodynamic descriptions of the liquid and solid Si-based Si-Al-Ca-Sr-Fe-Mg alloy phases have been set up based mainly on the experimental data available in the literature. The compound energy formalism is applied to liquid and all the mixture phases as well as stoichiometric compounds.

The six-element metal system contains 15 binary, 20 ternary, 15 quaternary, and 6 quinary subsystems. Since the metal system is in the Si-rich domain, the Si-free ternary and higher-order subsystems are not considered in the present study. To ensure the reliability of the model calculation, all 15 binary subsystems were modelled to cover the whole composition range, and temperatures from the liquid phase to the sub-liquidus solid phases.

The calculated Sr-Si binary phase diagram, based on the assessment of Li *et al.* (2011), is shown in Figure 1. Experimental phase equilibrium data reported by Palenzona and Pani (2004) and Rygalin *et al.* (2010) is also shown in the diagram. The assessment emphasized the eutectic and peritectic reaction temperatures and compositions.

The experimental Sr-Al phase equilibria reported by Closset and Gruzleski (1982), Vakhobov, Eshonov, and Dzhrurayev (1979), and Bruzzone and Merlo (1975) can be reproduced using the model parameters assessed by Zhong *et al.* (2004). The calculated phase diagram is shown in Figure 2.

The Ca-Sr phase diagram, assessed by the present authors based on the experimental liquidus and solidus data by Schottmiller,

* SINTEF Industry, Norway.

† Elkem Technology, Norway.

© The Southern African Institute of Mining and Metallurgy, 2018. ISSN 2225-6253. This paper was first presented at the INFACON XV: International Ferro-Alloys Congress, 25–28 February 2018, Century City Conference Centre and Hotel, Cape Town, South Africa

Thermodynamic evaluation of Sr-containing Si metals and silicate melts for Si-Sr alloy production

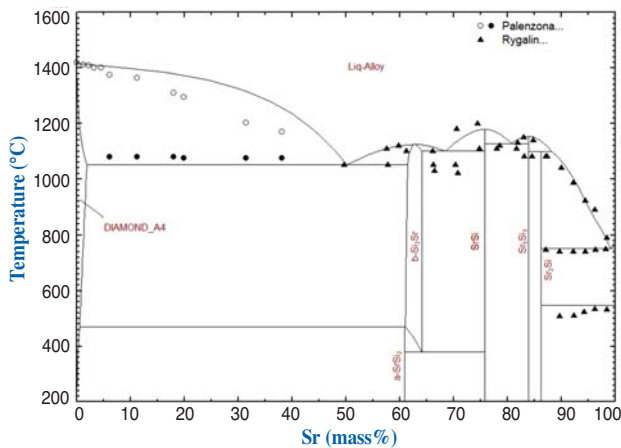


Figure 1—Calculated Si-Sr binary phase diagram (after Li *et al.*, 2011)

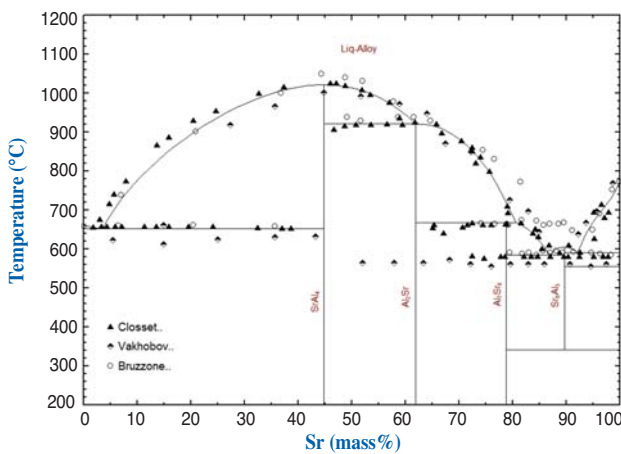


Figure 2—Calculated Sr-Al binary phase diagram (after Zhong *et al.*, 2004)

King, and Kanda (1958) is shown in Figure 3. These three binary subsystems, together with the Sr-Fe binary, are of great importance for the phase equilibria and elemental distributions of Sr-containing alloys.

There exist 10 Si-containing ternary subsystems which are also very important for the present thermodynamic descriptions, as shown in Table I. Only a few ternary systems have been thermodynamically assessed in the literature. Since the Sr concentrations in pure Si and FeSi alloys are in the range of dilute solution, *i.e.* < 5 wt%, ternary and higher-order contributions to the melts will not be significant. This means that the present database can represent thermochemical properties of the Si-based Sr-Al-Ca-Fe-Mg alloys at elevated temperatures.

The calculated Al-Al₂Si₂Sr pseudo-binary phase diagram is shown in Figure 4. In this ternary alloy system, the model calculation can reproduce the experimental phase boundaries (Sato *et al.*, 1985) quite well. The agreement between the calculated and measured phase equilibria by Vakhobov, Eshonov, and Dzhurayev (1979) is also satisfactory in the low-Sr composition domain.

Thermodynamic model calculations for the phase equilibria in the Si-Mg-Sr ternary as well as in the Si-Al-Ca-

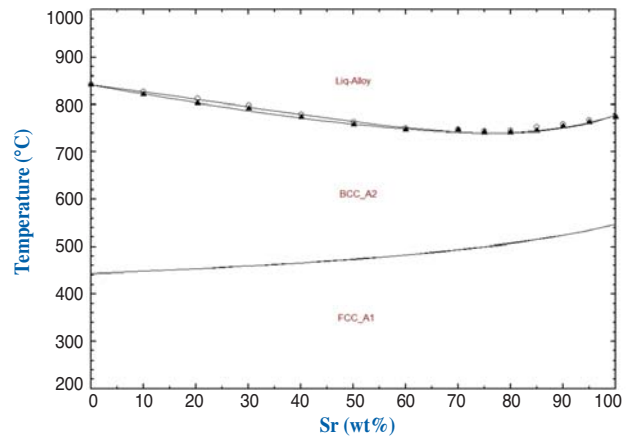


Figure 3—Calculated Ca-Sr binary phase diagram

Table I

Ternary subsystems used in the present database

No.	System			References
1	Si	Al	Sr	Sato <i>et al.</i> (1985), Vakhobov, Ganiev, and Djuraev (1975), Janz and Schmid-Fetzer (2009)
2	Si	Ca	Sr	No ref.
3	Si	Fe	Sr	No ref.
4	Si	Mg	Sr	Rokhlin and Dobatkina (2001), Gil-Santos <i>et al.</i> (2016)
5	Si	Al	Ca	Effenberg and Ilyenko (2004), Anglezio, Servant, and Ansara (1994a, 1994b)
6	Si	Al	Fe	Anglezio, Servant, and Ansara (1994a, 1994b)
7	Si	Ca	Fe	Anglezio, Servant, and Ansara (1994a, 1994b)
8	Si	Mg	Fe	Duo <i>et al.</i> (2007)
9	Si	Ca	Mg	Gröbner, Chumak, and Schmid-Fetzer (2003), Rokhlin, Evgeniya Lysova, and Materials Science International Team (2000)
10	Si	Al	Mg	Tang <i>et al.</i> (2012), Feufel <i>et al.</i> (1997)

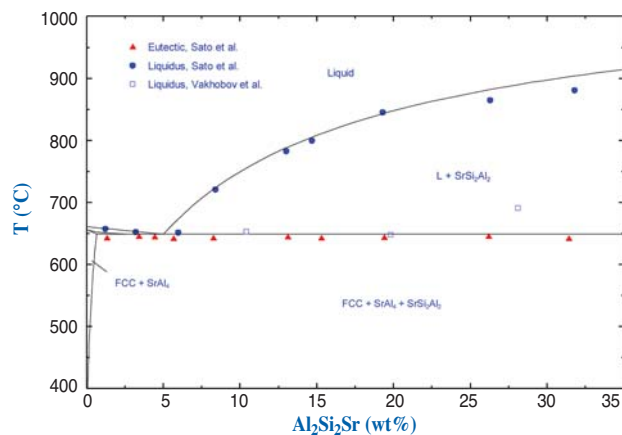


Figure 4—Calculated Al- Al₂Si₂Sr pseudo-binary phase diagram

Fe quaternary system were also examined with the experimental data in the literature. For the sake of simplicity, they are not presented here.

Thermodynamic evaluation of Sr-containing Si metals and silicate melts for Si-Sr alloy production

For the sake of simplicity, detailed descriptions of the experimental data as well as model assessment will not be presented here. The information related to other ternary oxide subsystems is summarized in Table III.

Slag/metal equilibria

The slag/metal Sr partition equilibria are the most interesting aspect of the present study. The partition of Sr between Si-Sr metals and SrO-SiO₂ binary slags at different temperatures is shown in Figure 8. The Sr distribution equilibria between 75FeSi alloys and SrO-SiO₂ binary slags at 1600°C are also shown in the same diagram.

It is notable that the Sr contents in 75FeSi are about 10 times lower than those in Si metals. This is due to the strong positive interaction between Fe and Sr, which can also be observed by the immiscibility of Fe and Sr.

Figure 9 shows the iso-Sr composition contours for pure Si in equilibrium with the ternary SiO₂-SrO-Al₂O₃ slags at 1600°C. The amphoteric property of Al₂O₃ is rather obvious, *i.e.* Al₂O₃ acts as a basic oxide in the SiO₂-rich area and an acid oxide in the SrO-rich domain. Figure 10 shows the similar equilibrium iso-Sr contours for the same system at 1700°C.

By comparing Figure 10 to Figure 9, we see that temperature does not play a key role in the Sr partition equilibria in this ternary slag system. This means that the silicothermic reduction of SrO is relatively independent of temperature. However, slag composition plays a vital role in the Sr contents in Si metals, in particular for the higher SrO slags. By increasing the SrO content in the slag from 55 wt% to 60 wt%, the final equilibrium Sr content in Si will increase from around 6-7 wt% to 18-31 wt% at 1600-1700°C.

The present thermodynamic models can also be used to evaluate the solidification of Si/75FeSi alloys, smelting behaviour of SrO-containing slags, as well as materials and energy balances during metallurgical processes. This will be discussed in our next publication.

Conclusions

Thermodynamic descriptions of the Si-based Sr-Al-Ca-Fe-Mg metal and SiO₂-SrO-CaO-MgO-Al₂O₃ oxide systems have been established and implemented in the commercial software package FactSage. Thermodynamic modelling of the Si-based Si-Sr-Al-Ca-Fe-Mg metal system was developed based on assessments of all binary systems as well as the Si-Sr-Al, Si-Sr-Mg, Si-Al-Mg ternary, and Si-Al-Ca-Fe quaternary subsystems.

No.	System			Reference
1	SiO ₂	Al ₂ O ₃	CaO	Eriksson and Pelton (1993)
2	SiO ₂	Al ₂ O ₃	SrO	This work
3	SiO ₂	Al ₂ O ₃	MgO	Jung, Deckerov, and Pelton (2004b)
4	SiO ₂	CaO	SrO	This work
5	SiO ₂	MgO	SrO	This work
6	Al ₂ O ₃	CaO	SrO	This work
7	Al ₂ O ₃	CaO	MgO	Jung, Deckerov, and Pelton (2004b)
8	CaO	MgO	SrO	This work
9	Al ₂ O ₃	MgO	SrO	This work

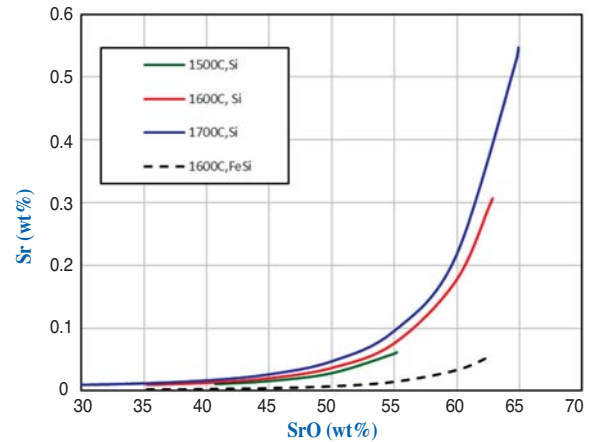


Figure 8—Calculated Sr distribution between Si75FeSi and SiO₂-SrO slag at different temperatures

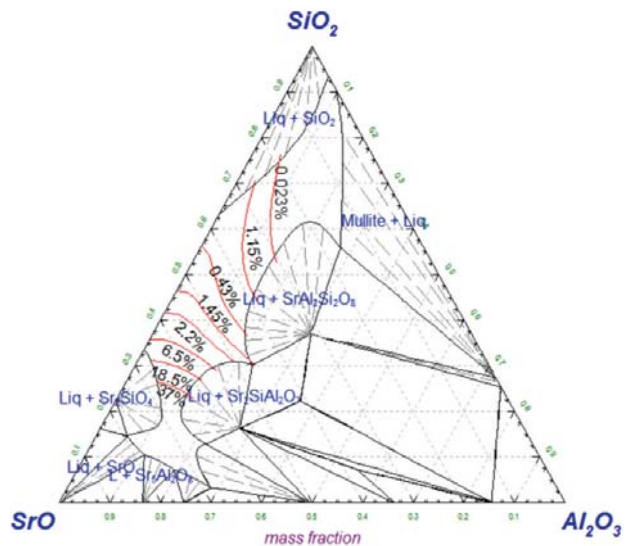


Figure 9—Calculated iso-Sr composition lines in Si metals represented in the SiO₂-SrO-Al₂O₃ ternary system at 1600°C

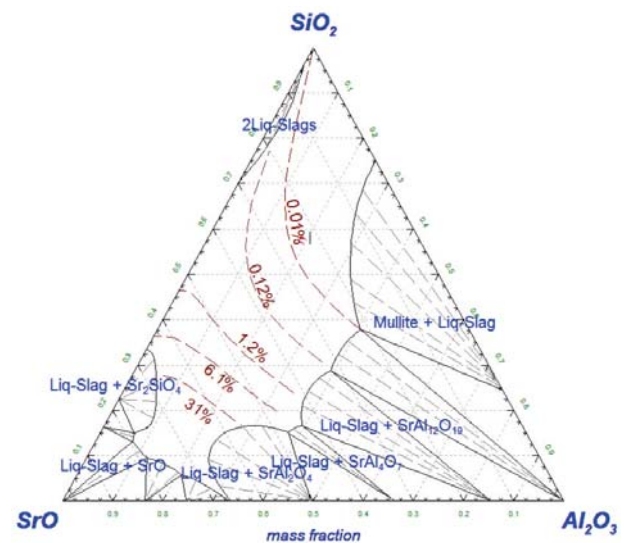


Figure 10—Calculated iso-Sr composition lines in Si metals represented in the SiO₂-SrO-Al₂O₃ ternary system at 1700°C

Thermodynamic evaluation of Sr-containing Si metals and silicate melts for Si-Sr alloy production

Phase relations in the SiO_2 -SrO, SrO- Al_2O_3 binary as well as the SiO_2 -SrO- Al_2O_3 , SiO_2 -SrO-CaO, and SiO_2 -SrO-MgO ternary system were evaluated and thermodynamically modelled based on existing literature data. Phase equilibria in the SiO_2 -SrO-CaO-MgO- Al_2O_3 higher-order oxide system were thus possible to calculate by the CALPHAD method.

The thermochemical databases have been applied to evaluate the Sr distribution equilibria between pure Si and SiO_2 -SrO slags as well as FeSi and SiO_2 -SrO slags. In addition, the equilibrium distribution of Sr between pure silicon and SiO_2 -SrO-CaO- Al_2O_3 slags was calculated. It is found that the Sr contents in Si metals are much higher than those in 75FeSi alloys. The Sr contents in Si metals will depend strongly upon the slag composition, and weakly upon the temperature.

Acknowledgements

This work was supported by the Research Council of Norway through the project CoRResi (project number: 235159/O30).

References

- ANGLEZIO, J.C., SERVANT, C., and ANSARA, I. 1994a. Contribution to the experimental and thermodynamic assessment of the Al-Ca-Fe-Si system. I. Al-Ca-Fe, Al-Ca-Si, Al-Fe-Si and Ca-Fe-Si systems. *Calphad - Computer Coupling of Phase Diagrams and Thermochemistry*, vol. 18. pp. 273-309.
- Anglezio, J.C., Servant, C., and Ansara, I. 1994b. A study of the Si-rich domain of the Al-Ca-Fe-Si quaternary system. *Calphad - Computer Coupling of Phase Diagrams and Thermochemistry*, vol. 18. pp. 311-318.
- BRUZZONE, G. and MERLO, F. 1975. The strontium-aluminium and barium-aluminium systems. *Journal of the Less Common Metals*, vol. 39. pp. 1-6.
- CLOSSET, B. and GRUZLESKI, J.E. 1982. Structure and properties of hypoeutectic Al-Si-Mg alloys modified with pure strontium. *Metallurgical Transactions A*, vol. 13. pp. 945-951.
- DEAR, P.S. 1957. Sub-liquidus equilibria for the ternary system SrO- Al_2O_3 - SiO_2 . Virginia Polytechnic Institute, Blacksburg, VA.
- DECTEROV, S., JUNG, I-H., and PELTON, A.D. 2002. Thermodynamic modeling of the FeO- Fe_2O_3 -MgO- SiO_2 system. *Journal of the American Ceramic Society*, vol. 85. pp. 2903-3910.
- DUO, Y., ZHAO, J.R., ZHANG, C., CHEN, H.L., and ZHANG, L.J. 2007. Thermodynamic modeling of the Fe-Mg-Si system. *Journal of Mining and Metallurgy Section B - Metallurgy*, vol. 43. pp. 39-56.
- EFFENBERG, G. and ILYENKO, S. 2004. Al-Ca-Si (aluminium - calcium - silicon). *Light Metal Systems. Part 1: Selected Systems from Ag-Al-Cu to Al-Cu-Er*. Springer, Berlin/Heidelberg.
- ERIKSSON, G. and PELTON, A.D. 1993. Critical evaluation and optimization of the thermodynamic properties and phase-diagrams of the CaO- Al_2O_3 , Al_2O_3 - SiO_2 , and CaO- Al_2O_3 - SiO_2 systems. *Metallurgical Transactions B - Process Metallurgy*, vol. 24. pp. 807-816.
- FEUFEL, H., GÖDECKE, T., LUKAS, H.L., and SOMMER, F. 1997. Investigation of the Al-Mg-Si system by experiments and thermodynamic calculations. *Journal of Alloys and Compounds*, vol. 247. pp. 31-42.
- FIELDS, J., PAUL, M., DEAR, S., and BROWN, J.J. 1972. Phase equilibria in the system BaO-SrO- SiO_2 . *Journal of the American Ceramic Society*, vol. 55. pp. 585-588.
- GHANBARI-AHARI, K. and BRETT, N.H. 1988. Phase equilibria and microstructure in the system zirconia-magnesia-silica-strontia. Part 2: The ternary system magnesia-silica-strontia. *British Ceramic Transactions*, vol. 87. pp. 103-106.
- GIL-SANTOS, A., MOELANS, N., HORT, N., and VAN DER BIEST, O. 2016. Identification and description of intermetallic compounds in Mg-Si-Sr cast and heat-treated alloys. *Journal of Alloys and Compounds*, vol. 669. pp. 123-133.
- GRÖBNER, J., CHUMAK, I., and SCHMID-FETZER, R. 2003. Experimental study of ternary Ca-Mg-Si phase equilibria and thermodynamic assessment of Ca-Si and Ca-Mg-Si systems, *Intermetallics*, vol. 11. pp. 1065-74.
- HAGEMAN, V.B.M. and OONK, H.A.J. 1986. liquid immiscibility in the SiO_2 + MgO, SiO_2 + SrO, SiO_2 + La_2O_3 , and SiO_2 + Y_2O_3 systems. *Physics and Chemistry of Glasses*, vol. 27. pp. 194-98.
- HANIC, F., CHEMEKOVA, T.Y., and UDALOV, Y.P. 1979. Strontium oxide-alumina system. *Russian Journal of Inorganic Chemistry (Zhurnal Neorganicheskoi Khimii)*, vol. 24. pp. 471-475.
- HUNTELAAR, M.E., CORDFUNKE, E.H.P., and OUWELTJES, W. 1992. The standard molar enthalpies of formation of $\text{SrSiO}_3(\text{s})$ and $\text{Sr}_2\text{SiO}_4(\text{s})$. *Journal of Chemical Thermodynamics*, vol. 24. pp. 139-143.
- JANZ, A. and SCHMID-FETZER, R. 2009. Thermodynamics and constitution of Mg-Al-Ca-Sr-Mn Alloys: Part I. Experimental investigation and thermodynamic modeling of subsystems Mg-Ca-Sr and Al-Ca-Sr. *Journal of Phase Equilibria and Diffusion*, vol. 30. pp. 146-156.
- JUNG, I.H., DECTEROV, S.A., and PELTON, A.D. 2004a. Critical thermodynamic evaluation and optimization of the MgO- Al_2O_3 , CaO-MgO- Al_2O_3 , and MgO- Al_2O_3 - SiO_2 systems. *Journal of Phase Equilibria and Diffusion*, vol. 25. pp. 329-345.
- JUNG, I-H., DECTEROV, S.A., and PELTON, A.D. 2004b. Critical thermodynamic evaluation and optimization of the MgO- Al_2O_3 , CaO-MgO- Al_2O_3 , and MgO- Al_2O_3 - SiO_2 systems. *Journal of Phase Equilibria and Diffusion*, vol. 25. pp. 329-345.
- LAPINA, I.V., SEMENOV, Y.V., and KHODAKOVSKII, I.L. 1989. Thermodynamic properties of calcium-, strontium-, and barium feldspars based on calorimetric data. *Geokhimiya*, vol. 7. pp. 1033-1032.
- LI, K., LIU, S., SHA, C., and DU, Y. 2011. A thermodynamic reassessment of the Si-Sr system. *Calphad*, vol. 35. pp. 594-600.
- MASSAZZA, F. and SIRCHIA, E. 1959. Equilibriums at the temperature of fusion in the ternary system SrO- Al_2O_3 -CaO. *Annali di Chimica*, vol. 49. pp. 1352-1370.
- PALENZONA, A. and PANI, M. 2004. The phase diagram of the Sr-Si system. *Journal of Alloys and Compounds*, vol. 373. pp. 214-219.
- PELTON, A.D. and BLANDER, M. 1986. Thermodynamic analysis of ordered liquid solutions by a modified quasichemical approach—Application to silicate slags. *Metallurgical Transactions B*, vol. 17. pp. 805-815.
- ROKHLIN, L.E.L. and MSIT® MATERIALS SCIENCE INTERNATIONAL TEAM. 2000. Ca-Mg-Sr ternary phase diagram evaluation - Phase diagrams, crystallographic and thermodynamic data: MSI Eureka report 10.16786.1.7. Springer Materials. http://materials.springer.com/msi/docs/sm_msi_r_10_016786_01
- ROKHLIN, L. and DOBATKINA, T. 2001. Mg-Si-Sr ternary phase diagram evaluation. *Ternary Evaluations*. Effenberg, G. (ed.). MSI, Materials Science International Services, Stuttgart.
- RYGALIN, B., PROKOFIEVA, V., PAVLOVA, L., and OKOLOV, Y.E.S. 2010. The Si-Sr and Si-Ba phase diagrams over the Si-rich composition range. *Calphad*, vol. 34. pp. 196-199.
- SATO, E., KONO, M., SATO, I., and WATANABE, H. 1985. Study on the phase diagram of Al-Si-Sr ternary alloy system. *Journal of Japan Institute of Light Metals*, vol. 35. pp. 71-78.
- SCHOTTMILLER, J.C., KING, A.J., and KANDA, F.A. 1958. The calcium-strontium metal phase system. *Journal of Physical Chemistry*, vol. 62. pp. 1446-1449.
- STARCZEWSKI, M. 1964. Treatise on solid state reactions in the ternary system SrO- Al_2O_3 - SiO_2 . *Zeszyty Naukowe Politechniki Slaskiej, Chemia*, vol. 22. pp. 5-75.
- TANG, Y., DU, Y., ZHANG, L.J., YUAN, X.M., and KAPTAY, G. 2012. Thermodynamic description of the Al-Mg-Si system using a new formulation for the temperature dependence of the excess Gibbs energy. *Thermochimica Acta*, vol. 527. pp. 131-142.
- VAKHOBOV, A.V., ESHONOV, K.K., and DZHURAYEV, T.D. 1979. The Al-Sr-Nd phase diagram. *Russian Metallurgy*. pp. 167-172.
- VAKHOBOV, A.V., GANIEV, I.N., and DJURAEV, T.D. 1975. *IZV. Akad. Nauk. USSR Met.*, 15.
- WU, P., ERIKSSON, G., and PELTON, A.D. 1993. Critical evaluation and optimization of the thermodynamic properties and phase-diagrams of the CaO-FeO, CaO-MgO, CaO-MnO, FeO-MgO, FeO-MnO, and MgO-MnO systems. *Journal of the American Ceramic Society*, vol. 76. pp. 2065-2075.
- ZHONG, YU., WOLVERTON, C., AUSTIN CHANG, Y., AND LIU, Z-K. 2004. A combined CALPHAD/first-principles remodeling of the thermodynamics of Al-Sr: unsuspected ground state energies by 'rounding up the (un)usual suspects'. *Acta Materialia*, vol. 52. pp. 2739-2754. ◆

Realising possibilities
from **mine to market.**



WorleyParsons provides innovative solutions for each step of the mining value chain. We combine world-leading, concept-to-completion expertise with design and major project delivery capabilities for the minerals and metals sector, from bulk commodities to rare earths, with complete mine-to-market solutions from inception to rehabilitation. Our Global Centre of Excellence for Mining and Minerals in South Africa has niche expertise in hard rock and precious minerals and metals, and we have achieved particular recognition for the delivery of complex processing plants and deep shaft mines.



WorleyParsons

resources & energy

worleyparsons.com

wprsainfo@worleyparsons.com

Introduction to Process Engineering School 2018 Volume I

Knowledge sharing
Innovative process designs
Empowering young process engineers

30–31 July 2018
Birchwood Hotel and OR Tambo
Conference Centre, JetPark
Johannesburg

OBJECTIVES

- Application of technology in the industry
- Sizing and specification of equipment
- Important factors to consider during design and new developments

TOPICS

DAY 1—SCREENING AND DRY SORTING

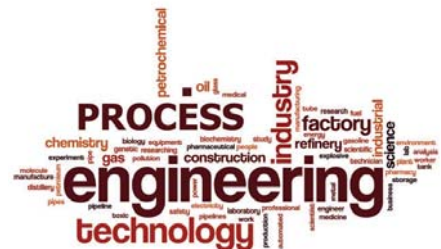
- Screening
- Dry sorting

DAY 2—FINES BENEFICIATION

- Flotation
- Reflux Classifiers

WHO SHOULD ATTEND

- Owners team members
- Professionals responsible for due diligence studies and project evaluations



Contact: Yolanda Ndimande
Conference Co-ordinator
Tel: +27 11 834-1273/7

Fax: +27 11 833-8156 or +27 11 838-5923

E-mail: yolanda@saimm.co.za

Website: <http://www.saimm.co.za>



3D models of proximity effects in large FeSi and FeMn furnaces

by E.V. Herland, M. Sparta, and S.A. Halvorsen

Synopsis

Many large furnaces used for production of ferroalloys are operated using three-phase alternating current. In such furnaces, there are significant skin and proximity effects caused by induction effects in, and between, the electrodes. Moreover, there may be high currents induced in the furnace steel shell. This causes additional proximity effects between the currents in the electrodes and alloy, and the induced currents in the lining and shell.

A numerical study of such effects in realistic 3D geometries of ferromanganese and ferrosilicon furnaces is presented. The models are used to estimate the induced currents in the steel shell as well as accurate alternating current distributions in the material layers within the furnace. Also, the active and reactive power densities within the furnace are studied. The results show that there are strong skin and proximity effects in the conductive material layers within the furnace. Both the electrode proximity effects and the proximity effects caused by the steel shell are computed. The latter can be significant, and should be included when high accuracy is required.

Keywords

ferroalloy furnace, electrical conditions, AC current, current density, skin and proximity effects.

Introduction

In many industrial ferroalloy furnaces, the required power is supplied by alternating electrical currents (AC). These currents produce electromagnetic fields that induce eddy currents in the conductive materials in the furnace. Two effects can be identified, depending on whether the eddy currents are induced in the conductor itself or in a nearby one: the *skin effect*, which causes the currents to accumulate near the surface of conductors, and the *proximity effect*, which induces currents in surrounding conductors (Lupi, 2017). The induced eddy currents can have a high intensity and effectively modify the current distribution.

For metal-producing furnaces, the skin and proximity effects have typically been studied in electrodes. Many studies include only one electrode – a strong simplification considering that there are several interacting electrodes in the furnace. Furthermore, models often assume axial symmetry, such that the calculations can be projected to the two-dimensional (2D) radial cross-section of the electrode (Larsen, Feldborg, and Halvorsen, 2013; Innvær, Fidje, and Ugland, 1986;

Innvær and Olsen, 1980; Innvær, Olsen, and Vatland, 1984; Halvorsen, Valderhaug, and Fors, 1999; Bermúdez *et al.*, 2003; Bermúdez, Bullón, and Pena, 1998; Gunnewiek *et al.*, 2004). The axisymmetric assumption simplifies and speeds up calculations, particularly when more complex situations such as thermoelectric or thermomechanical models are considered. Axisymmetric models will capture the skin effect, given that the AC formulation is used, but they will not capture proximity effects between electrodes. In addition to the axisymmetric models, 3D single-electrode models have been investigated numerically, both for Søderberg and composite ELSA electrodes (McDougall *et al.*, 2004; Innvær, Fidje, and Sira, 1985; Meyjes, Venter, and van Rooyen, 2010; Bermúdez, Rodriguez, and Salgado, 2005; Jonsson and Ingason, 1998). These models typically focus on the electrical, thermal, and mechanical conditions in, and close to, the baking zone.

There have also been several publications that focus on capturing the proximity effect between the electrodes in industrial furnaces. Analytical calculations of the skin and proximity effects have been performed in 2D horizontal cross-sections with the typical triangular electrode configuration with a phase shift between the electrodes (Dunski, 1962; Böchmann and Olsen, 1968; Hot, Haznadar, and Majer, 1980). Also, numerical case studies have been published, both in 2D (Larsen, 2006; Bermúdez *et al.*, 1999), and in 3D (Bermúdez, Rodriguez, and Salgado, 2005; McDougall, 2007). The results for the current density in the electrodes capture the asymmetric current distribution that arises when proximity effects are considered.

* Teknova AS, Norway.

© The Southern African Institute of Mining and Metallurgy, 2018. ISSN 2225-6253. This paper was first presented at the INFACON XV: International Ferro-Alloys Congress, 25–28 February 2018, Century City Conference Centre and Hotel, Cape Town, South Africa

3D models of proximity effects in large FeSi and FeMn furnaces

In addition to electrode models, there are also studies that include the interior of the furnace. These typically concentrate on modelling the process itself, with a simple rendering of the electrodes (McDougall, 2007). Finally, if the electrical conditions are modelled with direct current (DC) (Darmana *et al.*, 2012; Dhainaut, 2004; Halvorsen, Olsen, and Fromreide, 2016), both the skin and proximity effects are disregarded.

In the present work, AC electromagnetic models are studied for two cases, a 45 MW ferrosilicon (FeSi) furnace, and a 41 MW ferromanganese (FeMn) furnace. The main objective is to model the skin and proximity effects, within the electrodes as well as in the other material layers of the furnace. The models include the effects of the steel shell and the lining.

The models

Electromagnetics

For the metal-producing furnaces studied here, the AC frequency f is 50 Hz, and all electromagnetic fields are assumed to vary harmonically with time. Hence, the electric field $\mathbf{E}(\mathbf{r}, t)$ (V/m), which generally depends on time and space, can be written $\mathbf{E}(\mathbf{r}, t) = \text{Re}(e^{i\omega t} \mathbf{E}(\mathbf{r}))$, where Re denotes the real part of its argument, $\mathbf{E}(\mathbf{r})$ is the time-independent complex amplitude, and $\omega = 2\pi f$. In the following, all electromagnetic fields are denoted in terms of their complex amplitude fields. The electromagnetic fields inside the furnace are accurately described by the low-frequency approximation of the time-harmonic Maxwell's equations (Bermúdez, Gómez, and Salgado, 2014; Rodríguez and Valli, 2010):

$$\nabla \cdot \mathbf{E} = 0 \quad [1]$$

$$i\omega \mathbf{B} + \nabla \times \mathbf{E} = 0 \quad [2]$$

$$\nabla \cdot \mathbf{B} = 0 \quad [3]$$

$$\frac{1}{\mu} \nabla \times \mathbf{B} = \mathbf{J} \quad [4]$$

Here, $\mathbf{B}(\mathbf{r})$ is the magnetic field, $\mathbf{J}(\mathbf{r})$ (A/m^2) is the electric current density, and μ (H/m) is the magnetic permeability. The magnetic permeability is typically given by $\mu = \mu_r \mu_0$, where $\mu_0 = 4\pi \cdot 10^{-7}$ H/m is the constant magnetic permeability of vacuum and μ_r (dimensionless) is the relative magnetic permeability. Also, \mathbf{J} is related to \mathbf{E} through Ohm's Law

$$\mathbf{J} = \sigma \mathbf{E} \quad [5]$$

where σ (S/m) is the electrical conductivity.

Skin effect

By solving Equations [1]–[5], one finds that the electromagnetic fields and currents decay inside conductors, such that the currents effectively accumulate on the surface of the conductor (Bermúdez, Gómez, and Salgado, 2014; Ramo, Whinnery, and van Duzer, 1994), *i.e.*, the so-called skin effect, which is particularly evident at higher frequencies and for thicker conductors of high electrical conductivity or relative magnetic permeability. To exhibit an appreciable skin effect, the conductor must be large enough to accommodate significant amounts of self-induced eddy currents. That is,

the radius of the conductor must be larger than the skin depth δ (m), given by

$$\delta = \frac{1}{\sqrt{\pi f \mu \sigma}} \quad [6]$$

In most electrodes, it is a good approximation that the currents flow in the axial direction below the contact clamps. Then, in electrodes with a circular cross-section, it is possible to derive analytical expressions for the current density and the resistance of the electrode. These results are very useful and are frequently cited in the context of electrode current-carrying capacity (Dunski, 1962; Kennedy, 2012; Westly, 1975).

Proximity effect

The proximity effect can be regarded as the redistribution of current due to induced eddy currents opposing the electromagnetic variations caused by nearby conductors. Similar to the skin effect, the radius of the conductor must be comparable to or higher than δ in order to exhibit appreciable proximity effects. Additionally, as the electromagnetic fields caused by an AC current decrease with distance, the strength of the proximity effects will depend on how close the conductors are to each other. Previous investigations of 2D conductor configurations, similar to the horizontal cross-section of the triangular electrodes configuration studied here, have concluded that the dimensionless factor D/d (where D (m) is the electrode diameter and d (m) is the electrode centre-to-centre distance) is a key quantity in the evaluation of proximity effects (Dunski, 1962; Hot, Haznadar, and Majer, 1980). The proximity effects increase when D/d increases.

Model assumptions and limitations

The models investigated here focus on the skin and proximity effects in the material layers of the furnace and in the lower part of the electrode. For this reason, the baking zone, electrode clamps, electrode casing, busbars, and flexibles are not included in the models.

The material properties are assumed to be constant within each material layer. Specifically, σ does not vary with temperature. Therefore, the model cannot predict changes in the current density due to temperature variations. However, removing the changes in the currents caused by temperature variations makes it more straightforward to study the skin and proximity effects, which is the main purpose of this work.

In the FeSi case, a significant amount of the current is transported by arcs in the cavity between the electrode and the alloy or crater wall. The arc has been modelled in a simplified manner by defining a domain with a fixed σ near the electrode tip and between the electrode and the crater wall (see below). We note that an arc does not obey Ohm's Law in Equation [5], and the current and voltage signals will be distorted with some amounts of higher-order harmonics (see Valderhaug, 1992). These effects are not accounted for in these models. However, we expect the model results at $f = 50$ Hz to yield approximate results for the skin and proximity effects, probably somewhat underestimated as these effects are more pronounced at higher frequencies.

3D models of proximity effects in large FeSi and FeMn furnaces

In this work, currents in the steel shell and carbon linings of the furnace are of importance. The model assumes that these regions are continuous and isotropic, and any transition zones such as welded joints in the steel shell and cracks in the linings have not been accounted for.

Model geometries and properties

45 MW FeSi furnace

The model geometry of the FeSi furnace is shown in Figure 1. Briefly, at the tip of each electrode (2) a gas-filled cavity is formed (6), and at its bottom a pool of liquid metal is found (8). The dome of the cavity is usually referred to as the crater wall (7). An electric arc forms between the electrode and the crater wall or metal (5). Zones composed primarily of charge (3), silicon carbide (4), and solid slag (11) are included in the model. The carbon lining (9), oxide lining (10), and steel shell (12) complete the model. Table I provides important geometrical data, and Table II lists material data. In Figure 1 and Table II, the value for the skin depth is calculated using Equation [6].

The set-up of the interior material layers and most of the properties are based on the work of Tangstad, Ksiazek, and Andersen (2014) and Krokstad (2014). However, in industrial furnaces there are large uncertainties and variations associated with geometries and electrical properties of the material layers around the electrode tip. On the other hand, the modelled resistance is very sensitive, particularly to details of the arc and the crater wall. For these two layers, the properties and dimensions are chosen with the additional constraint that the total furnace resistance should be reasonable. The input electrode current in all three electrodes is $I_{RMS} = 132$ kA, assuming that the furnace is operated according to Westly's C_3 formula (Westly, 1974). Moreover, there is a 120° phase shift in the electrode currents, with an anticlockwise rotation.

41 MW FeMn furnace

The model geometry of the FeMn furnace is shown in Figure 2. At the tip of each electrode (2), there is a coke bed (6) and at its bottom there is a layer of molten metal (7). The charge zone has been divided into three different zones (3, 4, 5) with varying electrical conductivity. Finally, the carbon lining

Table I

Main furnace dimensions, FeSi model

Quantity	Value
Furnace diameter	11 m
Furnace height (steel shell height)	5.94 m
Electrode diameter, D	1.8 m
Electrode centre–centre distance, d	4.0 m
Steel shell thickness	40 mm
Electrode tip to alloy distance	200 mm

Table II

Material data, FeSi model. The numbers in parentheses refer to Figure 1

Material	σ (S/m)	μ_r	δ (m)
Gas (1, 6)	$1 \cdot 10^{-12}$	1	$7.1 \cdot 10^7$
Electrode (2)	$5 \cdot 10^4$	1	0.32
Charge (3)	10	1	23
Silicon carbide (4)	100	1	7.1
Arc (5)	400	1	3.6
Crater wall (7)	600	1	2.9
Alloy (8)	$1 \cdot 10^6$	1	0.071
Carbon lining (9)	$2 \cdot 10^4$	1	0.50
Oxide lining (10)	$1 \cdot 10^{-6}$	1	$7.1 \cdot 10^4$
Slag (11)	1	1	71
Steel shell (12)	$6.3 \cdot 10^6$	200	0.0020

(8), oxide lining (9), steel shell (10), and steel roof (11) are included in the model. Table III summarizes the important geometrical data, and Table IV provides the material data. The set-up of the interior material layers and most of the properties are based on the work of Dhainaut (2004) and Eidem (2008). There are some differences in the properties of the lining and steel materials between the FeMn and FeSi furnaces, but both are within the typical range for these materials. Realistic current and power conditions were obtained by adjusting the position of the electrode. The input electrode current in all three electrodes is $I_{RMS} = 134.3$ kA, and there is a 120° phase shift between the electrodes, with an anticlockwise rotation.

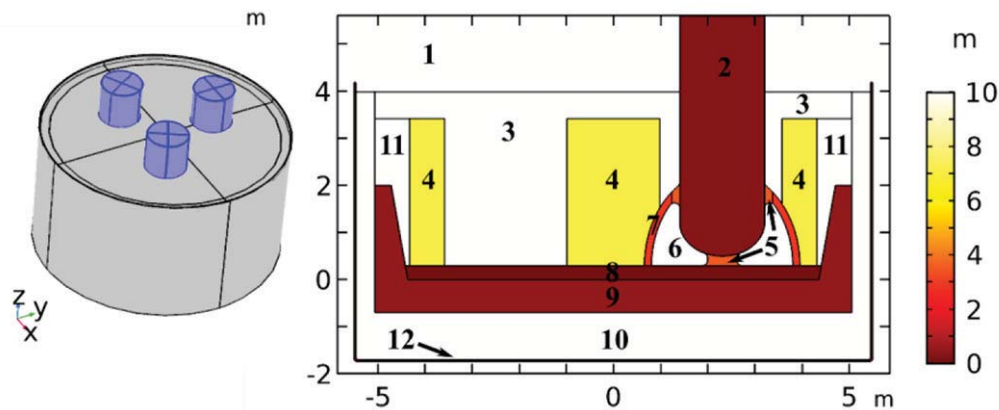


Figure 1—FeSi furnace model. Left: 3D model geometry (excluding air) with electrodes coloured. Right: material distribution in a cross-section (y - z plane). 1. Air, 2. electrode, 3. charge, 4. silicon carbide (SiC) layer, 5. arc, 6. cavity, 7. crater wall, 8. alloy, 9. carbon lining, 10. oxide lining, 11. slag, 12. steel shell. The colours show the skin depth δ , with white when $\delta \geq 10$ m

3D models of proximity effects in large FeSi and FeMn furnaces

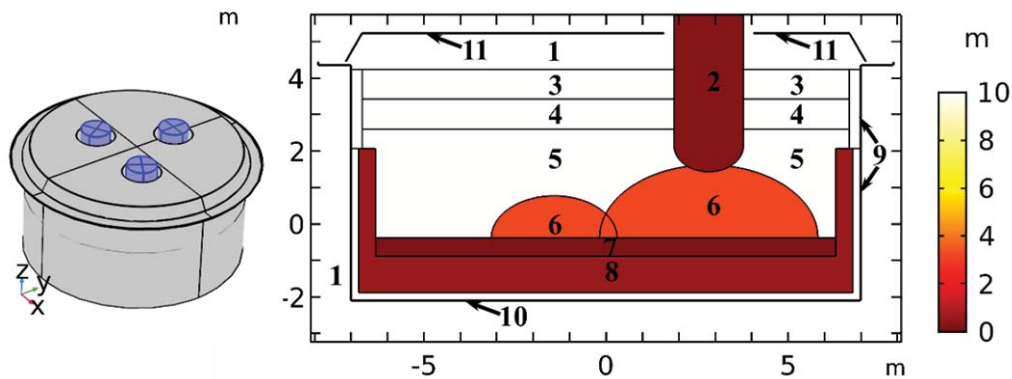


Figure 2—FeMn furnace model. Left: 3D model geometry (excluding air) with electrodes coloured. Right: Material distribution in a cross-section (y-z plane). 1. Gas, 2. electrode, 3. charge, 400°C, 4. charge, 800°C, 5. charge, 1200°C, 6. coke beds, 7. alloy, 8. carbon lining, 9. oxide lining, 10. steel shell, 11. steel roof. The colours show the skin depth δ , with white when $\delta \geq 10$ m

Table III

Main furnace dimensions, FeMn model

Quantity	Value
Furnace diameter	14 m
Furnace height (steel shell height)	6.47 m
Electrode diameter, D	1.9 m
Electrode centre–centre distance, d	4.9 m
Steel shell thickness	25 mm
Electrode tip to alloy distance	1.815 m

Table IV

Material data, FeMn model. The numbers in parentheses refer to Figure 2

Material	σ (S/m)	μ_r	δ (m)
Gas (1)	$1 \cdot 10^{-12}$	1	$7.1 \cdot 10^7$
Electrode (2)	$5 \cdot 10^4$	1	0.32
Charge, 400°C (3)	0.075	1	260
Charge, 800°C (4)	0.15	1	180
Charge, 1200°C (5)	15	1	18
Coke bed (6)	500	1	3.2
Alloy (7)	$1.5 \cdot 10^5$	1	0.18
Carbon lining (8)	$1.4 \cdot 10^4$	1	0.60
Oxide lining (9)	$1 \cdot 10^{-6}$	1	$7.1 \cdot 10^4$
Steel shell (10)	$3 \cdot 10^6$	100	0.0041
Steel roof (11)	$1 \cdot 10^6$	1	0.071

Numerical implementation and boundary conditions

The model equations and boundary conditions were implemented and solved numerically using COMSOL Multiphysics 5.3 with the Magnetic and Electric Fields interface (COMSOL Inc., 2017). The low-frequency Maxwell's equations are solved using a potential formulation for the equations. The equations are discretized with the finite element method using quadratic elements. To impose proper boundary conditions on the magnetic field, a large volume of air (with a diameter that is five times larger than the furnace diameter) is included around the furnace. For two electrodes, the total current with a phase shift of 120° is fixed at the boundary. For the third electrode, the current is given by current conservation.

As can be seen from Table II and Table IV, the skin depth δ of the furnace steel shell is approximately 2 mm for the FeSi model, and 4 mm for the FeMn model, *i.e.*, the skin depths are an order of magnitude smaller than the thickness of the shell. This means that the induced eddy currents in the steel shell will flow within a few millimetres of the surface, and only a negligible amount of the current will flow in the interior of the shell. Resolving the large current gradients within a few millimetres of the surface involves a high computational cost, hence the induced currents (and the associated impedance) of the steel shell have been modelled as surface currents, applying COMSOL's impedance boundary condition (COMSOL Inc., 2017). This approximation has been validated by comparison with one simulation that resolves the volume currents of the shell.

Results, case studies

For each case, two simulations have been performed. First, the model has been solved using the properties of air ($\sigma = 1 \cdot 10^{-12}$ S/m and $\mu_r = 1$) for the steel shell and roof. Effectively, this is the same as solving a model where the effects of the induced steel shell currents are disregarded. These results will capture the proximity effects between the electrodes, but will neglect the proximity effects between the steel shell and the electrodes. Secondly, we solve for the full model, including the effects of the steel domains. By comparing the two simulations it is possible to isolate the effects caused by the induced currents in the steel shell and roof.

In the following presentation of the results, we study the current density norm $|J|$, the active power density p (W/m^3), given by $p = |J|^2 / (2\sigma)$, and the reactive power density q (W/m^3), given by $q = (\pi f / \mu) |B|^2$. By integrating p and q over different material domains and the entire furnace, it is possible to study power consumption in different material layers, and the total power consumption and power factor for the full furnace.

45 MW FeSi furnace

Induced currents in the steel shell

When the furnace steel shell is included, the model results show that there are induced currents in the steel shell. In

3D models of proximity effects in large FeSi and FeMn furnaces

Figure 3, results for the current density in the steel shell are presented. The left figure shows the results from a fully resolved model. Here, it is clearly shown how the currents accumulate in thin layers on both sides of the steel shell with skin depth $\delta = 2$ mm (see Table II). These results justify the approximation of modelling the steel shell currents as surface currents. The induced currents are typically stronger on the inside surface than the outside. For example, at the level of the electrode tips, the average surface current is 5.05 kA/m on the inside, and 1.36 kA/m on the outside of the steel shell. On the horizontal bottom part, the average surface current is 2.58 kA/m on the inside, and 0.66 kA/m on the outside. The only exception is along the top edge, where the average surface current density is similar on both sides.

We observe that the shell currents essentially follow a pattern opposite to the currents of the electrodes. In the shell, close to an electrode, the inside shell currents are almost vertical, but in the opposite direction compared to the electrode current. In between the electrodes, they are mostly horizontal. Effectively, the shell currents form loops in the opposite direction to the furnace currents. Some of the shell currents continue to the outside, while most of the current loops close at, or near to, the top edge of the furnace shell. Here, the highest current densities are found.

It is interesting to calculate the strength of the currents that flow in the steel shell. To this end, the vertical component of the inside shell current has been integrated along a horizontal curve covering the one-third of the inner perimeter that is closest to electrode 1. Here, electrode 1 means the electrode on the y -axis (see Figure 1). The integration has been performed at vertical level $z = 2$ m (see Figure 1). The resulting shell current is 29.4 kA, which corresponds to approximately 22% of the current flowing in the electrode. There is a 179° phase difference with the electrode current, *i.e.*, the inside shell current is flowing in the opposite direction with respect to the nearby electrode current.

Current density

In Figure 4, results for the current density in a cross-section of the FeSi furnace are shown. The highest current densities

are found in the arc between the electrode tip and the alloy and in the skin of the alloy layer. There are also significant currents flowing in the electrode, crater wall, and the carbon lining. In the electrodes, the results of strong skin and proximity effects are clearly visible in the asymmetry of the current distribution. Specifically, more currents on the inside of the electrodes are caused by the proximity effects between the electrodes. In the alloy, owing to the small skin depth ($\delta = 7$ cm), there are very strong skin effects. The simulations also show that there are some currents flowing in the carbon lining. In the model, the carbon lining is connected to the alloy and serves as a parallel connection with the alloy for current flow between the electrodes.

At first glance, comparing the upper and middle figures of Figure 4, the proximity effects of the induced steel shell currents are small. However, by calculating the difference, *c.f.* the bottom figure, some changes can be seen in the electrode, alloy, and carbon lining. For example, in the electrode just above the crater wall, $|J|$ is about 7% higher on the outside, and about 3% smaller on the inside, when the induced steel shell currents are included in the model. In the alloy and lining, there is a considerable shift towards accumulation of currents in the bottom of these layers.

Active and reactive power densities

As mentioned above, the power density $p = |J|^2 / (2\sigma)$, *i.e.*, p is proportional to $|J|^2$. Then, within a region with the same σ , the power density variations caused by skin and proximity effects are stronger than the corresponding current density variations. On the other hand, as p is proportional to the material resistivity $1/\sigma$, most of the power in the model is deposited in the arc and the crater wall, and for these areas there are no significant skin and proximity effects.

The total active and reactive power of the model can be found by integrating the power density and the reactive power density over the volume of the furnace, and the results can be seen in Table V. The results show that $P = 45.0$ MW for the furnace. In the case when the steel shell effects are disregarded, $P = 44.9$ MW, *i.e.*, the furnace power consumption with induced steel shell currents is very similar to the power consumption when the steel shell currents are

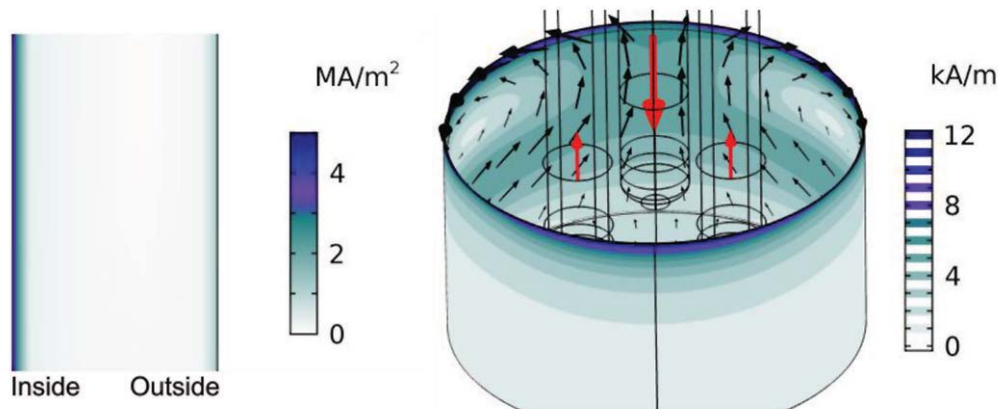


Figure 3—Induced currents, FeSi furnace steel shell. Left: current density distribution at coordinates $(x, y, z) = (0, 5.5, 2.0)$ m. Right: surface currents on the steel shell surface. Colours denote the surface current norm. Black arrows show direction and strength of the induced currents on the inside of the steel shell, and red arrows denote direction and strength of electrode currents, at phase $\phi = 0^\circ$. At $\phi = 0^\circ$, the current flowing into the middle electrode (electrode 1) is maximum (186.7 kA), and the current flowing out of the two other electrodes is halved (93.3 kA)

3D models of proximity effects in large FeSi and FeMn furnaces

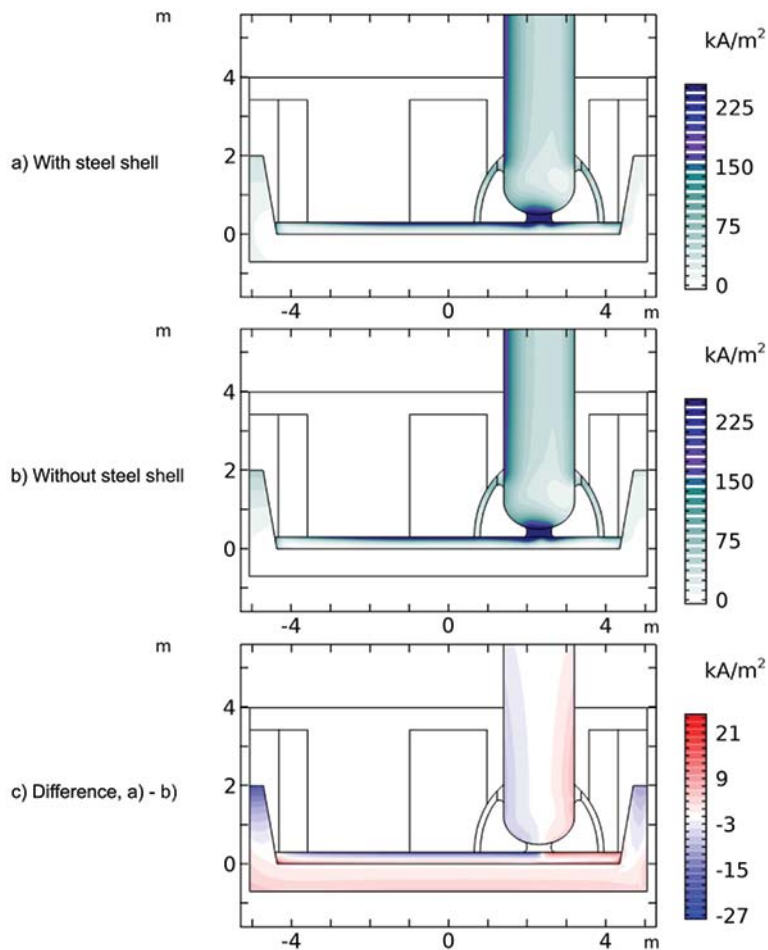


Figure 4—Current densities in the y-z plane, FeSi furnace (see Figure 1). The colour scale has been limited to a maximum of 250 kA/m²

Table V
Power distribution, FeSi furnace. Active and reactive power for each material layer

Material	P (MW)		Q (MW)	
	Steel shell	No steel shell	Steel shell	No steel shell
Air (1)	0.00	0.00	9.07	9.55
Electrodes (2)	3.14	3.20	2.54	2.59
Charge (3)	5.20	5.23	7.60	8.05
SiC (4)	3.01	3.03	2.03	2.16
Arc (5)	20.40	20.40	0.16	0.16
Cavity (6)	0.00	0.00	0.81	0.88
Crater wall (7)	12.44	12.44	0.30	0.32
Alloy (8)	0.09	0.10	0.09	0.10
Carbon lining (9)	0.34	0.46	0.26	0.21
Oxide lining (10)	0.00	0.00	0.49	0.36
Slag (11)	0.11	0.11	0.43	0.51
Steel shell (12)	0.29	0.00	0.29	0.03
Total	45.02	44.95	24.07	24.92

disregarded. For the reactive power, the results show that $Q = 24.1$ MW when the steel shell is included, compared with $Q = 24.9$ MW when not included. The power factor, given by $P/\sqrt{P^2 + Q^2}$, is 0.882 and 0.875 with and without the steel shell, respectively. Compared with operational data, we expect that the models will significantly underestimate the reactive power in the furnace, as busbars and flexibles are not included.

In Table V, the power values are also analysed for each material layer. Most of the power is deposited in the arc and crater wall, while some power is deposited in the charge, SiC, and electrodes. The rest of the layers contribute only small amounts. Note that the induced currents in the steel shell account for 0.7% of the total power consumption. For the power, there are no significant changes in the different layers when the steel shell effects are included in the model. This

3D models of proximity effects in large FeSi and FeMn furnaces

result suggests that the proximity effects of the steel shell only change the power distribution internally within the conductive layers of the furnace, whereas the total power for a given material layer is almost constant. For the reactive power contributions, the changes between the two models are slightly more pronounced, particularly in layers that are close to the steel shell.

Electrodes

In the following, the main results for the electrodes are presented. In the model (see Figure 1), the current flowing in the electrode may exit into three distinct material layers: the charge, via the side arcs into the crater wall, and via the tip arc into the alloy. By integrating over the respective boundaries, the results show that approximately 60 kA exits

through the side arc to the crater wall, 57 kA through the tip arc, and 14 kA to the charge.

In Figure 5, results for the power density in electrode 1 are presented. The results show that there are strong skin and proximity effects. Note that the power density is strongly biased towards the leading electrode. Comparing with the $|J|$ results in Figure 4, the variations along the circumference are much stronger for p . Approximately 1 m above the electrode tip, there are significant amounts of current flowing into the crater wall. Hence, for the bottom part of the electrode below the crater wall, the power density is significantly reduced.

The results in Figure 5 are obtained with the steel shell included in the model. In Figure 6, the results for the power density at the electrode perimeter are given at two different vertical positions, and cases with and without the steel shell

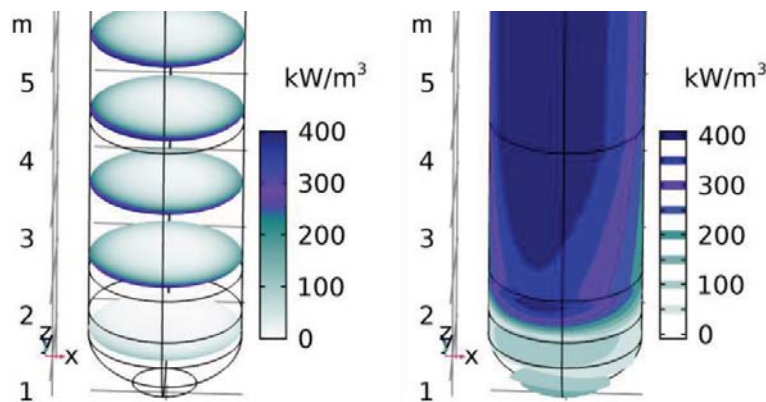


Figure 5—Power density, p , for electrode 1, FeSi model. Left: p on five different horizontal cross-sections. From top, the two first cross-sections are above the charge ($z \geq 4$ m). The third and fourth cross-sections are adjacent to the charge. The fifth cross-section is adjacent to the cavity. Right: iso-surface plot of p

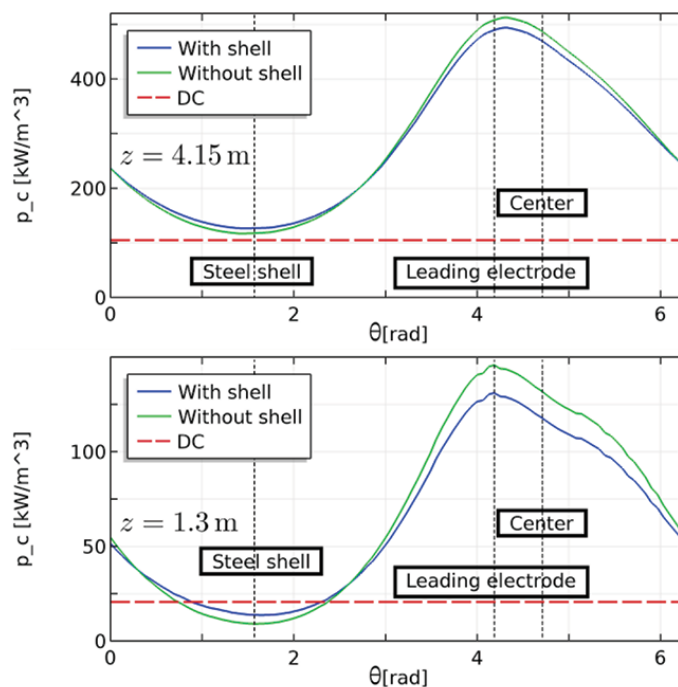


Figure 6—Circumferential power density profiles p_c as a function of the angle θ of electrode 1, FeSi model. The directions towards the steel shell, leading electrode, and furnace centre are indicated as dotted vertical lines. The vertical positions for the profiles are $z = 4.15$ m and $z = 1.3$ m, and correspond to the second and fifth cross-sections of Figure 5. The red horizontal dashed line is the power density for uniform current distribution (DC)

3D models of proximity effects in large FeSi and FeMn furnaces

are considered. The comparison with the uniform current distribution (red dashed line) clearly shows the importance of including skin and proximity effects for obtaining an accurate description of the power density within an electrode. Comparing the values of the lower figure with the top figure, the power distribution is relatively more asymmetric at $z = 1.3$ m compared with that above the crater wall. Including the steel shell results in a significant change in the power distribution, particularly in the lower part of the electrode. With the steel shell effects, more of the power is allocated towards the wall and less towards the leading electrode, reducing the asymmetry caused by the electrode–electrode proximity effect.

41 MW FeMn furnace

Induced currents in steel shell and roof

The model results in Figure 7 and Figure 8 show that there are strong induced currents in the steel shell and roof. The left panel of Figure 7 shows results for a fully resolved model exhibiting the steel shell skin effect. Compared with the FeSi model in Figure 3, the skin effect is less pronounced, as the skin depth is greater ($\delta = 4$ mm, see Table IV). As seen in both panels of Figure 7, the induced currents in the shell are typically stronger on the inside. At the level of the electrode tips, the average surface current is 4.34 kA/m on the inside and 1.38 kA/m on the outside, and on the horizontal bottom

part, the average surface current is 3.06 kA/m on the inside and 0.55 kA/m on the outside. Also, note that the shell currents essentially follow the same pattern as for the FeSi case detailed above.

Integrating the vertical component of the inside shell current along a horizontal curve covering the one-third of the inner perimeter that is closest to electrode 1 is used here as a measure of the current that flows in the steel shell. The integration has been performed at vertical level $z = 2.5$ m (see Figure 2). The result is 35.7 kA which corresponds to approximately 27% of the current flowing in the electrode. There is a 175° phase difference with the electrode current.

In Figure 8, results for the current densities in the steel roof are shown. Since the skin depth of the nonmagnetic steel roof is much higher than for the magnetic steel shell, there are much less skin effects in the roof, and hence the current density is more uniform. This is clearly seen in the left panel of Figure 8. In the right panel, the current densities on the surface of the roof are shown. There are high current densities associated with the lower edge close to the steel shell. By comparing the results in Figure 8 with the steel shell results in Figure 7, it is clear that the strong roof currents are found in close proximity to the locations of the strong shell currents, but with opposite direction. This indicates that these roof currents may be induced by the strong edge currents of the steel shell.

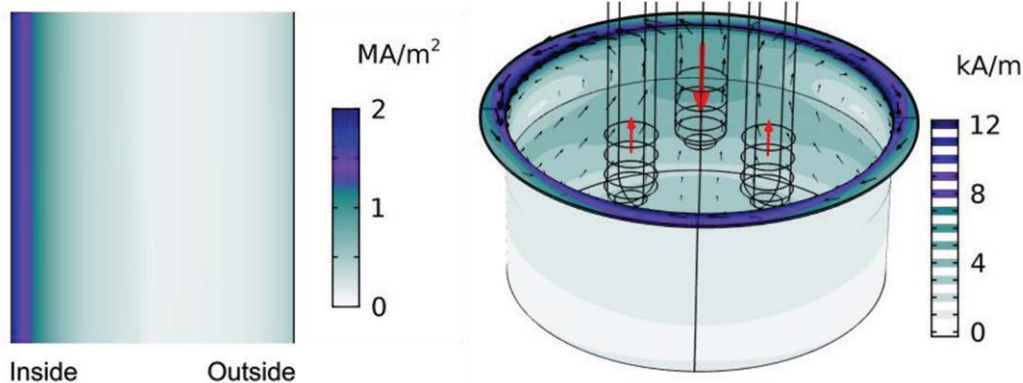


Figure 7—Induced currents, FeMn model steel shell. Left: current density distribution at coordinates $(x, y, z) = (0, 7.0, 2.0)$ m. Right: surface currents on the steel shell surface. Colours denote the surface current norm. Black arrows show direction and strength of the induced currents on the inside of the steel shell, and red arrows denote direction and strength of electrode currents, at phase $\phi = 0^\circ$. At $\phi = 0^\circ$, the current flowing into the middle electrode (electrode 1) is maximum (189.9 kA), and the current flowing out of the two other electrodes is halved (95.0 kA)

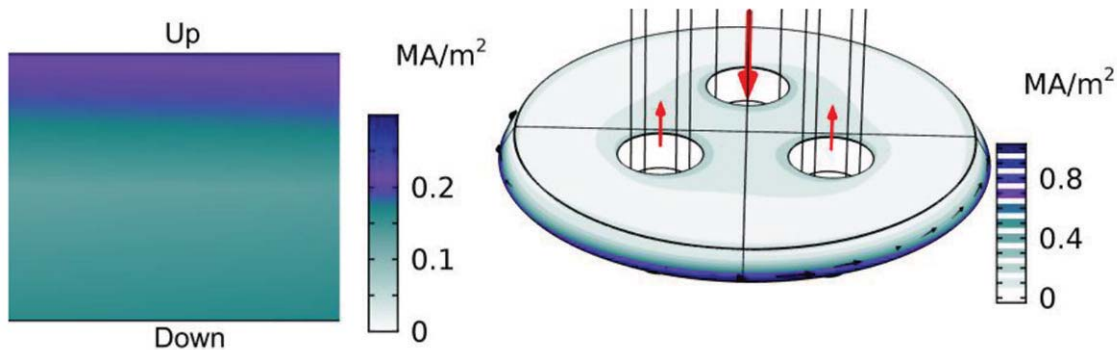


Figure 8—Induced currents, FeMn model steel roof. Left: current density distribution at coordinates $(x, y, z) = (0, 1.4, 5.2)$ m. Right: current densities on the steel shell surface. Colours denote the current density norm. Black arrows show direction and strength of induced currents on the downside of the steel roof, at phase $\phi = 0^\circ$ (same phase as Figure 7)

3D models of proximity effects in large FeSi and FeMn furnaces

Current density

In Figure 9, results for the current density in a cross-section of the FeMn furnace are shown. The highest current densities are found in the skin and tip of the electrode. There are also high current densities in the upper part of the coke bed and in the alloy. As for the FeSi case, the skin and proximity effects are clearly visible in the electrodes. There are also skin effects in the alloy, but compared with the FeSi case in Figure 4, these are less pronounced, as the skin depth ($\delta = 18$ cm) is greater. The results also show some currents flowing in the carbon lining.

As for the FeSi case, the changes in current density when including the steel shell and roof are confined to conductive layers. In the electrode, $|J|$ is about 7% higher on the outside, and about 4% smaller on the inside, when the induced steel shell currents are included in the model. Also, there is a shift towards accumulation of currents in the bottom of the alloy and carbon lining layers.

Active and reactive power densities

The results for the active and reactive power can be seen in Table VI. The power obtained is $P = 40.6$ MW. When the steel shell effects are disregarded, $P = 40.4$ MW. For the reactive power, the results show that $Q = 31.6$ MW when the steel shell is included, and $Q = 33.4$ MW when not included. The power factor, given by $P/\sqrt{P^2 + Q^2}$, is 0.789 and 0.771 with

and without the steel shell, respectively. However, one should expect that these models will significantly underestimate the reactive power in the furnace, as busbars and flexibles are not included. As for the FeSi case, the steel shell effects are not significant for the modelled furnace power, but the modelled reactive power is reduced by a few percent.

From the analysis for each material layer, approximately 80% of the power is deposited in the coke beds. Some power is deposited in the electrodes and in the charge close to the coke bed, while the rest of the layers consume only negligible amounts. Note that the induced currents in the steel account for 1.5% of the total power consumption. As for the FeSi case, these results suggest that the proximity effects of the steel shell mostly change the power distribution internally within the conductive layers of the furnace, whereas the total power for a given material layer is only marginally affected.

Electrodes

Dedicated results for the electrode are presented in Figures 10 and 11. Most of the current (111 kA) in the electrode exits into the coke bed. The rest (21 kA) exits into the layer of the charge. Compared with the FeSi model, most of the current in the electrode goes all the way to the electrode tip.

Consequently, there is a higher power density in the electrode tip region of the FeMn model. This can be seen by comparing Figure 10 with Figure 5. As for the FeSi case, there are strong

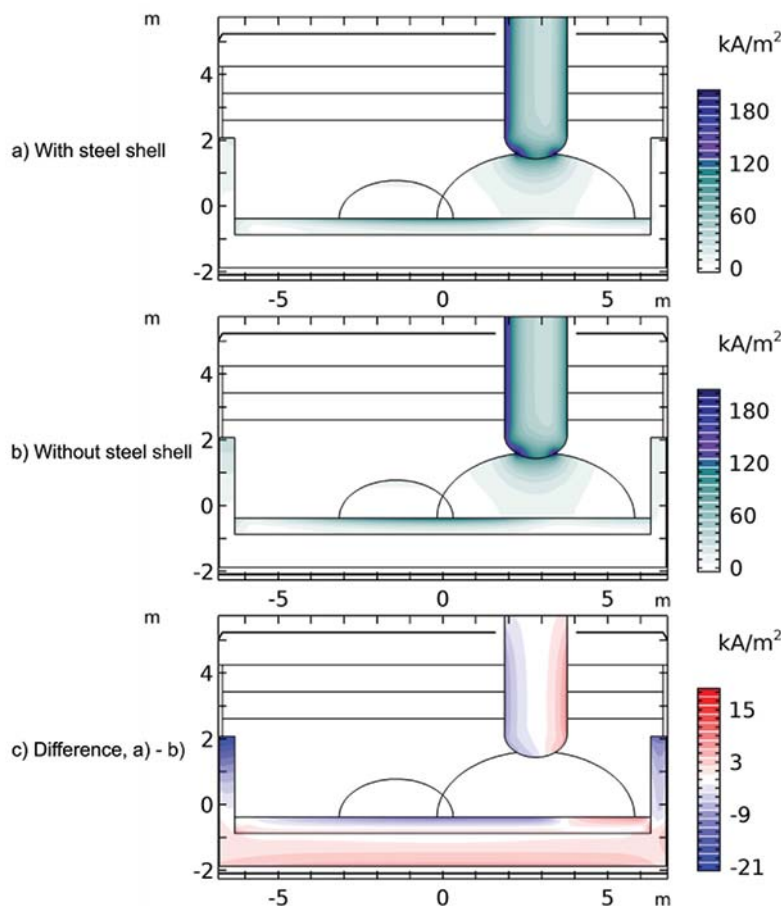


Figure 9—Current density in the $y-z$ plane, FeMn furnace (see Figure 2). The colour scale has been limited to a maximum of 200 kA/m²

3D models of proximity effects in large FeSi and FeMn furnaces

Table VI
Power distribution, FeMn furnace. Active and reactive power for each material layer

Material	P (MW)		Q (MW)	
	Steel shell	No steel shell	Steel shell	No steel shell
Gas (1)	0.00	0.00	9.17	10.12
Electrodes (2)	3.06	3.12	2.57	2.62
Charge, 400°C (3)	0.01	0.01	3.95	4.15
Charge, 800°C (4)	0.02	0.02	3.90	4.17
Charge, 1200°C (5)	3.46	3.47	7.11	7.71
Coke beds (6)	32.95	33.01	3.50	3.86
Alloy (7)	0.17	0.18	0.17	0.18
Carbon lining (8)	0.35	0.62	0.33	0.23
Oxide lining (9)	0.00	0.00	0.31	0.22
Steel shell (10)	0.47	0.00	0.46	0.02
Steel roof (11)	0.12	0.00	0.11	0.10
Total	40.61	40.44	31.58	33.39

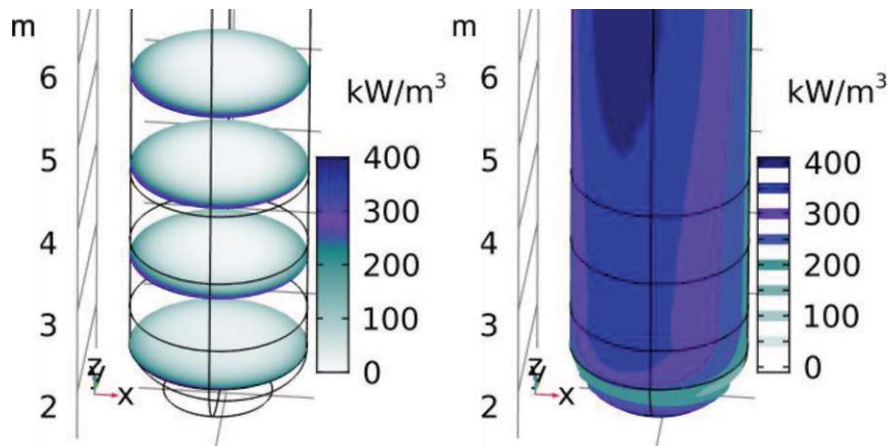


Figure 10—Power density, p , for electrode 1, FeMn model. Left: p on four different horizontal cross-sections. From top, the two first cross-sections are above the charge ($z \geq 4.3$ m). The third and fourth cross-sections are adjacent to the 800°C and 1200°C layers of the charge, respectively. Right: iso-surface plot of the power density

skin and proximity effects throughout the length of the electrode.

In Figure 11, the results for the power density at the electrode perimeter are given at two vertical positions, both with and without the effects of the steel shell and roof. The steel shell effects are similar to the FeSi case, *i.e.*, the power density increases towards the shell and decreases towards the leading electrode. These effects are most pronounced in the lower part of the electrode below the top edge of the steel shell.

It is also interesting to compare the strength of the proximity effect between the electrodes for both the FeSi and FeMn cases. This can be done by calculating the ratio $(p_{c,max} - p_{c,min})/p_{c,avg}$, where $p_{c,max}$, $p_{c,min}$ and $p_{c,avg}$, are the maximum, minimum, and average power densities along the electrode perimeter. For the FeSi case in Figure 6, the ratios are 1.31 and 1.85. For the FeMn case in Figure 11, the ratios are 1.11 and 0.94. This means that the electrode proximity effects are stronger in the FeSi furnace.

Conclusions

The use of the low-frequency description of the

electromagnetic fields, and including the linings, steel shell, and steel roof in the furnace model, makes the models particularly well-suited for studying the skin and proximity effects in the furnace. The model results show that strong currents are induced in the steel shell and roof. In the steel shell, the induced currents accumulate in the skin, whereas the currents are more distributed throughout the thickness of the nonmagnetic steel roof. On the inside of the shell, the model results exhibit a well-defined circulation pattern in opposite phase compared with proximate currents in the electrodes and hearth of the furnace.

The models yield detailed results for the current and power distributions in material layers within the furnace. The highest current densities are typically found in the electrodes and alloy, and in the material layers connecting these. These interconnecting domains (arc/crater wall in the FeSi model, and coke bed in the FeMn model) are where most of the power is deposited.

The results show that there are strong skin effects in the electrodes and alloy. Also, two different proximity effects are observed. The most significant proximity effect is the electrode–electrode interaction, which leads to strong redistribution of the currents within the electrodes.

3D models of proximity effects in large FeSi and FeMn furnaces

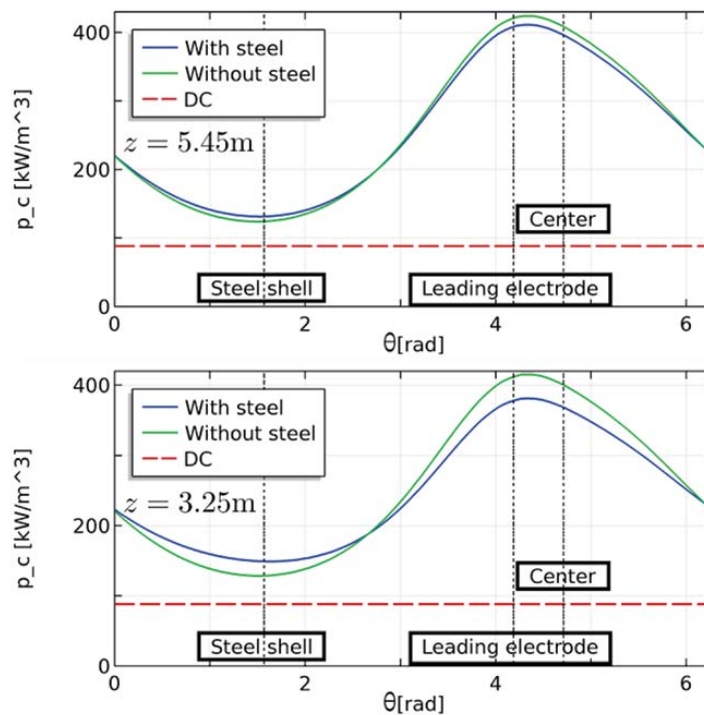


Figure 11—Circumferential power density profiles p_c , as a function of the angle θ , around electrode 1, FeMn model. The directions towards the steel shell, leading electrode, and furnace centre are given as dotted vertical lines. The vertical positions for the profiles are $z = 5.45$ m and $z = 3.25$ m, and correspond to the first and third cross-sections of Figure 10. The red horizontal dashed line is the power density for uniform current distribution (DC)

Additionally, when the steel shell is included in the model, the results show that there is an additional redistribution of furnace currents caused by proximity effects with the induced steel shell currents. In the electrodes, the steel shell proximity effect competes with the electrode–electrode proximity effect, and effectively reduces the asymmetry in the current and power density. For most material layers, the effects of including the steel shell in the model are negligible, but these may be of importance when studying current and power distributions in the most conductive areas of the furnace, such as the electrodes, the metal bath, and conductive lining. Also, for accurate modelling of the electrical conditions, the steel shell effects were found to modify the reactive power by a few percent.

Acknowledgements

This paper is published as part of the project Electrical Conditions and their Process Interactions in High Temperature Metallurgical Reactors (ElMet), in short Electrical Conditions in Metal Processes (ElMet), with financial support from The Research Council of Norway and the companies Alcoa, Elkem, and Eramet Norway.

References

- BERMÚDEZ, A., BULLÓN, J., and PENA, F. 1998. A finite element method for the thermo-electrical modelling of electrodes. *Communications in Numerical Methods in Engineering*, vol. 14, no. 6. pp. 581–593.
- BERMÚDEZ, A., BULLÓN, J., PENA, F., and SALGADO, P. 2003. A numerical method for transient simulation of metallurgical compound electrodes. *Finite Elements in Analysis and Design*, vol. 39, no. 4. pp. 283–299.
- BERMÚDEZ, A., CARMEN MUNIZ, M., PENA, F., and BULLÓN, J. 1999. Numerical computation of the electromagnetic field in the electrodes of a three-phase arc furnace. *International Journal for Numerical Methods in Engineering*, vol. 46. pp. 649–658.

- BERMÚDEZ, A., GÓMEZ, D., and SALGADO, P. 2014. *Mathematical Models and Numerical Simulation in Electromagnetism*. Springer International.
- BERMÚDEZ, A., RODRIGUEZ, R., and SALGADO, P. 2005. Finite element methods for 3D eddy current problems in bounded domains subject to realistic boundary conditions. An application to metallurgical electrodes. *Archives of Computational Methods in Engineering*, vol. 12, no. 1. pp. 67–114.
- BÖCKMANN, O. and OLSEN, L. 1968. Skin and proximity effects in electrodes of large smelting furnaces. *Proceedings of the 6th International Congress of Electroheat*, Brighton, UK, 13–18 May 1968.
- COMSOL Inc. 2017. *ACDC Module User's Guide*. Version: COMSOL 5.3. Burlington, MA.
- DARMAHA, D., OLSEN, J.E., TANG, K., and RINGDALEN, E. 2012. Modelling concept for submerged arc furnaces. *Proceedings of the Ninth International Conference on CFD in the Minerals and Process Industries*, Melbourne, Australia, 10–12 December 2012. CSIRO, Melbourne.
- DHAINAUT, M. 2004. Simulation of the electric field in a submerged arc furnace. *Infacon X, Proceedings of the Tenth International Ferroalloys Congress*, Cape Town, South Africa, 1–4 February 2004. South African Institute of Mining and Metallurgy, Johannesburg. pp. 605–613.
- DUNSKI, V. 1962. Répartition du courant dans les électrodes d'un four triphasé à arcs en régimes équilibré et déséquilibré. *Elektrowärme*, vol. 20, no. 10. pp. 503–511.
- EIDEM, P.A. 2008. *Electrical resistivity of coke beds*. PhD thesis, Norwegian University of Science and Technology, Trondheim, Norway.
- GUNNEWIEK, L.H., OSHINOWO, L., PLIKAS, T., and HAYWOOD, R. 2004. The application of numerical modelling to the design of electric furnaces. *Infacon X, Proceedings of the Tenth International Ferroalloys Congress*, Cape Town, South Africa, 1–4 February 2004. pp. 555–564.
- HALVORSEN, S.A., OLSEN, H.A.H., and FROMREIDE, M. 2016. An efficient simulation method for current and power distribution in 3-phase electrical smelting furnaces. *IFAC-PapersOnLine*, vol. 49, no. 20. pp. 167–172.
- HALVORSEN, S.A., VALDERHAUG, A.M., and FORS, J. 1999. Basic properties of the Person type composite electrode. *Proceedings of the 57th Electric Furnace Conference*, Pittsburgh, PA, 14–16 November 1999. pp. 185–204.
- HOT, E., HAZNADAR, Z., and MAJER, I. 1980. Improvement of electrode systems in electric reduction furnaces and a non-conventional model for current density measurement. *Proceedings of the 9th International Congress of the UIE*, Cannes, France, 20–24 October 1980.
- INNVER, R., FIDJE, K., and SIRA, K. 1985. Three dimensional calculations on smelting electrodes. *Proceedings of the 43rd Electric Furnace Conference*, Atlanta, GA, 10–13 December 1985. pp. 265–272.

3D models of proximity effects in large FeSi and FeMn furnaces

- INNVÆR, R., FIDJE, K., and UGLAND, R. 1986. Effect of current variations on material properties and thermal stresses in Søderberg electrodes. *Infacon IV, Proceedings of the Fourth International Ferroalloys Congress*, Rio de Janeiro, Brazil, 31 August – 3 September 1986. Finardi, J., Nascimento, J.O. and Homem de Melo, F.D. (eds.). Associacao Brasileira dos Produtores de Ferro-Ligas-Abrafe, Sao Paulo pp. 321–330.
- INNVÆR, R. and OLSEN, L. 1980. Calculation of thermal stresses in Søderberg electrodes. *Proceedings of the 9th International Congress of the UIE*, Cannes, France, 20–24 October 1980. pp. 2–11.
- INNVÆR, R., OLSEN, L., and VATLAND, A. 1984. Operational parameters for Søderberg electrodes from calculations, measurements, and plant experience. *Mintek 50. Proceedings of the International Conference on Mineral Science and Technology*, Johannesburg, South Africa, 26–30 March 1984. pp. 787–794.
- JONSSON, M.T. and INGASON, H.T. 1998. A three dimensional simulation model for a Søderberg electrode. *Infacon VIII, Proceedings of the Eighth International Ferroalloys Congress*, Beijing, China, 7–10 June 1998. pp. 383–388.
- KENNEDY, M.W. 2012. Electric slag furnace dimensioning. *Proceedings of the International Smelting Technology Symposium*, Orlando, FL, 11–15 March 2012. pp. 279–290.
- KROKSTAD, M.A. 2014. Elektrisk resistivitet i industrielle SiC-lag. MSc thesis, Norwegian University of Science and Technology, Trondheim, Norway.
- LARSEN, B., FELDBORG, H., and HALVORSEN, S.A. 2013. Minimizing thermal stress during shutdown of Søderberg electrodes. *Infacon XIII, Proceedings of the Thirteenth International Ferroalloys Congress*, Almaty, Kazakhstan, 9–12 June 2013, pp. 453–466.
- LARSEN, H.L. 2006. Current distribution in the electrodes of industrial three-phase electric smelting furnaces. *Proceedings of the 2006 Nordic COMSOL Conference*, Copenhagen, Denmark, 20 November 2006.
- LUPI, S. 2017. *Fundamentals of Electroheat*. Springer International, Switzerland.
- McDOUGALL, I. 2007. Finite element modelling of electric current in AC submerged arc furnaces. *Infacon XI. Proceedings of the Eleventh International Ferroalloys Congress*, New Delhi, India, 18–21 February 2007. Das, R.K. and Sundaresan, T.S. (eds.). Indian Ferro Alloys Producers Association pp. 630–637.
- McDOUGALL, I., SMITH, C.F.R., OLMSTEAD, B., and GERICKE, W.A. 2004. A finite element model of a Søderberg electrode with an application in casing design. *Infacon X, Proceedings of the Tenth International Ferroalloys Congress*, Cape Town, South Africa, 1–4 February 2004. South African Institute of Mining and Metallurgy, Johannesburg pp. 575–584.
- MEYJES, R., VENTER, J., and VAN ROOYEN, U. 2010. Advanced modelling and baking of electrodes. *Infacon XII, Proceedings of the Twelfth International Ferroalloys Congress*, Helsinki, Finland, 6–9 June 2010. Vartiainen, A. (ed.). Outotec Oyj. pp. 779–788.
- RAMO, S., WHINNERY, J.R., and VAN DUZER, T. 1994. *Fields and Waves in Communication Electronics*. Wiley.
- RODRIGUEZ, A.A. and VALLI, A. 2010. *Eddy Current Approximation of Maxwell Equations*. Springer-Verlag Italia.
- TANGSTAD, M., KSIAZEK, M., and ANDERSEN, J. 2014. An industrial Si furnace excavation – results and observations. *Proceedings of Silicon for the Chemical and Solar Industry XII*, Trondheim, Norway, 23–26 June 2014.
- VALDERHAUG, A.M. 1992. Modelling and control of submerged-arc ferrosilicon furnaces. PhD thesis, Norwegian Institute of Technology.
- WESTLY, J. 1974. Resistance and heat distribution in a submerged-arc furnace. *Infacon I, Proceedings of the First International Congress on Ferro-alloys*, Johannesburg, South Africa, 22–26 April 1974. pp. 121–127.
- WESTLY, J. 1975. Critical parameters in design and operation of the submerged arc furnaces. *Proceedings of the 33rd Electric Furnace Conference*, Houston, TX, 9–12 December 1975. pp. 47–53. ◆

The SAIMM Journal all you need to know!

- ★ Less 15% discount to agents only
- ★ PRE-PAYMENT is required
- ★ The Journal is printed monthly
- ★ Surface mail postage included
- ★ ISSN 2225-6253

The SAIMM Journal gives you the edge!

- * with cutting-edge research
- * new knowledge on old subjects
- * in-depth analysis



SUBSCRIBE TO 12 ISSUES
January to December 2018
of the SAIMM Journal

R2157.10

LOCAL



US\$551.20

OVERSEAS

per annum per subscription

For more information please contact: **Tshepiso Letsogo**
The Journal Subscription Department

Tel: 27-11-834-1273/7 • e-mail: saimmreception@saimm.co.za or journal@saimm.co.za
Website: <http://www.saimm.co.za>

A serious, 'must read' that equips you for your industry—Subscribe today!



The use of satellite observations of fire radiative power to estimate the availabilities (activity patterns) of pyrometallurgical smelters

by J.P. Beukes*, P.G. Van Zyl*, M. Sofiev†, J. Soares‡, H. Liebenberg-Enslin§, N. Shackleton§, and A.-M. Sundström†

Synopsis

Pyrometallurgical smelters consume significant amounts of fossil fuels. Notwithstanding emission abatement technologies, these smelters emit various gaseous pollutants and fine particulate matter, which are important from an air quality perspective. Additionally, carbon dioxide (CO₂) and black carbon (BC), the two most important atmospheric climate forcing species, are also emitted. It is important to model the contribution, transport, and impact of pollutants emitted by pyrometallurgical smelters. In order to do this, atmospheric modellers require an accurate emission inventory, which indicates emissions (how much of what species by which processes), emission periods, stack/emission heights, and emission velocities (if emitted through stacks). However, in many countries atmospheric modellers do not have access to a proper emission inventory, or they are legally prohibited from obtaining such information. The current paper demonstrates how fire radiative power (FRP) observations by the Moderate Resolution Imaging Spectro-radiometer (MODIS) instruments on board the Aqua and Terra satellites can be used to estimate the availabilities of pyrometallurgical smelters. Such temporal activity patterns will assist modellers to re-create air quality scenarios for regions more accurately.

Keywords

MODIS, remote sensing, fire radiative power, large point sources, estimated availabilities, pyrometallurgical smelters.

Introduction

From an atmospheric science perspective, emission inventories (how much of what pollutant species are emitted, where and when) are poorly developed in many countries. South Africa, which is the largest industrialized economy in southern Africa, can be considered as an example. At present South African environmental legislation requires significant atmospheric emitters to supply emission data to the government, but this information is protected by some legal safeguards and this has thus far prevented a comprehensive peer-reviewed emission inventory from becoming available in the public domain. Applications can be made to the Air Pollution Control Officer to access some information on the atmospheric emission licences of the aforementioned emitters, but this process is lengthy and does not yield all the required information. Therefore, atmospheric modelling studies undertaken for this region have to a large extent depended on global emission inventory databases (e.g. Kuik *et al.*, 2015; Lourens *et al.*, 2016) that might

not contain sufficient detail. Also, it is almost impossible for atmospheric scientists to account for fluctuations in the temporal activity patterns (if a source emits or not) of large point sources so as to provide temporally resolved emission inventories.

In this paper we demonstrate how satellite-derived fire data can be used to locate and reflect the activity patterns of large point sources. Open biomass burning, both natural (e.g. lightning-induced fires) and anthropogenic (e.g. intentional or accidental grassland, savannah, or forest fires), has long been recognized as one of the most significant sources of atmospheric pollutant species such as carbon dioxide (CO₂), carbon monoxide (CO), particulate matter (PM), black carbon (BC), and precursors for secondary pollutants (e.g. Vakkari *et al.*, 2014; Chiloane *et al.*, 2017). This has led to a multitude of studies using satellite-derived fire and/or burned area detection data to improve fire emission estimates and explain pollutant observations (e.g. Mafusire *et al.*, 2016). However, comparatively little attention has been given to alternative uses of these satellite-derived fire data-sets.

Methods

Fire radiative power (FRP) observations

Fire radiative power (FRP) data for the period January 2001 to March 2016 was obtained from the active fire observations by the

* Chemical Resource Beneficiation, North-West University, Potchefstroom, South Africa.

† Finnish Meteorological Institute, Finland.

‡ Environment and Climate Change Canada, Canada.

§ Airshed Planning Professionals (Pty) Ltd, South Africa.

© The Southern African Institute of Mining and Metallurgy, 2018. ISSN 2225-6253. This paper was first presented at the INFACON XV: International Ferro-Alloys Congress, 25–28 February 2018, Century City Conference Centre and Hotel, Cape Town, South Africa

The use of satellite observations of fire radiative power

Moderate Resolution Imaging Spectro-radiometer (MODIS) instruments on board the Aqua and Terra satellites (Justice *et al.*, 2002; Kaufman, Kleidman, R.G., and King, 1998). FRP data is similar to the Advanced Fire Information System (AFIS) system (AFIS, 2018) (<https://southernafrica.afis.co.za/> [accessed 13 February 2018]). The FRP data-set indicates the location of savannah, grassland, and forest fires (Figure 1a) that were active at the date of detection, but could also indicate false positive 'fires' for point sources with significant thermal emissions, *e.g.* pyrometallurgical smelters where activities such as metal/slag tapping (Figure 1b) or off-gas flaring (Figure 1c) could result in substantial thermal emissions.

Case study industry and area of interest

In this paper ferrochrome (FeCr) smelters were considered as examples of significant point sources of atmospheric emissions. These smelters produce a relatively crude alloy consisting principally of chromium and iron, which is subsequently used mainly in the manufacturing of stainless steel (Basson and Daavittila, 2013). South Africa holds the largest chromium ore (chromite) reserves and is one of the largest FeCr producers (Basson and Daavittila, 2013). Most of the FeCr smelters in South Africa are located relatively close to the Bushveld Complex, a geological feature that holds the chromite reserves. The locations of these smelters in relation to the Bushveld Complex are indicated in Figure 2.

Detection of large point sources and determination of availability patterns

Although the locations of significant point-source emissions, such as FeCr smelters, are known in South Africa, this might not be the case everywhere. Therefore, the first demonstrated use of FRP data within the context of this paper was the confirmation of the location of FeCr smelters as false positive 'fires'. This was achieved by considering repetitive active fires (*i.e.* fires occurring regularly on more or less the same spot) observed during the non-fire season in the South African interior.

The second demonstrated use of FRP data was to estimate the temporal activity patterns (operational or not) of FeCr smelters, which is commonly referred to in the pyrometallurgical industry as plant/smelter availability. The availabilities of FeCr smelters are directly linked to international trends such as the demand for stainless steel and the unit price for chromium, regional aspects such as

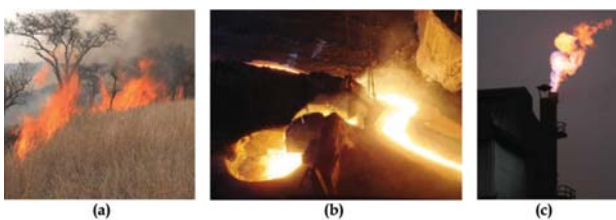


Figure 1—A typical grassland-savannah fire in southern Africa (a), the location of which will be stored in the fire radiative power (FRP) data-set if the fire was active at the time of the satellite overpass and the thermal emissions were strong enough to be detected. Slag/metal tapping (b), or off-gas flaring (c) could result in false positive 'fires' being detected and stored in the FRP data-set

electricity and carbonaceous reducing agent prices and availabilities, as well as smelter-specific issues such as planned/unplanned shutdowns to repair/rebuild production units (Kleynhans *et al.*, 2017). It is impossible for atmospheric scientists to know this information, since industry does not commonly make it known in the public domain. In this paper the frequency of repetitive active fires within a 2 km radius around FeCr smelters was used to estimate monthly smelter availabilities. The enlarged map in Figure 2 indicate in blue the 2 km radii circles around FeCr smelters in the western limb of the Bushveld Complex, which is the most developed area of this geological feature. Additionally, active fires are indicated with red dots.

The CALPUFF (Version 7) atmospheric dispersion modelling suite was used for the simulation of ambient air pollutant concentrations to indicate the effect plant availabilities could have on such concentrations. CALPUFF is a multi-layer, multi-species non-steady state puff dispersion model that can simulate the effects of time- and space-varying meteorological conditions on pollutant transport, transformation, and removal (www.lem.org.cn/u/cms/www/201307/05161203d9ap.pdf, accessed 15 June 2018)). CALPUFF is intended for use on scales from tens of metres to hundreds of kilometres from a source. CALMET and CALPUFF contain the simulation engines to calculate the three-dimensional atmospheric boundary-layer conditions, as well as the dispersion and removal mechanisms of pollutants released into this boundary layer. The CALPOST code was used to assist with the preparation of output data.

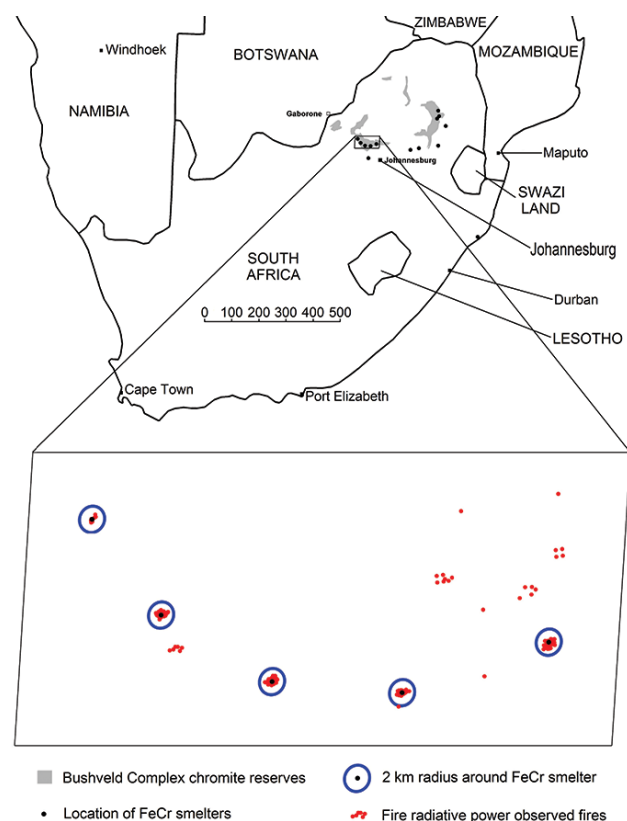


Figure 2—Map of southern Africa, with the locations of ferrochrome smelters and the Bushveld Complex (greyscale area) indicated. The enlarged area indicates the 2 km radii circles around smelters, with the 'fires' detected therein

The use of satellite observations of fire radiative power

Satellite retrieval of pollutant concentrations

In addition to dispersion modelling (indicated in the previous section), planetary boundary layer (PBL) sulphur dioxide (SO₂) concentrations were used to verify the effect that plant availabilities had on ambient pollutant concentrations. The satellite data used originated from the NASA Ozone Monitoring Instrument (OMI). Specifically, the SO₂ PBL product Level 3 data (Krotkov *et al.*, 2006, 2008) was used. The OMI SO₂ PBL product describes the SO₂ concentration integrated over the entire atmospheric column, while the term 'PBL' refers to the *a-priori* profile assumed in the retrieval. The resolution of retrieval for OMI PBL SO₂ was 0.25 × 0.25°. More details regarding such retrievals can be found in Sundström *et al.* (2015).

Results and discussion

The main fire season for the northern South African interior is typically during the dryer and colder period of June to September, while fires in the Western Cape Province typically occur from November to March (Chiloane *et al.*, 2017). Figures 3a and 3b indicate the active fires that were detected with MODIS FRP for the period June to September 2009 and November 2008 to March 2009, respectively. These results present the conventional type of use of MODIS FRP data. As is evident from Figure 3, there are clear temporal and spatial patterns in observed fires in southern Africa. It is beyond the scope of this paper to explore these aspects further; but it is interesting to note that although the number of active fires detected decreases significantly during the wetter period (November 2008 to March 2009, indicated in Figure 3b as an example), in the northern South African interior, where most of the industrial activities are located, some fires were still detected. Obviously some of this data (Figure 3b) represents real fires, but it was also found that repetitive fires indicated anthropogenic activities that have a strong enough thermal signal to be observed with the MODIS FRP satellite sensors. It was, for instance, found that the locations of large pyrometallurgical smelters were clearly indicated by such repetitive fires. As previously mentioned, this could be due to activities such as slag/metal tapping or off-gas flaring, which might emit thermal signals strong enough to be detected.

In an attempt to convert the frequency of the abovementioned repetitive fires into useful plant availability data, a simple algorithm was formulated. This entailed several steps. Firstly, the locations of interest were

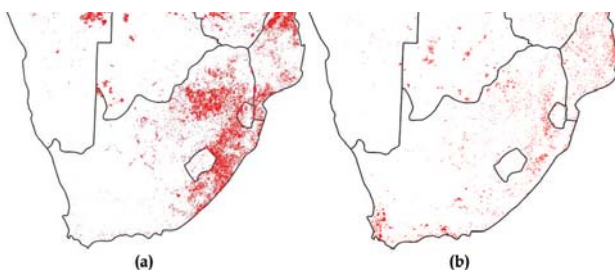


Figure 3—MODIS Fire Radiative Power (FRP) detected active fires during the burning season in the interior from June to September 2009 (a) and during the burning season in the Western Cape Province from November 2008 to March 2009 (b)

established. As previously stated, the case study industry considered in this paper is the FeCr industry. Circles with 2 km radii were drawn around each identified FeCr smelter. The repetitive fires occurring each month within the 2 km radius of each smelter were then counted. Then, 3-month moving averages were calculated for each smelter, based on the previous, current, and next month being considered (*e.g.* for February 2009 the moving average was calculated from active fires observed from January to March 2009). The 3-month moving averages were then divided by the 75th percentile for that specific smelter (*i.e.* the 75th highest 3-month moving average over the entire period considered). These fractions were then converted to percentages. The percentage values were then grouped into five smelter availability category ranges:

- (i) Percentages ≤ 10% were taken as representing zero smelter availabilities
- (ii) 10% > percentages ≤ 25% were taken as representing 5 to 25% smelter availabilities
- (iii) 25% > percentages ≤ 50% were taken as representing 25 to 50% smelter availabilities
- (iv) 50% > percentages ≤ 75% were taken as representing 50 to 75% smelter availabilities
- (v) Percentages > 75% were taken as representing 75 to 100% smelter availabilities.

The use of the abovementioned 3-monthly averages instead of individual monthly FRP-observed repetitive fire counts, the division by the 75th percentile instead of the largest monthly active fire count, and the grouping of the smelter availabilities into ranges instead of presenting discrete monthly availabilities were all measures that were implemented into the algorithm to account for the repetitive fire data being relatively erratic. The erratic nature of the data was not due to limitations of the observation sensors, but rather to the fact that the daily satellite overpasses will not capture all the high-radiation events (*e.g.* moving hot slag after tapping, hot slag/metal protruding beyond the cover of a slag bay directly after tapping). Observations of all (or almost all) such high-radiation events will be possible only with geostationary satellite observations, which are currently not available for southern Africa. There are thus significant limitations to the data and how accurate smelter availabilities can be calculated from it.

The calculated availabilities for several smelters over the period January 2001 to March 2015, using the abovementioned algorithm, are presented in Figure 4. These smelters were chosen since the authors knew that they were either commissioned and/or underwent expansion(s) during the period considered.

The availability data of the smelters indicated in Figure 4 was subsequently briefly reviewed, to assess the usefulness of the calculated availabilities. Since actual smelter availabilities are not available in the public domain, commissioning/expansion/stoppage data that is available in the 'grey' literature (*e.g.* company websites and/or non-accredited or non-peer-reviewed mining, metallurgical, and business-related magazines) was used for this assessment.

- For International Ferro Metals (IFM), the calculated availabilities indicate a brief period of operation in mid-2005, when the smelter was not yet commissioned.

The use of satellite observations of fire radiative power

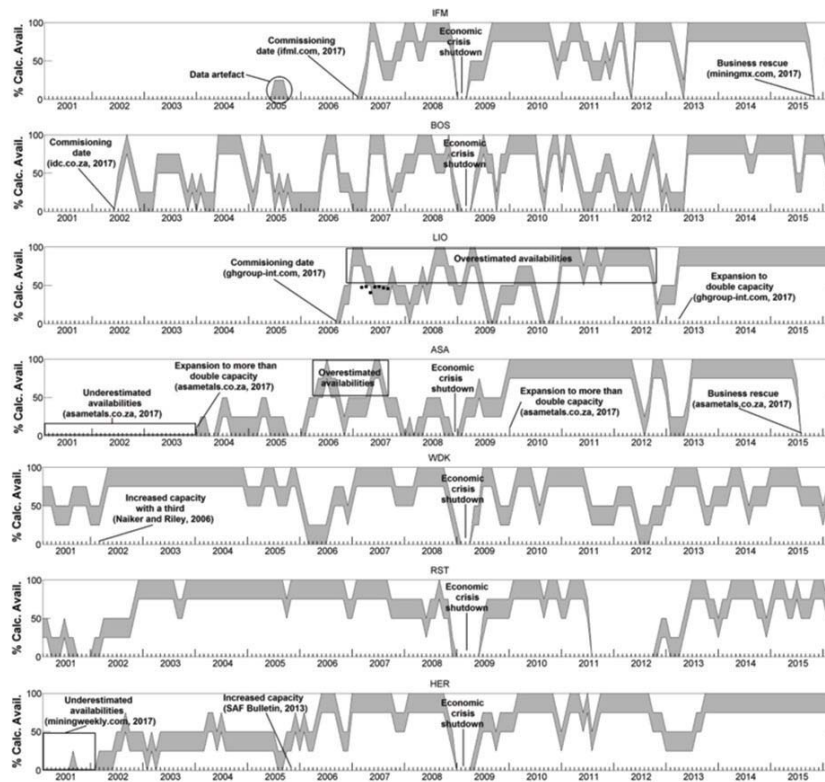


Figure 4—Calculated smelter availability ranges for International Ferro Metals (IFM), the Boshhoek smelter (BOS), Lion Ferrochrome (LIO), ASA Metals (ASA), Wonderkop smelter (WDK), Rustenburg smelter (RST), and Heric Ferrochrome (HER over the period January 2001 to March 2015

However, smelter operation over such a short period is clearly a data artefact, which should be ignored.

Thereafter the availability data correctly indicates commissioning of the smelter in January/February 2006 (International Ferro Metals, 2017) and also the stoppage due to business rescue in the third quarter of 2015 (<http://www.miningmx.com/news/ferrous-metals/13749-international-ferro-metals-goes-into-business-rescue/> [accessed 25 January 2017]).

- ▶ The calculated availabilities for the Boshhoek smelter (BOS) correctly indicate the commissioning in mid-2002 (Industrial Development Corporation, 2017).
- ▶ The commissioning date of Lion Ferrochrome (LIO) and the doubling of its production capacity are correctly indicated by the calculated availability data as the third quarter 2006 and first quarter 2013, respectively (GH Group, 2017). However, considering that the algorithm calculates all availabilities in terms of the largest production capacity, it is clear that the availabilities during 2006 to mid-2012 are overestimated at times.
- ▶ For ASA Metals (ASA) the calculated availability data does not reflect the operation of the smelter prior to 2004. This might be due to the fact this this smelter was one of the smaller smelters at the time, and its radiative power signal was not detected. Also, the physical design of the smelter at the time might have prevented detection of the signal (*e.g.* slag bays that totally shelter tapped slag/metal and open/semi-closed furnaces that do not combust CO off-gas in flares). However, after the expansion at the end of 2003 and beginning of 2004 (ASA Metals, 2017), the radiative fire data indicated the operation of the smelter in the

correct availability range. Limited overestimated availabilities, considering the maximum production capacity during the evaluated period, are indicated during short periods in 2006 and 2007. The expansion at the beginning of 2010

(<http://www.asametals.co.za/history.html> [accessed 1 February 2017]) and the stoppage due to business rescue in mid-2015 (ASA Metals, 2017) are correctly indicated.

- ▶ The expansion of the Wonderkop smelter (WDK) is correctly indicated by the calculated availability data in the first quarter of 2002 (Naiker and Riley, 2006).
- ▶ For Heric Ferrochrome (HER) the availability data prior to the first quarter of 2002 is underestimated, again maybe since it was a smaller smelter at the time and/or due to smelter design preventing radiative power detection. However, the expansions in the first quarter of 2002 and the third quarter of 2005 are correctly indicated (Mining Weekly, 2005).

Apart from the availabilities of the abovementioned smelters, the calculated availabilities of the Rustenburg smelter (RST) are also indicated in Figure 4. This was specifically done since RST, IFM, BOS, WDK, and HER are all located within a relatively small area in the western limb of the Bushveld Complex (see Figure 2 for spatial perspective). From the availability data presented in Figure 4 it is very interesting to note that all the aforementioned smelters were offline (zero plant availability) towards the end of 2008/beginning of 2009 as a result of the 2008 financial crisis. It is relatively well known that commodity prices and demand were very high prior to the 2008 global financial crisis, therefore it can be assumed that most of the South

The use of satellite observations of fire radiative power

African FeCr producers decided to shut the smelters down during this time rather than operate at a loss.

Atmospheric scientists and air quality managers are interested in temporally resolved emission inventories and how changes in emissions affect air quality (concentrations of pollutants). To estimate the effect that the simultaneous shutdowns of all the FeCr smelters in the western Bushveld Complex had on atmospheric pollutant levels, monthly average nitrogen oxides (NO_x), SO₂ and particulate matter smaller than 10 µm (PM₁₀) concentrations that would have originated from these smelters in February 2009 are indicated in Figures 5a, 5b, and 5c, respectively. February 2009 was specifically chosen since all the smelters were offline then. These modelled (using CALPUFF Version 7, as previously indicated) concentration patterns (Figure 5) should be considered as a sensitivity analysis rather than absolute atmospheric concentrations, since numerous assumptions were made during these simulations. These include assuming that all emission points for a specific smelter occurred at the same coordinates. Also, stack heights, emission velocities, emitted species, and amounts of emissions were classified according to the technologies utilized and were taken as similar at smelters using similar technologies. Notwithstanding these assumptions, the results clearly indicate that emissions that would have occurred during February 2009 if the smelters had been operational would have contributed to pollutant levels in the area.

To further investigate the usefulness of the calculated plant availabilities, satellite-retrieved PBL SO₂ concentrations for February 2009 (when the smelters were deemed to be offline, using the method proposed in this paper) were compared to those of February 2008 when the smelters were in full operation (Figures 6a and 6b, respectively). As is evident from the difference between the two months (*i.e.*

concentrations in February 2009 minus concentrations in February 2008), which is presented in Figure 6c, the PBL SO₂ concentrations in February 2009 were much lower than in February 2008. This supports the notion that many smelters in the western Bushveld Complex were offline (zero plant availability) in February 2009, as indeed calculated by the method proposed in this paper. SO₂ was specifically chosen as the pollutant of interest since many smelters in the western Bushveld Complex are platinum group metal (PGM) smelters (Jacobs, 2006), which emit relatively high SO₂ concentrations. Therefore, the differences observed in Figure 6c are not only due to the FeCr smelters, which were thus far considered as example pyrometallurgical point sources, but rather to a combined effect of all the sources in the western Bushveld Complex.

Conclusions

This paper indicates the potential for satellite-derived plant availabilities to be calculated for large anthropogenic emission point sources. Such availabilities will significantly assist atmospheric scientists and air quality managers to interpret measured atmospheric concentrations and to conduct more accurate atmospheric modelling studies. The comparatively crude algorithm presented here was able to indicate commissioning and/or expansion(s) of FeCr smelters relatively accurately. However, calculated plant availabilities could not be compared with real plant availabilities, due to a lack of such data for South Africa in the public domain. Also, false positive 'fires' from point sources, are identified by the MODIS FRP administrators and are currently removed from the data-set, which makes the aforementioned comparisons even more difficult.

Notwithstanding the limitations of the method presented in this paper, the calculated plant availability data proved that

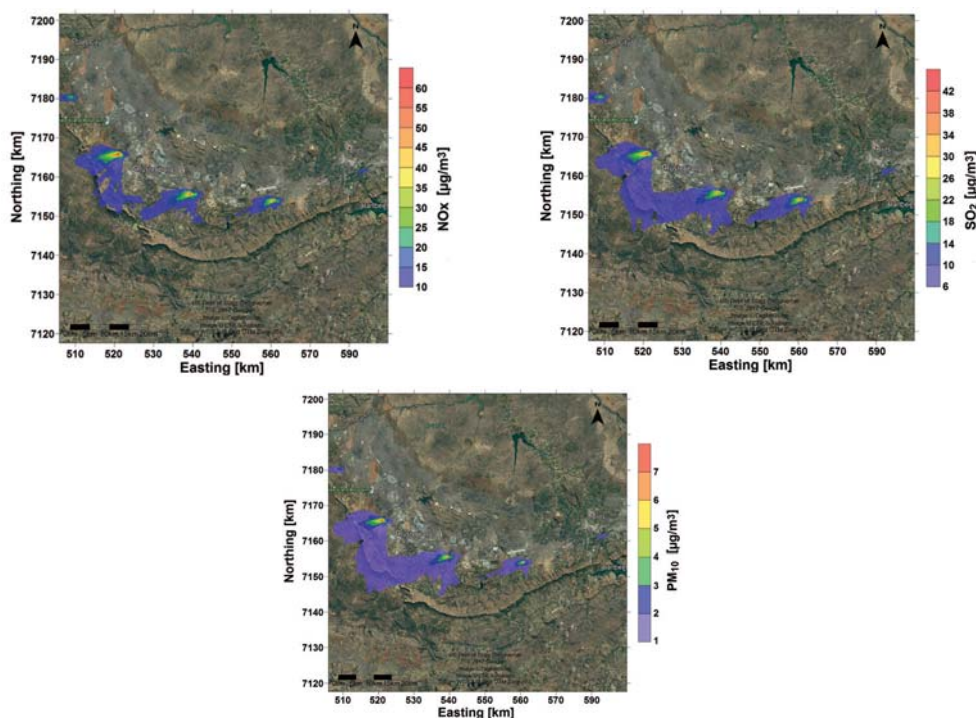


Figure 5—Modelled monthly average nitrogen oxides (NO_x) (a), sulphur dioxide (SO₂) (b), and particulate matter smaller than 10 µm (PM₁₀) (c) concentrations that would have originated from smelters in the western Bushveld Complex in February 2009 had these smelters been operational

The use of satellite observations of fire radiative power

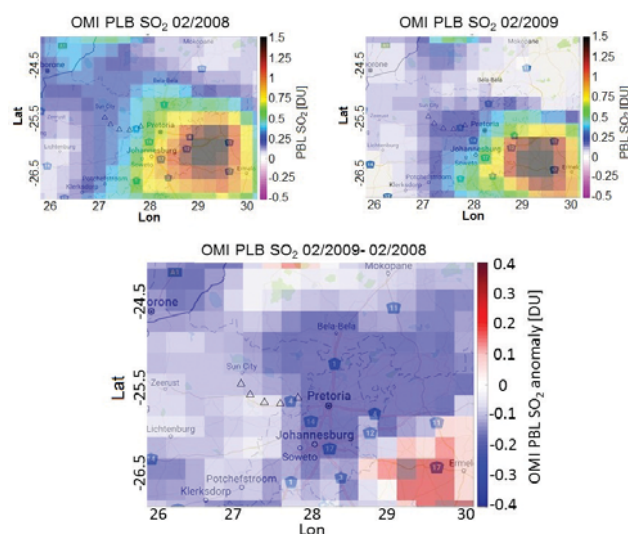


Figure 6—Planetary boundary layer (PBL) SO₂ concentrations derived from the NASA Ozone Monitoring Instrument (OMI) (Krotkov *et al.*, 2006, 2008) for (a) February 2009 and (b) February 2008, as well as the difference between February 2009 and February 2008 (c)

most of the smelters were not operational (zero plant availability) during or directly after the financial crisis in 2008/2009, at which time a significant decrease in several atmospheric pollutants was reported on a regional basis in South Africa (Conradie, 2018). This decrease was most likely due to many smelters stopping operation, which would have resulted in a significant decrease in atmospheric pollution, as proven with dispersion modelling and satellite retrievals.

Based on the positive results indicated here, satellite-derived plant availabilities for large point sources should receive more research attention. However, significant advances will be possible only if false positive ‘fires’ from point sources are captured in a separate data-set, instead of being removed from the current MODIS FRP data-set.

References

- AFIS (Advanced Fire Information System). 2018. <https://southernafrica.afis.co.za/> [accessed 13 February 2018].
- ASA METALS. 2017. <http://www.asametals.co.za/history.html> [accessed 2 February 2017].
- BASSON, J. and DAAVITILA, J. 2013. High carbon ferrochrome technology. *Handbook of Ferroalloys: Theory and Technology*. Gasik, M. (ed.). Elsevier, UK. <http://dx.doi.org/10.1016/B978-0-08-097753-9.00009-5>
- CHILOANE, K.E., BEUKES, J.P., VAN ZYL, P.G., MARITZ, P., VAKKARI, V., JOSIPOVIC, M., VENTER, A.D., JAARS, K., THITTA, P., KULMALA, M., WIEDENSOHLER, A., LIOUSSE, C., MKHATSWA, G.V., RAMANDH, A., and LAAKSO, L. 2017. Spatial, temporal and source contribution assessments of black carbon over the northern interior of South Africa. *Atmospheric Chemistry and Physics*, vol. 17. pp. 6177–6196. doi:10.5194/acp-17-6177-2017
- CONRADIE, E.H. 2018. Spatial and temporal deposition of selected biogeochemical important trace species in South Africa. PhD thesis, North-West University, Potchefstroom, South Africa.
- GH GROUP 2017. <http://www.ghgroup-int.com/gh-consulting-engineers/projects-profile/> [accessed 26 January 2017]
- INDUSTRIAL DEVELOPMENT CORPORATION. 2017. <http://www.idc.co.za/20years/timeline/idc-impact-for-20-years/2001-s> [accessed 26 January 2017].
- INTERNATIONAL FERRO METALS. 2017. <https://www.ifml.com/about-us/history-timeline.html> [accessed 25 January 2017].
- JACOBS, M. 2006. Process description and abbreviated history of Anglo Platinum’s Waterval Smelter, Southern African. *Proceedings of Pyrometallurgy 2006*. Jones, R.T. (ed.). Southern African Institute of Mining and Metallurgy, Johannesburg.
- JUSTICE, C., GIGLIO, L., KORONTZI, S., OWENS, J., MORISETTE, J., ROY, D., DESCLITRES, J., ALLEAUME, S., PETTICOLIN, F., and KAUFMAN, Y. 2002. The MODIS fire products. *Remote Sensing of Environment*, vol. 83. pp.244–262.
- KAUFMAN, Y.J., KLEIDMAN, R.G., and KING, M.D. 1998. Potential global fire monitoring from EOS-MODIS. *Journal of Geophysical Research: Atmospheres*, vol. 103, D24. pp. 32215–32238.
- KLEYNHANS, E.L.J., BEUKES, J.P., VAN ZYL, P.G., and FICK, J.I.J. 2017. Techno-economic feasibility of a pre-oxidation process to enhance prereluction of chromite. *Journal of the Southern African Institute of Mining and Metallurgy*, vol.117. pp.457–468. doi:10.17159/2411-9717/2017/v117n5a8
- KROTOKOV, N., CARN, S., KRUEGER A., BHARTIA, P., and YANG, K. 2006. Band residual difference algorithm for retrieval of SO₂ from the Aura Ozone Monitoring Instrument (OMI). *IEEE Transactions on Geoscience and Remote Sensing*, vol. 44. pp.1259–1266.
- KROTOKOV, N., McCLURE, B., DICKERSON, R., CARN, S., LI, C., BHARTIA, P., YANG, K., KRUEGER, A., LI, Z., LEVELT, P., CHEN, H., WANG, P., and LU, D. 2008. Validation of SO₂ retrievals from the Ozone Monitoring Instrument over NE China. *Journal of Geophysical Research*, vol. 113, D16S40. doi:10.1029/2007JD008818
- KUIK, F., LAUER, A., BEUKES, J.P., VAN ZYL, P.G., JOSIPOVIC, M., VAKKARI, V., LAAKSO, L., and FEIG, G.T. 2015. The anthropogenic contribution to atmospheric black carbon concentrations in southern Africa: a WRF-Chem modeling study. *Atmospheric Chemistry and Physics*, vol. 15. pp. 8809–8830, doi:10.5194/acp-15-8809-2015
- LEM. 2017. www.lem.org.cn/u/cms/www/201307/05161203d9ap.pdf [accessed 31 October 2017].
- LOURENS, A.S.M., BUTLER, T.M., BEUKES, J.P., VAN ZYL, P.G., FOURIE, G.D., and LAWRENCE, M.G. 2016. Investigating atmospheric photochemistry in the Johannesburg-Pretoria megacity using a box model. *South African Journal of Science*, vol. 112, no. 1/2. Article no. 2015-0169. 11 pp. doi:10.17159/sajs.2016/2015-0169
- MAFUSIRE, G., ANNIGARN, H.J., VAKKARI, V., BEUKES, J.P., JOSIPOVIC, M., VAN ZYL, P.G., and LAAKSO, L. 2016. Submicrometer aerosols and excess CO as tracers for biomass burning air mass transport over southern Africa. *Journal of Geophysical Research: Atmospheres*, vol. 121. pp. 10262–10282. doi:10.1002/2015JD023965
- MINING WEEKLY. 2005. <http://www.miningweekly.com/article/hernic-strides-to-longterm-profitability-2005-01-28> [accessed 2 February 2017].
- Naiker, O. and Riley, T. 2006. Xstrata alloys in the profile. *Proceedings of Pyrometallurgy 2006*. Jones, R.T. (ed.). Southern African Institute of Mining and Metallurgy, Johannesburg. pp. 297–306.
- SUNDSTRÖM, A.-M., NIKANDROVA, A., ATLSKINA, K., NIEMINEN, T., VAKKARI, V., LAAKSO, L., BEUKES, J.P., AROLA, A., VAN ZYL, P.G., JOSIPOVIC, M., VENTER, A.D., JAARS, K., PIENAAR, J.J., PIKETH, S., WIEDENSOHLER, A., CHILOANE, E.K., DE LEEUW, G., and KULMALA, M. 2015. Characterization of satellite-based proxies for estimating nucleation mode particles over South Africa. *Atmospheric Chemistry and Physics*, vol. 15. pp. 4983–4996. doi:10.5194/acp-15-4983-2015
- VAKKARI, V., KERMINEN, V.-M., BEUKES, J.P., THITTA, P., VAN ZYL, P.G., JOSIPOVIC, M., VENTER, A.D., JAARS, K., WORSNOP, D.R., KULMALA, M., and LAAKSO, L. 2014. Rapid changes in biomass burning aerosols by atmospheric oxidation. *Geophysical Research Letters*, vol. 41. pp. 2644–2651. doi:10.1002/2014GL059396



Impact of air granulation on the ferrochrome value chain in metallurgical smelter complexes

by F. Hannemann, M. Bradfield, M. Mahdi, L.L.C. So, and D. Metcalfe

Synopsis

South African ferrochrome producers typically operate single tap-hole furnaces with alloy and slag separation occurring post-taphole by means of a skimmer block. Both streams are then cast directly onto a prepared surface, or in some cases a layer-casting process is employed using hot metal ladles. These processes all require significant cooling time followed by extensive *in situ* crushing operations, leading to a high burden and cost in terms of time and on-site material handling. Moreover, the slag is then further crushed and screened in a chrome recovery plant to liberate any entrained alloy, and subsequently discarded as waste.

Air granulation has achieved commercial success in other sectors and typical South African ferrochrome operations can also benefit. Air granulation promises lower production costs by elimination of casting, cooling, break-up, and crushing activities; improved alloy liberation by elimination of middlings; and improved safety due to faster cooling without water sprays. There is also a market for subsequent use of air-granulated ferrochrome slag as a valuable product, due to its potential improved physical properties over slow cooled variants.

Air granulation is being tested to evaluate its effect on the ferrochrome value chain within a typical South African metallurgical complex. Here we report the results of this first-of-its-kind work, and explore strategies for successful integration.

Keywords

slag handling, air granulation, dry granulation, energy recovery, granulation, ferroalloys, ferrochrome.

Introduction

Slag handling currently represents a significant safety, environmental, operational, and financial concern for ferroalloy production. Most smelters produce a slag-to-alloy mass ratio of 1.1 to 1.3, therefore, slag handling and processing represents a significant part of typical operations. Slag handling differs by site based on environmental legislation, available space, and site location. The two most common slag handling processes are (1) air cooling and dry handling, which is by far the most common process in South African ferroalloy production, and (2) wet granulation in a high-pressure water stream and wet handling.

Slow cooling and dry handling

In the majority of South African ferroalloy furnaces, metal and slag exit the same tap-hole. Two methods of separating metal and slag have historically been used, both relying on density differences: (1) transportation of

slag using ladles or slag pots, and (2) a carbon block 'skimmer tapping arrangement' method, which is generally more labour-intensive but cheaper in terms of reduced equipment operating costs since ladles and hot metal cranes are not required. However, skimmer tapping can result in slag contamination of the metal. In both cases, slag is ultimately dumped or tapped onto the ground for initial slow cooling by natural air convection. Sometimes water sprays are also used to accelerate cooling; however, full solidification often requires several hours. Front end loaders or excavators are used to break up and extract the hot slag for transport to an open area before crushing. It typically takes several more days of cooling before the slag can be safely loaded into a crusher. Typically, crushing is completed by jaw crushing followed by cone crushing, after which the material is sent for density separation with pneumatic jigs and spirals

Dumping or tapping of liquid slag on the ground and subsequent slow cooling leads to various operational challenges. Firstly, the break-up and extraction by front end loaders or excavators is dangerous, because the initial cooling time allowed is often not enough for the slag to fully solidify, due to tapping frequency and tapping layout. Mobile equipment often handles the slag after only 2 to 3 hours because of the need for rapid turnaround in the tapping area, which means partially molten slag is handled. This poses dangers to both personnel and equipment, despite the use of specially modified mobile equipment for 'hot' environments, with replacement or maintenance costs being much

* Hatch Ltd, South Africa.

© The Southern African Institute of Mining and Metallurgy, 2018. ISSN 2225-6253. This paper was first presented at the INFACON XV: International Ferro-Alloys Congress, 25-28 February 2018, Century City Conference Centre and Hotel, Cape Town, South Africa



Impact of air granulation on the ferrochrome value chain in metallurgical smelter complexes

higher than for conventional machines. Secondly, break-up and extraction of slag is time-consuming, and generates excessive amounts of dust. Spraying water into the slag pit is a common solution to accelerate cooling and reduce dust, but the potential for molten material/water explosions remains ever-present, and pooling of water can delay further tapping operations. Moreover, the water that is used is typically lost and increases plant water demand. Lastly, transportation of slow-cooled slag from the pit to downstream crushers and metal separators poses additional safety and operational risks. Transportation of semi-molten slag by mobile machinery requires dedicated roads, specialized equipment, and training. It also increases the area in which special precautions need to be taken to avoid contact between molten material and water. The repeated loading and transporting combined with crushing steps results in multiple dust sources and increased diesel consumption by mobile machinery.

Water granulation

Although not nearly as common in South Africa as dry slag handling, water granulation is used in a significant part of the industry globally. There are two major types of water granulation system: (1) at the end of the launder attached directly to the furnace, or (2) at a dedicated facility designed to accept slag pots or ladles. For safe and successful water granulation, it is critical to maintain the temperature, flow, and pressure of water in accordance with the temperature and flow of the molten material. The high-pressure water stream impacts the molten slag stream, breaking it apart to form small granules approximately 2 mm in diameter. The slag is rapidly solidified in the initial water blast and then cools further in a settling tank. Various options exist for slag dewatering and subsequent transfer to either a stockpile or a metal recovery plant.

There are significant operational, environmental, and safety challenges related to water granulation. Firstly, typical water granulation requires about 10 t of water per ton of slag granulated, out of which roughly 1 t of water is lost by evaporation. This has both environmental and financial implications, and in some areas makes the technology infeasible due to limitations on water consumption. The energy costs associated with pumping and cooling large volumes of water increase the operating cost of the process. Precautions are also required for the overall treatment and de-sludging of the water circuit to remove the build-up of deleterious metals and potentially harmful/toxic dissolved species. Further, the placement of the water granulation facility within the molten material zone of a furnace is hazardous, and requires special procedures for mitigating risks. If the facility is located directly in front of the furnace, control of molten material flowing through the tap-hole and into the water stream is critical. Therefore, continuous monitoring and maintenance of the tap-hole itself is extremely important.

Dry granulation

Both slow cooling and water granulation pose problems with safety, dust emission, energy consumption, environmental footprint, and cost – and there is value in implementing a new technology which addresses these problems. Dry slag granulation has been developed and commercialized over the

past two decades with a focus on addressing the downfalls of traditional slag-handling methods. The three most common dry slag granulation categories are:

1. *Mechanical granulation*—Molten slag is broken up, dispersed, and quenched by mechanical means, such as rotating drums, blades (Bergquist, 1912; Metz, Schockmel, and Mersch, 1982; Orlander, Cotsworth, and MacKenzie, 1984; MacKenzie and Horvat, 1999, or shot material (Zhang *et al.*, 2013; Fujii *et al.*, 1982).
2. *Centrifugal granulation*—Molten slag is ejected radially outward by centrifugal force, during which it is broken up into small droplets, dispersed, and quenched into solidified granules. Examples include spinning disc and cups (Pickering *et al.*, 1985; Maruoka *et al.*, 2004; McDonald, 2013; Mizuoshi and Akiyama, 2003; Legille and Metz, 1979).
3. *Air granulation*—Air impinges on a molten slag flow, during which the slag is broken up into droplets, dispersed, and quenched into solidified granules. Compared to mechanical and centrifugal granulation, air granulation involves limited slag-to-machine contact, thus reducing the potential for equipment damage and failure, and the associated safety risks.

Air granulation technology

State of the technology

Hatch has successfully commercialized air granulation technology, which is currently implemented for slag handling at both ferrous (electric arc furnace, basic oxygen furnace, ladle furnace metallurgy) and non-ferrous (zinc and silicomanganese producers). In addition, a full-scale air granulation unit was commissioned in March 2018 for granulation of converter slag at a platinum group metals (PGM) facility in South Africa, serving as the first of its kind globally. Slag heat recovery is also possible and has been implemented at two commercial sites.

The major advantages of this technology include improved safety in slag handling (due to limited exposure of equipment and operators to hot molten slag, elimination of water and steam explosions), potential for slag heat recovery (via hot air for direct use or steam generation), production of higher value slag products with tunable properties (for example for use in abrasives, cement, or as aggregate), and reduction in the costs of slag handling (due to lower temperatures, lower maintenance requirements, and increased production uptime).

A schematic of air granulation technology is provided in Figure 1. Molten slag discharged from the furnace is conveyed to a slag feeding chute located in front of granulation chamber, either via slag launders or by slag pots/ladles. An air jet granulates, quenches, and disperses the slag into the granulation chamber, as shown in Figure 2. The air jet to slag mass ratio is in the range of 0.5 to 3, and the air jet is at relatively low pressures of less than 20 kPa. Inside the chamber, the granulation blast air passes co-currently to the hot granules to cool the particles and to obtain a hot gas stream. The cooled and solidified granules, shown in Figure 3, can be continuously conveyed out of the chamber to be packaged or periodically collected (for non-

Impact of air granulation on the ferrochrome value chain in metallurgical smelter complexes

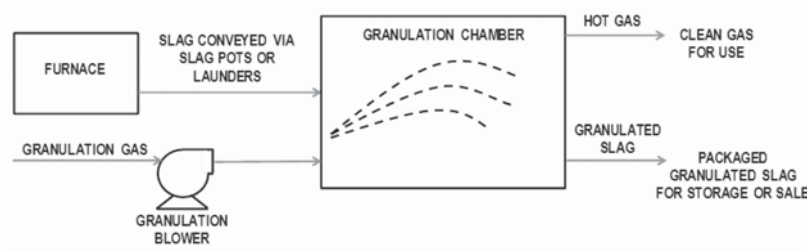


Figure 1 – Schematic process flow diagram of air granulation technology



Figure 2—A current commercial application of air granulation technology

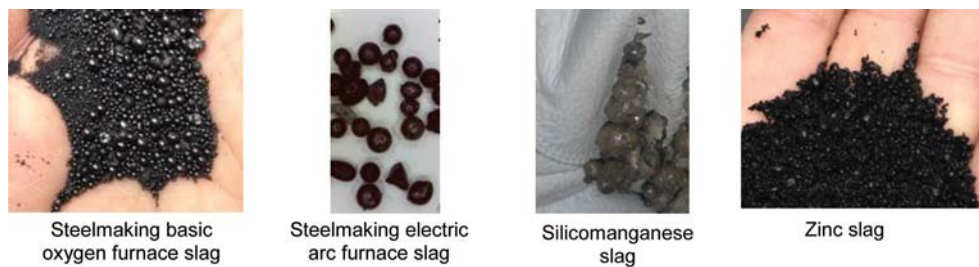


Figure 3 – Air-granulated slags from commercial operations

continuous tapping operations) for classification by size, for storage, and/or for sale. The recovered hot exhaust gas is directed to equipment that uses this heat and/or an off-gas handling system.

Air granulation technology for ferroalloy production

Potential benefits of air granulation technology for ferroalloy producers

There are several motivations for exploring the use of air granulation technology for ferroalloy producers.

Lower operating cost

Slag treatment and handling constitutes an unavoidable but necessary cost in the production of ferro-alloys. The removal, treatment, and disposal of slag are considered a direct cost on the bottom line, with no expectation of revenue generation. Industries other than ferroalloys have successfully created a market into which all the slag produced is sold as a value-

added product. This potential exists in the ferroalloy industry too, with crushed slag products already being used in downstream applications such as brickmaking. The creation of a viable revenue-generating slag product through air granulation would drastically enhance the viability and sustainability of a production complex by producing a second distinct revenue stream over and above alloy production.

Environmental footprint

Ferroalloy producers are now under increasing pressure not only to cease dumping of slag on-site, but also to remediate existing slag disposal sites and to provide a cleaner footprint. Global concerns for sustainability and resource consumption mean that ferroalloy producers need to reduce energy and water consumption, and utilize resources more efficiently while simultaneously decreasing their impact on the immediate environment. Water is becoming a more scarce commodity in South Africa and producers are being constrained in terms of access to water and enforcement of water-use licences.

Impact of air granulation on the ferrochrome value chain in metallurgical smelter complexes

This means using less water in water granulation or switching to dry cooling, reducing or eliminating dust created by crushing and loading, as well as reducing transportation of materials to minimize diesel consumption. Furthermore, slag storage continues to represent a significant environmental legacy for plants that cannot convert slag into a usable product. Air granulation addresses all of these challenges while having the lowest capital and operating cost.

Alloy liberation

For recovery of entrained alloy droplets, the majority of ferroalloy production sites employ a dedicated chrome recovery sub-plant which utilizes density separation to extract remaining alloy from the slag prior to the long-term storage or sale of the slag material. The recovered metal tends to have a higher slag content than the furnace metal, and so is usually sold at a slight discount or recycled internally to casting beds or to the furnaces. The size distribution of the slag is critical to the metal recovery and grade obtained by this process. The recovery peaks in the 1–10 mm size range for most ferroalloy producers, although most plants will have a series of crushing steps. The larger size fraction has lower slag contamination and particles below 1 mm will typically exhibit metal recovery rates 10% less than other size fractions. Crushed slow-cooled slag has a wide particle size distribution, resulting in variable performance in the metal recovery plant as well, as throughput limitations depend on the design of the plant. Although water granulation provides a narrower size distribution, limitations are imposed by the temperature and flow rates of both slag and water as well as slag composition. Air granulation allows for improved tuning of particle size distribution, which could benefit alloy liberation and metal recovery in existing jigging processes

Air granulation also presents an additional potential benefit to the metal recovery circuit. In the granulation process, metal-rich slag particles may be separated from metal-poor slag particles (due to density differences, metal-rich slag particles have a shorter flight path and land closer to the granulating air stream than metal-poor slag particles). The metal-rich slag particles can then be fed to the metal recovery circuit, thereby reducing the total tonnage of material processed by the metal recovery plant.

Heat recovery

The molten slag discharged from a metallurgical furnace constitutes a tremendous energy stream and, in some cases,

can contain up to 80% of the total energy input to the process (Rodd *et al.*, 2010). This energy represents a significant cost which is currently not recovered. In ground cooling, this energy is passively dissipated to the environment and is not reclaimed. In water granulation, energy recovery from hot water has been attempted on a pilot scale using several different technologies (Kotaro, Masahiko, and Tomoyuki, 1979; Kobe, Kakogawa, and Toyada, 1978; Kakogawa, 1982; Hooykas, 1979), but none of these have been commercialized due to the associated high costs and low quality of the heat source. Air granulation with slag heat recovery, on the other hand, has been found commercially viable in several facilities.

In discussions with producers, many saw the technological fit of air granulation within the ferrochrome sector. However, the lack of precedence in the ferroalloy industry and the lack of experimental data meant key questions were unanswered. These questions included:

- (1) Is air granulation of ferrochrome slag technically feasible?
- (2) Is the particle size distribution of air-granulated ferrochrome slag suitable and beneficial for metal recovery and/or alloy liberation?
- (3) Are the physical and chemical properties of air-granulated ferrochrome slag suitable for its use in the desired market? More specifically, would air granulation stabilize the leachability of hexavalent chromium?

Testing of air granulation technology on ferrochrome slag was undertaken to answer such questions.

On-site air granulation trials of ferrochrome slag

To test the concept of air granulation of ferrochrome slags with minimal risk and cost, a laboratory-scale air granulation system was developed. This system consists of small-scale equipment that mimics the key design principles of the full-scale air granulation system, yet can be easily transported to site for testing. The system can granulate approximately 1 kg of slag per minute. Images of this portable system are shown in Figure 4. For this small system, a tapping operator uses sampling spoons to obtain slag samples directly from the settling furnace launder during normal operation, and then feeds the sample directly in front of an air nozzle blowing into a chamber. Production slags can be tested directly *in situ* to produce experimental samples on site under actual operating conditions.



Figure 4—Laboratory-scale air granulation system used for on-site granulation of ferrochrome slag

Impact of air granulation on the ferrochrome value chain in metallurgical smelter complexes

Preliminary results

Testing with laboratory-scale air granulation equipment was completed over a one-week period at a South African ferrochrome producer in 2017. The equipment comprised graphite sampling spoons, a blower, a nozzle, and a granulation chamber that was located alongside the tap-hole launder, near the tap-hole. Slag was sampled from the flowing slag stream immediately upstream of the skimmer block. Proximity to the launder was important to ensure that the small volumes of molten slag samples remained hot between sampling and pouring into the air stream.

Technical feasibility

Air granulation of ferrochrome slag is technically feasible despite the spoon-sampled slag cooling quickly – a limitation only of the laboratory-scale apparatus due to the low volume of the sample spoon. The quick cooling and limited superheat meant the slag had greater viscosity than material in other air granulation trials, which led to substantial volumes of solidified slag either remaining in the sampling spoon or falling and accumulating beneath the air stream. Furthermore, a controlled flow of molten slag into the air stream was not achieved as large chunks of material caused flow surges, which means that quantification of key process parameters will require further testing. However, despite these challenges, preliminary observations indicate that the scaled-down process successfully granulated the molten slag into small particles, which at the full scale will be much simpler to handle and process for metal recovery. No smoke or dust was observed to emanate.

Morphology and particle size distribution of air granulated slag

Figure 5 shows images of the particles produced from the laboratory-scale air granulation trials. The particles ranged in size from approximately 1 mm to 50 mm. The particles were dense and could not be crushed by hand. Larger particles of > 10 mm resembled crushed stone or aggregate. The particles greater than 10 mm can be attributed to quick-cooling slag being poured from the sampling spoon where it had solidified before passing through the air stream, therefore not being granulated. These larger particles are not representative of actual yield from air granulation and are artefacts of the laboratory-scale set-up. Smaller particles of < 10 mm were

generally spherical. The shape and morphology of these particles were consistent with those from electric arc furnace and basic oxygen furnace steel slags, despite major differences in composition, temperature, and viscosity of the molten raw materials. The particle size distribution (PSD) of the < 10 mm particles was determined. The average PSD for five tests is shown in Figure 6. The particles had an average particle size of approximately 6 mm. The large variation in PSD between the five tests, shown by the error bars, is a result of the limited control of slag temperature, and therefore flow rate, when using the laboratory-scale set-up.

Composition

Granulated ferrochrome slag was collected from the chamber, as well as the non-granulated slag remaining in the spoon. This non-granulated slag was intended to be a baseline against which changes in composition resulting from air granulation could be determined, particularly relating to emissions and other forms of slag oxidation. Preliminary results indicate no compositional changes in the slag due to air granulation. This is in line with experience in steel and non-ferrous slag, wherein chemical compositional changes in slag resulting from air granulation are not observed.

Cr(VI)

To evaluate the chemical stability of the granulated slag, the leaching characteristics of the product, especially with regard to hexavalent chromium (Cr(VI)), will be investigated. A novel analytical technique is being developed to determine

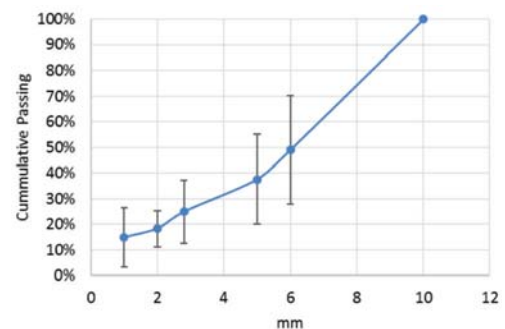


Figure 6—Average particle size distribution of granulated ferrochrome slag. Error bars show one standard deviation

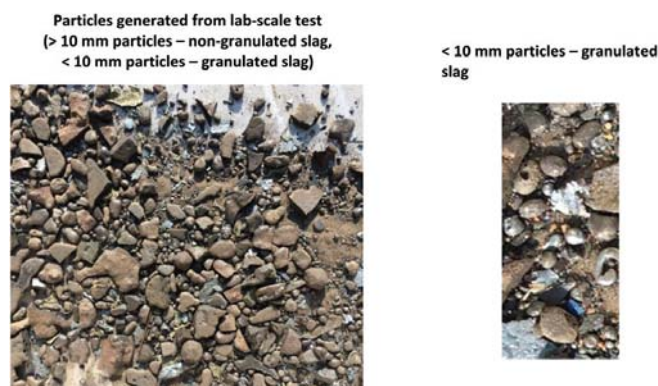


Figure 5—Solid ferrochrome slag generated in laboratory-scale air granulation trials

Impact of air granulation on the ferrochrome value chain in metallurgical smelter complexes

the Cr(VI) concentration in the granulated slag without causing oxidation of Cr(III) to Cr(VI) during sample preparation – which is a known concern in Cr(VI) analysis (Glastonbury, 2010). Oxidation of Cr(III) during sample preparation causes the true Cr(VI) content of the sample to be overestimated, which can lead to erroneous conclusions, potentially curtailing commercial applications of the tested material.

Future work

To address the limitations of slag superheat and poor flow control, a larger pilot-scale system is recommended as the next step in the development of air granulation for ferrochrome slag. Hatch has developed a larger scale, pilot version of the air granulation system which allows for a 300 kg sample to be fed to the granulation chamber, as shown in Figure 7. This system allows the contents of 1 t slag ladles to be processed, or can be retrofitted downstream of the skimmer block to process slag directly from the tap-hole launder. The latter is recommended to ensure that sufficient heat is retained in the slag prior to granulation testing, and to enable a pilot campaign that closely reflects the eventual full-scale implementation. The larger pilot-scale system also allows for larger quantities of granulated material to be collected and tested in the metal recovery plant and/or studied for marketability.

Conclusions

Air granulation technology offers an improved way of handling ferroalloy slag compared with slow cooling and water granulation. The advantages offered by air granulation include a lower operating cost, reduced environmental footprint (including reduced water consumption), potential to improve alloy liberation, and potential for slag heat recovery. It is believed that these advantages will justify investment in further development and future transfer of this technology to the ferroalloy industry. Air granulation technology has been fully commercialized in the steel sector, and adoption by the ferroalloy sector demands a diligent approach to thoroughly verify its technical and economic feasibility. Preliminary results from small-scale test work demonstrate that air granulation is technically feasible for ferrochrome slag processing. Detailed analysis of the granulated product is still

ongoing, with intentions for further testing at a larger pilot-scale and determination of commercial applications for granulated ferroalloy slag.

References

- BERGQUIST, J. 1912. Process of disintegrating molten slag. US patent 1047370. 17 December 1912.
- FUJII, H., TANAKA, K., NAKAMURA, M., OKUNO, R., HASHIZUME, S., KATAYAMA, H., and FUJITA, T. 1982. Apparatus for heat recovery from molten slag. US patent 4350326A. 21 September 1982.
- GLASTONBURY, R.I. 2010. Cr(VI) generation during sample preparation of solid samples –A chromite ore case study. *Water SA*, vol. 36, no. 1. pp. 105–110.
- HOOVAKS, C.W.J. 1979. A process and apparatus for recovering energy from molten slag. European patent 0023727 B1. 3 August 1979.
- KAKOGAWA, H.F. 1982. Apparatus for heat recovery from molten slag. US patent, 4350326. 21 September 1982.
- KOBE, R.O., KAKOGAWA, H.F., and TOYADA, K. 1978. Recovery of heat from molten slag from metallurgical processes. US patent 4111159 A. 5 September 1978.
- KOTARO, I., MASAHIKO, M., and TOMOYUKI, O. 1979. Method for recovering heat from molten slag and an apparatus therefor. US patent 4147332 A. 3 April 1979.
- LEGILLE, E. and METZ, P. 1979. Mechanical disintegration. US patent 4153440A. 8 May 1979.
- MACKENZIE, P.A. and HORVAT, D.T. 1999. Process and apparatus for making expanded slag. US patent 5944861. 31 August 1999.
- MARUOKA, N., MIZUUCHI, T., PURWANTO, H., and AKIYAMA, T. 2004. Feasibility study for recovering waste heat in the steel making industry using a chemical recuperator. *ISIJ International*, vol. 44, no. 2. pp. 257–262.
- MCDONALD, I. 2013. World Intellectual Property Organization patent 2013029935A1. 7 March 2013.
- METZ, P., SCHOCKMEL, R., and MERSCH, R. 1982. Method of making slag sand and slag wool. US patent 4352764. 5 October 1982. ARBED SA.
- MIZUOSHI, T. and AKIYAMA, T. 2003. Cold experiments of rotary vaned-disks and wheels for slag atomization. *ISIJ International*, vol. 43, no. 209. pp. 1469–1471.
- ORLANDER, M., COTSWORTH, R.P., and MACKENZIE, P. 1984. Apparatus for the pelletization of heat-liquifiable solid materials. US patent 4451221. 24 May 1984.
- PICKERING, S., HAY, N., ROYLANCE, T., and THOMAS, G. 1985. New process for dry granulation and heat recovery from molten blast furnace slag. *Ironmaking and Steelmaking*, vol. 12, no. 1. pp. 14–20.
- RODD, L., KOEHLER, T., WALKER, C., and VOERMANN, N. 2010. Economics of slag heat recovery from ferronickel slags. *Proceedings of the 49th Annual Conference of Metallurgists (COM2010)*, Vancouver. Canadian Institute of Mining, Metallurgy and Petroleum, Montreal. pp. 1–12.
- ZHANG, H., WANG, H., ZHU, X., QIU, Y.-J., LI, K., CHEN, R., and LIAO, Q. 2013. A review of waste heat recovery technologies towards molten slag in steel industry. *Applied Energy*, vol. 112. pp. 956–966. ◆



Figure 7 – Pilot-scale air granulation system



Basic parameters in the operation and design of submerged arc furnaces, with particular reference to production of high-silicon alloys

by T.E. Magnussen*

Synopsis

A review of the basic parameters in the operation of submerged arc furnaces is given. The importance of controlling the electrical operating parameters in accordance with the principles presented by Jens Westly in the 1970s is highlighted.

Basically, the specific energy consumption for production of high-silicon alloys depends on the silicon recovery and the furnace efficiency. Silicon recovery depends mainly on the raw material quality, but also on furnace design. The furnace efficiency depends on the furnace operating resistance and the loss resistance, which are again related to the furnace design.

A case from practical furnace operation is presented, showing how the furnace dimensioning and design affect the furnace efficiency and hence the specific energy consumption. Possibilities for further improvement of furnace efficiency and reduction of the loss resistance are discussed.

Keywords

submerged arc furnaces, high-silicon ferroalloys, electrical operating parameters, specific energy consumption, furnace efficiency factor, loss resistance.

Introduction

It is the author's impression that chemical reactions and equilibria have normally been the main focus in the evaluation and studies of process performance of high-silicon alloys production. Electrical operating parameters did not always receive the same degree of attention from metallurgists.

In the author's experience, it is very important to also pay attention to electrical parameters in furnace operation.

Operating resistance and the Westly factor

For a three-phase furnace, the operating resistance R in $m\Omega$ is defined as follows:

$$R = P / (3 \cdot I^2) \quad [1]$$

where P is the furnace power in kW, measured on the primary side of the furnace transformers, and I is the electrode current in kA.

The operating resistance is selected by the furnace operator within certain limits, determined by the furnace mix composition, to obtain a satisfactory electrode penetration and good tapping conditions.

The normal way of controlling the operating resistance is to operate the furnace on constant electrode current by adjusting the

electrode positions, and at the same time maintaining a constant furnace load.

The operating resistance depends on the required quality of the product, the raw material properties, the composition of the raw material charge mix, and optimum utilization of electrical energy.

For a given process and charge mix composition, it is a matter of experience to find the optimum operating resistance.

In the early days of the ferroalloy industry, the fundamental formula in furnace design was the Andrae formula, introducing the k -factor (Andrae, cited in Westly, 1974):

$$R \cdot \pi \cdot D = k \quad [2]$$

where R is the operating resistance in $m\Omega$, D is the electrode diameter in metres, and k the peripheric resistance (k -factor) in $m\Omega \cdot m$.

According to Andrae, the value of the k -factor varies with the process, the raw materials, and the specific load of the electrodes.

Later, adjustments were proposed to the Andrae formula by Kelly (Kelly, cited in Westly, 1974), Persson (Persson, cited in Westly, 1974), and others, suggesting how the value of the k -factor depended on the power density in the electrodes.

Jens Westly studied operating data from a large number of electric reduction furnaces, and published the result of his work on several occasions during the 1970s (Westly, 1974, 1975, 1979). These references are highly recommended.

Westly suggested the following correction of the Andrae formula:

$$k^2 \cdot i = \text{constant} \quad [3]$$

where k is the k -factor in $m\Omega \cdot m$, and i the electrode current density in A/cm^2 .

* *Vatvedt Technology AS, Norway.*

© *The Southern African Institute of Mining and Metallurgy, 2018. ISSN 2225-6253. This paper was first presented at the INFACON XV: International Ferro-Alloys Congress, 25-28 February 2018, Century City Conference Centre and Hotel, Cape Town, South Africa*

Basic parameters in the operation and design of submerged arc furnaces

By combining Equations [2] and [3], Westly (1974) deduced the following correlation:

$$I \propto (P)^{2/3} \tag{4}$$

where I is the electrode current in kA, and P the furnace power in MW.

Based on the above, Westly introduced a new factor, the Westly factor (C_3) which is defined as:

$$C_3 = I/(P)^{2/3} \tag{5}$$

For a given process and a given raw material mix composition, the value of the Westly factor (C_3) is basically constant and independent of the furnace load. Reference is made to the furnace load diagram given in Figure 1.

The Westly factor has been found to be extremely useful as a guideline for furnace operation and dimensioning, particularly in relation to upscaling of furnaces.

The principle of heat distribution

Westly also (1974) introduced the principle of heat distribution.

Equation [1] rearranged gives the formula for the furnace load P (kW):

$$P = 3 \cdot R \cdot I^2 \tag{6}$$

where R is the operating resistance in $m\Omega$ and I the electrode current in kA.

With reference to the above formula, furnace operators will normally tend to operate on the highest possible operating resistance in order to obtain the highest possible load on their furnace. However, there is a practical limit for the operating resistance that can be used, determined by the heat distribution factor C :

$$C = P_C/P = R/R_C \tag{7}$$

where P_C is the energy generation in the furnace charge, P is the total energy generation, R is the operating resistance, and R_C the resistance of the furnace charge.

C may take values between 0 and 1. As R_C is given by the raw material mix composition, C is controlled by the choice of the furnace operating resistance R .

If R is too high compared to R_C , the proportion of the total energy input consumed in the melting of raw materials will be too high, and too little will be available for reduction.

This phenomenon is well-known from production of high-silicon alloys. If a furnace is operated on too high an operating resistance compared to the resistance of the charge mix, too much of the energy input will be used for melting of raw materials compared to the energy available for reduction of silicon. This will result in an excess of slag in the furnace and insufficient reduction of silicon, as well as impurities such as aluminium and calcium. This situation may be interpreted as a problem with the carbon balance, whereas the real cause of the problem is that the operating resistance is too high compared to the resistance of the charge mix.

Typical signs are slag formation and low metal temperatures, causing tapping problems. Further, the electrical instruments will tend to show little response to raising or lowering of the electrodes, indicating that the current does not pass from the electrode tips, but from the sides of the electrodes, causing abnormal electrode wear.

To conclude, the operating resistance cannot be chosen at random, but in due consideration of the resistivity of the charge mix.

The significance of the furnace reactance

For a three-phase furnace, the furnace reactance X in $m\Omega$ is defined as follows:

$$X = Q/(3 \cdot I^2) \tag{8}$$

where Q is the reactive furnace power in kVar, measured on the primary side of the furnace transformers, excluding the load of capacitor banks, and I is the electrode current in kA.

Whereas the furnace load is depending on the operating resistance and the electrode current, it is independent of the furnace reactance.

The reactance must be taken into account when designing the transformers for a new furnace. The furnace reactance affects the required transformer capacity as well as the secondary voltage range for the transformers. It also affects the size of the capacitor banks for correction of the power factor on the electrical power supply grid.

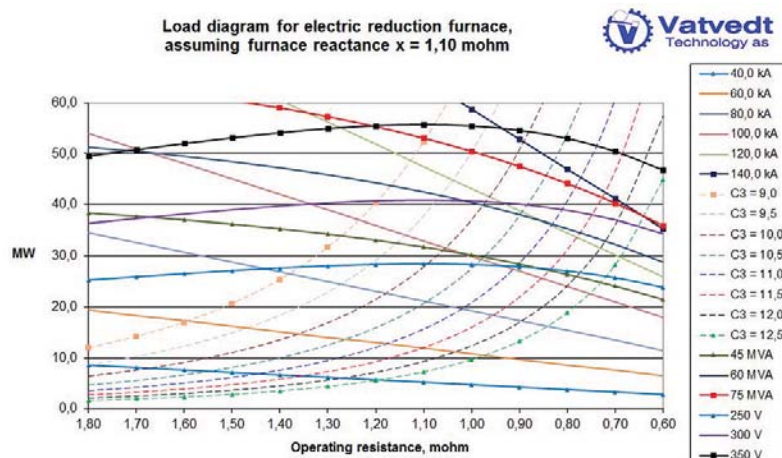


Figure 1—Load diagram for an electric reduction furnace

Basic parameters in the operation and design of submerged arc furnaces

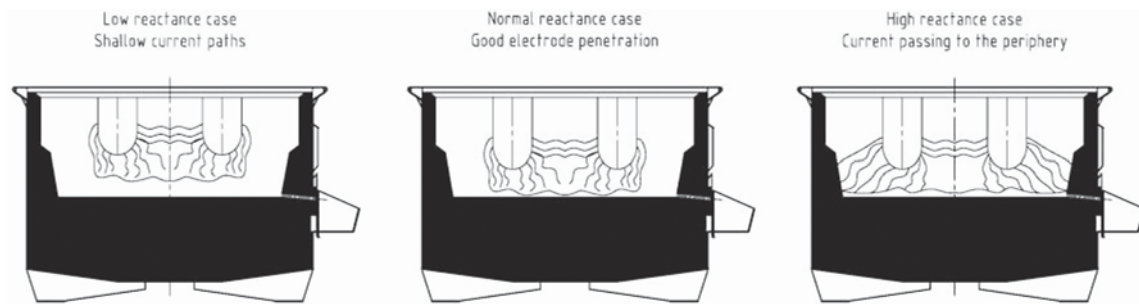


Figure 2—Typical locations of current paths for different furnace crater conditions

Somewhat simplified, we can say that the furnace reactance is proportional to the area surrounded by the current circuit.

The furnace reactance increases with increasing electrode spacing, and decreases with increasing electrode diameter. A high electrode holder position and low electrode tip to hearth position, with current paths located at a low level in the furnace crucible, will give a high furnace reactance, and *vice versa*.

Based on experience, it is worthwhile to register and study the value and the trends of the furnace reactance in daily operation, since it gives an indication of factors such as the electrode length and electrode penetration. In other words, it gives interesting information regarding the operating conditions of the furnace.

Figure 2 indicates the typical locations of the current paths for different furnace crater conditions.

Furnace power factor

A consequence of the Westly formula is that the operating resistance R decreases with increasing furnace size.

Referring to the expression for the furnace power factor:

$$\cos \Phi = R / (R^2 + X^2)^{1/2} = R / Z \quad [9]$$

where Z is the furnace impedance in $m\Omega$,

a natural consequence of increasing furnace size is that the furnace power factor decreases. The power factor of large furnaces today is normally less than 0.707. At the time, some people thought this may be a problem for the furnace operation; but normally, it is not.

However, with decreasing power factor, it is becoming more difficult to balance the power load and the charge mix consumption between the electrodes in the furnace. If the power factor is very low, towards 0.5 and lower, this balance becomes quite critical, since the electrode to hearth resistance is fairly close to the short circuit condition

Today, most power supply companies require installation of equipment for power factor compensation in order to avoid too low a power factor on the power grid. Capacitor banks are installed for this purpose. The most common, simple and sturdy arrangement is to install capacitor banks in shunt connection on the primary side of the furnace transformers. However, if the furnace power factor is very low, it is normally preferable to install the capacitor banks in series. In this case, the problems of unbalance of the load and charge mix consumption between the electrodes as described above can be avoided.

Electrical parameters for each electrode

The resistance and reactance values calculated as described above give the average values for the electrodes in a three-phase furnace, based on the active and reactive power measured on the primary side of the furnace transformers.

It is also interesting to establish electrical measurements for each electrode in order to monitor and control the conditions on each phase.

These measurements have to be based on a secondary voltage measurement between each phase and the furnace hearth. For this purpose, we measure the voltage between knife contacts on the electrode casing and an artificial zero point underneath the furnace.

Based on the secondary voltage and the secondary current measurement, it is possible to measure active power, reactive power, resistance, and reactance for each electrode.

The challenge with these measurements is the strong electromagnetic field surrounding the furnace, which causes induction in the cables for voltage measurement, thereby influencing the accuracy of the electrical data. Even though we try to reduce the influence of the induction by symmetrical arrangement of the cabling around the furnace and adjustable resistances in the measurement circuits, there will still be some inaccuracy in the voltage measurements and the electrical data deduced from them.

Factors affecting the specific power consumption for high-silicon alloys

It is well known that the specific power consumption (kWh/mt Si) depends on the silicon recovery.

Above all, the silicon recovery is dependent on the raw material quality and the charge mix composition. The use of reductants with high reactivity *versus* SiO gas will increase the silicon recovery. The use of reductants of smaller size will increase the available surface area of the reductants for exposure to SiO gas, and will therefore be beneficial for increasing the silicon recovery.

Furthermore, the silicon recovery is also affected by the furnace design.

The following features of our furnace design are implemented to improve the silicon recovery:

- Design of day bins and furnace bins to avoid segregation
- Rotating charging tubes
- Rotating furnace body.

Basic parameters in the operation and design of submerged arc furnaces

In particular, the use of rotating charging tubes has turned out to be very beneficial in order to improve the silicon recovery.

However, the specific power consumption is also dependent on the furnace efficiency factor.

The furnace efficiency factor indicates how efficiently the supplied electrical energy is being utilized in the furnace:

$$\eta = (P - P_L)/P = 1 - (P_L/P) \quad [10]$$

where

η is the furnace efficiency factor

P is the furnace power in MW

P_L is the power in MW lost by ohmic resistance in secondary conductors and electrodes, as well as by induction loss and other electrical losses.

The specific power consumption for production of high-silicon alloys can be expressed by the following formula:

$$(1/\eta) * ((K_1/\mu) + K_2) \quad [11]$$

where η is the furnace efficiency factor, μ is the silicon recovery ($\mu = 1$ corresponds to 100% silicon recovery), and K_1 and K_2 are constants.

With reference to the data given by Schei, Tuset, and Tveit (1998), the formula for the specific power consumption can be written as follows:

$$(1/\eta) * ((7837/\mu) + 768.7) \quad [12]$$

Figure 3 shows the specific power consumption as a function of the silicon recovery for different values of the furnace efficiency factor.

The specific power consumption decreases with increasing furnace efficiency and increasing silicon recovery. In order to reduce the specific power consumption, we need to affect these two factors.

The furnace efficiency factor can also be expressed by the following formula:

$$\eta = (R - R_L)/R = 1 - (R_L/R) \quad [13]$$

where R is the total resistance or operating resistance, as referred to above, and R_L is the loss of resistance in secondary conductors, electrodes, and by induction.

The furnace efficiency increases with increasing R and with decreasing R_L . Whereas R is basically selected by the

furnace operator as mentioned above, R_L is determined by the furnace design, physical dimensions, and electrical conditions in the furnace crucible.

The furnace operating resistance R depends on the charge mix composition and the raw material quality. The main factors that cause an increase in the operating resistance R are the following:

- Smaller sizing of reductants
- Increased proportion of coal in charge mix
- Use of wood chips.

The above measures should be used and are being used by furnace operators today to increase the furnace efficiency and hence reduce the specific energy consumption. These measures come in addition to the effect of using more reactive reductants in order to improve the silicon recovery as mentioned above.

The furnace loss resistance R_L depends on furnace design and dimensioning. The following factors contribute to decreasing loss resistance:

- Materials with high electrical conductivity in furnace components
- Optimized cross-sectional area of current conductors
- Nonmagnetic materials to reduce eddy currents.

We take all these factors into account as part of our furnace design, with the aim to achieve the lowest possible loss resistance.

In addition, the loss resistance can be influenced by the conditions in the smelting crater, as shown in the example below.

Examples from practical furnace operation

Equation [12] is very useful for analysing furnace performance, as demonstrated by the following example.

The author once had the opportunity to study two silicon metal furnaces in the same plant and of the same capacity, operating at about the same furnace load, using the same raw materials and charge mix composition.

The strange thing about these furnaces was that, in simplified terms, they had about the same silicon recovery, but not the same specific power consumption.

Table I lists the data for the two furnaces, A and B, for a given reference period. Using the above formulae, the furnace

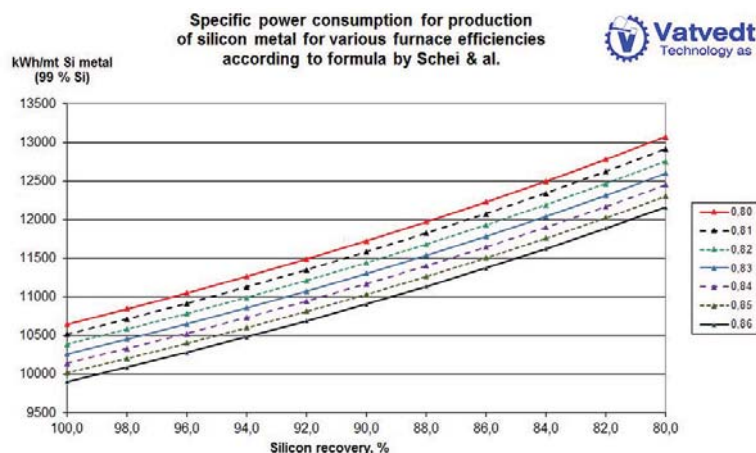


Figure 3—Specific power consumption for production of silicon metal

Basic parameters in the operation and design of submerged arc furnaces

Table I
Operating data for silicon metal furnaces, based on liquid metal production

Furnace	A	B
Electrode diameter, mm	1 143	1 205
Approximate electrode spacing centre to centre, m	2.80	2.74
Approximate inner furnace crucible diameter, m	6.60	6.60
Furnace load, MW	19.50	19.90
Operating resistance, mΩ	1.333	1.309
Westly factor (C ³)	9.64	9.70
Furnace reactance, mΩ	1.310	1.273
Specific power consumption, kWh/t	12 371	11 795
Silicon recovery, %	82.17	84.55
Furnace efficiency factor	0.826	0.844
Loss resistance, mΩ	0.232	0.205
Short circuit resistance, mΩ	0.313	0.278
Short circuit reactance, mΩ	1.477	1.202

efficiency factor η and the loss resistance R_L were calculated. In addition, a measurement of the short circuit resistance and the short circuit reactance was carried out by melting down the furnace and taking the electrical readings with the electrodes resting on the furnace hearth.

As shown in the table, the furnace efficiency factor is higher and the loss resistance lower for furnace B than for furnace A. In addition, the silicon recovery is somewhat higher.

It is thought that the reason for the higher furnace efficiency and lower loss resistance for furnace B compared to furnace A is the larger electrode diameter and smaller electrode spacing. It seems reasonable that the larger electrode diameter on furnace B is at least part of the reason for the difference in loss resistance.

Moreover, the electrodes had an inclination with the electrode tips pointing towards the periphery of the furnace crucible, probably caused by an inactive zone with a solid cone in the centre of the furnace. This phenomenon was more predominant on furnace A than on furnace B. Given this factor, there is reason to believe that part of the current in the furnace crucible was passing from the outside of the electrodes near the electrode tips, out to the carbon sidewall lining and along the periphery of the furnace crucible over to the neighbouring electrodes. The wear pattern of the electrodes also supported this theory, with higher wear on the electrode surface facing the carbon sidewall lining.

The short circuit measurements also support the above theory. The calculated short circuit resistance was about 13% higher on furnace A than on furnace B, and the calculated short circuit reactance was about 23% higher. Furthermore, this supports the above comments with respect to how the location of current paths in the furnace crater has an influence on the furnace reactance.

As a consequence of the above findings, the electrode spacing on furnace A was reduced, resulting in a substantial improvement in the furnace performance.

Table II lists the data for the furnace supplied by Vatvedt to ChEMK in Chelyabinsk, Russia in 2014, for the production of ferrosilicon. Compared to the data for the silicon metal furnaces above, the furnace efficiency is higher and the loss resistance is lower.

Table II
Operating data for furnace 57, ChEMK, based on liquid production basis 75% ferrosilicon

Electrode diameter, mm	1 200
Electrode spacing centre to centre, m	2.70
Inner crucible diameter, m	6.80
Furnace load, MW	18.04
Operating resistance, mΩ	1.244
Westly factor (C ₃)	10.11
Furnace reactance, mΩ	0.983
Specific power consumption, kWh/t	7 997
Silicon recovery, %	93.60
Furnace efficiency factor	0.857
Loss resistance, mΩ	0.178

Consequences of increasing furnace size

As mentioned above, the operating resistance decreases with increasing furnace size. Normally, the loss resistance also decreases with increasing furnace size, due to the increased cross-sectional area of the current conductors. Therefore, generally, increasing the furnace size has no adverse effect on the furnace efficiency.

However, large furnaces are more sensitive to variations in raw material quality. A consistent quality of raw materials and electrode paste is very important in order to achieve stable operating conditions and good efficiency for large furnaces. The consequence of operational disturbances and furnace shutdowns are normally more severe for a large furnace than for smaller ones.

Generally, the investment cost per megawatt and the manpower cost per ton of product is lower for large furnaces. In our opinion, this is the main reason why large furnaces are preferable to smaller furnaces for new projects of a given overall production capacity in an established industrial environment.

Further developments in furnace design

Vatvedt has recently been working on improvements in design of the electrode column, including the development of contact clamps and pressure rings of our own manufacture. Our company supplies contact clamps and pressure ring segments made of pure electrolytic copper. The water-cooled shields are made of stainless steel.

In particular, we are now looking at the design of the area of the electrode column above the top of the contact clamps. Figure 4 illustrates the conventional design of this area.

A well-known problem in operation of furnaces of this design using Söderberg electrodes, particularly for large furnaces, is that there is an abundance of thermal energy developed in the area above the contact clamps, caused by induction heating due to the strong electromagnetic fields. This surplus heat causes melting and heating of electrode paste; sometimes resulting in overheating of the liquid paste, paste segregation and high liquid paste levels. This is resulting in poor quality of the baked electrode, causing disturbances in the electrode operation and increased risk of hard as well as soft electrode breakages (Skjeldestad *et al.*, 2015).

When considering this problem in more detail, calculations have confirmed that with the conventional design of this area, the available heat generation by

Basic parameters in the operation and design of submerged arc furnaces

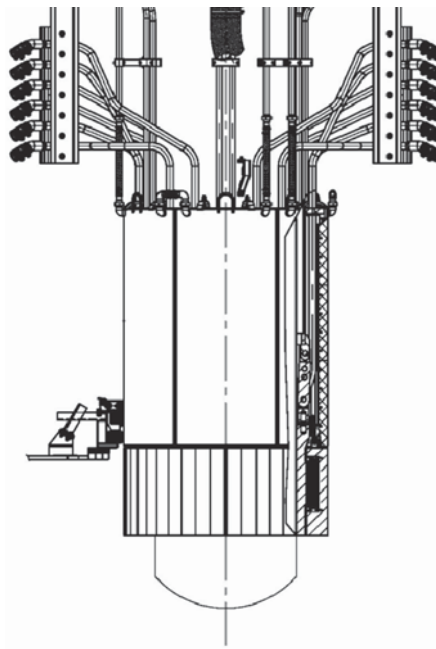


Figure 4—Typical design of lower part of electrode column

induction heating is much larger than what is required for melting and heating of the electrode paste before baking. In other words, this is a waste of energy, which is adversely affecting the furnace efficiency.

Based on some initial studies, it is thought that by making some design modifications in the area above the top of the contact clamps, it would be possible to achieve a considerable reduction of the induction heating in this area. This reduction of energy loss will have a corresponding effect on reduction of the specific energy consumption per ton of alloy.

In addition, the problem of overheating and segregation of electrode paste with its adverse effects on electrode quality and operation, which is the case on many furnaces today, is likely to be eliminated. Therefore, it will be a win-win situation.

Even with this reduction of the induction heating above the top of the contact clamps, calculations have shown that there will still be enough induction heating available for melting and heating of the electrode paste.

Conclusions

It is very important to pay attention to electrical parameters in furnace operation. The studies conducted and the formulae developed by Westly in the 1970s are very useful as guidelines for furnace operation as well as for furnace dimensioning, particularly in relation to upscaling of furnaces.

The specific power consumption (kWh/mt Si) for the production of high-silicon alloys depends on the silicon recovery as well as on the electrical efficiency of the furnace, expressed as the furnace efficiency factor. The specific power consumption decreases with increasing silicon recovery and increasing furnace efficiency.

Above all, the silicon recovery is dependent on the raw material quality and the charge mix composition. The silicon recovery is also affected by the furnace design.

The furnace efficiency factor depends on the operating resistance of the furnace, which again depends on the resistivity of the furnace charge mix. Smaller sizing of the reductants, an increased proportion of coal, and use of wood chips will contribute to increased resistivity of the charge mix, which will make it possible to operate with an increased operating resistance.

Further, the furnace efficiency factor is depending on furnace design and dimensioning, which is affecting the electrical losses from the furnace. The importance of proper design and material selection for furnace components are highlighted. The significance of the furnace dimensioning is illustrated by an example from practical furnace operation.

Possibilities for improvements in furnace design, and the electrode column design in particular, were highlighted with the aim of reducing electrical losses and hence improving furnace efficiency even further.

References

- SCHÉL, A., TUSET, J.K., and TVEIT, H. 1998. Production of high silicon alloys. Tapir Forlag, Trondheim, Norway
- SKJELDESTAD, A., TANGSTAD, M., LINDSTAD, L., and LARSEN, B. 2015. Temperature profiles in Søderberg electrodes. *Proceedings of INFACON XIV, the Fourteenth International Ferroalloys Congress*, Kiev, Ukraine, 31 May–4 June 2015. pp.327–337. <http://www.pyrometallurgy.co.za/InfaconXIV/327-Skjeldestad.pdf>
- WESTLY, J. 1974. Resistance and heat distribution in a submerged-arc furnace. *Proceedings of INFACON I, the First International Ferroalloys Congress*, Johannesburg, South Africa, 22–26 April 1974. pp. 121–127.
- WESTLY, J. 1975. Critical parameters in design and operation of the submerged-arc furnaces. *Proceedings of the AIME Electric Furnace Conference*, Houston, TX, 9–12 December 1975. pp. 47–53. <http://library.aimehq.org/library/books/Electric%20Furnace%201975/Electric%20Furnace%201975%20-%2020019.pdf>
- WESTLY, J. 1979. Dimensions des fours de reduction pour Fe-Si et d'autres Ferro-alliages, *Journal de Four Electrique*, Janvier 1979. ◆



Chrome ore mineralogy and the furnace mass and energy balance

by N.J. Sweeten*, S.M.C. Verryn†, J. Oberholzer‡, and J.H. Zietsman*

Synopsis

The effect of ore mineralogy on ferroalloy smelter operation is not sufficiently understood. The ore mineralogy can influence energy and reductant requirements, melting and reaction rates, and effectiveness of prereduction. These are all important factors to consider for furnace design, warranting a deeper study of the effect of ore mineralogy on ferroalloy production processes. This work focuses on smelting furnace mass and energy balances. Furnace mass and energy balances are among the most fundamental calculations done on a regular basis, from the project feasibility stage right through to everyday operations. Whether the energy balance is calculated by a tried and tested spreadsheet calculation, or by applying thermodynamic fundamentals using tools such as FactSage or EMSIM, most engineers simply use a chemical analysis of the raw materials. This ignores the potential effect of the ore's true mineralogical composition and may cause errors, the magnitude of which are not fully understood. In this paper we present the results of mineralogical analyses of South African, Zimbabwean, and Khazakstan chrome ores and compare energy balance results based on standard chemical assays to results based on mineralogical information.

Keywords

chromite smelting, ore mineralogy, mass balance, energy balance.

Background

Ferroalloy furnace technologies have developed over the years through tried and tested experience. With the technology available today, it is near-sighted to believe that experience will be enough to stay ahead into the future. The companies that control the ferroalloy industry in the future will be those that are able to absorb the most knowledge and draw insights from it to develop better processes.

Most ferrochrome plants take regular ore samples and perform ICP or XRF analyses to determine the chemical composition. These tests measure the contents of various metallic elements, such as Cr, Fe, Si, Mg, and Ca, and report results based on assumed oxidation states. The resulting assays are expressed in terms of Cr_2O_3 , FeO, SiO_2 , MgO, CaO, and various trace elements. In our experience, most producers, and even authors in the literature, use this assay directly in their calculations (Xu, 2013).

The enthalpy of formation of one ton of chromite (FeCr_2O_4) is -1458 kJ/mol, but if the

chromite is assumed to be equivalent amounts of FeO and Cr_2O_3 , the enthalpy of formation is only -1393 kJ/mol – a difference of 77.4 kWh/t chromite. These results show that handling ore mineralogy incorrectly has the potential to affect the calculation of the furnace energy requirement. Ex Mente performs numerous furnace mass and energy balance investigations, so it is valuable to us to have insight into the effect of ore mineralogy so that we can make our calculations as accurate as possible. This paper therefore aims to answer the question: To what extent does ore mineralogy influence the furnace mass and energy balance?

Method

One approach to answer these questions would be direct measurement of the energy required to melt an ore sample, and the reductant required to achieve a specific recovery. Instrumentation for this kind of work is extremely sensitive and it is time-consuming and expensive to obtain accurate results. It was therefore decided to use straightforward ICP-OES and XRD results, and reconcile them as far as possible, and calculate the reductant and energy requirements using Factsage (Bale *et al.* 2009) equilibrium calculations. Each of these methods is described in this section.

Ore samples

Several samples were used for this work from different orebodies in South Africa, Zimbabwe, and Khazakstan, as shown in Table I. Grab samples of 2–3 kg were obtained and were crushed, milled, and split at UIS Analytical

* Ex Mente, South Africa.

† XRD Analytical and Consulting, South Africa.

‡ UIS Analytical Services, South Africa.

© The Southern African Institute of Mining and Metallurgy, 2018. ISSN 2225-6253. This paper was first presented at the INFACON XV: International Ferro-Alloys Congress, 25–28 February 2018, Century City Conference Centre and Hotel, Cape Town, South Africa



Chrome ore mineralogy and the furnace mass and energy balance

Table I

Ore samples used in this work

Sample name	Country of origin	Mine/description
LG6 A	South Africa	LG6
LG6 B	South Africa	LG6 run-of-mine (ROM)
MG4 A	South Africa	MG4
MG4 B	South Africa	MG4 lumps
ZIM A	Zimbabwe	Ngezi
ZIM B	Zimbabwe	Ngezi
ZIM C	Zimbabwe	Mapanzuri
Marico	South Africa	Marico
Khaz	Khazakistan	Unknown

Services to ensure homogeneity between the samples used for chemical and mineralogical analysis. Since the samples are grab samples they are not necessarily representative of the orebodies.

Chemical analysis

All samples were dried, and their moisture content determined to ensure that assay results are reported on a dry basis. For determination of elemental composition, samples were first subjected to sodium peroxide (Na_2O_2) fusion, followed by dilute hydrochloric acid dissolution. The solutions were then analysed by inductively coupled plasma optical emission spectroscopy (ICP-OES). ICP-OES involves nebulizing a sample of the solution and injecting it into a plasma. The various elements are identified and quantified through their unique optical emission spectra. ICP-OES was used for the analysis of both major and minor elements.

In addition to the elemental analysis, the oxidation states of iron ($\text{Fe}^{2+}/\text{Fe}^{3+}$ ratio) were determined by selective dissolution of Fe^{3+} with hydrochloric acid, while assuming that Fe^{2+} in the chromite will not dissolve. The solution was then analysed by ICP-OES to determine the Fe^{3+} concentration. This procedure is proposed here as a new method for determining the $\text{Fe}^{2+}/\text{Fe}^{3+}$ ratio of chromite ores. This property is typically difficult or impossible to measure by other methods.

In the LECO analysis, carbon and sulphur contents were determined by using a high-frequency combustion instrument with infrared detection. Hydrogen and nitrogen contents were determined using a H/N elemental analyser.

To complete the chemical analysis, the loss on ignition (LOI) was determined. This was done by determining the mass change of a sample while heating it to a temperature of 1000°C for 2 hours, in air. The heating process releases crystal water, water from hydroxide compounds, CO_2 from carbonates, and SO_2 from sulphates. The analysis therefore aims to determine the content of such volatile matter in the sample. LOI tests in an oxidizing atmosphere can return a negative result, indicating a gain on ignition. This can be the result of, for example, FeCr_2O_4 being oxidized to $\text{Fe}_2\text{O}_3 + \text{Cr}_2\text{O}_4$.

Mineralogical analysis

The ore mineralogical composition was determined by X-ray powder diffraction (XRD) (Loubser and Verry, 2008). XRD identifies and quantifies the phases in a sample from their

unique powder diffraction patterns. This technique uses the crystalline structure of the different minerals and is therefore able to distinguish between spinels such as FeCr_2O_4 and MgAl_2O_4 and other oxide phases.

Reconciliation

The goal of the reconciliation was to convert the chemical and mineralogical assays to calculated mineralogical assays that reflect the same chemical composition as the chemical analysis results, while remaining as close as possible to the measured mineralogical composition. This was done by manually assigning elements to known minerals and equilibrating the remainder of the assay to calculate an approximated chemical composition of multi-component minerals such as spinels.

Thermodynamic equilibrium

Calculating thermochemical equilibrium is an important part of the reconciliation procedure. FactSage (Bale *et al.*, 2009) contains data based on thousands of experiments and uses rigorous optimization routines to determine the equilibrium state of elements in hundreds of phase structures. The equilibrium state is the state of the lowest Gibbs free energy and therefore the most likely condition that will be reached, given enough time.

Ores are unlikely to be at thermodynamic equilibrium due to the numerous processes that led to their formation and the weathering that changed their structures over the years. It is therefore necessary to manipulate the equilibrium calculations to achieve a representative assay.

FactSage takes account of solid solutions such as spinels and pyroxenes that consist of various constituents. The calculations incorporate the heats of mixing of these various phases, which is more accurate than assuming that FeCr_2O_3 and MgCr_2O_3 are two separate spinels, when in fact they are together in solution.

Mass and energy balance

A simplified mass and energy balance was calculated for each of the ores. Several assumptions were made to simplify the calculations:

1. Pure graphite (C) was used as the reductant to remove the effect of ash and volatile matter from actual reductants.
2. No flux was added to any of the calculations. Fluxing design is critical to ensure effective furnace operation, but flux adds complications that might obscure the ore effects that are the focus here.
3. The reagents (ore and graphite) were equilibrated at 1700°C . This temperature was used throughout this study to allow for comparison on the same basis.
4. A chrome recovery to alloy of 95% was selected for the furnace and the graphite was adjusted to achieve this recovery for each case.

Results and discussion

Chemical analysis

Table II shows the chemical analysis results for the ore samples. The LG6 A ore has the highest content of Cr_2O_3 , the lowest SiO_2 , and the highest Cr/Fe ratio of the South African ores. The Zimbabwean ores have much higher Cr/Fe ratios.

Chrome ore mineralogy and the furnace mass and energy balance

Table II

Chemical analysis results (in mass %) for the ferrochrome ores under consideration

	LG6 A	LG6 B	MG4 A	MG4 B	ZIM A	ZIM B	ZIM C	Marico	Khaz
Main									
Cr ₂ O ₃	43.13	39.77	30.99	29.97	39.62	42.54	34.8	49.708	49.1232
Fe ₂ O ₃	0.81	0.96	0.44	0.72	5.44	2.5	2.29	0.71	0.62
FeO	23.29	21.92	21.77	21.64	13.02	14.51	13.16	20.25	11.24
Cr/Fe	1.6	1.5	1.2	1.2	1.9	2.2	2	2.1	3.7
Major gangue									
SiO ₂	3.47	7.97	15.4	15.84	9.52	10.41	14.42	4.03	6.22
Al ₂ O ₃	15.53	14.14	14.7	14.88	12.2	11.6	11.1	12.5	8.07
CaO	0.47	0.71	3.13	3.97	0.23	0.22	0.27	0.2	0.2
MgO	10	11.68	10.06	9.74	16.38	15.12	21	10.4	21.1
Minor gangue									
TiO ₂	0.63	0.59	0.83	0.98	0.34	0.39	0.32	0.45	0.15
MnO	0.29	0.29	0.23	0.24	0.26	0.24	0.16	0.2	0.13
V ₂ O ₅	0.34	0.3	0.32	0.34	0.19	0.2	0.17	0.63	0.2
Trace									
K ₂ O	0.03	0.033	0.034	0.044	0.019	0.024	0.023	0.008	0.035
Zn	0.093	0.084	0.078	0.081	0.089	0.073	0.06	0.1	0.065
Ba	0.003	0.003	0.005	0.003	0.003	0.002	0.001	0.001	0.001
Cu	0.002	0.002	0.003	0.003	0.001	0.002	0.002	0.001	0.002
Ni	0.083	0.081	0.086	0.084	0.127	0.123	0.142	0.062	0.13
Other									
CO ₂	0.121	0.337	0.059	0.029	0.311	0.289	0.326	0.106	0.242
H ₂ O	< 0.005	< 0.005	< 0.005	< 0.005	1.591	0.304	0.769	0.954	2.178
N	0	0	0	0	0.059	0.03	0.01	<0.01	<0.01
S	0.003	0.007	0.008	0.003	0.004	0.01	0.007	<0.003	0.024
Moisture	0	0	0	0	0.48	0.34	0.08	0.06	0.06
LOI	-0.42	-0.16	-0.74	-0.44	2.81	2.15	2.79	-0.98	1.98

Table III

XRD analysis results (in mass %) for South African LG6 samples, with and without plagioclase

Mineral	Chemical formula	LG6 A	LG6 A new	LG6 B	LG6 B new
Chromite	FeCr ₂ O ₄	23.06	25.65	16.81	19.21
Chromite1	FeCr ₂ O ₄	14.38	16.32	22.28	23.39
Magnesiochromite	MgCr ₂ O ₄	40.89	40.72	32.56	31.35
Chlorite	Mg ₅ Al ₂ Si ₃ O ₁₀ (OH) ₈	1.45	1.64	3.37	2.19
Plagioclase	NaAlSi ₃ O ₈ , CaAl ₂ Si ₂ O ₈	13.02		14.75	
Enstatite	MgSiO ₃		8.51		16.35
Vermiculite		6.46	6.75	7.71	7.22
Dolomite	CaMg(CO ₃) ₂	0.74	0.40	2.52	0.30

They also tend to have less Al₂O₃ and higher MgO than South African ores. The South African ores exhibited a gain on ignition; this is likely due to iron being oxidized during the test. The assays all summed to less than 100%, which is typical for chemical analysis results. The Zimbabwean ores were slightly wet, whereas the South African ores contained no moisture. All calculations in this work were done on a dry-ore basis to standardize the calculations.

The H and C results from the LECO analyses were converted to H₂O and CO₂ respectively. No H was detected in

the South African samples, but the LECO is designed for analysing coals, so it is not optimized for detecting small amounts of H.

Mineralogical analysis

Table III shows two sets of XRD results for the LG6 A and LG6 B samples, and Table IV shows the results for the remaining ores. Three different spinel phases were detected by XRD; they are named chromite, chromite1, and magnesiochromite by the XRD software.

Chrome ore mineralogy and the furnace mass and energy balance

Table IV

XRD analysis results (in mass %) for other ores

Mineral	Chemical formula	MG4 A	MG4 B	ZIM A	ZIM B	ZIM C	Marico	Khaz
Chromite	FeCr ₂ O ₄	40.39	51.83	42.51	61.36	64.29	97.51	87.21
Chromite1	FeCr ₂ O ₄			33.50	17.45			
Lizardite	Mg ₃ Si ₂ O ₅ (OH) ₄			9.79	10.36	11.46		12.79
Chlorite	Mg ₅ Al ₂ Si ₃ O ₁₀ (OH) ₈			5.14	3.30	4.19		
Haematite	Fe ₂ O ₃			5.60	2.19	0.83		
Goethite	FeO(OH)			3.47	5.35	0.06		
Enstatite	MgSiO ₃	19.37	11.59			13.12		
Diopside	MgCaSi ₂ O ₆	1.60	7.93			6.05	2.49	
Plagioclase	NaAlSi ₃ O ₈ , CaAl ₂ Si ₂ O ₈	31.63	21.37					
Kaolinite	Al ₂ Si ₂ O ₅ (OH) ₄	0.00	0.34					
Talc	Mg ₃ Si ₄ O ₁₀ (OH) ₂	1.37	1.36					
Smectite		1.82	2.71					
Actinolite	Ca ₂ Fe ₅ Si ₈ O ₂₂ (OH) ₂	3.82	2.87					

The LG6 chemical analysis results showed very little CaO in the ore, and no Na. Therefore, it is unlikely that the ore contains as much plagioclase as suggested by the preliminary XRD results in Table III. Plagioclase and enstatite peaks can, however, overlap in the diffractogram. The XRD results were therefore updated to favour enstatite, which is much more likely given the chemical composition of the sample. This illustrates the importance of critically analysing any laboratory results, and of providing the mineralogist with a chemical assay to assist in interpreting XRD results. Chromites of different compositions were detected and the simplified chemical formulae shown in the table do not necessarily reflect the actual composition.

The XRD results show that the LG6 ores contain chlorite and vermiculite. These are both hydrated minerals, but the chemical composition results show that the hydrogen contents of the ores are below the 0.05% detection limit of the LECO. For this reason, the ores were assumed to contain 0.05% water.

Mineralogical reconciliation

The mineralogical reconciliation was performed to convert the chemical analysis into a calculated mineralogical assay as close as possible to the measured mineralogical composition. The mass and energy balance was then compared using the measured chemical assay and the calculated mineralogical assay. In the reconciliation, the chemical assays were used as the primary source of information, since chemical analyses are fully quantitative and more accurate than XRD analysis. The chemical analysis results were therefore used as the basis, with the XRD results as a guide.

South African LG and MG ores

The following steps were used to produce a calculated mineralogical assay from the measured chemical and mineralogical assays.

1. The trace elements were removed from the chemical assay to simplify the thermochemical equilibrium calculations. The assay was normalized by proportionally increasing the gangue elements in their oxide forms (SiO₂, CaO, MgO, and Al₂O₃) so that the

final assay summed to 100%. This allows for trace elements to be substituted by gangue minerals, rather than normalizing the entire assay, which would increase the amounts of iron and chromium above their measured values, causing an over-estimation of chrome production.

2. The carbon from the LECO analyses was used to form dolomite, and the required amounts of CaO and MgO were removed from the chemical assay. The amount of dolomite calculated for the MG ores is below the typical XRD detection limit, which is why it was not identified by XRD. Dolomite is the most likely carbon-containing phase, therefore it was assumed that all the carbon is present in dolomite.
3. The remaining CaO was used to form plagioclase.
4. It was assumed that the ores contain 0.05% water. The LECO test is unable to detect water below this limit. This assumption was made because the XRD results suggest that there are hydrated minerals in the ores. This water was used to make chlorite.
5. The remainder of the assay was equilibrated at 25°C to approximate the spinel and orthopyroxene phases. The equilibrium phases allowed in the calculation were restricted to produce the desired result:
 - (i) LG6 A and B
 - (a) Only MgO, FeO, Al₂O₃, and Cr₂O₃ were provided as inputs to the calculation.
 - (b) Three spinel phases were allowed to form because three distinct spinel phases were observed by XRD.
 - (c) MgO, FeO, Al₂O₃, and Cr₂O₃ were allowed to form as individual compounds.
 - (d) A stable gas phase was forced by adding Ar. This was done to improve numerical stability and speed of convergence.
 - (ii) MG4 and MG4
 - (a) Only SiO₂, MgO, FeO, Al₂O₃, and Cr₂O₃ were provided as inputs to the calculation.
 - (b) One spinel phase was allowed to form because only one spinel phase was detected by XRD.

Chrome ore mineralogy and the furnace mass and energy balance

Table V

Mineralogical reconciliation results (in mass %) for South African ores

Phase	Chemical composition	LG6 A	LG6 B	MG4 A	MG4 B
Dolomite	CaMg(CO ₃) ₂	0.25	0.71	0.12	0.06
Plagioclase (anorthite)	CaAl ₂ Si ₂ O ₈	2.10	2.61	16.07	20.31
Chlorite	Mg ₅ Al ₂ Si ₃ O ₁₀ (OH) ₈	0.39	0.39	0.39	0.39
Spinel 1	Mostly MgCr ₂ O ₄ and FeCr ₂ O ₄	58.67	54.10	58.80	54.68
Spinel 2	Mostly FeAl ₂ O ₄ and MgAl ₂ O ₄	26.54	23.08		
Spinel 3	Fe ₃ O ₄	0.13	0.46		
Orthopyroxene	Mostly Mg ₂ Si ₂ O ₆ , some FeMgSi ₂ O ₆	0.00	0.00	15.31	12.68
Quartz	SiO ₂	2.66	7.02		
Wustite	FeO	5.36	5.76	7.94	10.32
Periclase	MgO	2.66	4.71		
TiO ₂		0.63	0.59	0.83	0.98
MnO		0.29	0.29	0.23	0.24
V ₂ O ₅		0.34	0.30	0.32	0.34
Total		100.00	100.00	100.00	100.00

- (c) MgO, FeO, Al₂O₃, and Cr₂O₃ were allowed to form as individual compounds.
- (d) Orthopyroxene, talc, and clinopyroxene were allowed to form. There was no remaining CaO to form clinopyroxene, or water to form talc.
- (e) A stable gas phase was again forced with Ar.

The results are shown in Table V.

Zimbabwean ores

The reconciliation for the Zimbabwean ores was similar, but with some changes to reflect the different mineralogical and chemical assay results:

1. The gangue portion of the assay was normalized to account for the mass of the trace elements.
2. The LECO results suggest that there is a small amount of carbon in the ore. The most likely source of this is dolomite. No dolomite was detected by XRD, but it is likely that it is below the detection limit. The carbon was therefore allocated to the dolomite phase.
3. For ZIM A and ZIM B, the XRD results suggest that there is more Fe³⁺ (in haematite and goethite), than the chemical results allow for. All the Fe³⁺ was set aside for these phases, and divided between goethite and haematite in the ratios suggested by the XRD results. For the ZIM C ore, the haematite and goethite are less than the amount of Fe³⁺. The Fe³⁺ required to make up the amounts of goethite and haematite from the XRD results was set aside and the remainder of the Fe³⁺ was allocated to the spinel phase.
4. Some of the water was already allocated to the goethite phase, as indicated above. The remaining water, from the chemical results, was allocated to the lizardite and chlorite phases in the ratio between the phases suggested by the XRD results.
5. The spinels were generated by equilibrating the remaining elements in oxide form at 25°C.

The results for the Zimbabwean ores are shown in Table VI.

Other ores

The Marico and Khazakstan ores are similar in that they both have an extremely high content of a single spinel phase. These samples were received at a later stage in the investigation, so there was insufficient time to perform as meticulous a reconciliation as was done for the other ores. Nevertheless, the results are included here for interest's sake. Similar steps were taken to reconcile the mineralogies of these ores.

1. The gangue portion of the assay was normalized to account for the mass of the trace elements.
2. The chemical assay was then equilibrated with restricted phases:
 - a. One spinel phase was allowed.
 - b. Each of the simple oxides for the available elements was allowed to form to ensure that the mass balance could be calculated.
 - c. For the Marico ore, clinopyroxene (diopside) was allowed, and for the Khazakstan ore lizardite was allowed.
3. The elements that did not fit into the spinel or accompanying phases were left as pure substances, as shown in Table VII.

The results for the Marico and Khazakstan ores are shown in Table VII.

Mass and energy balance

Table VIII show the mass and energy balance results for three cases for each of the ores:

1. Assay as given by chemical analysis, with all Fe as FeO.
2. Assay as given by chemical analysis, with forms of iron as determined by analytical work.
3. Mineralogical assay calculated through reconciliation.

Mass balance

The differences in the mass balance depend solely on the oxidation state of the iron in the ore. A new method is proposed to measure the Fe²⁺/Fe³⁺ ratio of chrome ore, but

Chrome ore mineralogy and the furnace mass and energy balance

Table VI

Mineralogical reconciliation results (in mass %) for Zimbabwean ores

Phase	Chemical composition	ZIM A	ZIM B	ZIM C
Dolomite	CaMg(CO ₃) ₂	0.65	0.61	0.68
Haematite	Fe ₂ O ₃	3.49	0.78	0.83
Goethite	Fe ₂ O ₃ (H ₂ O)	2.17	1.91	0.06
Lizardite	Mg ₃ Si ₂ O ₅ (OH) ₄	6.92	0.64	4.30
Chlorite	Mg ₅ Al ₂ Si ₃ O ₁₀ (OH) ₈	3.63	0.20	1.57
Spinel 1	MgCr ₂ O ₄ , FeCr ₂ O ₄	52.95	57.15	47.57
Spinel 2	FeAl ₂ O ₄ , MgFe ₂ O ₄	19.39	19.90	19.43
Orthopyroxene	Mostly Mg ₂ Si ₂ O ₆ , some FeMgSi ₂ O ₆			
Lime	CaO	0.03	0.04	0.07
Quartz	SiO ₂	5.57	10.53	12.42
Periclase	MgO	4.41	7.39	12.30
Wüstite	FeO			0.11
TiO ₂		0.34	0.39	0.32
MnO		0.26	0.24	0.16
V ₂ O ₅		0.19	0.20	0.17
Total		100.00	100.00	100.00

Table VII

Mineralogical reconciliation results (in mass %) for other ores

Phase	Chemical composition	Marico	Khaz
Haematite	Fe ₂ O ₃	0.55	
Lizardite	Mg ₃ Si ₂ O ₅ (OH) ₄		14.56
Spinel 1	MgCr ₂ O ₄ , FeCr ₂ O ₄	90.15	82.96
Orthopyroxene	Mostly Mg ₂ Si ₂ O ₆ , some FeMgSi ₂ O ₆	7.09	
Lime	CaO		0.2
Periclase	MgO		1.7
TiO ₂		0.45	0.15
MnO		0.20	0.13
V ₂ O ₅		0.63	0.2

this method requires validation against standard samples to ensure its effectiveness.

The Fe²⁺/Fe³⁺ ratio directly affects the mass balance because if the iron is more oxidized, more reductant is required to reduce it. There are two reasons to believe that the methods of iron analysis may be underestimating the Fe³⁺ content:

1. The XRD results, particularly for the Zimbabwean ores, suggest much higher haematite and goethite than the measured Fe³⁺ content accounts for.
2. All the equilibrium calculations had 'left-over' FeO that did not 'fit' in the spinel phases. This is obviously an unrealistic result, and is another possible indication that more of the iron might be present as Fe³⁺.

Preliminary calculations using the Zimbabwean ores, which were based more strongly on the XRD results, suggested a much higher Fe³⁺ content because of the haematite and goethite measured by XRD. This resulted in carbon requirements as much as 15% higher than calculated when assuming all iron is present as FeO. This result

correlates with industrial experience of higher reductant requirements for Zimbabwean furnaces than South African ones. The reductant requirement results are therefore inconclusive until the ore Fe²⁺/Fe³⁺ ratio can be confirmed.

Energy balance

The difference in iron oxidation states does not have as significant an impact on the energy balance as the difference indicated by the approximated mineralogical assay. This shows that using phases such as spinels to represent the ore has a more significant effect on the energy balance than knowing the Fe²⁺/Fe³⁺ ratio.

The difference in the energy balance when using a chemical assay and the approximated mineralogical assays developed in this work is in the order of 5%. This means that, provided the calculated mineralogical assay is a more accurate representation of the ore, then using a chemical assay for energy balance calculations results in the smelting energy requirement being underestimated by approximately 5%. In practice, this 5% is being consumed in the furnace, but it is most likely accounted as heat losses rather than due to the theoretical smelting energy requirement of the ore.

Differences between ores

Any discussion on the differences between the ores analysed in this paper is limited, because the samples used are not necessarily representative of the various orebodies. In addition, different fluxes would be required for the different ores and these have not been considered. It is, however, interesting to draw some preliminary conclusions.

The South African ores tend to have lower smelting energy requirements than the Zimbabwean ores. LG6 A ore has the lowest energy requirement and highest yield of alloy per ton of ore. ZIM B has the lowest energy requirement and highest yield of alloy per ton ore of the Zimbabwean ores.

Conclusions and recommendations

Mass balance

The amount of reductant required has been shown to be

Chrome ore mineralogy and the furnace mass and energy balance

Table VIII

Mass and energy balance results for South African ores

	Fe recovery	Cr recovery	t ore/t alloy	kg C/t alloy	MW/t alloy
LG6 A					
1	99.9%	95.0%	2.018	334.109	2.749
2	99.9%	95.0%	2.018	335.325	2.755
3	99.9%	95.0%	2.018	335.325	2.887
			Increase	0.36%	5.00%
LG6 B					
1	99.8%	95.0%	2.169	334.066	2.906
2	99.8%	95.0%	2.169	335.608	2.914
3	99.8%	95.0%	2.169	335.608	3.048
			Increase	0.46%	4.87%
MG4 A					
1	99.7%	95.0%	2.528	328.072	3.180
2	99.7%	95.0%	2.528	328.875	3.184
3	99.7%	95.0%	2.528	328.875	3.359
			Increase	0.24%	5.65%
MG4 B					
1	99.7%	95.0%	2.567	326.525	3.184
2	99.7%	95.0%	2.567	327.868	3.191
3	99.7%	95.0%	2.567	327.868	3.369
			Increase	0.41%	5.82%

Mass and energy balance results for Zimbabwean ores

ZIM A					
1	99.8%	95.0%	2.374	368.710	3.292
2	99.8%	95.0%	2.375	378.344	3.337
3	99.8%	95.0%	2.375	378.344	3.510
			Increase	2.61%	6.64%
ZIM B					
1	99.8%	95.0%	2.313	352.937	3.192
2	99.8%	95.0%	2.314	357.215	3.213
3	99.8%	95.0%	2.314	357.215	3.347
			Increase	1.21%	4.85%
ZIM C					
1	99.7%	95.0%	2.731	361.533	3.563
2	99.7%	95.0%	2.731	366.212	3.585
3	99.7%	95.0%	2.731	366.212	3.747
			Increase	1.29%	5.16%

Mass and energy balance results for other ores

Khaz					
1	99.8%	95.0%	2.29	394.06	3.43
2	99.8%	95.0%	2.29	395.09	3.44
3	99.8%	95.0%	2.28	396.69	3.59
			Increase	0.67%	4.75%
Marico					
1	99.9%	95.0%	1.93	355.81	2.88
2	99.9%	95.0%	1.93	356.82	2.88
3	99.9%	95.0%	1.93	357.26	2.99
			Increase	0.41%	3.99%

strongly dependent on the Fe²⁺/Fe³⁺ ratio. A new method was proposed and used to determine the oxidation states of iron. The XRD results and reconciliation suggest that the Fe³⁺ contents may be higher than measured by this new method. It is recommended that the method be validated using standard samples of known iron oxidation state to improve its accuracy, and that it be routinely used when analysing ore samples for mass and energy balances.

Energy balance

The energy balance results suggest that the calculated energy requirement is approximately 5% higher when using the approximated mineralogical assays compared to chemical assays. These results are by no means conclusive, because they are also based upon several assumptions, but they have shown that using a mineralogical composition makes a difference in the energy balance. These results should be verified using analytical techniques for measuring the actual energy requirement directly.

With today's strong focus on maximizing energy efficiency, it is critical to obtain as good an understanding of the furnace energy balance as possible. Understanding ore mineralogy is an important part of this. One option for improving this understanding is to smelt ore samples under controlled conditions, measure the actual energy requirement, and compare that to these approximated results. Another is to measure the heat of formation of the ore directly. The feasibility of both these options is speculative at this stage.

These results may not be so critical to operating plants that have long since made accommodations for their energy balances, but they are worthwhile for designers of future furnaces to understand. The analyses performed in this work are not expensive, and the method proposed here can be used to reconcile the analyses and produce more accurate assays for mass and energy balances.

Finally, to answer the initial question: ore mineralogy does influence both mass and energy balance calculations for ferrochrome smelting furnaces. The extent of this influence depends on the specific ore, but it has been shown that both reductant and energy requirement calculations are impacted. Reductant requirement differences are small enough to be within the band of uncertainty due to variations in raw material composition, and sampling and analytical error. Smelting energy requirement differences appear to be more significant, and these could prove to be important when switching between different raw materials, or when doing feasibility and design calculations for new plants.

References

- BALE, C.W., BÉLISLE, E., CHARTRAND, P., DECTEROV, S. A., ERIKSSON, G., GHERIBI, A., HACK, K., JUNG, I-H., MELANÇON, J., PELTON, A.D., PETERSEN, S., and ROBELIN, C. 2009. FactSage thermochemical software and databases — recent developments. *Calphad*, vol. 33. pp. 295–311.
- LOUBSER, M. and VERRYIN, S. 2008. Combining XRF and XRD analyses and sample preparation to solve mineralogical problems. *Journal of the Geological Society of South Africa*, vol. 111. pp. 229–238.
- PAN, X. 2013. Effect of South Africa chrome ores on ferrochrome production. *Proceedings of the International Conference on Mining, Mineral Processing and Metallurgical Engineering (ICMMME'2013)*, Johannesburg, South Africa, 15–16 April 2013. pp. 106–110. ◆

BACK TO THE FUTURE

6th August 2018—Technical Workshop • 7–8th August 2018—Conference
Lagoon Beach Conference Venue, Cape Town, South Africa



BACKGROUND

The theme of this first geometallurgy conference 'Back to the future' is inspired by looking both into the past and the future: the concept of Geometallurgy goes back to some of the earliest mining activities when mineral recognition, mining, separation and concentration were undertaken simultaneously. Over time, changes in operational structures, product expansion and specialisation ultimately led to the diminishment and breakdown of this holistic approach.

In the last two decades 'Geometallurgy' has become a sophisticated yet entirely logical return to this integrated approach to mine planning. In a world of exponentially increasing ore heterogeneity and economic complexity, Geometallurgy is effectively a highly structured, integrated multi-disciplinary collaboration for optimising the value of an ore deposit. The approach is premised on acquiring multi-dimensional, spatially constrained (blocked) ore body knowledge that quantifies and qualifies all aspects of ore body variability. This data must include each element's response to blasting, excavation, crushing, grinding, separability and the environment and of course, its economic factors. These discrete elemental data sets are modelled to optimise a mine plan which takes into account the respective threshold criteria for each of the dataset components. Geometallurgy provides for truly integrated mine planning, ore flow management and processing from exploration to operations and through to final closure and rehabilitation. (Think of it as 4D Whittle on steroids, but for the entire mine life cycle, not just the optimised pit or stope envelope for the mining operation).

Looking into the future, we need to visualise what our 'ideal' mining operation in Southern Africa should look like, how it will function, and be equipped to articulate what we need to do to achieve this. Geometallurgy is a critical tool in achieving this.

KEYNOTES

Prof. Alice Clark
*Director of Production Centres, SMI-BRC & SMI-JKMRC,
University of Queensland, Australia*

Sello Kekana
*Head of Technical Training and Development, Ivanhoe
Mines*

Alistair Macfarlane, *Minerals Council South Africa*

Matt Mullins
Director: Tecoma Strategies

Dr Carlo Philander
*Regional Manager South Africa
Mineral Resources Development
Tronox*

Sponsors

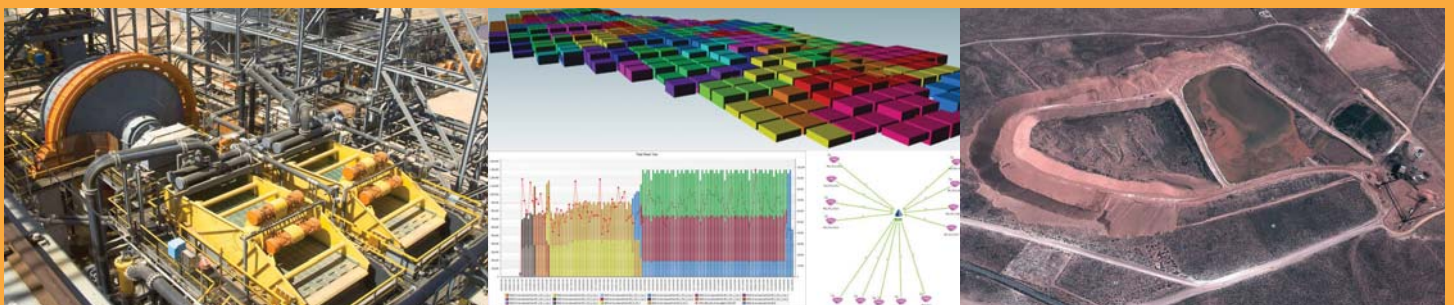


www.scantech.com.au



For further information contact: Camielah Jardine, Head of Conferencing, SAIMM, P O Box 61127, Marshalltown 2107

Tel: +27 11 834-1273/7, Fax: +27 11 833-8156 or +27 11 838-5923, E-mail: camielah@saimm.co.za, Website: <http://www.saimm.co.za>





Working towards an increase in manganese ferroalloy production in South Africa – a research agenda

by J.D. Steenkamp*, W.G. Bam†, E. Ringdalen‡,
M. Mushwana*, S.A.C. Hockaday*, and N.A. Sithole*

Synopsis

Although South Africa is endowed with one of the largest land-based deposits of manganese ore, in the order of 80% of the ore mined is exported for beneficiation elsewhere. The past 15 years has seen a decline in the production of manganese ferroalloys locally due to a steep rise in the price of electricity, among other factors. As local beneficiation of South Africa's resources is a national priority, a research agenda to increase manganese ferroalloy production in South Africa was developed. Inputs were obtained from various role-players in the value chain, including local smelter operations, research institutions both local and abroad, and companies providing support to the industry. Ninety-five research opportunities were identified and grouped into twenty-one research themes. The results are reported here in the context of a review of relevant Infacon papers and Mintek reports. As implementation of such a research agenda could be done through the development of a technology roadmap, the paper concludes with an example from Norway where a roadmap was developed to increase the use of natural gas in metal production.

Keywords

research themes, manganese ferroalloy production, South Africa.

Introduction

Despite its importance in the production of steel, manganese is also considered a *relatively rare metal* (Reijnders, 2016). Reijnders (2016) defined relatively rare metals as: 'geochemically relatively scarce (having an upper crustal abundance < ~0.025 mass per cent)' or 'subject to national stockpiling to prevent shortages in alloy production'. Although manganese is the 12th most abundant element in the Earth's crust, with an average concentration of 0.1% (Olsen, Tangstad, and Lindstad, 2007), ores of commercial importance are geographically limited. Therefore countries, including the USA (Corathers, 2017), manage national stockpiles of ore and alloys.

In South Africa, manganese was discovered in 1907 at Black Rock and initially mined in Hout Bay near Cape Town, from where small quantities were exported in 1917 (Pienaar and Smith, 1992). Mining in the Postmasburg area started in 1922 and in the Kalahari Manganese Field (KMF), one of the largest land-based deposits of manganese ores of commercial importance (Corathers, 2017), in 1954. This natural resource has been

beneficiated in the country since 1937, when high-carbon ferromanganese (HCFeMn) was produced using blast furnace technology (Basson, Curr, and Gericke, 2007). In 1942, a technology step-change occurred when a 3 MVA submerged arc furnace (SAF) was used for the first time to produce HCFeMn.

In 2016, South Africa accounted for 78% of the world's identified manganese resources and 29% of the world's reserves (Corathers, 2017). Currently, South Africa has an installed manganese ferroalloys capacity of about 1.2 Mt/a, applying SAF technology in the production of HCFeMn and silicomanganese (SiMn) – see Table I. Medium-carbon ferromanganese (MCFeMn) is produced at two sites using converter technology.

Data provided by Mintek's Mineral Economics and Strategy Unit indicated that until 2001, in the order of 50% of manganese ore produced was smelted locally. Since then, local sales have remained stagnant but export sales have increased to such an extent that 84% of the ore produced in 2014 was exported. In a report available in the public domain (Directorate: Mineral Economics, 2016), the Department of Mineral Resources of South Africa reported this amount at 70% in 2014. The increase in ore exports is mainly due to increased production capacity for manganese ferroalloys in Asia and Oceania, specifically China (Steenkamp and Basson, 2013).

Due to the lucrative export market for ore, the steep increase in electricity tariffs, and the price of manganese ferroalloys remaining fairly constant (van Zyl, Bam, and Steenkamp,

* Mintek, South Africa.

† Stellenbosch University, South Africa.

‡ SINTEF, Norway.

© The Southern African Institute of Mining and Metallurgy, 2018. ISSN 2225-6253. This paper was first presented at the INFACON XV: International Ferro-Alloys Congress, 25–28 February 2018, Century City Conference Centre and Hotel, Cape Town, South Africa

Working towards an increase in manganese ferroalloy production in South Africa

Table I

Installed capacity for manganese ferroalloys in South Africa

Operating company	Commodity	Production rate (kt/a)	MVA installed
Metalloys	HCFeMn	480	312
Assmang Cato Ridge	HCFeMn	240	116
Assmang Machadodorp*	HCFeMn	270	132
Transalloys	SiMn	180	161
Mogale**	SiMn	40	40
TOTAL		1210	761

* On care and maintenance

** Currently converted to FeCr production

2016; van Zyl, 2017), the production and sales of manganese ferroalloys in South Africa have been declining, resulting in job losses among other impacts. Only around 40% of the installed capacity listed in Table I is currently in use (personal communications with various plant personnel, 2017). In a country with an official unemployment rate of 25.3% in 2015 (Stats SA, 2016), there is a need for the development of a national research agenda (Phaal, Farrukh, and Probert, 2004) to increase beneficiation of manganese ore in South Africa. The aim of the study presented here was to define such a research agenda from a multi-organizational perspective (Phaal, Farrukh, and Probert, 2004) and look at not only supporting existing operations, but also working towards step-change technologies.

Methodology

The term *value chain* can be used to describe the full range of activities performed to bring a product from its conception to end-use and beyond (Gereffi and Fernandez-Stark, 2011). Such maps can be useful to determine the interdependencies between various products and processes. A recent version of the manganese value chain map was described by van Zyl (2017). The section applicable to this study is indicated in Figure 1 and consists of three stages.

- **Stage A—Geology, mining, and beneficiation:** The manganese orebody under investigation was limited to the KMF, based in the Hotazel area of the Northern Cape Province of South Africa. Products produced in Stage A include lumpy ore and fine ore upgraded in the form of sinter, to meet the chemical, phase chemical, and physical (size) requirements of SAF technology applications in South Africa. Waste streams were streams that did not meet these criteria.
- **Stage B—Reduction:** The reduction step consisted of the production of SiMn or HCFeMn using SAF technology with the products from Stage A being the main sources of manganese. Waste streams generated included slag, dust and off-gas, and unsaleable metallic fines.
- **Stage C—Refining:** The refining step consisted of the production of MCFeMn using converter technology, the HCFeMn from Stage B being the main source of manganese. As with Stage B, waste streams generated

included slag, dust and off-gas, and unsaleable metallic fines.

With the value chain defined in Figure 1 as a basis, the method followed to identify and evaluate the research opportunities and themes is summarized in Figure 2.

- **Phase 1—**Six categories were identified using a process broadly similar to that proposed by Jabareen (2008) and depended on four main sources: (i) the shareholder performance agreement between Mintek and the South African government for 2015, (ii) the Mintek Pyrometallurgy Research Roadmap for 2015, (iii) an overview of the manganese ferroalloy industry by Steenkamp and Basson (2013), and (iv) a follow-up study by van Zyl (2017). The research categories are presented in Table II. Knowledge leaders from South Africa, Norway, and Namibia, were identified in the fields of operations (13), research and development (26), and support (13). They were invited to participate in a workshop included in the programme of the Second School on Manganese Ferro-alloy Production hosted in South Africa on 27 and 28 June 2016.
- **Phase 2—**The First School on Manganese Ferro-alloy Production was hosted in 2012 in South Africa in order to support local smelters and foster collaboration between researchers in the field based in South Africa and Norway. The intention of the Second School on Manganese Ferro-alloy Production was to build on

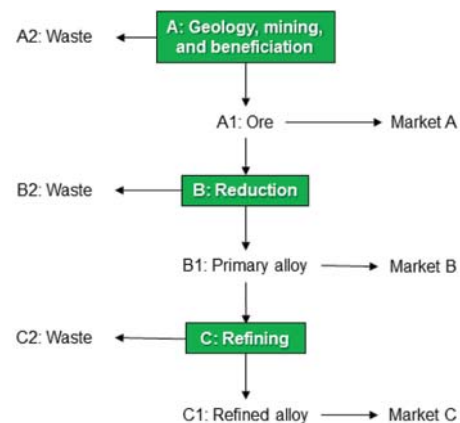


Figure 1—Various stages in the value chain map under investigation

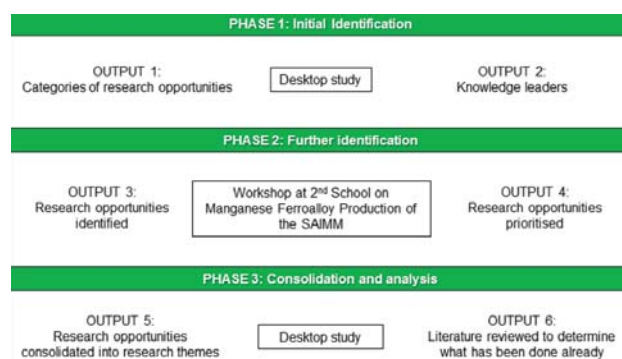


Figure 2—Research phases followed in identifying a research agenda to increase manganese ferro-alloy production in South Africa

Working towards an increase in manganese ferroalloy production in South Africa

Research categories and their aims, and research themes identifies per category	
Increased environmental efficiency Aim: to operate eco-efficient processing technologies and minimize landfill as a waste management solution	
1. Handling, recycling, and re-using waste products (including dust, slag, and metal fines) 2. Using alternative reductants and sources of electricity to reduce carbon emissions	
Increased resource efficiencies Aim: to utilize South African resources more efficiently by increasing recovery of saleable manganese to high-value products, including manganese ferroalloy products not currently in the market	
3. Improving knowledge of geometallurgy 4. Treating ore fines 5. Treating low-grade ore 6. Improving processes by focusing on resource efficiencies	
Increased energy efficiencies Aim: to efficiently recover smelter energy from waste streams, and to reduce electricity consumption via alternative energy sources or applications	
7. Using alternative sources of fuel 8. Pretreating ore 9. Recovering energy, mainly from off-gas 10. Determining electrode tip position 11. Minimizing metal fines generation 12. Revisiting furnace designs 13. Improving converter technology 14. Finding alternatives to converting	
Increased productivity of labour Aim: to increase the skills levels of people operating plants in South Africa to enhance South Africa's global competitiveness	
15. Developing skills levels 16. Creating incentives	
Reduced dependency on rail capacity Aim: to utilize rail capacity towards the transportation of high-value products	
17. Reducing the dependency on rail 18. Developing railway infrastructure	
Other Aim: to capture research opportunities that do not fall into categories listed above	
19. Creating tax benefits (or other incentives) for local beneficiation of ores through smelting 20. Mining manganese nodules (ocean-based) 21. Diversifying product ranges by producing higher value products	

these collaborations by hosting a workshop for the collaborative identification of research opportunities. When introducing the workshop towards the end of the series of lectures, all delegates were invited to participate. The school was attended by 71 delegates and the workshop by about 36 participants (completion of the attendance register was voluntary). Approximately 50% of the workshop participants were the invited knowledge leaders.

The facilitation methodology followed at the workshop is summarized in Figure 3 and described as follows:

1. Six workshop stations were set up. These consisted of (i) one station per value chain stage focusing on how *existing technology* applied at operations could be improved in each of the research opportunity categories, and (ii) one station per value chain stage focusing on how *step-change technologies* could contribute to the competitiveness of the South African manganese industry.

2. Workshop participants divided themselves into six groups. These groups were rotated amongst the six stations for ten minutes at a time. This enabled all workshop participants to contribute to each of the six stations. The participants were tasked with (i) identifying the key research opportunities and (ii) identifying where these opportunities fit in the categories (if at all).
 3. The groups from the same value chain stages were combined and given twenty minutes to determine a prioritized list of research opportunities for each value chain stage.
 4. Thereafter, all the knowledge leaders were reconvened and tasked with agreeing on the overall priorities that would best support the long-term competitiveness of the manganese industry in South Africa, for the entire value chain.
- *Phase 3*—In total, 95 research opportunities were identified, 50% in support of existing operations and



Working towards an increase in manganese ferroalloy production in South Africa

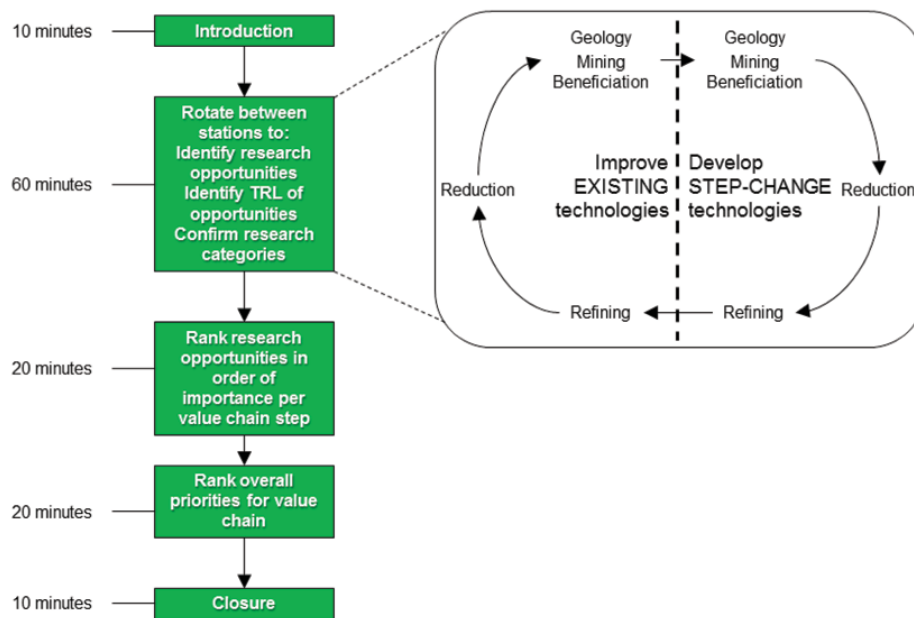


Figure 3—Workshop methodology

50% to develop step-change technologies. The research opportunities were revised to ensure there was no duplication or errors, and summarized into tables. The research opportunities were then consolidated into 21 research themes, which are presented in Table II. A more complete data-set is available online at <http://www.pyrometallurgy.co.za/InfaconXV/9999-Steenkamp-Tables.docx>

To obtain an understanding of the extent to which these research themes and opportunities have been investigated in South Africa and abroad, a review of relevant Infacon papers and Mintek reports was conducted. The results of the review are reported in the next section. Also included in the review are relevant papers published elsewhere that formed part of the existing knowledge base of the authors.

Literature review

Environmental efficiency

Handling, recycling, and re-using waste products

Waste products from manganese ferroalloy production are dust (formed in sinter belts and in SAFs), slag, and metal fines. Environmental concerns include problems experienced in the short term, *i.e.* exposure of employees and communities to dust, and as well as the long term, *i.e.* disposal on waste dumps where prevention of groundwater contamination by manganese leached from the waste products is a major challenge.

Dust suppression during sintering is a key area of concern. To address the problem, a two-stage system was implemented in which the baghouse system on the cooling section was separate from the one on the sintering section. The latter was considered a novelty (Osypenko *et al.*, 2015). Cleaning of off-gas emitted by SAFs results in two types of waste products: dry dust in bag filter off-gas cleaning

systems and sludge in wet scrubber systems. In both instances, dust is disposed of as landfill. To minimize air pollution from these landfill sites, bag plant dust is agglomerated (Davey, 2004; and also according to work done at Mintek in 1987). Not only can the dust then be disposed of at landfill sites, but agglomeration techniques also allow for recycling of dust, together with metal fines, to SAFs (Davey, 2004). Alternative treatment methods proposed for sludge handling include drying and sintering to fume the zinc present in the sludge (Hamano *et al.*, 2010) or smelting in a centralized facility to produce high-MnO slag (to be recycled as feedstock to a SiMn smelter) together with a small amount of alloy rich in phosphorus and boron, and fume containing > 99% of the zinc and > 90% of the alkalis (Gaal, Tangstad, and Ravary, 2010). Melting of metal fines in a separate DC arc furnace was also investigated at Mintek in the 1980s, and found to be technically feasible. Converter dust produced during the refining of HCFeMn contains significant amounts of MnO (Lee *et al.*, 2010). Applications as soft ferrite, lubricant in oil drilling, and pigment for refractory, were considered. An aluminothermic reduction process was also developed to produce an alloy containing > 90% Mn at 86% Mn recovery (Lee *et al.*, 2010).

When it meets environmental requirements, slag is typically used as road base or as aggregate (Gaal, Tangstad, and Ravary, 2010) but in South Africa slag produced in HCFeMn production is disposed of as landfill. Manganese can be recovered from these slags by pyrometallurgical or hydrometallurgical means. Metallothermic reduction processes are based on FeSi, Si, Al, or pig iron as reductants (Banda and Lagendijk, 2017a, 2017b; Dashevskiy *et al.*, 2013; Kamata, Kuzi, and Tsujimura, 1992), and sulphuric acid is used to leach manganese (Groot *et al.*, 2013; Kazadi *et al.*, 2013, 2016; Sancho *et al.*, 2015). In both cases, it is not only the recovery of manganese that is of economic interest, but also the production of high-value byproducts that can be used as cement extenders.

Working towards an increase in manganese ferroalloy production in South Africa

Using alternative reductants and sources of electricity to reduce carbon emissions

CO₂ emissions are harmful to the environment. As they use carbothermic reduction processes (with coke, anthracite, and coal as reductants), manganese ferroalloy producers are also producers of CO₂. In South Africa, the problem is exacerbated by the fact that electricity is produced mainly at coal-fired power stations. Charcoal (Monsen, Tangstad, and Midtgaard, 2004; Monsen *et al.*, 2007) or other biofuels (Zhao, Zhu, and Cheng, 2010) from renewable sources could potentially be used as reductants in smelting, to reduce carbon emissions. Alternatively, hydrogen gas (H₂) could be utilized in the prereduction of manganese ores (Kononov, Ostrovski, and Ganguly, 2007), with methane as potential source of H₂ and CO through the cracking of CH₄ (Anacleto, Ostrovski, and Ganguly, 2004; Bhalla and Eric, 2015; Ostrovski, Anacleto, and Ganguly, 2004). Potential green technologies for power generation include photovoltaic (PV) plants, wind power, concentrated solar power (CSP) plants, and tidal energy, and for transportation, electrical or fuel-cell-driven equipment. The application of CSP in the preheating and sintering of manganese ores is currently being investigated (Hockaday, Dinter and Harms 2016; Hockaday *et al.*, 2017).

Resource efficiency

Improving knowledge of geometallurgy

Geometallurgy is the linking of geology, mining, and metallurgy, and understanding the implications of these links (Chetty, 2008). In smelter operations it leads to improved understanding of input materials and their effects on smelter operations. In the SAF, manganese ore is reduced in the solid state by CO gas to MnO and Fe, and in the liquid state in the coke bed to Mn and Si. If the ore reaches 800°C without being fully reduced to MnO and Fe, the CO₂ produced in the solid-state reduction reactions will increase the reductant and energy consumption due to the endothermic Boudour reaction (Tangstad *et al.*, 2004; Visser *et al.*, 2013). Therefore, for solid-state reactions ore properties of importance are the oxidation state (Featherstone, 1974; Chetty and Gutzmer, 2008), reducibility (Kumar, Ranganathan, and Sinha, 2007), and more specifically CO gas reactivity (Tangstad *et al.*, 2001; Pochart *et al.*, 2007; Visser *et al.*, 2013). For liquid-state reactions, electrical conductivity (Miyachi, Mochida, M., and Fuchi 2001; Miyachi *et al.*, 2004) and melting properties (Ringdalen, Gaal, and Ostrovski, 2010; Visser *et al.*, 2013) are important. In terms of other raw materials, the CO and slag reactivities of the carbon materials are of importance (Grishchenko *et al.*, 2015; Monsen, Tangstad, and Midtgaard, 2004; Pistorius, 2002; Safarian *et al.*, 2006, 2008; Safarian and Kolbeinsen, 2008), as is the dissolution rate of the quartz into slag (Maroufi *et al.*, 2015).

Treatment of ore fines

As SAF technology typically requires a burden that is gas-permeable, particles less than 6 mm in size are screened out either at the mine or at the smelter. These ore particles still meet the chemical requirements for smelting. To agglomerate these particles, sinter-strand technology with coke breeze as

fuel source is applied on the industrial scale (Pienaar and Smith, 1992). Sintering also results in savings in transport cost per manganese unit, and decreased energy consumption in the SAF. Baghouse dust, scrubber sludge, quartz fines, HCFeMn slag fines, coke fines, and alloy fines could also be added to the sinter mix if sintering occurs at the smelter (Crawford *et al.*, 1995; Malan *et al.*, 2004). Prereduction of ore fines in a fluidized bed reactor (Crawford *et al.*, 1995) with subsequent smelting in a DC arc furnace has been tested at pilot scale. Technologies incorporating a dual energy source consisting of an inductor and oxygen-enriched combustion zone have been evaluated up to demonstration scale (Coetsee *et al.*, 2015).

Treatment of low-grade ore

Today, Mamatwan-type ore is not only beneficiated locally but also exported for processing overseas. Ironically, in the 1970s Mamatwan-type ore was deemed unsuitable for processing in a SAF due to the high carbonate contents (Featherstone, 1974) but SAF operators adjusted their practices to allow for higher carbonate contents. Managing the Mn/Fe ratio of the ores from the Northern Cape Province remains a challenge and a significant amount of ore with low manganese content is available. To increase the Mn/Fe ratio, wet or dry magnetic separation of fine ore with subsequent agglomeration of the nonmagnetic fraction through sintering or briquetting could be applied (Kutsin *et al.*, 2015). Prior to magnetic separation, a magnetizing roasting step, with or without subsequent milling, could improve separation (Ghorpade, 1995; Kivinen, Krogerus, and Daavittila, 2010; Samuratov, Baisanov, and Tolymbekov, 2010 and also at Mintek in 1981 and 1987). Alternatively, pig iron and high, MnO slag could be produced in a blast furnace and the slag further processed in a SAF (Ghorpade, 1995; Zhang, 1992).

Process improvements focusing on resource efficiencies

Proposed process improvements specifically associated with resource efficiencies included increasing the sinter/ore ratio into the SAF, combining silicon carbide (SiC) and carbon (C) as reductants in SiMn production, and removal of alkalis (including potassium) prior to smelting. No references on such applications were found during the review.

Energy efficiency

Alternative sources of fuel

Apart from the green technologies already listed as alternative sources of energy, shaft furnace (Suzuki and Masukawa, 1992) or blast furnace (Basson, Curr, and Gericke, 2007; Featherstone, 1974) technology could also be considered as these furnaces utilize the combustion of coke and/or pulverized coal in order to meet the process energy requirement. On the other hand, switching to fossil fuel-fired furnaces will increase a plant's CO₂ output and reduce its environmental efficiency. In the South African context, where electricity is produced mainly in coal-fired power stations, power generation should be taken into account when studying the environmental efficiency of any alternative. A desktop study is currently underway at Mintek to evaluate

Working towards an increase in manganese ferroalloy production in South Africa

the feasibility of COREX and FINEX technology for HCFeMn production (Sithole, Bam, and Steenkamp, 2018).

Pretreatment of ore

Preheating, precalcination, or prereduction, particularly of carbonate-rich manganese ores, has the potential to reduce the electrical energy requirement by 25 to 35% (Kalenga Xiaowei, and Tangstad, 2013; Tangstad, Ichihara, and Ringdalen, 2015). Sintering is an example of a calcination process in which the carbonate content of ore is lowered (Pienaar and Smith, 1992). On the industrial scale, a rotary kiln has been installed upstream from a SAF for prereduction of the ore (Tangstad Ichihara, and Ringdalen, 2015). Leaching of carbonate-rich ores to reduce the carbonate content has also been proposed (Featherstone, 1974).

Energy recovery from off-gas

Many SAFs operated in South Africa are of open furnace designs where the off-gas, slag, and alloy all contains latent heat that could be recovered and used elsewhere. Furthermore, by converting SAFs to closed designs one could potentially reduce energy losses and allow for the utilization of carbon monoxide (CO) in off-gas for preheating and/or prereduction, or generation of electricity (Ghorpade, 1995; Hunsbedt *et al.*, 2007; Kitamura, 1983).

Electrode tip position determination

Coke bed management is important in SAF operations (Lee and Tangstad, 2010). Development of technology to determine the electrode tip position would be useful. Development of a thermodynamic and/or electrical model to measure the level of the coke bed has been found to be useful (Yamamoto *et al.*, 1986).

Minimizing metal fines generation

The market for manganese ferroalloy fines is basically nonexistent as steel producers have specific size requirements for products that meet the requirements of their material handling and feeding systems, as well as process conditions. In SiMn production, casting alloy in a double-strand casting machine resulted in much less fines generated compared to layer casting (Bezemer, 1995).

Revisiting furnace designs

Revisiting furnace designs and dimensions (Nishi, Saitoh, and Teguri, 2007; Swamy *et al.*, 2001; Bisaka, Griesel, and Bouwer, 2004), including improved refractory design for decreased wear and improved efficiencies (O'Shaughnessy and Le Roux, 2015; Steenkamp, 2014; Steenkamp, Pistorius, and Tangstad, 2015a, 2015b; 2015c), could be useful from an energy efficiency perspective, as would the development of reliable measurement techniques for temperature, refractory wear (Sadri, Gebiski, and Shameli, 2010), and water leak detection (Eidem, Egeland, and Baumann, 2013). As DC technology could potentially allow for improved energy efficiency by decoupling power input from coke bed resistivity, revisiting application of the technology in different configurations could also be useful (Jones, Barcza, and Curr, 1993) and work in this regard has been undertaken at Mintek in 2016.

Improving converter technology

As with the SAFs, improving existing converter technology (Burger and Masukawa, 2004; Cowx *et al.*, 2015) by improving energy efficiency or developing a thermodynamic model (Nell and Nolet, 2010) to describe converter refining of HCFeMn would be useful in attempts at improving operational efficiencies.

Alternatives to converting

Alternatives to converting that were proposed included refining liquid alloy straight from tapping and utilizing argon-oxygen degasser (AOD) and vacuum-oxygen degasser (VOD) type processes applied in steelmaking in manganese ferroalloy production. No references to any of these applications were found in the literature – the latter being technically not feasible due to the high vapour pressure of manganese – but alternative methods were identified. These included solid-state decarburization of carbon-rich manganese carbide powders in a flowing stream of carbon dioxide (Bhonde and Angal, 2004), refining of SiMn in a two-stage process consisting of a smelting step in an electric arc furnace followed by treatment in a shaking ladle (Jinhua and Zhizhong, 1992), and silicothermic reduction of manganese-bearing slags used to produce MCFeMn (Channon and See, 1977). The latter technique was applied on an industrial scale in South Africa (Bezemer, 1995), but the facility is currently decommissioned. In Japan (Yamamoto *et al.*, 1986), a similar process was replaced by converter technology.

Productivity of labour

The research topics listed in this section contain only a summary of the research opportunities identified in the workshop. A literature study on any of the topics or themes falls beyond the scope of this document.

Developing skills levels

In terms of skills development, it was proposed that local training centres were to be established, teaching not only technical skills but also transferring knowledge on the value chain, basic economics, and basic metallurgy. Furthermore, employees should be given the opportunity to use current plant problems as potential topics for postgraduate studies, one such potential topic being an evaluation of the economic feasibility of the various alternative technologies listed here. As an example: in Norway, producers of ferroalloys release employees for a three-year period to study full-time towards a PhD at the Norwegian University of Science and Technology. Often, the research topic is chosen and (partially) funded by the producer. This arrangement benefits the producer through the development of new knowledge, as well as its employees. Such studies will build the capacity studies of local universities and ensure quality education for future generations.

Creating incentives

It was proposed that companies commit to educate children of employees, implement profit sharing schemes for employees, and create incentives for labour to multi-skill. In terms of

Working towards an increase in manganese ferroalloy production in South Africa

academic support, remuneration of academics should be increased as should research funds. Discussion of this topic is beyond the scope of this paper.

Dependency on rail capacity

Reducing dependency on rail

To reduce dependency on rail capacity it was proposed that mining, pretreatment, and/or smelting processes be integrated close to the mine-site, resulting in only value-added products being transported rather than transporting gangue together with the manganese values. Reagents used in processing should be sourced closer to the smelter. Furthermore, clustering synergistic industries, where one plant uses the products of another, would be ideal, *e.g.* integrating a FeMn smelter with a steel plant (Kitamura, 1983; Yamamoto *et al.*, 1986). It was proposed that fines/slimes be transported pneumatically.

Developing railway infrastructure

Development of railway infrastructure within Africa, as well as improving railway transport security, could be useful, but discussion of this topic is beyond the scope of this paper.

Other

Creating tax benefits

Creating tax benefits (or other incentives) for local beneficiation of ores through smelting could be useful. Discussion of this topic is beyond the scope of this paper.

Mining manganese nodules (ocean-based)

Manganese nodules were leached in a laboratory-scale study to produce copper, nickel, and cobalt (Alex *et al.*, 2007). The leach residue, being rich in Mn and Si, was agglomerated and smelted in a DC furnace in combination with HCFeMn slag to produce SiMn. The economic feasibility of such a technology should be definitely be included in future studies.

Diversifying product ranges by producing higher value products

As the bulk of manganese ferroalloys are utilized in steelmaking, product ranges could be diversified by producing alloys that are more attractive to the steel industry. These include alloys that support the production of clean steel with very low levels of phosphorous, sulphur, and inclusions (Safarian and Kolbeinsen, 2013; Sjoqvist, Jonsson, and Berg, 2001) or specialized products with high levels of a desirable component (N or Si). Typically, all P present in the ore and reductants reports to the alloy phase (Pochart *et al.*, 2007; Tangstad *et al.*, 2004; Visser *et al.*, 2013) and subsequent dephosphorization of alloy can be done using BaO-MnO-BaF₂ slag (Chaudhary, Minj, and Goel, 2007). Sulphur distribution can be influenced by the basicity and CaO content of the slag (Saridikmen, Kucukkaragoz, and Eric, 2007). Titanium can be removed from SiMn alloy by purging with nitrogen (Chu, Chen, and Zeng, 2015). The nitrogen content of LCFeMn can be increased by solid-state nitriding with a mixture of nitrogen and hydrogen gas (Ghali *et al.*, 2010) to produce an alloy that could potentially replace nickel in stainless steel

production. Low-carbon SiMn with 20–30% Si is produced by upgrading standard SiMn alloy through the addition of Si wastes from the ferrosilicon industry (Park *et al.*, 2010), which not only increases the Si content of the alloy due to dissolution, but the carbon content is also reduced through the formation of SiC. Granulation of SiMn to produce a powder that can be stored in bags as raw material for electrolytic manganese production, and utilization of converter dust, rich in manganese, as alternative to electrolytic manganese were listed as ideas at the event, but no literature sources found on these topics during the review.

The way forward

Transforming ideas and proposed technologies into industrial applications that contribute to company profits and an improved society takes a long time. A roadmap is a tool that could ease the way towards implementation (Phaal, Farrukh, and Probert, 2004) and would be a useful aid in the implementation of the research agenda developed here. As a starting point, an example from Norway where a roadmap was developed to increase the use of natural gas in metal production is presented.

The Norwegian government prepared a series of roadmaps to guide the country towards reducing its CO₂ emissions by 2030 and 2050, in terms of the Paris Climate Agreement. The exercise included a roadmap for the process industry (Norsk Industri, 2006). In order to break down the proposed initiatives into more specific actions, research institutes (SINTEF and NTNU) and industry together prepared a roadmap for the use of gas in metal production (Dalaker *et al.*, 2017). The same methodology could be used for preparing a roadmap for increased manganese ferroalloy production in South Africa.

The work started by defining who the roadmap was written for and what the goals were. The two main goals were (1) to describe to the authorities the conditions and public framework needed to obtain the desired changes in industry, and (2) to give examples of potential technologies to develop. To achieve these goals, industry must be heavily involved in document preparation, and at the same time the document must be neutral and not represent specific companies. The current roadmap (Dalaker *et al.*, 2017) was therefore prepared by the research institutes, with industry involvement from several companies through cooperation on a dedicated project and several targeted workshops. The project was funded by SINTEF, the Norwegian Research Council, and industry partners acting either as individual companies or through the Norwegian Ferroalloy Producers Research Association.

The roadmap started by contextualizing the objectives and describing their importance. Then, to demonstrate that technological solutions were available, a wide range of relevant technologies were described. Technologies with a high potential were included notwithstanding whether they would require a long time (10–20 years) to implement or whether they could be industrialized in the near future. Technology readiness levels (TRLs), derived from the European Union Commission's definitions, and environmental impact were shown for each technology.

The section describing the need for public framework conditions, addressed mainly to the authorities, was divided

Working towards an increase in manganese ferroalloy production in South Africa

into two sections and described (1) prerequisites for technology development and (2) prerequisites for industrial use. Education and high competence in both academia and industry are required for technology development. Competence within specific areas described in the roadmap, as well as in general education, is needed. A good research infrastructure and a system for public funding of long-term research projects are also important. Industrialization of the new technologies, which is the main goal of the work, requires predictable conditions within several areas of the industry, and in this regard the authorities have a great influence. Availability and prices of operational inputs such as electricity and raw materials, as well as suitable infrastructure, fall under these conditions. Investment in new technologies is often hindered by lack of risk capital. Measures to increase the availability of risk capital and decrease the risk taken by the industrial companies are means to enhance introduction of new technologies.

As illustrated, a roadmap is a tool to inform role-players about the possibilities and requirements needed to reach specific objectives. A similar approach and roadmap could pave the way towards increased manganese ferroalloy production in South Africa.

Conclusions

To increase the production of manganese ferroalloys in South Africa, a research agenda was developed at a workshop hosted as part of the Second School on Manganese Ferroalloy Production in June 2016. The agenda consists of 21 research themes distilled from 95 research opportunities identified by participants in the workshop. The literature review that was conducted subsequent to the workshop indicated that the problems identified are not unique to the South African context. In particular, challenges associated with high prices of electricity and raw materials, as well as the need for higher yields and a stronger market for alloys, are also experienced elsewhere in the world. Many of the ideas generated at the workshop were not new as they have been addressed in the past, even on an industrial scale, locally or in other parts of the world. To implement the agenda, collaborative research between industry and research institutions and between institutions locally and overseas would be required. Studies should focus on the South African context: challenges with the supply of raw materials and energy as well as the need to develop human capital, and should evaluate both the technical and the economic feasibility of solutions proposed. A technology roadmap is a useful tool for directing such a collaborative research exercise, and the development of such a roadmap by industry and research institutions is strongly encouraged. Implementation of the roadmap will require support from the authorities.

Acknowledgements

This paper is published with the financial support and permission of Mintek. Inputs from delegates participating in the workshop at the 2nd School on Manganese Ferro-alloy Production are gratefully acknowledged.

References

- ALEX, T.C., GODIWALLA, K.M., KUMAR, S., and JANA, R.K. 2007. Extraction of silicomanganese from marine and low grade mineral resources. *Proceedings of INFACON XI*, New Delhi, India, 18-21 February 2007. Indian Ferro-Alloy Producers Association. pp. 206-214.
- ANACLETO, N., OSTROVSKI, O., and GANGULY, S. 2004. Reduction of manganese oxides by methane-containing gas. *ISIJ International*, vol. 44, no. 9. pp. 1480-1487.
- BANDA, W. and LAGENDIJK, H. 2017a. Metallothermic production of cement extender from manganese waste slags. *Proceedings of the 3rd Young Professionals Conference*, Pretoria, South Africa, 9-10 March 2017. Southern African Institute of Mining and Metallurgy, Johannesburg. pp. 331-334.
- BANDA, W. AND LAGENDIJK, H. 2017b. Metallothermic production of cement extender from manganese waste slags. *Proceedings of the 5th International Slag Valorisation Symposium*, Leuven, Belgium, 3-5 April 2017. KU Leuven.
- BASSON, J., CURR, T.R., and GERICKE, W.A. 2007. South Africa's ferro alloys industry - present status and future outlook. *Proceedings of INFACON XI*, New Delhi, India, 18-21 February 2007. Indian Ferro-Alloy Producers Association. pp. 3-24.
- BEZEMER, K. 1995. The silicomanganese production process at Transalloys. *Proceedings of INFACON VII*. Trondheim, Norway, 11-14 June 1995. Tveit, H., Tuset, J.K., and Page, I.G. (eds.). Norwegian Ferroalloy Producers Research Organization (FFF). pp. 573-580.
- BHALLA, A. and ERIC, R.H. 2015. Reduction behavior of manganese ore using methane gas. *Proceedings of INFACON XIV*, Kiev, Ukraine, 1-4 June 2015. pp. 461-469.
- BHONDE, P.J. and ANGAL, R.D. 2004. Rate control mechanism in solid state decarburization of ferromanganese. *Proceedings of INFACON X*, Cape Town, South Africa, 1-4 February 2004. Southern African Institute of Mining and Metallurgy, Johannesburg. pp. 163-172.
- BISAKA, K., GRIESEL, J., and BOUWER, P.H.F. 2004. Optimisation of SiMn production at Transalloys. *Proceedings of INFACON X*, Cape Town, South Africa, 1-4 February 2004. Southern African Institute of Mining and Metallurgy, Johannesburg. pp. 239-244.
- BURGER, R. and MASUKAWA, M. 2004. The production of refined ferromanganese at Cato Ridge alloys. *Proceedings of INFACON X*, Cape Town, South Africa, 1-4 February 2004. Southern African Institute of Mining and Metallurgy, Johannesburg. pp. 254-260.
- CHANNON, W.P. and SEE, J.B. 1977. The reduction of fluxed and non-fluxed manganese ores by ferromanganese silicide. Staff paper no. 1868. Mintek, Johannesburg, South Africa.
- CHAUDHARY, P.N., MINJ, R.K., and GOEL, R.P. 2007. Development of a process for dephosphorisation of high carbon manganese. *Proceedings of INFACON XI*, New Delhi, India, 18-21 February 2007. Indian Ferro-Alloy Producers Association. pp. 289-296.
- CHETTY, D. 2008. A geometallurgical evaluation of the ores of the northern Kalahari manganese deposit, South Africa. PhD thesis, University of Johannesburg, Johannesburg, South Africa.
- CHETTY, D. and GUTZMER, J. 2008. Quantitative X-ray diffraction as a tool for smelting optimization of Kalahari manganese ores. *Proceedings of the Ninth International Congress for Applied Mineralogy*. Brisbane, Australia, 8-10 September 2008. pp. 419-427.
- CHU, S.J., CHEN, P.X., and ZENG, S.L. 2015. Research on de-titanium of silicomanganese ferroalloy by blowing N₂. *Proceedings of INFACON XIV*, Kiev, Ukraine, 1-4 June 2015. pp. 497-504.
- COETSEE, T., MULLER, J., GROENEWALD, J., DU TOIT, A., and ZEELIE, D. 2015. The AlloyStream process for HCFeMn production. *Proceedings of INFACON XIV*, Kiev, Ukraine, 1-4 June 2015. pp. 91-98.
- COWX, P., NORDHAGEN, R., KADKHODABEIGI, M., ELS, L., and KERO, I. 2015. The use of fine water spray to suppress fume emissions when casting refined ferromanganese. *Proceedings of INFACON XIV*, Kiev, Ukraine, 1-4 June 2015. pp. 81-90.
- CORATHERS, L.A. 2017. Mineral commodity summaries 2017. *U.S. Geological Survey*. pp. 106-107.
- CRAWFORD, D.P., MAYFIELD, P.L.J., BREN, A.D., and OLSEN, A.H. 1995. Direct production of ferromanganese from Gemco sand concentrate and coal. *Proceedings of INFACON VII*, Trondheim, Norway, 11-14 June 1995. Tveit, H., Tuset, J.K., and Page, I.G. (eds.). Norwegian Ferroalloy Producers Research Organization (FFF). pp. 239-248.

Working towards an increase in manganese ferroalloy production in South Africa

- DALAKER, H., RINGDALEN, E., KOLBEINSEN, L., and MÅRDALEN, J. 2017. Road-map for gas in the Norwegian metallurgical industry: greater value creation and reduced emissions. SINTEF, Trondheim, Norway.
- DASHEVSKIY, V.Y., ALEKSANDROV, A.A., KANEVSKIY, A.G., and LEONTIEV, L.I. 2013. Extraction of manganese from the slag of silicothermal reduction of metallic manganese. *Proceedings of INFACON XIII*, Almaty, Kazakhstan, 9–12 June 2013. pp. 157–164.
- DAVEY, K. 2004. The development of an agglomerate through the use of FeMn waste. *Proceedings of INFACON X, the Tenth International Ferroalloys Congress*, Cape Town, South Africa, 1–4 February 2004. Southern African Institute of Mining and Metallurgy, Johannesburg. pp. 272–280.
- Directorate: Mineral Economics. 2016. South Africa's Mineral Industry 2014/2015. Department of Mineral Resources, Pretoria, South Africa, p. 128.
- EIDEM, P.A., EGELAND, K.A., and BAUMANN, D. 2013. Improved safety for manganese alloy smelting. *Efficient Technologies in Ferroalloy Industry: Proceedings of INFACON XIII*, Almaty, Kazakhstan, 9–12 June 2013, pp. 164–174.
- FEATHERSTONE, R.A. 1974. Applications of Mamatwan manganese ore. *Proceedings of INFACON I*, Johannesburg, South Africa, 22–26 April 1974. Southern African Institute of Mining and Metallurgy, Johannesburg. pp. 263–271.
- GAAL, S., TANGSTAD, M., and RAVARY, B. 2010. Recycling of waste material from the production of FeMn and SiMn. *Proceedings of INFACON XII*, Helsinki, Finland, 6–9 June 2010. Outotec Oyj. pp. 81–88.
- GEREFFI, G. and FERNANDEZ-STARK, K. 2011. Global Value Chain Analysis: A Primer. Center on Globalization, Governance & Competitiveness.
- GHALI, N.S., EISSA, M.M., MISHREKY, M.L., and EL-FAWAKHRY, M.K. 2010. Kinetics of nitriding process of ferromanganese alloy. *Proceedings of INFACON XII*, Helsinki, Finland, 6–9 June 2010. pp. 611–618.
- GHORPADE, S.Y. 1995. Strategic plan to abate pollution and beneficiate low grade manganese ore at Simiore's metal and ferroalloys plant. *Proceedings of INFACON VII*, Trondheim, Norway, 11–14 June 1995. Tveit, H., Tuset, J.K., and Page, I.G. (eds.). Norwegian Ferroalloy Producers Research Organization (FFF). pp. 151–164.
- GRISHCHENKO, S.G., OVCHARUK, A.N., OLSHANSKY, V.I., FILIPPOV, I.Y., TARAN, A.Y., CHALENKO, V.I., DUDYAK, V.N., and PAVLENKO, S.V. 2015. Mastering of ferrosilicon manganese melting with highly reactive reducing agent. *Proceedings of INFACON XIV*, Kiev, Ukraine, 1–4 June 2015. pp. 65–72.
- GROOT, D.R., KAZADI, D., PÖLLMANN, H., DE VILLIERS, J.P.R., REDTMANN, T., and STEENKAMP, J.D. 2013. The recovery of manganese and generation of a valuable residue from ferromanganese slags by a hydrometallurgical route. *Proceedings of INFACON XIII*, Almaty, Kazakhstan, 9–12 June 2013. pp. 1051–1060.
- HAMANO, T., SHEN, R., ZHANG, G., BROWN, P., and OSTROVSKI, O. 2010. Process of manganese furnace dust: drying and zinc oxide reduction. *Proceedings of INFACON XII*, Helsinki, Finland, 6–9 June 2010. pp. 143–154.
- HOCKADAY, S.A.C., DINTER, F., and HARMS, T.M. 2016. Opportunities for concentrated solar thermal heat in the minerals processing industry. *4th Southern African Solar Energy Conference (SASEC) 2016*, Stellenbosch University in Stellenbosch, South Africa, 31 October – 2 November 2016.
- HOCKADAY, S.A.C., REYNOLDS, Q.G., DINTER, F., and HARMS, T.M. 2017. Solar thermal treatment of manganese ores. *Proceedings of SolarPACES 2017*, Santiago, Chile, 26–29 September 2017.
- HUNSBEDT, L., COWX, P.M., FLATABØ, R., JOHANSEN, K.E., and BUSTNES, J.A. 2007. Environmental challenges for Norwegian Mn- Industry. *Proceedings of INFACON XI*, New Delhi, India, 18–21 February 2007. Indian Ferro-Alloy Producers Association. pp. 446–456.
- JABAREEN, Y. 2008. A new conceptual framework for sustainable development. *Journal of Environment, Development and Sustainability*, vol. 10. pp. 179–192.
- JINHUA, Z. and ZHIZHONG, L. 1992. The development of technology for the production of refined ferromanganese in China. *Proceedings of INFACON VI*, Cape Town, South Africa, 8–11 March 1992. Southern African Institute of Mining and Metallurgy, Johannesburg. pp. 145–147.
- JONES, R.T., BARCZA, N.A., and CURR, T.R. 1993. Plasma Developments in Africa. *Proceedings of the Second International Plasma Symposium: World Progress In Plasma Applications*, Palo Alto, California, 9–11 February 1993.
- KALENGA, M., XIAOWEI, P., and TANGSTAD, M. 2013. Manganese alloys production: Impact of chemical compositions of raw materials on the energy and materials balance. *Proceedings of INFACON XIII*, Almaty, Kazakhstan, 9–12 June 2013. pp. 647–654.
- KAMATA, R., KUZU, Y., and TSUJIMURA, H. 1992. The production of special SiMn using the gas and powder injection process. *Proceedings of INFACON VI*, Cape Town, South Africa, 8–11 March 1992. Southern African Institute of Mining and Metallurgy, Johannesburg. pp. 139–143.
- KAZADI, D., GROOT, D.R., PÖLLMANN, H., DE VILLIERS, J.P.R., and REDTMANN, T. 2013. Utilization of ferromanganese slags for manganese extraction and as cement additive. *Proceedings of the International Conference on Advances in Cement and Concrete Technology in Africa*, Johannesburg, South Africa, 28–30 January 2013. pp. 983–995.
- KAZADI, D.M., GROOT, D.R., DE VILLIERS, J.P.R., STEENKAMP, J.D., and PÖLLMANN, H. 2016. Control of silica polymerisation during ferromanganese slag sulfuric acid digestion and water leaching. *Hydrometallurgy*, vol. 166. pp. 214–221.
- KITAMURA, M. 1983. Improvement of the electric power consumption in silicomanganese smelting. *Proceedings of INFACON III*, Tokyo, Japan, 8–11 May 1983.
- KIVINEN, V., KROGERUS, H., and DAAVITILLA, J. 2010. Upgrading of Mn/Fe ratio of low-grade manganese ore for ferromanganese production. *Proceedings of INFACON XII*, Helsinki, Finland, 6–9 June 2010. pp. 467–476.
- Kononov, R., Ostrovski, O., and Ganguly, S. 2007. Carbothermal solid state reduction of manganese ores. *Proceedings of INFACON XI*, New Delhi, India, 18–21 February 2007. Indian Ferro-Alloy Producers Association. pp. 259–267.
- KUMAR, M., RANGANATHAN, S., and SINHA, S.N. 2007. Kinetics of reduction of different manganese ores. *Proceedings of INFACON XI*, New Delhi, India, 18–21 February 2007. Indian Ferro-Alloy Producers Association. pp. 241–246.
- KUTSIN, V.S., OLSHANSKY, V.I., FILIPPOV, I.Y., and CHUMAKOV, A.A. 2015. The development of fine manganese concentrate lumping technology at PJSC Nikopol Ferroalloy Plant. *Proceedings of INFACON XIV*, Kiev, Ukraine, 1–4 June 2015. pp. 22–26.
- LEE, K.J., MIN, D.S., PARK, C.S., PARK, Y.K., JO, C.H., and HONG, S.H. 2010. High purity Mn metal from Mn oxide dust produced during FeMn refining process. *Proceedings of INFACON XII*, Helsinki, Finland, 6–9 June 2010. pp. 197–206.
- LEE, Y.E. and TANGSTAD, M. 2010. Electric parameters for an efficient smelting performance of HCFeMn alloy. *Proceedings of INFACON XII*, Helsinki, Finland, 6–9 June 2010. pp. 569–578.
- MALAN, J., BARTHEL, W., and DIPPENAAR, B.A. 2004. Optimising manganese sinter plants process parameters and design. *Proceedings of INFACON X*, Cape Town, South Africa, 1–4 February 2004. Southern African Institute of Mining and Metallurgy, Johannesburg. pp. 281–290.
- MAROUFI, S., CIEZKI, G., JAHANSHAHI, S., SUN, S., and OSTROVSKI, O. 2015. Dissolution of silica in slag in silicomanganese production. *Proceedings of INFACON XIV*, Kiev, Ukraine, 1–4 June 2015. pp. 479–487.
- MIYAUCHI, Y., MOCHIDA, M., and FUCHI, Y. 2001. High thermal electrical property of manganese ore in production of high carbon ferromanganese. *Proceedings of INFACON IX*, Quebec City, Canada, 3–6 June 2001. The Ferroalloys Association, Washington. pp. 263–243.
- MIYAUCHI, Y., NISHI, T., SAITO, K., and KIZU, Y. 2004. Improvement of high-temperature electric characteristics of manganese ores. *Proceedings of INFACON X*, Cape Town, South Africa, 1–4 February 2004. Southern African Institute of Mining and Metallurgy, Johannesburg. pp. 155–162.
- MONSEN, B., TANGSTAD, M., and MIDTGAAR, H. 2004. Use of charcoal in silicomanganese production. *Proceedings of INFACON X*, Cape Town, South Africa, 1–4 February 2004. Southern African Institute of Mining and Metallurgy, Johannesburg. pp. 392–404.
- MONSEN, B., TANGSTAD, M., SVERTSEN, M., ISHAK, R., and MIDTGAARD, H. 2007. Charcoal for manganese alloy production. *Innovations in Ferro Alloy Industry. Proceedings of INFACON XI*, New Delhi, India, 18–21 February 2007. Indian Ferro-Alloy Producers Association. pp. 297–310.
- NELL, J. and NOLET, I. 2010. Development of a dynamic model for a manganese oxygen refining (MOR) converter. *Proceedings of INFACON XII*, Helsinki, Finland, 6–9 June 2010. pp. 579–588.
- NISHI, T., SAITOH, K., and TEGURI, D. 2007. The build-up of additional HCFeMn production capacity by the deepening of a furnace. *Proceedings of INFACON XI*, New Delhi, India, 18–21 February 2007. Indian Ferro-Alloy Producers Association. pp. 183–190.
- NORSK INDUSTRI. 2006. The Norwegian process industries' roadmap: combining growth and zero emissions by 2050.

Working towards an increase in manganese ferroalloy production in South Africa

- OLSEN, S.E., TANGSTAD, M., and LINDSTAD, T. 2007. Production of Manganese Ferroalloys. Tapir Academic Press, Trondheim, Norway.
- O'SHAUGHNESSY, P. and LE ROUX, F. 2015. Evaluation of furnace refractory linings after sixteen years of producing silicomanganese. *Proceedings of INFACON XIV*, Kiev, Ukraine, 1–4 June 2015. pp. 278–299.
- OSTROVSKI, O., ANACLETO, N., and GANGULY, S. 2004. Reduction of manganese ores by methane containing gas. *Transformation through Technology. Proceedings of INFACON X*, Cape Town, South Africa, 1–4 February 2004. Southern African Institute of Mining and Metallurgy, Johannesburg. pp. 173–183.
- OSYPENKO, V.V., OSYPENKO, V.D., SHUVAYEV, S.P., and KORKODOLA, I.I. 2015. Development and introduction of an innovative technology of exhaust gas purification for manufacture of manganese agglomerate. *Proceedings of INFACON XIV*, Kiev, Ukraine. 1–4 June 2015, pp. 724–732.
- PARK, J.H., PARK, G.H., PARK, C.I., MIN, D.J., JO, C.H., and LEE, Y.E. 2010. Thermodynamics of carbon removal by molten slags from manganese alloy melts. *Proceedings of INFACON XII*, Helsinki, Finland. pp. 601–610.
- PHAAL, R., FARRUKH, C.J.P., and PROBERT, D.R. 2004. Technology roadmapping - A planning framework for evolution and revolution. *Technological Forecasting and Social Change*, vol. 71, Issue 1–2, pp. 5–26.
- PIENAAR, P.C. and SMITH, W.F.P. 1992. A case study of the production of high-grade manganese sinter from low-grade Mamatwan manganese ore. *Proceedings of INFACON VI*, Cape Town, South Africa, 8–11 March 1992. Southern African Institute of Mining and Metallurgy, Johannesburg. pp. 131–138.
- PISTORIUS, P.C. 2002. Reductant selection in ferro-alloy production: The case for the importance of dissolution in the metal. *Journal of the Southern African Institute Mining and Metallurgy*, vol. 102, no. 1. pp.33–36.
- POCHART, G., JONCOURT, L., TOUCHARD, N., and PERDON, C. 2007. Metallurgical benefit of reactive high grade ore in manganese alloys manufacturing. *Proceedings of INFACON XI*, New Delhi, India, 18–21 February 2007. Indian Ferro-Alloy Producers Association. pp. 217–230.
- REIJNDERS, L. 2016. Conserving functionality of relatively rare metals associated with steel life cycles: a review. *Journal of Cleaner Production*, vol. 131. pp. 76–96.
- RINGDALEN, E., GAAL, S., and OSTROVSKI, O. 2010. Ore properties in melting and reductions in silicomanganese production. *Proceedings of INFACON XII*, Helsinki, Finland. pp. 487–496.
- SADRI, A., GEBSKI, P., and SHAMELI, E. 2010. Refractory wear and lining profile determination in operating electric furnaces using stress wave non-destructive testing (NDT). *Proceedings of INFACON XII*, Helsinki, Finland. pp. 881–890.
- SAFARIAN, J., GRONG, Ø., KOLBEINSEN, L., and OLSEN, S.E. 2006. A process model for the carbothermic reduction of MnO from high carbon ferromanganese slag - The model. *ISIJ International*, vol. 46. pp. 1120–1129.
- SAFARIAN, J. and KOLBEINSEN, L. 2013. Purity requirements for Mn-alloys for producing high manganese TRIP and TWIP steels. *Proceedings of INFACON XIII*, Almaty, Kazakhstan, 9–12 June 2013. pp. 175–184.
- SAFARIAN, J. and KOLBEINSEN, L. 2008. Kinetic of carbothermic reduction of mno from high-carbon ferromanganese slag by graphite materials. *ISIJ International*, vol. 48. pp. 395–404.
- SAFARIAN, J., TRANELL, G., KOLBEINSEN, L., TANGSTAD, M., GAAL, S., and KACZOROWSKI, J. 2008. Reduction kinetics of MnO from high-carbon ferromanganese slags by carbonaceous materials in Ar and CO atmospheres. *Metallurgical and Materials Transactions B*, vol. 39. pp. 702–712.
- SAMURATOV, Y., BAISANOV, A., and TOLYMBEKOV, M. 2010. Complex processing of iron-manganese ore of central Kazakhstan. *Proceedings of INFACON XII*, Helsinki, Finland. pp. 517–520.
- SANCHO, J., RECIO, J.C., FUENTES, A., AYALA, J., BERNARDO, J.L., and RODRIGUEZ, C. 2015. Electrolytic manganese from ferroalloy production furnace flying dust. *Proceedings of INFACON XIV*, Kiev, Ukraine, 1–4 June 2015. pp. 759–762.
- SARIDIKMEN, H., KUCUKKARAGOZ, C.S., and ERIC, R.H. 2007. Sulphur behaviour in ferromanganese smelting. *Innovations in Ferro Alloy Industry. Proceedings of INFACON XI*, New Delhi, India, 18–21 February 2007. Indian Ferro-Alloy Producers Association. pp. 312–320.
- SITHOLE, N.A., BAM, W.G., and STEENKAMP, J.D. 2018. Comparing electrical and carbon combustion based energy technologies for the production of high carbon ferromanganese: A literature review. *Proceedings of INFACON XV*, Cape Town, South Africa, 25–28 February 2018. Southern African Institute of Mining and Metallurgy, Johannesburg.
- SJOQVIST, T., JONSSON, P., and BERG, H. 2001. The effect of ferro manganese cleanness on inclusions in steel. *Proceedings of INFACON IX*, Quebec City, Canada, 3–6 June 2001. pp. 411–420.
- STATS SA. 2015. Labour market dynamics in South Africa. Statistics South Africa, Pretoria, South Africa. p. 3.
- STEENKAMP, J.D. 2014. Chemical wear of carbon-based refractory materials in a silicomanganese furnace tap-hole. PhD thesis, University of Pretoria, Pretoria, South Africa.
- STEENKAMP, J.D. and BASSON, J. 2013. The manganese ferroalloys industry in southern Africa. *Journal of the Southern African Institute of Mining and Metallurgy*, vol. 113. pp. 667–676.
- STEENKAMP, J.D., PISTORIUS, P.C., and TANGSTAD, M. 2015a. Wear mechanisms of carbon-based refractory materials in silicomanganese tap-holes - Part 1: equilibrium calculations and slag and refractory characterisation. *Metallurgical and Material Transactions B*, vol. 46B. pp. 653–667.
- STEENKAMP, J.D., PISTORIUS, P.C., and TANGSTAD, M. 2015b. Wear mechanisms of carbon-based refractory materials in SiMn tap-holes - Part 2: In-situ observation of chemical reactions. *Metallurgical and Material Transactions B*, vol. 46B. pp. 668–679.
- STEENKAMP, J.D., PISTORIUS, P.C., and TANGSTAD, M. 2015c. Chemical wear analysis of a tap-hole on a SiMn production furnace. *Journal of the Southern African Institute of Mining and Metallurgy*, vol. 115. pp. 199–208.
- SUZUKI, S. and MASUKAWA, M. 1992. High-productivity operation of a shaft-type ferromanganese smelting furnace. *Proceedings of INFACON VI*, Cape Town, South Africa, 8–11 March 1992. Southern African Institute of Mining and Metallurgy, Johannesburg. pp. 149–154.
- SWAMY, K.N., ROBERTSON, D.G.C., CALVERT, P., and KOZAK, D. 2001. Factors affecting carbon consumption in the production of high carbon ferromanganese. *Proceedings of INFACON IX*, Quebec City, Canada, 3–6 June 2001. pp. 293–301.
- TANGSTAD, M., CALVERT, P., BRUN, H., and LINDSETH, A.G. 2004. Use of Comilog ore in ferromanganese production. *Proceedings of INFACON X*, Cape Town, South Africa, 1–4 February 2004. Southern African Institute of Mining and Metallurgy, Johannesburg. pp. 213–222.
- TANGSTAD, M., ICHIHARA, K., and RINGDALEN, E. 2015. Pretreatment unit in ferromanganese production. *Proceedings of INFACON XIV*, Kiev, Ukraine, 1–4 June 2015. pp. 99–106.
- TANGSTAD, M., SIBONY, M., WASBO, S., and TRONSTAD, R. 2001. Kinetics of the prereluction of manganese ores. *Proceedings of INFACON IX*, Quebec City, Canada, 3–6 June 2001. pp. 202–207.
- VAN ZYL, H.J. 2017. Identifying barriers to growth in mineral value chains: an analytical framework approach. Master's dissertation, University of Stellenbosch, Stellenbosch, South Africa.
- VAN ZYL, H.J., BAM, W.G., and STEENKAMP, J.D. 2016. Identifying barriers faced by key role players in the South African manganese industry. *Proceedings of the 27th SAIIE Annual Conference*, Stonehenge in Africa, North West Province, South Africa, 27–29 October 2016..
- VISSER, M., SMITH, H., RINGDALEN, E., and TANGSTAD, M. 2013. Properties of Nchwaning and Gloria ore in the production of Mn ferroalloys. *Proceedings of INFACON XII*, Helsinki, Finland, 6–9 June 2010. pp. 553–566.
- YAMAMOTO, K., ITO, S., TERADA, S., SOEJIMA, T., and KURITA, Y. 1986. Improvement of energy efficiency by process computer for ferroalloy electric furnace, and production of medium or low carbon ferromanganese by direct decarbonization of FMnH melt. *Proceedings of INFACON IV*, Rio de Janeiro, Brazil, 31 August – 3 September, 1986. Associação Brasileira dos Produtores de Ferro-Ligas-Abrafe pp. 63–78.
- ZHANG, T. 1992. The two-stage production of high-carbon ferromanganese in a blast furnace: A method for the treatment of a lean manganese ore. *Proceedings of INFACON VI*, Cape Town, South Africa, 8–11 March 1992. Southern African Institute of Mining and Metallurgy, Johannesburg. pp. 155–159.
- ZHAO, Y., ZHU, G., and CHENG, Z. 2010. Thermal analysis and kinetic modeling of manganese oxide ore reduction using biomass straw as reductant. *Hydrometallurgy*, vol. 105. pp. 96–102. ◆



Influence of the power supply on the behaviour of DC plasma arcs – a modelling study

by Q.G. Reynolds

Synopsis

Direct current (DC) arc furnaces account for a significant proportion of installed pyrometallurgical capacity worldwide. Their applications include steel recycling and smelting of various materials such as ferrochromium, ferronickel, ilmenite, and other alloys. The rectifier power supply for such units is a major capital cost item, and errors in the design can result in considerable limitations being placed on the operating window of the furnace. In the present paper, computational plasma arc models developed using open-source software tools are applied to gain insight into the nature of interactions between the DC rectifier's transient behaviour, passive circuit elements such as smoothing chokes, and the dynamics of the arc. The effect of parameters such as choke inductance and thyristor firing angle is examined and interpreted with regard to possibilities for optimization of the design and operation of DC furnace power supplies in the future.

Keywords

DC arc furnace, power supply, arc dynamics, computational modelling.

Introduction

Open bath electric arc furnaces (EAFs), and in particular direct current (DC) arc furnaces, are used extensively in the metallurgical industry for a number of processes, including steel recycling and the production of ferroalloys such as ferrochromium and ferronickel (Jones, 2014). Many of the unique properties of DC arc furnaces that make them attractive for such processes are results of the presence of one or more plasma arcs, high-temperature, high-velocity jets of ionized gas that conduct electricity between the tip of the graphite electrode and the surface of the molten bath of process material inside the furnace vessel. Arcs are efficient mechanisms for converting electrical energy into thermal and mechanical energy, and act to heat and stir the bath intensely in the areas onto which they impinge (Jones *et al.*, 2011).

A number of electrical components are required in order to provide power to a DC EAF, as shown in simplified form in Figure 1. From the electrical grid or an equivalent high-voltage alternating current (AC) source, voltage and current are adjusted to appropriate levels using a transformer, then converted to DC using a rectifier – generally a thyristor-type design – and finally passed into the furnace via an inline inductor (Bowman and Kruger,

2009). Over short timescales the power delivered to the furnace is maintained by calculating a current set-point from the measured voltage (using $P = VI$) and passing that set-point to the power electronics controller in the rectifier, where it is used to adjust the firing angle of the thyristors in the rectifier – this has the effect of constantly modifying the voltage presented across the furnace and inductor circuit. The inductor serves two purposes: first, it filters high-frequency electrical fluctuations from the arc, which can result in undesirable harmonics being injected back through the furnace power supply and into the grid, and secondly, it acts as an energy reservoir to regulate current flow through the arc during these rapid high-frequency fluctuations.

Thyristor rectifiers operate by the regular opening (or 'firing') of thyristors, solid-state semiconductor devices, in a certain pattern so as to permit conduction between pairs of AC phases in a set provided by a transformer. Thyristors allow current to pass in only one direction, and then only after they have received a firing signal; as a result, adjustment of the delay of the firing signal relative to the zero-voltage point between pairs of phases (the 'firing angle') permits control of the output voltage of the rectifier. Once a thyristor is fired, it remains 'latched' in a conducting state until the current it is carrying drops below a certain threshold. Typically, this means that control adjustments to the DC output voltage of a thyristor rectifier can be made only at finite time intervals related to the number of distinct AC phases available from the transformer. Common industrial configurations include 6-, 12-, 18-, and 24-

* Mintek, South Africa.

© The Southern African Institute of Mining and Metallurgy, 2018. ISSN 2225-6253. This paper was first presented at the INFACON XV: International Ferro-Alloys Congress, 25–28 February 2018, Century City Conference Centre and Hotel, Cape Town, South Africa



Influence of the power supply on the behaviour of DC plasma arcs – a modelling study

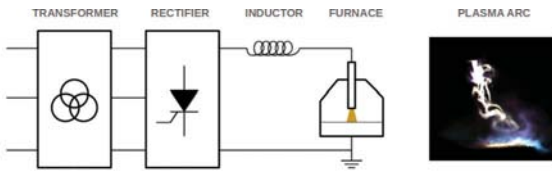


Figure 1—Basic elements of a DC arc furnace circuit (after Bowman and Kruger, 2009)

pulse (6, 12, 18, or 24 control actions in one full AC cycle respectively). An example waveform for a three-phase AC, 6-pulse system is shown in Figure 2. The firing angle α is indicated, as are the two phase voltages being fired against each other at any given time.

During a single pulse interval, the time-dependent output voltage produced by an ideal thyristor rectifier can be represented as the difference between two sine waves describing the pair of AC voltage phases being fired against one another:

$$V_P = \frac{V_{AC}}{2} \left[\cos\left(2\pi\omega t - \frac{2\pi}{N_P} + \alpha\right) + \cos(2\pi\omega t + \alpha) \right] \quad [1]$$

$$0 < t < t_{\max} \quad t_{\max} = \frac{1}{\omega N_P}$$

Here, V_P is the rectifier output voltage, V_{AC} is the peak-to-peak voltage of the input AC phases, ω is the input AC frequency, and N_P is the number of pulses. The mean DC voltage during a single pulse interval may be derived from Equation [1] as:

$$V_{DC} = \frac{V_{AC} N_P}{2 \pi} \cos \alpha \sin \frac{2\pi}{N_P} \quad [2]$$

The rectifier output voltage V_P feeds a circuit consisting of an inductor and a plasma arc in series. Any variability of current over time generates a voltage across the inductor, which in turn affects the voltage available to the arc. A simple circuit model using an ideal inductor may be constructed as:

$$V_P(t) = L \frac{dI}{dt} + V_a(I, t) \quad [3]$$

Here, L is the inductance of the inductor, I is the arc current, and V_a is the arc voltage.

In the case of an idealized, perfect constant-current rectifier, current does not vary over time and the inductor potential therefore remains zero; in order to achieve this, V_P must be controlled to be equal to V_a at all times. In the case of a thyristor rectifier (for a single pulse interval), V_P is given by Equation [1] and V_a and I both vary as functions of time for the duration of the pulse, depending on the properties of the arc and inductor.

In the present work, some preliminary explorations of Equation [3] are conducted using computational methods to calculate the arc's electrical response, and to evaluate the system behaviour as a function of several parameters relevant to the design and operation of DC furnace power supplies.

Model development

In order to capture the rapid transient behaviour of the plasma arc over short time intervals, a computational

magnetohydrodynamic model is used. Such models combine fluid flow, heat transfer, and electromagnetism in a coupled system which is solved using numerical methods. Several assumptions are made: the plasma in the arc is in local thermodynamic equilibrium, in which all physical properties of the plasma fluid are described as complex functions of temperature, and the flow is incompressible, which is valid for low-current arcs in which the velocities do not approach or exceed mach 1. The governing equations for computational plasma arc models under such conditions have been described in more detail elsewhere (Reynolds, 2015, 2017) but are presented here for reference:

$$\frac{\partial(\rho \mathbf{u})}{\partial t} + \nabla \cdot (\rho \mathbf{u} \mathbf{u}) + \nabla P = \quad [4a]$$

$$\nabla \cdot \boldsymbol{\tau}_{ij} + \mathbf{j} \times \nabla \times \mathbf{A} - \rho \mathbf{g}$$

$$\frac{\partial \rho}{\partial t} + \nabla \cdot (\rho \mathbf{u}) = 0 \quad [4b]$$

$$\frac{\partial(\rho C_p T)}{\partial t} + \nabla \cdot (\rho C_p \mathbf{u} T) = \quad [4c]$$

$$\nabla \cdot \left(k \nabla T + \frac{5k_B \mathbf{j} T}{2e} \right) + \frac{\mathbf{j} \cdot \mathbf{j}}{\sigma} - Q_R$$

$$\mathbf{j} = -\sigma \left(\nabla \Phi + \frac{\partial \mathbf{A}}{\partial t} - \mathbf{u} \times \nabla \times \mathbf{A} \right)$$

$$\nabla \cdot \mathbf{j} = 0 \quad \nabla^2 \mathbf{A} = -\mu_0 \mathbf{j} \quad [4d]$$

Here, \mathbf{u} is the velocity vector field in the arc, P is the pressure field, \mathbf{j} is the electric current density, \mathbf{A} is the magnetic vector potential, Φ is the electric potential, and T is the temperature field. $\boldsymbol{\tau}_{ij}$ is the viscous stress tensor. ρ is the plasma density, C_p is its heat capacity, k is its thermal conductivity, and σ is its electrical conductivity. Q_R is the volumetric radiation emission coefficient for the plasma (a strong function of temperature), k_B is the Boltzmann constant, e is the fundamental charge, and μ_0 is the magnetic permeability of free space. Boundary conditions must be supplied to complete the solution of Equation [4], and are presented elsewhere (Reynolds, 2015, 2017).

Equation [4] is solved numerically using the finite volume method, in which the geometric region of interest is broken up into a large number of volume elements over which rigorous mass, momentum, and energy balances are

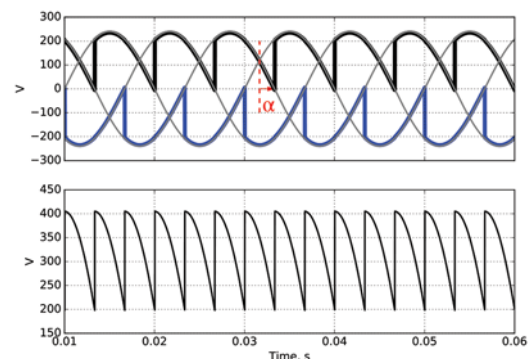


Figure 2—(Top) AC phases showing firing angle and positive and negative DC components, (bottom) resulting DC output voltage

Influence of the power supply on the behaviour of DC plasma arcs – a modelling study

performed to give a set of coupled equations for the field values at each element. This set of equations is solved at each discrete time-step in the model using matrix methods. Models used a geometric resolution of 350 000 volume elements for approximately 3×10^6 degrees of freedom. The models were implemented using version 5.0 of the OpenFOAM® open source computational mechanics framework (OpenFOAM Foundation, 2017), and executed using Linux-based high-performance computing facilities.

The furnace geometry used in the models is shown in Figure 3. The molten bath of process material is at A and is treated as a flat surface forming the anode electrical connection. The body of the graphite electrode is at B, and the conductive tip of the electrode is at C and forms the cathode. Boundary D is open to the atmosphere inside the furnace freeboard. Because of the very rapid nature of arc and rectifier dynamics (of the order of 1 ms) compared to the dynamics of free surface flow in slag or metal melts (of the order of 100 ms), treatment of the anode surface as static for the duration of a rectifier pulse is deemed to be an acceptable approximation. It should be noted, though, that the shape of the anode surface at any given instant is unlikely to be flat as considered here – the arc imparts significant mechanical force to the free surface of the melt and substantial disruption of the interface is expected as a result (Reynolds, 2017). However for the purposes of this study it was felt that consideration of variable geometry at the anode would introduce additional uncertainty and complexity into the results and detract from the topic of focus, which is the electrical behaviour. Study of such variations is therefore left to future work on the subject.

The plasma arc model is combined with the circuit model (Equation [3]) using a backward Euler numerical integration method. In the case of a constant-current power supply the voltage supplied at the cathode in the arc model, V_a , is iteratively adjusted to the point at which the current produced by the arc model matches the desired current set-point at each time-step. In the case of a thyristor supply, V_a is iteratively adjusted until the current produced by the arc model satisfies the relationship in Equation [3] at each time-step, based on the values of V_P and L .

In order to quantify the system behaviour, an ensemble forecasting approach is applied. Ensemble forecasts entail running multiple simulations to predict outcomes from a collection of similar starting conditions, and then analysing the degree of variation in the results (Leutbecher and Palmer, 2008). In the case of the combined plasma arc and circuit model, this was achieved by first running a long simulation at constant current, then randomly extracting from the results a set of conditions with instantaneous arc voltages similar to the mean value. These conditions were then used as the

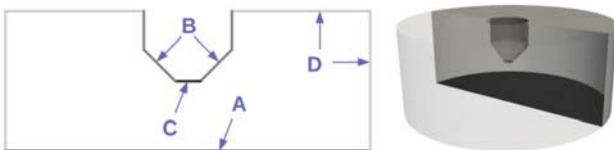


Figure 3—Geometry and boundaries used for computational arc models, with visualization of a half-section of the model region to show 3D structure at right

starting points for simulations of a single pulse interval of a thyristor power supply, *i.e.*, the period during which external control actions are not possible and the system simply responds to the supply voltage V_P , given by Equation [1]. The resulting deviation of current I away from the constant current set-point over the pulse interval was taken as an indication of the controllability of the power supply.

Results and discussion

The base case parameters used in the study are given in Table I, and are representative of a small pilot-scale DC arc furnace.

Here, H_A is the arc length from electrode tip to anode surface, d_E is the electrode diameter, and d_C is the diameter of the cathode tip. I_{SP} is the fixed current that is applied during constant-current simulations. T_E and T_A are the maximum permitted temperatures on the electrode and anode boundaries respectively, and T_F is the inlet temperature of gas from the surrounding freeboard region.

Generation of ensemble member starting conditions

In order to produce the ensemble starting conditions used by all subsequent simulations, the base case model was set up to run for 100 ms of in-model time while operating in constant current mode. An impulsive start initial condition was used in which a column of high-temperature plasma was inserted between the electrode tip and the anode surface, at zero velocity. The evolution of arc voltage with time is depicted in Figure 4, and shows clearly how the rapid chaotic motion of the arc column influences its electrical characteristics.

The average arc voltage for the period after the initial conditions had decayed was approximately 195.7 V. Ten points close to this value were randomly selected from the data output by the constant current simulation, indicated as solid circles in Figure 4. Field data at these points was saved and used as the initial condition for each member of the ensemble forecast. Visualizations of the arc's temperature field for each ensemble starting condition are shown in Figure 5.

Combined circuit model – base case results

Using the base case parameters in Table I, the combined circuit model using a thyristor power supply was executed for each member of the ensemble starting conditions. The value of V_{AC} used in Equation [1] was found from Equation [2] for each ensemble member, with V_{DC} equal to the instantaneous arc voltage at the start of the simulation. The simulations were run for a single pulse interval – in the case of a 12-pulse thyristor system at 50 Hz, this is a period of 1.67 ms.

Table I

Base case model parameters

Parameter	Value	Parameter	Value
H_A	0.1 m	I_{SP}	1000 A
d_E	0.1 m	Plasma gas	Air
d_C	0.02 m	T_E	4100 K
T_F	2000 K	T_A	3000 K
L	100 μ H	N_P	12
α	30° ($\pi/6$)	ω	50 Hz

Influence of the power supply on the behaviour of DC plasma arcs – a modelling study

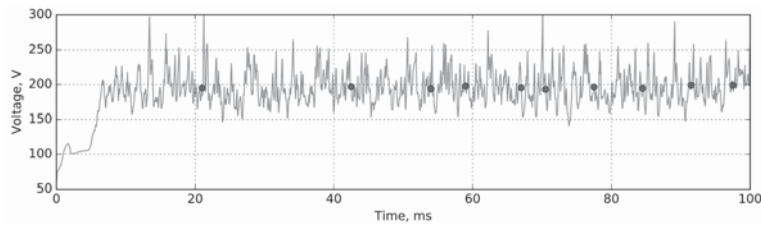


Figure 4—Evolution of arc voltage over time, constant current 1000 A

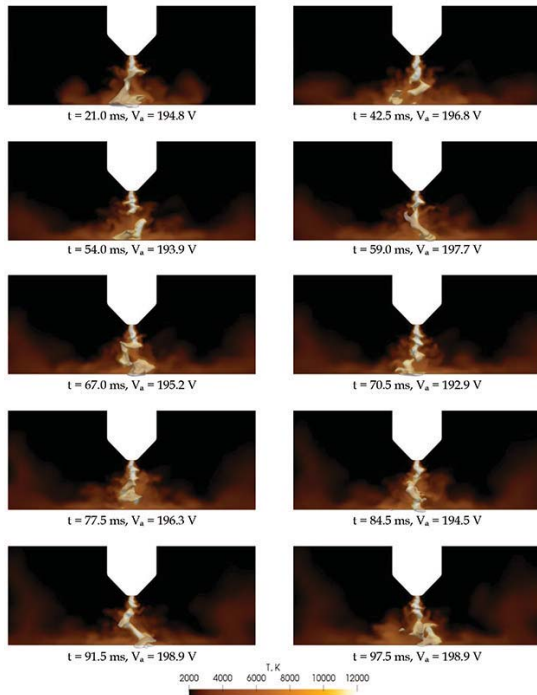


Figure 5—Visualizations of the arc temperature field for each ensemble member (the 3D temperature contour for 7500 K is also shown)

Results from a single ensemble member simulation are shown in Figure 6. The presence of an inductive load in the circuit causes deviations between the power supply voltage V_p and the arc voltage V_a , which are balanced by the inductor voltage generated by the variation of the arc current with time.

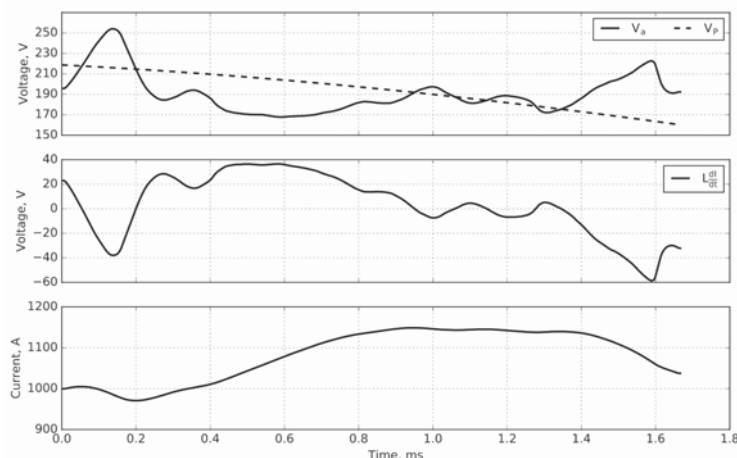


Figure 6—(Top) arc and power supply voltages, (middle) inductor voltage, (bottom) circuit current over time, single simulation

Results from all ten ensemble simulations at base case conditions are shown in Figure 7. The total range of currents covered by the simulation trajectories is shown in grey shading.

It can be seen that although all simulations start at the initial current of 1000 A, it is possible to have movement away from this value in both positive and negative directions during a single thyristor pulse.

Combined circuit model – effect of inductance

In order to study the effect of the inductor on the system behaviour, the inductance L was varied between 0 and 400 μH while keeping all other parameters fixed at base case conditions. The spread of currents over the duration of a single thyristor pulse was calculated from the set of ensemble trajectories from simulations at each inductance value. The ensemble results for 0, 10, and 50 μH are shown in Figure 8.

It is clear that with insufficient inductance present, the circuit current over a single thyristor pulse is capable of diverging rapidly to very large or very small values (see also Figure 9), making control of such a system challenging.

In real systems a small amount of inductance is generally unavoidable due to the circuit loop between furnace and rectifier (of the order of 10–20 μH). Although this is not enough to prevent arc extinction or over-current, it does have some mitigating effect on the range of currents attained in the model. Adding a moderately sized DC line inductor ($> 50 \mu\text{H}$) significantly decreases the variation in current possible over a single pulse interval, making control at pulse-interval time-steps more feasible.

The range of currents obtained for each value of L simulated is shown in Figure 10, demonstrating the limitation of current variation by larger inductors.

Influence of the power supply on the behaviour of DC plasma arcs – a modelling study

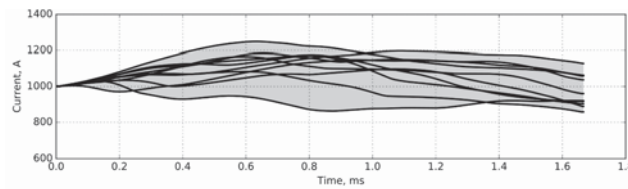


Figure 7—Circuit current over time, all ensemble members

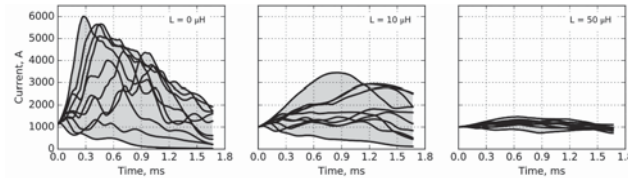


Figure 8—Ensemble simulation results for circuit current at different values of L

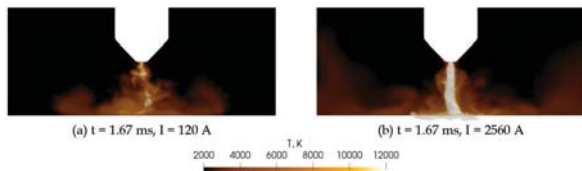


Figure 9—Selected member results from ensemble simulation at $L = 10 \mu\text{H}$; (a) arc extinction due to current decay, (b) over-current excursion

Circuit model – effect of firing angle

The effect of changing the firing angle α was examined by varying the value between 0° (0) and 75° ($5\pi/12$) while keeping all other parameters fixed at base case conditions. This is equivalent to changing the peak-to-peak AC voltage, for example by selecting different tap settings on the transformer while keeping the system operating point fixed. As per Equation [1], this causes changes in the variation in V_P over the duration of a pulse, as shown in Figure 11.

To determine the impact this has on the combined circuit model, the spread of currents over the duration of a single thyristor pulse was calculated using the set of ensemble trajectories from simulations at each firing angle value, as before. The results for 0° , 60° , and 75° are given in Figure 12.

The range of currents attained for each value of firing angle simulated is given in Figure 13. Increasing the firing angle increases the variability in V_P , which in turn increases the variability in I .

It is interesting to observe that although the current ranges at the *end* of a pulse remain reasonably similar, the currents rise and fall more appreciably *during* the pulse for larger firing angles. Larger values of L would also be expected to mitigate this effect.

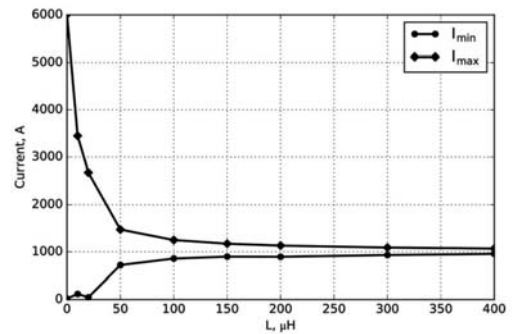


Figure 10—Minimum and maximum currents observed in ensemble results as a function of L

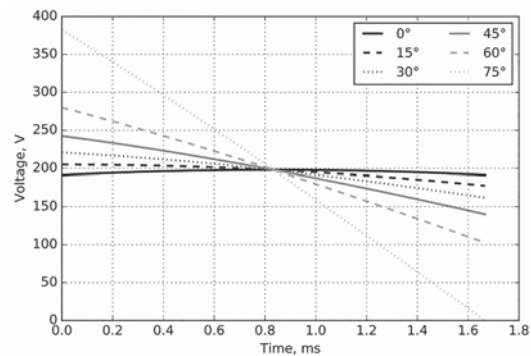


Figure 11— V_P as a function of time for a single thyristor pulse at different firing angles, for $V_{DC} = 195.7 \text{ V}$

Circuit model – effect of pulse count

The effect of using a different number of pulses in the design of the thyristor power supply was examined by changing the value of N_P between 6 and 24, while keeping all other variables fixed at the base case values. As per Equation [1],

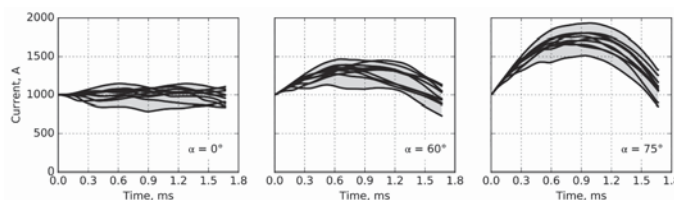


Figure 12—Ensemble simulation results for circuit current at different values of α

Influence of the power supply on the behaviour of DC plasma arcs – a modelling study

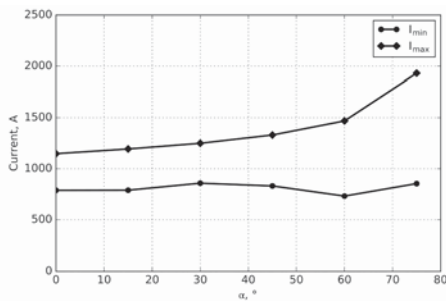


Figure 13—Minimum and maximum currents observed in ensemble results as a function of α

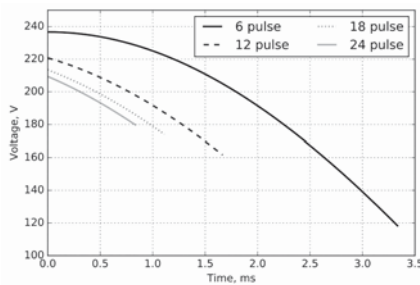


Figure 14— V_P as a function of time for a single thyristor pulse at different pulse counts, for $V_{DC} = 195.7$ V

larger pulse counts lead to shorter pulse intervals and therefore a reduction in the variability of V_P over the pulse – this is shown graphically in Figure 14.

As with the firing angle effect, larger pulse counts are generally expected to exhibit smaller variations in DC current. The model results bear this out to some degree; as shown in Figure 15 the spread of currents resulting from a single 6-pulse interval is considerably greater than that of a 24-pulse interval.

The range of currents observed in each ensemble simulation for different N_P values is shown in Figure 16.

Up to a point, increasing the number of pulses reduces the current variability, but then appears to level off in effectiveness. It is, however, important to recall that these results are for a fixed value of L ; in practice, both L and N_P are optimized together for a given power supply design to effect a desired reduction in current variability over a pulse interval.

Conclusions

A combined circuit model of the behaviour of DC furnace power supplies was successfully developed using computational plasma arc models. The model was used to examine the effect of changing basic parameters of a typical thyristor power supply for a small-scale pilot furnace.

Increasing the series inductance in the DC circuit was seen to reduce current deviations due to arc behaviour over the duration of a single thyristor pulse, an important requirement for the correct operation of power electronics controllers. Low pulse-count designs (particularly 6-pulse) and operation at high firing angles were seen to be undesirable conditions that may lead to increased variability in the current delivered by the power supply. This preliminary work suggests that there may be scope to improve on existing DC furnace designs by taking into account not only the dynamics introduced by the rectifier power electronics, but also the dynamics of the arc; these are typically considerably

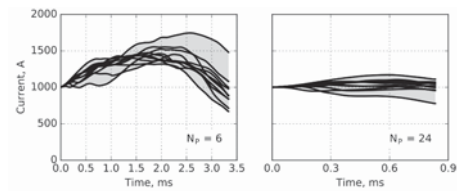


Figure 15—Ensemble simulation results for circuit current at different values of N_P

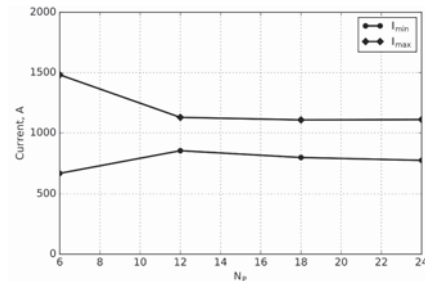


Figure 16—Minimum and maximum currents observed in ensemble results as a function of N_P

more erratic and unpredictable in nature, particularly at higher current levels.

Further work is strongly recommended to build on the results of this initial study. Comparison with electrical data gathered from existing DC arc furnaces is a necessary step for validation of the existing models and will be prioritized going forward. High-speed electrical measurements capable of fully resolving the circuit behaviour within the duration of a single thyristor pulse will be necessary for such work, which should ideally cover both pilot plant and industrial furnaces to reveal any scale effects not captured by the present models. Extension of the arc models to systems closer to industrial scale would be of value in providing a useful virtual prototyping environment for power supply and furnace designers. In addition, integration of more sophisticated circuit simulations to include realistic thyristor power supply effects such as commutation, line impedances, and protection and safety circuitry would allow such effects to be studied in detail in terms of their impact on the arc, and vice versa.

Acknowledgements

This paper is published by permission of Mintek. The author gratefully acknowledges access to resources at the CSIR Centre for High Performance Computing in Cape Town, South Africa for execution and analysis of computational modelling results.

References

- BOWMAN, B. and KRUGER, K. 2009. Arc Furnace Physics. Verlag Stahleisen, Düsseldorf, Germany.
- JONES, R.T. 2014. DC arc furnaces – past, present, and future. *Proceedings of the Extraction and Processing Division Symposium on Pyrometallurgy in Honor of David G.C. Robertson, TMS Annual Meeting & Exhibition 2014*, San Diego CA, USA, 16-20 February 2014. pp. 129–139.
- JONES, R.T., REYNOLDS, Q.G., CURR, T.R., and SAGER, D. 2011. Some myths about DC arc furnaces. *Journal of the Southern African Institute of Mining and Metallurgy*, vol. 111. pp. 665–673.
- LEUTBECHER, M. and PALMER, T.N. 2008. Ensemble forecasting. *Journal of Computational Physics*, vol. 227. pp. 3515–3539.
- OPENFOAM FOUNDATION. 2017. OpenFOAM® software. <https://openfoam.org/>
- REYNOLDS, Q.G. 2015. Interaction of dust with the DC plasma arc – a computational modelling investigation. *Journal of the Southern African Institute of Mining and Metallurgy*, vol. 115. pp. 395–407.
- REYNOLDS, Q.G. 2017. Computational modeling of arc-slag interaction in DC furnaces. *JOM*, vol. 69, no. 2. pp. 351–357. ◆



Fluxing of South African chromite ore with colemanite

by M.W. Erwee, I.J. Geldenhuys, M.B. Sitefane, and M. Masipa

Synopsis

South African chromite ores are smelted using SiO_2 - and CaO -containing fluxes, normally as quartz and limestone respectively. The purpose of SiO_2 is to lower the melting point of the ore, while CaO is added to ensure that the slag that forms on smelting is fluid enough to enable slag/alloy separation and tapping from the furnace. Colemanite is a borate mineral originating primarily from Turkey, and has the nominal, ideal composition $\text{CaB}_3\text{O}_4(\text{OH})_3 \cdot \text{H}_2\text{O}$. B_2O_3 readily fluxes chromite, and low amounts of this compound can yield a lowering of the melting temperature similar to that obtained using SiO_2 . In addition, colemanite already contains CaO , which aids in making the resulting slag more fluid.

Laboratory-scale smelting tests were conducted at Mintek over the course of 18 months. The work included evaluation of a variety of boron-containing materials to replace conventional fluxes. The results of the tests and modelling work are presented in this paper.

Keywords

chromite, smelting, ferrochrome, colemanite, boron, energy.

Introduction

The BOFLUX project was an initiative launched by Mintek and two other partners (see acknowledgements) in response to the second ERA-MIN joint call in 2014 on sustainable supply of raw materials in Europe. At the time, both chromium and borate minerals were on the 2014 EU critical raw materials list (European Commission, 2014). In this document, it was stated that South Africa held 80% of the world's chromite resources, while Turkey held 98% of the world's borate minerals.

The project was based on the premise that several process improvements to chromite smelting would be possible using borate minerals as fluxes in place of conventional fluxes. The improvements envisaged were lower impurity levels (higher Cr grade), reduced operating temperatures, reduced flux consumption, reduced slag to metal ratios, and lower energy consumption. Similar work on laboratory and industrial scales has been conducted in, *inter alia*, Kazakhstan in the production of ferrosilicon and ferrosilicochrome (Akberdin *et al.*, 2013). This prompted an investigation into whether similar benefits were possible for South African chromite smelting operations, starting with

fundamental and laboratory-scale research, the results of which could be used as a guideline for further work.

In this paper, conventional fluxing of chromite ore in South African operations is discussed to set the scene, followed by the principles behind fluxing with borates, in this case, specifically colemanite. Results from laboratory-scale tests done at Mintek, in which conventional fluxes were tested against borates, then follow.

Conventional smelting of chromite in South Africa

Chromite sources and smelting operations in South Africa

Chromite ores in South Africa originate mainly from the Bushveld Complex. Broadly, the MG1, MG2, and LG6 seams in the Complex are mined to produce feed for chromite smelting, while the UG2 Reef is mined as a source of platinum group metals (PGMs). The 'discard' streams from UG2 ore processing have become a valuable raw material for ferrochrome producers, as was predicted some 14 years ago (Cramer, Basson, and Nelson, 2004).

The composition of chromite varies substantially, and a comprehensive overview of each ore or concentrate is beyond the scope of this paper. The typical compositions of some South African chromite ores are given in Table I (Geldenhuys, 2013).

It is very important to point out that ores listed in Table I are just a few examples of what is used by the industry. Several smelting operations rely on various other chromite sources with varying Cr_2O_3 contents, Cr/Fe ratios, and gangue mineral content.

* Mintek, South Africa.

© The Southern African Institute of Mining and Metallurgy, 2018. ISSN 2225-6253. This paper was first presented at the INFACON XV: International Ferro-Alloys Congress, 25–28 February 2018, Century City Conference Centre and Hotel, Cape Town, South Africa

Fluxing of South African chromite ore with colemanite

Table I

Typical composition of South African chromites (major components listed, mass %) (Geldenhuys, 2013)

Origin	Cr ₂ O ₃	FeO	MgO	Al ₂ O ₃	SiO ₂	Cr/Fe
LG6	46.6	25.0	10.8	15.1	0.6	1.6
UG2	42.6	27.4	9.3	14.9	1.2	1.4
MG	42.9	28.5	8.8	15.7	3.0	1.3

South African chromite ores and concentrates are blended to obtain a Cr/Fe ratio that is high enough to produce 'charge chrome', a special grade of high-carbon ferrochrome (HCFerCr). Charge chrome contains approximately 50–53% Cr, 6–8% C, 4–6% Si, and the balance Fe, with minor impurities such as S and P (Gasik, 2013).

Not all ferrochrome in South Africa is produced via the submerged arc furnace (SAF) route. Some 8–10% of other ferrochrome products (*e.g.* plasma chrome, a low-carbon FeCr alloy) is produced using DC furnace technology.

The type of furnace, operating temperature, and slag chemistry are all factors that affect the recovery of Cr from chromite and hence the quality of the final product. The Cr/Fe ratio of the ore largely determines the Cr content of the product from a particular furnace. Typical figures for chrome recoveries in various furnaces are given in Table II (Gasik, 2013). The energy required for smelting is also given (kWh/t FeCr product).

The chromite feed material is often pelletized and then either prereduced or sintered before it is charged to a SAF. A broad outline of process operations for ferrochrome production in South Africa is given in Figure 1. Note, that it is no longer common for most producers to use lumpy ore as primary feed material.

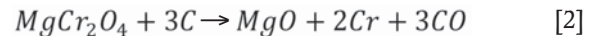
Fundamentals of fluxing in conventional ferrochrome production

Chromite ore contains a mixture of complex spinel minerals and pyroxenes. Most of the chrome and iron in chromite is present as (Fe,Mg)(Cr,Al)₂O₄ spinel. A graphical representation of the spinel structure is given in Figure 2. After processed through a beneficiation plant, the ore concentrate consists of up to 95% spinel.

If, for example, the composition of the ore is expressed as a mixture of ideal spinel minerals, the LG6 type ore composition could be recalculated to be approximately 21.3% MgAl₂O₄, 23.3% MgCr₂O₄, 42.2% FeCr₂O₄, 12.6% Fe₃O₄, and 0.6% SiO₂.

The purpose of smelting is to reduce most of the Cr₂O₃ in the MgCr₂O₄ and FeCr₂O₄ spinel phases to Cr and separate it from the main gangue components, MgO, Al₂O₃, and SiO₂, which form a slag phase.

Reduction of chrome spinel occurs both directly and indirectly in different parts of the furnace. This process is complex and is very well described by Hayes (2004). Simplified, the overall reactions for reduction of chrome and iron oxide in the chrome spinel by carbon are:



As a side reaction, due to process temperatures between 1700°C and 1750°C, some SiO₂ is reduced to Si, which dissolves into the alloy:



Inevitably, reduction of Fe²⁺ and Fe³⁺ in the ore will occur at the typical smelting temperatures of above 1650°C and hence dilute the final FeCr product with Fe. Further dilution of the product takes place by reduction of the limited amount of iron oxides in the reductant as well as reduction of SiO₂ from ore, reductant, and fluxes to Si.

Table II

Chrome recovery and energy consumption for different furnaces used for FeCr production, partially adapted from (Gasik, 2013) and personal communication with producers

Type of furnace	Chrome recovery	SEC* (kWh/t)
Open AC furnace (without raw material screening)	70–75%	4000–4300
Closed AC furnace (with pelletized feed and preheating)	83–88%	3100–3400
Prereduction followed by closed AC furnace	88–92%	2400**
Closed DC furnace	88–92%	3850–4200

*SEC: Specific energy consumption

**Electrical energy consumed, *i.e.* excludes energy required for burning fuel in the prereduction kiln

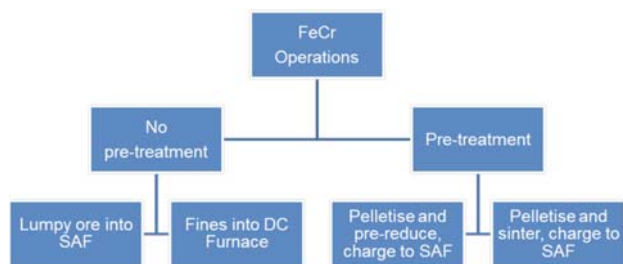


Figure 1—Broad categories of FeCr smelting operations in South Africa

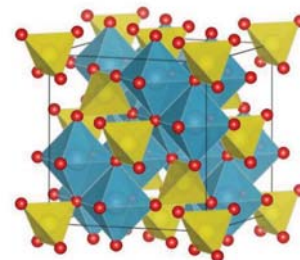


Figure 2—A graphical representation of a complex spinel phase (crystallography365.wordpress.com). In general, spinel can be represented as AB₂O₄. Yellow tetrahedra represent A; blue octahedra, B; red, oxygen anions

Fluxing of South African chromite ore with colemanite

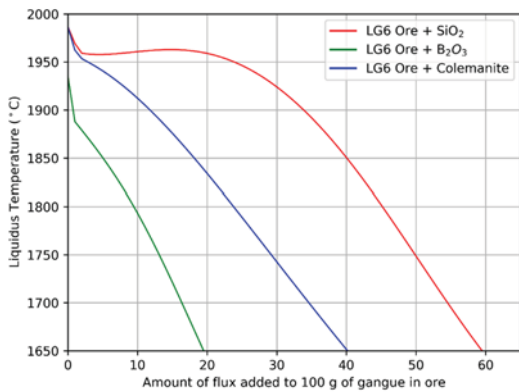


Figure 5—Effect of fluxes on melting point of an ore-gangue mixture of initial composition: 57% Al_2O_3 , 41% MgO , and 2% SiO_2

From Figure 5, it is clear that to reach a liquidus temperature of approximately 1650°C , the required amount of B_2O_3 is almost one-third of the amount of SiO_2 that would be required. Interestingly, but not surprisingly, the amount of colemanite required is between that of pure SiO_2 and B_2O_3 . The reason for this is that colemanite, in addition to B_2O_3 , contains CaO , which raises the melting point of an $\text{MgO-Al}_2\text{O}_3\text{-SiO}_2$ mixture. However, the CaO component aids in reducing the viscosity of the resulting slag (see Figure 6).

There is however, a caveat to using colemanite as a flux for chromite smelting. Unlike SiO_2 , which is thermodynamically more difficult to reduce with carbon in comparison with Cr_2O_3 and FeO_x during smelting, B_2O_3 is almost as easy to reduce as Cr_2O_3 and CrO in slag, as seen on a modified Ellingham-Richardson type diagram (Figure 7).

Solid lines represent reaction $\text{M} + \text{O}_2 \rightleftharpoons \text{MO}_2$ for all compounds at unit activity, while corresponding dashed lines represent the same reactions but at non-standard activity. Ranges for activity values are based on thermodynamic simulations described later in this paper ($\text{M} = \text{Cr}, \text{Si}, \text{B}, \text{and C}$). It is important to also mention that the reduction of B_2O_3 to volatile B_2O_2 gas is also possible at higher temperatures, which is not shown on this diagram, nor are any reactions involving borides, carbides, or carbo-borides. However, in a simple way, what should be apparent from the diagram is that CrO , Cr_2O_3 , SiO_2 , and B_2O_3 all compete for carbon (FeO_x not included).

Aside from contaminating the final product, B_2O_3 reduction will consume excess reductant and also remove B_2O_3 from the slag, making the fluxing effect less effective.

The potential impact of colemanite as flux

The use of colemanite flux was expected to lower the energy requirement for smelting since it would reduce smelting temperatures to 1650°C , decrease the amount of Si in the alloy (which is typically between 4–6%), which in turn would lead to a higher grade of Cr; and lower slag volumes, which could lead to increased throughput in the furnace. In addition, it was anticipated that lower losses of alloy by entrainment in the slag would occur due to lower slag viscosity. However, the potential benefits of using colemanite as flux must be offset against the cost.

Energy consumption and cost of production for chromite smelting

Whereas other countries such as India, Kazakhstan, Finland, China, and Turkey have increased their production of FeCr over the last 3 years, the production of FeCr in South Africa

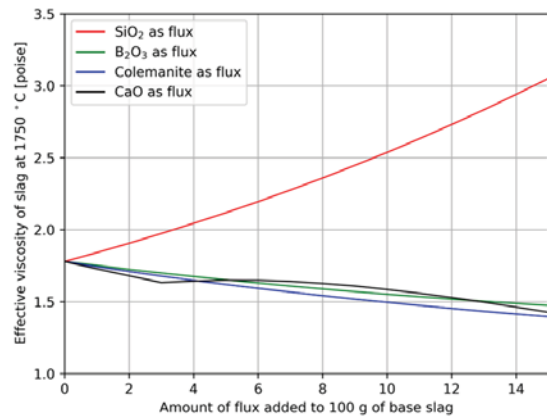


Figure 6—Effect of various fluxes on the viscosity of a chromite smelting slag based on LG6 gangue minerals (calculated using FactSage 7.1)

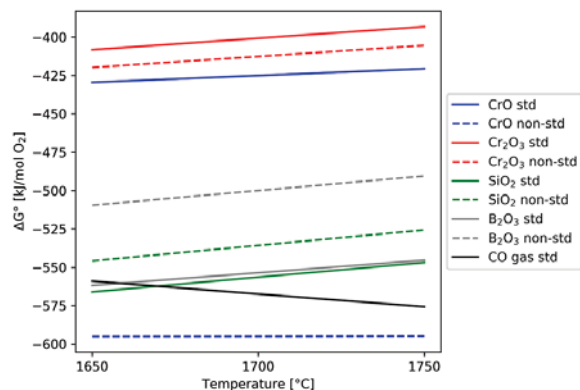


Figure 7—Free energy change of reactions between various compounds with 1 mole of O_2

Table III

Cost of production of FeCr in South Africa, 2016 (Pariser, 2017)

Exchange rate, R/US\$	14.71	
% Cr in FeCr	49.6	
Variable costs	Cost (US cents / lb Cr)	% of total
Raw materials		
Chromite ore	13.87	29.1
Reductants	7.31	15.3
Others ¹ (fluxes, electrode paste)	1.46	3.1
Energy	18.15	38.1
Operating costs	1.69	3.5
Semi-fixed costs		
Labour	3.51	7.4
G&A, maintenance	1.71	3.5
Total direct cash production cost	47.69	

¹Ex-works

Fluxing of South African chromite ore with colemanite

has declined from approximately 3.774 Mt/a in 2014 to 3.596 Mt/a. Among the most important reasons cited for this is the high cost of electricity. The electricity price in South Africa has almost quadrupled over the last decade (Pariser, 2017).

The direct cash production cost of FeCr in South Africa comprises three main elements: electricity, chromite ore, and reductants. All other costs (labour, maintenance, electrode paste, fluxes, *etc.*) make up a relatively minor portion (15%) of this cost.

It is clear that the largest operating cost in the FeCr production process in South Africa is electricity – in 2016 it was a staggering 38.1% of the total production cost. The cost of fluxes and electrode paste is a mere 3.1%; however, fluxes can play an important role in lowering the energy requirement for smelting.

An extensive review of a FeCr furnace energy balance was done by Ringdalen (2015). That work (and similar calculations at Mintek) established that the majority (approx. 75% of the total) of the energy consumed in a furnace is at temperatures above 1200°C, where reduction of chromite and melting of both gangue and metal occur inside the coke bed.

Of particular importance is the effect of different parameters on the overall energy requirement of the furnace. A selected few are shown in Table IV.

With the overall energy requirement for smelting between 3.5 to 4.0 MWh/t, the savings might seem marginal, but if a combination of savings can be achieved, then a worthwhile benefit can be realized.

Thermodynamic modelling and parameter space search

Thermodynamic modelling was done to help guide test work for this project. The modelling was done using FactSage™ 7.1 (Bale, 2016). Databases used were FTOxid (for oxide solutions, including slag), SGTE (for the resulting alloy phase), and FactPS (for gases, pure oxides, and pure elements). Models were implemented using ChemApp v 6.4.5 via the ChemAppForPy API (version 0.1.4). ChemApp is a free-energy minimization module and is also the backbone to the 'Equilib' module of FactSage, hence the two are used interchangeably as they yield the same result. Free-energy minimization is a method used to determine the composition of a combination of multiple species at specific conditions (in this case temperature and pressure) that minimize the total Gibbs free energy of the system. Several thousand permutations were considered using the thermodynamic model.

The optimal level of flux would be such that:

- ▶ The smelting temperature can be lowered to 1650°C or less
- ▶ All of the gangue (mainly MgAl₂O₄ spinel) is dissolved
- ▶ The metal product is not contaminated (at least not more than usual)
- ▶ The viscosity of the slag is as low as possible
- ▶ The energy requirement for smelting is as low as possible.

All of the simulations were done at different smelting temperatures with the amounts of reductant and flux as variables. One subset of the results of the modelling is shown here as an example. The case presented in this section of the paper is for a metallurgical-grade chromite ore with high-grade colemanite flux and anthracite. The temperature used in the simulation was 1650°C. More specific detail on the actual composition of the ore is given in the experimental section of the paper.

Note that the energy requirement was calculated on the basis that the slag, alloy, and gas are all at the same temperature. This is not true for industrial operations, but allows for a relative and consistent comparison between the different cases considered.

Each bar in the three-dimensional plots in Figure 8 is for one discrete simulation. First, the energy requirement for smelting is presented in Figure 8a. As expected, the energy requirement for smelting increases as more flux is used. Note that later in the paper a comparison is made with conventional smelting cases.

In Figure 8b, the amount of undissolved spinel is shown. As expected, higher levels of colemanite result in lower levels of undissolved spinel at low reductant levels. The lowest reductant level is the stoichiometric amount of carbon required for full reduction of all chrome and iron oxide in the ore; the maximum is 50% more than the stoichiometric amount on a mass basis. Notice that at lower levels of colemanite, the amount of undissolved spinel decreases initially with the amount of reductant, but then increases again. This is due to the reduction of B₂O₃ by carbon, which makes the flux ineffective for spinel dissolution. Further evidence of this is in the percentage Cr and percentage B recovery to metal (see Figures 8d and 8f).

Therefore, a careful balance between the amount of reductant, flux, and temperature is required. This is common for normal fluxes (SiO₂ and CaO), but requires even more attention when borate minerals are used.

Aside from boron contamination of the product, losses due to entrainment can also occur if there is no clear balance

Table IV

Energy savings for a SAF producing FeCr (adapted from Ringdalen, 2015)

Parameter	Saving in energy requirement for smelting
Lower slag temperature by 100°C	approx. 60 kWh/t
Preheat raw material by 100°C	approx. 76 kWh/t
Lower undissolved chromite content in slag by 5% Cr ₂ O ₃)	approx. 122 kWh/t
Drying wet material from 5 to 2% moisture	approx. 81 kWh/t
Decrease Si in alloy by 2%	approx. 72 kWh/t

Fluxing of South African chromite ore with colemanite

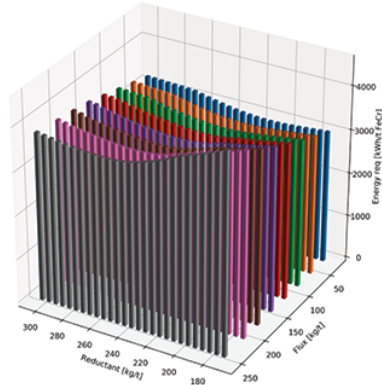


Figure 8a – Energy requirement

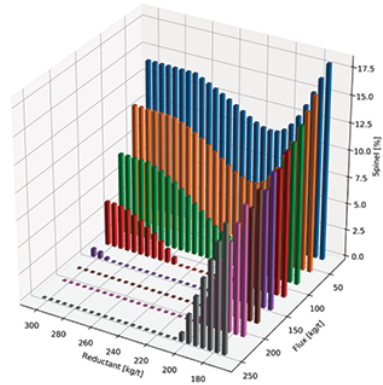


Figure 8b – Undissolved spinel

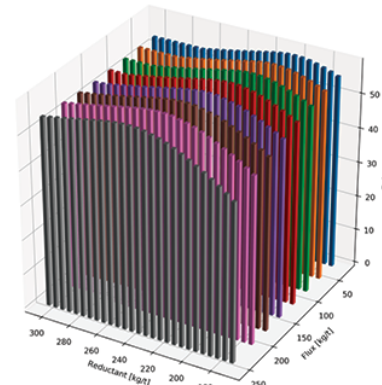


Figure 8c – Cr in metal (%)

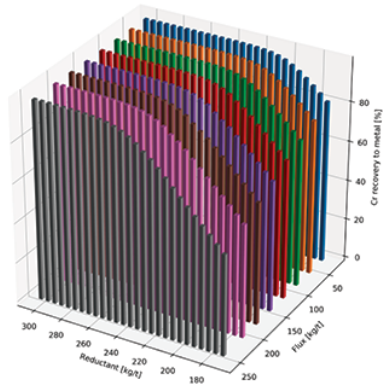


Figure 8d – Cr recovery to metal (%)

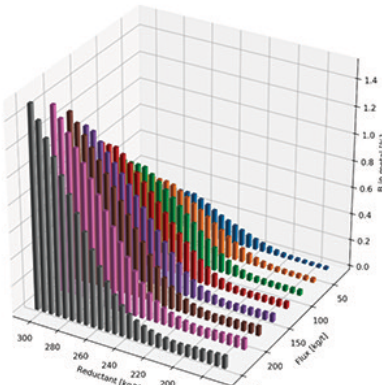


Figure 8e – B in metal (%)

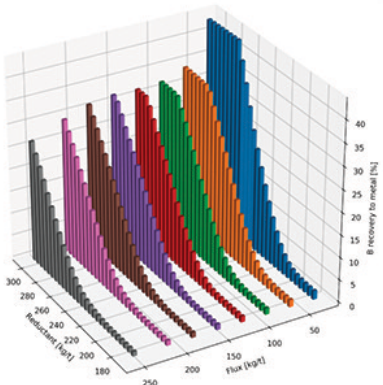


Figure 8f – B recovery to metal (%)

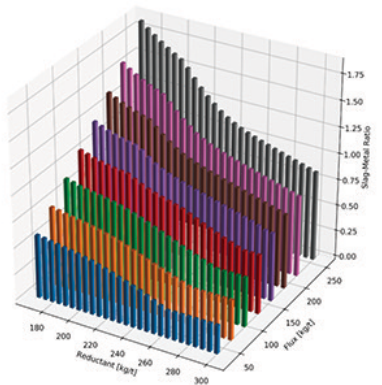


Figure 8g – Slag/metal ratio

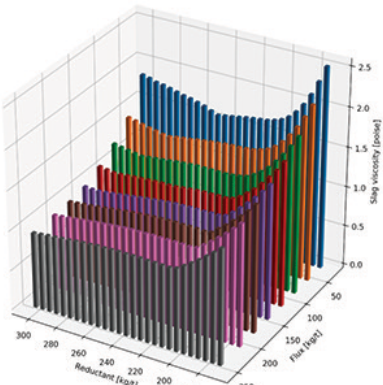


Figure 8h – Effective slag viscosity

Figure 8—Thermodynamic modelling results

Fluxing of South African chromite ore with colemanite

between carbon and flux addition. In this case, however, all is not lost (see Figure 8h). Despite lower levels of B_2O_3 in the slag, CaO that enters the furnace with colemanite aids in lowering the slag viscosity in almost all cases.

Test work was planned based on all of the modelling results, taking into account all of the factors such as energy consumption, slag viscosity, and possible contamination of the product with boron (with subsequent loss of boron from the slag). The amount of flux added depended on the grade of both the ore and the colemanite sources. Only a small subset of the results is presented in this paper.

Experimental methods

Overall, laboratory-scale crucible tests were conducted for about 18 months. Various grades of chromite ores, as well as different types of borate minerals, were tested. These included pure B_2O_3 , various grades of ulexite ($NaCaB_5O_6(OH)_6 \cdot 5H_2O$), as well as various grades of colemanite. In this paper, only a subset of all of the results is given – that of two grades of both chromite and colemanite. The tests with colemanite were benchmarked against tests with SiO_2 only, B_2O_3 only, and using conventional smelting regimes.

It is imperative to state that crucible-based test work for smelting has inherent limitations and that larger, pilot-scale testing would be required to assess all of the possible benefits of any of one flux over the others. However, crucible-based test work is of great value for assessing the relative performance of one smelting regime compared to another, since many of the variables can be fixed and the other parameters changed systematically to observe the effect on smelting performance.

Raw materials

Two chromite ores were tested: one with a high Cr/Fe ratio typical for charge chrome production and the other with a low Cr/Fe ratio. Only the results for tests using the chromite ore with a high Cr/Fe ratio are presented in this paper, as the other results will be given in future publications. Flux materials were reagent-grade SiO_2 , CaO, and B_2O_3 and two grades of colemanite, referred to here as high-grade colemanite (HGC) and low-grade colemanite (LGC). The reductant in all cases was anthracite sourced locally, which is often used in chromite smelting operations. The compositions of each material are given in Tables V to VII.

Test conditions

The amount of anthracite required as reductant was calculated on the basis of the total amount of carbon required for full reduction of Cr_2O_3 (as $FeCr_2O_4$ and $MgCr_2O_4$) and FeO_x (as $FeCr_2O_4$ and Fe_3O_4) to Cr and Fe respectively. These are termed low-carbon cases (18% reductant in this case). As reduction of SiO_2 and B_2O_3 was expected, a set of tests referred to as high-carbon cases was also done, where the amount of anthracite added was 1.5 (*i.e.* 27%) more on a mass basis than the low-carbon case. For the conventional recipe, 25% of the feed was anthracite.

The amount of flux was based on the amount required to fully dissolve residual $MgAl_2O_4$ in the slag as predicted using the thermochemical calculations done in FactSage, but the amount of HGC was varied between 3 and 9% to check the sensitivity of the smelting process to varying amounts of flux as compared to the conventional recipe. Fluxes tested were:

- SiO_2 only (10%)
- Varying amounts of pure B_2O_3 (3, 4.3, 5, and 8%)

Table V

Normalized, average composition of the ore tested² (mass %)

Ore	Cr_2O_3	Al_2O_3	CaO	FeO	SiO_2	MgO	MnO	TiO_2	Cr/Fe
High Cr/Fe ore	44.12	12.61	0.81	22.77	6.61	12.30	0.22	0.56	1.71

Table VI

Normalized, average composition of the borate minerals (mass %)

Flux	CaO	FeO	SiO_2	MgO	LOI ³	B_2O_3	Na_2O
High-grade colemanite	27.0	0.04	4.0	3.0	25.46	40	0.5
Low-grade colemanite	26.0	-	13.0	-	34	27.0	-

Table VII

Composition of the reductant used for all tests (mass %)

Fixed carbon	Moisture	Volatiles	Ash	Al_2O_3	CaO	Fe_2O_3	MgO	SiO_2	TiO_2
80.5	1.6	6.2	11.7	2.9	0.5	0.7	0.1	5.4	0.2

²As determined by ICP-OES (accredited method developed by Mintek)

³Crystal water, moisture, and any volatile matter

Fluxing of South African chromite ore with colemantite

- ▶ Varying amounts of HGC (3, 6, and 9%)
- ▶ A fixed amount of LGC (which would be suitable as per the prediction)
- ▶ CaO + SiO₂ (conventional recipe of 9.5% SiO₂ + 7.5% CaO).

The temperatures selected were 1650°C and 1750°C for all the tests with borate minerals, and only at 1750°C for the conventional recipe.

Furnace set-up and test procedure

Raw materials were milled in a swing mill after drying at 105°C overnight in a muffle furnace. The materials were mixed in small plastic bags after weighing, and the mixtures were placed into either a high-density pure MgO or a graphite crucible. The charge was compacted mechanically into the crucibles and small holes made in the material bed to enhance the release of gas evolved during testing.

The prepared crucibles were loaded in batches of four into a 30 kW induction furnace. The four crucibles were placed inside a large graphite crucible, which is used as susceptor inside the water-cooled coil of the induction furnace. The large susceptor is insulated using bubble alumina and an insulating castable material. A graphite lid was placed over the graphite susceptor. A B-type thermocouple was placed through the lid to measure the temperature inside the furnace and argon gas was purged using an alumina lance, also placed through the lid. Additional insulation was provided by a ceramic blanket to avoid excessive radiative heat losses. Furnace power was initially set at 2.5 kW and increased every 30 minutes by 0.5 kW until the required test temperature of 1650°C or 1750°C was reached. The test was left to run at the required temperature for one hour, after which the furnace was switched off and left to cool overnight.

The metal and slag were recovered from the crucibles after breaking the crucibles apart. The slag was not always fully recovered due to attack on the crucible. Where possible, all bulk pieces of metal were collected for weighing. Analysis of metal and slag was by means of ICP-OES for Cr, Fe, Si, Mn, Ti, and V, by LECO for C and S, and ICP-MS for B.

Results and discussion

Laboratory-scale crucible tests

Three factors were compared for the smelting tests – the relative amount of bulk alloy that formed, the percentage Cr in the metal, and main impurity levels, in this case Si and B. The relative amount of bulk alloy formed serves as an indication of the effectiveness of the flux used to facilitate metal-slag separation.

The amount of bulk alloy formed refers to the recoverable lump of alloy that settled at the bottom of the crucible after testing. Metal entrained in the slag phase is often difficult to physically separate and is not, on a laboratory scale, deemed appropriate to compare based on previous experience at Mintek. Since the slag is contaminated with metal in most cases (as will be shown later in this section), the slag analysis was disregarded in all calculations. Consequently, the mass recovery of Cr was also not calculated. The bulk alloy phase was found to be more homogenous (little entrainment of slag particles found) and hence was used for comparison. For all practical purposes, a comparative study of the quality of the alloy was more suitable, since the recovery

of elements in industrial processes is almost always different from that in laboratory tests.

The percentage Cr in the alloy is compared for the different tests. It is important to realize that the absolute value of Cr can be affected by the method of analysis. In this project, the standard deviation on the percentage Cr for the method used was ±0.15.

The level of major impurities plays an important role in the valuing of high-carbon ferrochrome. Any element apart from Cr is not paid for, and penalties are payable when the material does not meet specification. For comparative purposes, the total Si and B percentages were compared, since these are interdependent. The standard deviations on the analysis errors for Si and B are ±0.1% and, ±10 ppm respectively.

Results are presented in bar-chart format for easy comparison. Where no bar is presented on the chart, the test (or set of tests) failed. Failed tests are tests where no discernible metal and slag phase could be identified and separated due to severe entrainment. These 'failed' tests were repeated at least once to ensure that the result was consistent. Error bars on the charts indicate the standard deviation for the particular quantity. Where there is no error bar, a single test was done for the particular case. The variability of these tests was usually confirmed by a similar case. This was done for two reasons: firstly, so that the test would be more relevant for actual industrial furnace operations, and secondly to limit the number of tests that could be carried out within the budget for this project.

Results of tests using chromite ore with a high Cr/Fe ratio

No separable bulk alloy could be produced at 1650°C using the conventional recipe or levels of less than 6% of either lower- or higher-grade colemantite. The best result achieved, in terms of the amount of metal, was with 4.3% pure B₂O₃. Whether it would be cost-effective to use pure B₂O₃ as flux is yet to be explored, as it is even more expensive than colemantite or a combination of conventional fluxes.

The tests at 1750°C showed no statistically significant difference between using low- or high-grade colemantite rather than conventional fluxes. Operating at a temperature of 1750°C also defeats one of the major aims of the project: operating at lower temperatures.

The amount of alloy formed is not the only parameter that needs to be considered. Grade is assessed by not only the total Cr in the product, but also by the level of impurities, in this case Si and B, as this would affect the customer downstream.



Figure 9—An example of the bulk alloy pellets that form and are collected from a smelting test (bright grey/silver is alloy)

Fluxing of South African chromite ore with colemanite

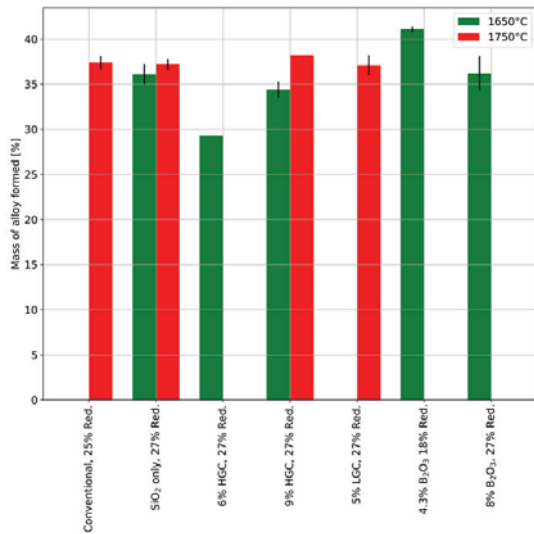


Figure 10—Summary of results (mass of alloy formed) for chromite with high Cr/Fe ratio (error bars indicate standard deviation on tests). The percentage values stated refer to the amount of material added as a percentage of the amount of ore added (e.g. '6% HGC, 27% Red' refers to a case where 6 g of flux and 27 g of reductant was added to 100 g of ore)

The Cr content of the metal for each of the cases where bulk alloy was formed is shown in Figure 11. In all but one case, the minimum specification for charge chrome (50%Cr) was achieved. Just as for the amount of metal formed, it seems that there is no statistically discernible difference when comparing conventional smelting at 1750°C and using approximately 9% high- or 5% low-grade colemanite at 1650°C. However, the fact that an alloy can be formed at 1650°C using HGC with this ore is promising, as this implies that the overall operating temperature can be decreased, yielding more-or-less the same result as with conventional fluxes at 1750°C.

As part of the thermodynamic calculations in FactSage 7.1, the energy requirement for smelting was also calculated. The results are given in Table VIII, along with the expected viscosity of the slag, also calculated using the Viscosity module of FactSage 7.1. Smelting chromite at 1650°C with 9% HGC would save roughly 3% on the total energy requirement compared to smelting using conventional fluxes at 1750°C. The reason that this value is lower than expected is the fact that some 25-30% by mass of the colemanite is present as crystal water. Calcination of colemanite before use in a furnace would reduce the energy requirement even more. However, if one takes a longer term view, the reduced operating temperature can have significant benefits for a

smelter.

Finally, the contamination of the product needs to be quantified. The contents of Si and B, the main impurities in the alloy, are given in Table IX. As expected, less Si is present in tests where borates were used. This could be attributed to two factors – firstly, less SiO₂ is present to be reduced in the first place, and secondly, that B₂O₃ is preferentially reduced compared with SiO₂. The amount of B present in the alloy is higher at 1750°C than 1650°C, which was also expected.

One question remains regarding boron contamination of the alloy. There is no formal boron specification for HCFerCr that the authors could find in any standard or literature. However, during the production of stainless steel, there might be a very tight specification on the amount of boron present.

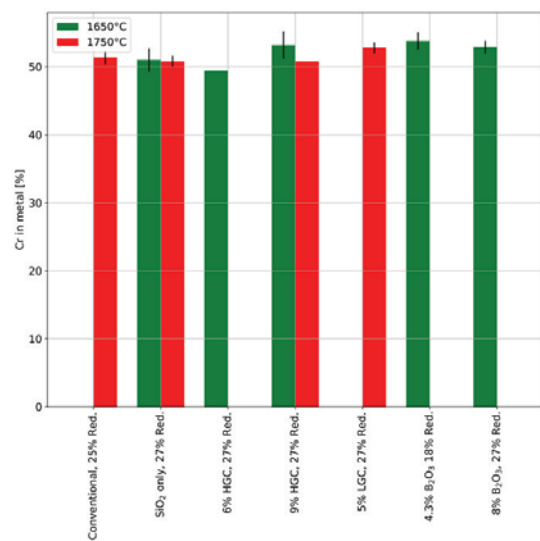


Figure 11—Summary of results (Cr grade) for chromite with high Cr/Fe ratio (error bars indicate standard deviation on tests)

Table IX

Impurity levels for alloy formed from chromite with a high Cr/Fe ratio

Fluxing regime	T = 1650°C		T = 1750°C	
	%Si (±SD)	%B (±SD)	%Si (±SD)	%B (±SD)
Conventional	-	-	1.03 ± 0.22	-
SiO ₂ only	5.38 ± 1.47	-	7.71 ± 0.8	-
6% HGC	1.26 ± 0.07	-	-	-
9% HGC	2.98	1.21	3.1	4.9
5% LGC	-	-	1.8 ± 0.6	0.18 ± 0.01

Table VIII

Theoretical slag viscosities and energy requirements for smelting

Fluxing regime	1650°C		1750°C	
	Slag viscosity (poise)	Energy requirement (MWh/t FeCr)	Slag viscosity (poise)	Energy requirement (MWh/t FeCr)
Conventional	1.8	3.15	1.7	3.45
SiO ₂ only	2.7	3.29	1.8	3.60
6% HGC	1.5	3.27	0.9	3.60
9% HGC	1.3	3.33	0.8	3.64
5% LGC	1.8	3.25	1.1	3.58

Fluxing of South African chromite ore with colemanite

This is beyond the scope of this particular paper, and is being investigated. The authors have done some initial tests on converting of HCFcCr with the aim of boron removal.

The full details of the decarburization test work are not given here, since the results need to be confirmed. In brief, a sample of ferrochrome metal produced during testing was decarburized in an alumina crucible in an induction furnace. An alumina lance was used to inject pure oxygen into the melt. A synthetic slag of 40%CaO-40%SiO₂-10%MgO and 10%Al₂O₃ was added to the melt periodically to aid the converting process. A temperature of 1600°C was maintained. Samples were taken and analysed using ICP (for metal components) and LECO for C. The initial and final composition of the alloy sample is given in Table X.

A plot of the boron content as a function of time (Figure 12) shows that boron removal follows an exponential, rather than linear, relationship, indicating possible first-order kinetics for removal. After 32 minutes of blowing time, the boron content of the melt was reduced to 25% of the original value, showing that removal of boron from the melt is indeed possible. A side effect of this process is the increased concentration of impurities such as P, which will have to be removed in a later stage of blowing or a separate process step. This implies that steelmakers would necessarily have to adjust parameters in their operations when using boron-containing ferrochrome.

Conclusions and future work

Fluxing of chromite ore with borate ores shows promise, but many factors need to be taken into account to gain maximum benefit from it. Results from laboratory tests show that it is indeed possible to reduce operating temperatures from 1750°C to 1650°C using colemanite in place of conventional fluxes. The amount and grade of alloy formed when using colemanite as flux at 1650°C was more-or-less the same as in the conventional smelting case at 1750°C. In some cases (*e.g.*

with pure B₂O₃ as flux) it was found that the grade of the alloy was increased by some 1–2% Cr, which implies that some more test work with borates is required to obtain a full picture of the potential benefits. Boron contamination of up to 1% could be a problem, but it seems that boron removal might be possible and this should be studied in more detail.

Furthermore, tests need to be conducted at pilot scale in a longer term campaign to confirm the results found at the laboratory scale. This is especially important to determine the optimal level of flux and reductant relevant to furnace operations and investigate other factors, such as the conductivity of the slag, when B₂O₃ is present. The ultimate success of colemanite as a flux will depend greatly on the relative cost of flux balanced against the short- and longer term benefits realized, especially since conventional fluxes are cheap and are sourced locally, while borates would have to be sourced from, for example, Turkey.

Acknowledgements

This paper is published by permission of Mintek. The authors would like to thank Mintek, ERAMIN, and the South African Department of Science and Technology for sponsoring the work. The contributions of our colleagues are gratefully acknowledged.

Finally, the authors wish to thank the partners of the BOFLUX consortium (Ab Etiproducts Oy, Finland and Siyanda Chrome Company Pty Ltd) for their support with material and in-depth discussions during the project – without them, this project would not have been possible. Mintek also acknowledges the support of NIPMO in the ongoing maintenance of its IP portfolio.

References

- AKBERDIN, A., KIM, A.S., ILMAZ, O., ISLETMELERI, G., and ZHUCKOV, V. 2013. Boron in ferroalloy production. *INFACON XIII, Proceedings of the Thirteenth International Ferroalloys Congress*, Almaty, Kazakhstan. pp. 325–334. <http://www.pyrometallurgy.co.za/InfaconXIII/0325-Akberdin.pdf>
- EUROPEAN COMMISSION. 2014. <http://eur-lex.europa.eu/legal-content/EN/TXT/PDF/?uri=CELEX:52014DC0297&from=EN> [accessed 12 February 2018].
- CRAMER, L., BASSON, J., and NELSON, L. 2004. The impact of platinum production from UG2 ore on ferrochrome production in South Africa. *Journal of the South African Institute of Mining and Metallurgy*, vol. 104, no. 9. pp. 517–527.
- GASIK, M. 2013. *Handbook of Ferroalloys: Theory and Technology*. Elsevier, Waltham, USA.
- CRYSTALLOGRAPHY 365. 2014. <https://crystallography365.wordpress.com/2014/09/24/the-worlds-most-underappreciated-gemstone-red-spinel/>
- GELDENHUYS, I. 2013. Aspects of DC chromite smelting at Mintek: An overview. *INFACON XIII, Proceedings of the Thirteenth International Ferroalloys Congress*, Almaty, Kazakhstan. pp. 31–47.
- HAYES, P. 2004. Aspects of SAF smelting of ferrochrome. *INFACON X: Proceedings of the Tenth International Ferroalloys Congress*, Cape Town, South Africa. Southern African Institute of Mining and Metallurgy, Johannesburg. pp. 1–14.
- HOLAPPA, L. and XIAO, Y. 2004. Slags in ferroalloys production – review of present knowledge. *Journal of the South African Institute of Mining and Metallurgy*, vol. 104, no. 7. pp. 429–438.
- JONES, R.T. and ERWEE, M.W. 2016. Simulation of ferro-alloy smelting in DC arc furnaces using Pyrosim and FactSage. *Calphad*, vol. 55. pp. 20–25.
- PARISER, H. 2017. Re-positioning South Africa. *Proceedings of the SAIMM Chrome Colloquium*, Mintek, Randburg, South Africa, 19–20 June 2017. Southern African Institute of Mining and Metallurgy, Johannesburg.
- RINGDALEN, E.R. 2015. Energy consumption during HCFcCr-production at Ferbasa. *INFACON XIV, Proceedings of the Sixteenth International Ferroalloys Congress*, Kiev, Ukraine. pp. 668–675.
- WACLAWSKA, I. 1988. Thermal decomposition of colemanite. *Thermochimica Acta*, vol. 126. pp. 307–318. ◆

Table X

Initial and final composition of the alloy melt subjected to decarburization using pure oxygen

t (min)	Cr (%)	Si (%)	Mn (%)	Fe (%)	P (%)	B (ppm)	Cr (%)	Ti (%)
0	8.54	1.23	0.27	44.3	0.04	1815	46.2	0.27
32	7.32	0.63	0.23	48.0	0.20	480	48.7	0.21

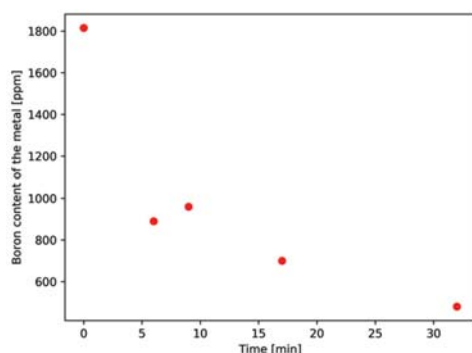


Figure 12—Boron removal from a ferrochrome alloy at 1600°C in contact with a synthetic slag

NATIONAL & INTERNATIONAL ACTIVITIES

2018

30–31 July 2018 — Introduction to Process Engineering School 2018 Volume 1
Birchwood Hotel and OR Tambo Conference Centre, JetPark, Johannesburg
Contact: Yolanda Ndimande
Tel: +27 11 834-1273/7, Fax: +27 11 838-5923/833-8156
E-mail: yolanda@saimm.co.za
Website: <http://www.saimm.co.za>

6–8 August 2018—Geometallurgy Conference 2018 ‘Back to the Future’
Lagoon Beach Conference Venue, Cape Town
Contact: Camielah Jardine
Tel: +27 11 834-1273/7, Fax: +27 11 838-5923/833-8156
E-mail: camielah@saimm.co.za
Website: <http://www.saimm.co.za>

14–15 August 2018 — The SAMREC and SAMVAL CODES ‘Advanced Workshop: Can you face your peers?’
The Wits Club, University of the Witwatersrand, Johannesburg
Contact: Yolanda Ndimande
Tel: +27 11 834-1273/7, Fax: +27 11 838-5923/833-8156
E-mail: yolanda@saimm.co.za
Website: <http://www.saimm.co.za>

29–31 August 2018 — MineSafe 2018 Technical Conference and Industry day
Gallagher Convention Centre, Johannesburg
Contact: Camielah Jardine
Tel: +27 11 834-1273/7, Fax: +27 11 838-5923/833-8156
E-mail: camielah@saimm.co.za
Website: <http://www.saimm.co.za>

4 September 2018 — Micro TBM Tunnelling Seminar 2018 ‘Come to the fore in South Africa’
The Wits Club, University of the Witwatersrand, Johannesburg
Contact: Yolanda Ndimande
Tel: +27 11 834-1273/7, Fax: +27 11 838-5923/833-8156
E-mail: yolanda@saimm.co.za
Website: <http://www.saimm.co.za>

10–11 September 2018 — ASM Conference 2018 ‘Fostering a regional approach to ASM transformation in sub-Saharan Africa’
Nasrec, Johannesburg (Electra Mining)
Contact: Yolanda Ndimande
Tel: +27 11 834-1273/7, Fax: +27 11 838-5923/833-8156
E-mail: yolanda@saimm.co.za
Website: <http://www.saimm.co.za>

18–19 September 2018 — 4th Young Professionals Conference
‘Creating a sustainable African minerals industry through applied innovation’
Focus Rooms, The Core, Sunninghill, Sandton
Contact: Camielah Jardine
Tel: +27 11 834-1273/7, Fax: +27 11 838-5923/833-8156
E-mail: camielah@saimm.co.za
Website: <http://www.saimm.co.za>

14–17 October 2018 — Furnace Tapping 2018 Conference
Nombolo Mdhluli Conference Centre, Kruger National Park, South Africa
Contact: Camielah Jardine
Tel: +27 11 834-1273/7, Fax: +27 11 838-5923/833-8156
E-mail: camielah@saimm.co.za
Website: <http://www.saimm.co.za>

24 October 2018 — 15th Annual Student Colloquium ‘Mining and Metallurgy in a sustainable world’
Johannesburg
Contact: Yolanda Ndimande
Tel: +27 11 834-1273/7, Fax: +27 11 838-5923/833-8156
E-mail: yolanda@saimm.co.za
Website: <http://www.saimm.co.za>

25–26 October 2018 — Higher Education Development in the Extractive Industry Workshop 2018
Glenhove Conference Centre, Melrose Estate, Johannesburg
Contact: Yolanda Ndimande
Tel: +27 11 834-1273/7, Fax: +27 11 838-5923/833-8156
E-mail: yolanda@saimm.co.za
Website: <http://www.saimm.co.za>

2019

11–12 March 2019— 7th Sulphur and Sulphuric Acid 2019 Conference
Swakopmund Hotel, Swakopmund, Namibia
Contact: Camielah Jardine
Tel: +27 11 834-1273/7, Fax: +27 11 838-5923/833-8156
E-mail: camielah@saimm.co.za
Website: <http://www.saimm.co.za>

24–25 June 2019— Ninth International Conference on Deep and High Stress Mining 2019 Conference
Misty Hills Conference Centre, Muldersdrift, Johannesburg
Contact: Camielah Jardine
Tel: +27 11 834-1273/7, Fax: +27 11 838-5923/833-8156
E-mail: camielah@saimm.co.za
Website: <http://www.saimm.co.za>

13–15 November 2019 — XIX International Coal Preparation Congress & Expo 2019
New Delhi, India
Contact: Coal Preparation Society of India
Tel/Fax: +91-11-26136416, 4166 1820
E-mail: cpsidelhi.india@gmail.com, president@cpsi.org, inrksachdev01@gmail.com, hi_sapru@monnetgroup.com

Company Affiliates

The following organizations have been admitted to the Institute as Company Affiliates

3M South Africa (Pty) Limited	Duraset	Multotec (Pty) Ltd
AECOM SA (Pty) Ltd	Elbroc Mining Products (Pty) Ltd	Murray and Roberts Cementation
AEL Mining Services Limited	eThekwini Municipality	Nalco Africa (Pty) Ltd
Air Liquide (Pty) Ltd	Expectra 2004 (Pty) Ltd	Namakwa Sands(Pty) Ltd
AIRT Sheet Metal	Exxaro Coal (Pty) Ltd	Ncamiso Trading (Pty) Ltd
Alexander Proudfoot Africa (Pty) Ltd	Exxaro Resources Limited	New Concept Mining (Pty) Limited
AMEC Foster Wheeler	Filtaquip (Pty) Ltd	Northam Platinum Ltd - Zondereinde
AMIRA International Africa (Pty) Ltd	FLSmith Minerals (Pty) Ltd	PANalytical (Pty) Ltd
ANDRITZ Delkor(Pty) Ltd	Fluor Daniel SA (Pty) Ltd	Paterson & Cooke Consulting Engineers (Pty) Ltd
Anglo Operations Proprietary Limited	Franki Africa (Pty) Ltd-JHB	Perkinelmer
Anglogold Ashanti Ltd	Fraser Alexander (Pty) Ltd	Polysius A Division Of Thyssenkrupp Industrial Sol
Arcus Gibb (Pty) Ltd	G H H Mining Machines (Pty) Ltd	Precious Metals Refiners
Atlas Copco Holdings South Africa (Pty) Limited	Geobruigg Southern Africa (Pty) Ltd	Rand Refinery Limited
Aurecon South Africa (Pty) Ltd	Glencore	Redpath Mining (South Africa) (Pty) Ltd
Aveng Engineering	Hall Core Drilling (Pty) Ltd	Rocbolt Technologies
Aveng Mining Shafts and Underground	Hatch (Pty) Ltd	Rosond (Pty) Ltd
Axis House Pty Ltd	Herrenknecht AG	Royal Bafokeng Platinum
Bafokeng Rasimone Platinum Mine	HPE Hydro Power Equipment (Pty) Ltd	Roytec Global (Pty) Ltd
Barloworld Equipment -Mining	IMS Engineering (Pty) Ltd	RungePincockMinarco Limited
BASF Holdings SA (Pty) Ltd	Ivanhoe Mines SA	Rustenburg Platinum Mines Limited
BCL Limited	Joy Global Inc.(Africa)	Salene Mining (Pty) Ltd
Becker Mining (Pty) Ltd	Kudumane Manganese Resources	Sandvik Mining and Construction Delmas (Pty) Ltd
BedRock Mining Support Pty Ltd	Leco Africa (Pty) Limited	Sandvik Mining and Construction RSA(Pty) Ltd
BHP Billiton Energy Coal SA Ltd	Longyear South Africa (Pty) Ltd	SANIRE
Blue Cube Systems (Pty) Ltd	Lonmin Plc	Sebilo Resources (Pty) Ltd
Bluhm Burton Engineering Pty Ltd	Lull Storm Trading (Pty) Ltd	SENET (Pty) Ltd
Bouygues Travaux Publics	Magnetech (Pty) Ltd	Senmin International (Pty) Ltd
CDM Group	Magotteaux (Pty) Ltd	Smec South Africa
CGG Services SA	MBE Minerals SA Pty Ltd	Sound Mining Solution (Pty) Ltd
Minerals Council South Africa	MCC Contracts (Pty) Ltd	SRK Consulting SA (Pty) Ltd
Coalmin Process Technologies CC	MD Mineral Technologies SA (Pty) Ltd	Technology Innovation Agency
Concor Opencast Mining	MDM Technical Africa (Pty) Ltd	Time Mining and Processing (Pty) Ltd
Concor Technicrete	Metalock Engineering RSA (Pty)Ltd	Timrite Pty Ltd
Council for Geoscience Library	Metorex Limited	Tomra (Pty) Ltd
CRONIMET Mining Processing SA Pty Ltd	Metso Minerals (South Africa) Pty Ltd	Ukwazi Mining Solutions (Pty) Ltd
CSIR Natural Resources and the Environment (NRE)	Minerals Operations Executive (Pty) Ltd	Umgeni Water
Data Mine SA	MineRP Holding (Pty) Ltd	Webber Wentzel
Department of Water Affairs and Forestry	Mintek	Weir Minerals Africa
Digby Wells and Associates	MIP Process Technologies (Pty) Limited	WorleyParsons RSA (Pty) Ltd
DMS Powders	Modular Mining Systems Africa (Pty) Ltd	
DRA Mineral Projects (Pty) Ltd	MSA Group (Pty) Ltd	

MINE SAFE 2018

Striving for Zero Harm
Driving Excellence through Compliance

Gallagher Convention Centre,
Johannesburg



Technical Conference and Industry day

29–30 August 2018—Conference
31 August 2018—Industry Awards Day

WHO SHOULD ATTEND

- The conference should be of value to:
- Safety practitioners
 - Mine management
 - Mine health and safety officials
 - Engineering managers
 - Underground production supervisors
 - Surface production supervisors
 - Environmental scientists
 - Minimizing of waste
 - Operations manager
 - Processing manager
 - Contractors (mining)
 - Including mining consultants, suppliers and manufacturers
 - Education and training
 - Energy solving projects
 - Water solving projects
 - Unions
 - Academics and students
 - DMR.

For further information contact:

Camielah Jardine
Head of Conferencing, SAIMM
Tel: +27 11 834-1273/7
Fax: +27 11 833-8156 or +27 11 838-5923
E-mail: camielah@saimm.co.za
Website: <http://www.saimm.co.za>

OBJECTIVES

The conference will focus on improving health, safety and the environmental impact in the mining and metallurgy industry and highlight actions to be taken. It will act as a platform for learning and allow people to share ideas on safety, health and the environment as well as local communities relationship (issues).

This conference aims to bring together management, DMR, Chamber of Mines, Unions and health and safety practitioners at all levels from the industry to share best practice and successful strategies for zero harm and a value-based approach to health and safety. It will address the main challenges in the mining industry such as logistics, energy and safety of employees, contractors and the communities.

SPONSORSHIP

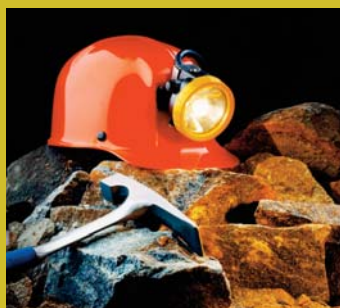
Sponsorship opportunities are available. Companies wishing to sponsor or exhibit should contact the Conference Co-ordinator.



SAIMM
THE SOUTHERN AFRICAN INSTITUTE
OF MINING AND METALLURGY



SUPPORTED BY:



Conference Announcement

MINING WITH



ELBROC
MINING PRODUCTS (PTY) LTD

ELBROC OMNI PROP

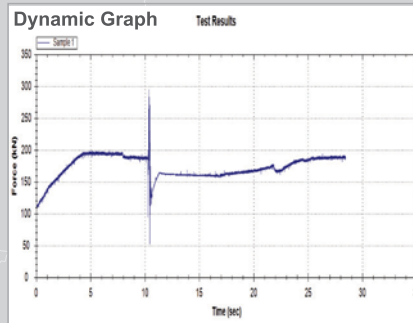
Dynamic Support

The Omni sacrificial and re-usable hydraulic prop performs in accordance with COMRO guidelines for rock-burst and rock-fall conditions.

- Safe remote installation
- Resilient in rock-burst conditions
- Superb energy absorption
- Can accommodate numerous seismic events
- Constant support resistance
- Reusable
- Light, easy and quick to install
- Cannot be over extended
- Standard attachments
- Controlled yielding

OMNI 89

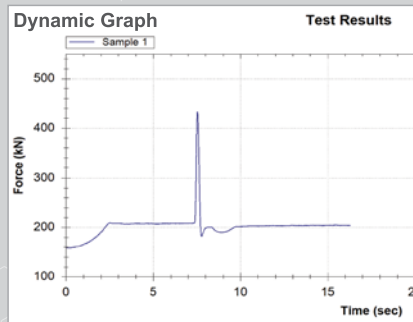
- 89mm diameter
- 20 ton support resistance
- Blast on dynamic load bearing
- Covers stoping widths up to 2.0m
- Light weight



OMNI 89

OMNI 127

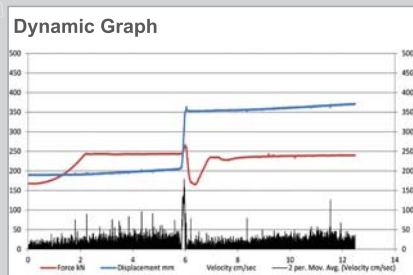
- 127mm diameter
- 20 ton support resistance
- Blast on dynamic load bearing
- Covers stoping widths up to 4.5m



OMNI 127

OMNI 150

- 150mm diameter
- 20 & 40 ton support resistance
- Blast on dynamic load bearing
- Covers stoping widths up to 6m
- Longer lengths available



OMNI 150
20 Ton

OMNI 150
40 Ton



FOR OUR FULL PRODUCT RANGE PLEASE VISIT OUR WEBPAGE

a member of the



Tel: 011 974-8013 • sales@elbroc.co.za

www.elbroc.co.za

